



HAL
open science

Phase transformations, microstructure heterogeneities and resulting mechanical properties in as-quenched and tempered martensitic steels

Juan Macchi

► **To cite this version:**

Juan Macchi. Phase transformations, microstructure heterogeneities and resulting mechanical properties in as-quenched and tempered martensitic steels. Materials Science [cond-mat.mtrl-sci]. Université de Lorraine, 2022. English. NNT : 2022LORR0248 . tel-04008736

HAL Id: tel-04008736

<https://hal.univ-lorraine.fr/tel-04008736>

Submitted on 28 Feb 2023

HAL is a multi-disciplinary open access archive for the deposit and dissemination of scientific research documents, whether they are published or not. The documents may come from teaching and research institutions in France or abroad, or from public or private research centers.

L'archive ouverte pluridisciplinaire **HAL**, est destinée au dépôt et à la diffusion de documents scientifiques de niveau recherche, publiés ou non, émanant des établissements d'enseignement et de recherche français ou étrangers, des laboratoires publics ou privés.



**UNIVERSITÉ
DE LORRAINE**

**BIBLIOTHÈQUES
UNIVERSITAIRES**

AVERTISSEMENT

Ce document est le fruit d'un long travail approuvé par le jury de soutenance et mis à disposition de l'ensemble de la communauté universitaire élargie.

Il est soumis à la propriété intellectuelle de l'auteur. Ceci implique une obligation de citation et de référencement lors de l'utilisation de ce document.

D'autre part, toute contrefaçon, plagiat, reproduction illicite encourt une poursuite pénale.

Contact bibliothèque : ddoc-theses-contact@univ-lorraine.fr
(Cette adresse ne permet pas de contacter les auteurs)

LIENS

Code de la Propriété Intellectuelle. articles L 122. 4

Code de la Propriété Intellectuelle. articles L 335.2- L 335.10

http://www.cfcopies.com/V2/leg/leg_droi.php

<http://www.culture.gouv.fr/culture/infos-pratiques/droits/protection.htm>

Thèse

Présentée et soutenue publiquement pour l'obtention du titre de

DOCTEUR DE L'UNIVERSITE DE LORRAINE

Mention : Science des Matériaux

par **Juan A. Macchi**

Phase transformations, microstructure heterogeneities and resulting mechanical properties in as-quenched and tempered martensitic steels

Soutenu le 12 décembre 2022

Membres du jury :

Président du jury	Lionel GERMAIN	Professeur, UL LEM3, Metz, France
Rapporteurs :	Anne-Françoise GOURGUES-LORENZON	Professeure, MINES-Paris PSL, Paris, France
	Alexis DESCHAMPS	Professeur, UGA SIMAP, Grenoble, France
Examineur :	Christopher HUTCHINSON	Professeur, Monash University, Victoria, Australie
Membres invités :	Sabine DENIS	Professeure, UL IJL, Nancy, France
	Guillaume GEANDIER	Chargé de recherche CNRS, IJL, Nancy, France
	Frédéric BONNET	Ingénieur de Recherche, ArcelorMittal Maizières SA, Metz, France
Directeur de thèse :	Sébastien ALLAIN	Professeur, UL IJL, Nancy, France
Codirecteur de thèse	Julien DA COSTA TEIXEIRA	Chargé de recherche CNRS, IJL, Nancy, France

Acknowledgements

I would like to firstly thank deeply Anne-Françoise Gourgues and Alexis Dechamps who have accepted to be the “rapporteur(e)s” of the present manuscript. I apologize in advance by its length. I thank Lionel Germain and Christopher Hutchinson who accepted to be “examineurs” (I hope that it will worthy of the long night).

My profound gratitude to my PhD director Sébastien Allain and co-director Julien Teixeira for their guidance and advices, not only regarding my scientific work and development but also about my personal perspectives. I am sorry for the overwork especially when our presentation style differs. My acknowledgement to Guillaume Geandier by his patience (including listening to the music coming from our office), the time shared during the data recollection campaigns at DESY, Hamburg and explanations regarding x-ray data treatment. I would like to particularly recognize Sabine Denis for her pertinent metallurgy signalments as well as for her passionate courses. Frédéric Bonnet is also thanked for his accompaniment throughout these almost 4 years from the master internship to the end of this PhD.

A necessary thank you to all the people who have help in this project (F. Danoix from GPM Rouen; P. Barges, A. Pachon, M. Salib, D. Serra from ArcelorMittal) as well as the engineers, PhD students and interns of the department. To J. Ghanbaja and M. Emo (CC3M at the IJL) a special thanks for your time and involvement in teaching me some of the secrets of the TEM use.

I especially thanks the scientific exchange with Steve Gaudez and Mathias Lamari, the time-laugh-music shared with Clélia Couchet and Felix Royer with whom I have the pleasure of sharing office. Some of those enjoyable moments were also shared with Cecile Rampelberg.

There are some acknowledgements that are extremely difficult to be described by words but I want to give them a shot:

Thanks Hélène for the patience during the writing of the present manuscript and for all the lovely shared experiences.

To my family who I miss deeply every day and without them I could have never reached any of my personal goals. Pa, Ma Lau y Martu los quiero al infinito y más allá!

Résumé étendu

Ce résumé ne reprend que les points principaux de l'étude et est donc non exhaustif. Nous engageons donc le lecteur à lire le document principal pour y retrouver l'intégralité de nos résultats.

Contexte

Les aciers martensitiques ont été utilisés de longue date par l'homme pour des usages agricoles (faux, pioches ...) ou militaires (katana, épées, armures...). On les retrouve encore à l'heure actuelle dans de nombreuses applications où l'on recherche une haute résistance mécanique à la rupture (y compris en fatigue) ou à l'usure. C'est par exemple le cas des trains d'atterrissage des avions ou des carrosseries automobiles. La martensite est l'une des phases les plus résistantes des aciers, avec une limite d'élasticité et une résistance à la traction élevées. Ces propriétés mécaniques permettent d'offrir des structures sûres et légères. En effet, l'épaisseur d'une pièce réalisée avec un matériau conventionnel peut être réduite, et sa masse en conséquence, si elle est réalisée avec un acier martensitique, sans modifier ses performances mécaniques globales. L'allègement des structures est l'une des méthodes clés pour réduire la consommation énergétique, les émissions de gaz à effet de serre et l'empreinte environnementale au sens large de tous les moyens de transport. Les aciers martensitiques ont donc toute leur importance du point de vue socio-économique.

Un exemple notable : l'un des concepts métallurgiques qui a révolutionné le marché et les méthodes de production des pièces automobiles au cours des 20 dernières années est sans aucun doute l'emboutissage à chaud (*hot-stamping* en anglais, également appelé *press-hardening*). Ce procédé consiste à emboutir une pièce à haute température dans l'état austénitique et, ensuite, à la tremper entre outils pour obtenir une structure à l'état martensitique. L'étude des aciers pour emboutissage à chaud (ou *Press-hardening steels* (PHS)) présente donc un fort intérêt industriel et environnemental.

Introduction et problématique

Du point de vue cristallin, la martensite est une phase ferritique cubique centrée (CC), ou légèrement quadratique centrée, formée par la transformation displacive et sans diffusion de l'austénite, phase cubique à faces centrées (CFC), la phase stable à haute température des aciers au carbone. Le processus d'obtention de la martensite consiste ainsi en une austénitisation complète suivie d'un refroidissement rapide, appelé "trempe", du domaine des hautes températures jusqu'à la température ambiante. Ce refroidissement rapide permet d'éviter toute autre transformation diffusive comme la transformation ferritique, perlitique ou bainitique avant la transformation en martensite. Cette dernière commence sous une température seuil, appelée M_s pour *martensite start*, comme définie sur la Figure 1. Comme la transformation martensitique est displacive et indépendante du temps, la cinétique de transformation martensitique est souvent décrite dans la littérature par la célèbre équation de Koistinen-Marburger (KM) qui affirme que la fraction transformée dépend uniquement de la température considérée et de la M_s de l'austénite. Cette

transformation rapide ne permet pas aux atomes de carbone de diffuser hors de la nouvelle structure ferritique, qui est donc métastable du point de vue thermodynamique. Elle s'accompagne aussi d'une déformation de transformation importante et donc de phénomène de relaxation plastique. La martensite brute de trempe contient donc naturellement de fortes densités de dislocations et présente de fortes contraintes internes non relaxées à l'échelle de la microstructure. Une autre spécificité des microstructures martensitiques bas carbone, sujet de l'étude, est leur organisation microstructurale. Elles présentent une structure aciculaire, dite en lattes, avec une microtexture particulière héritée d'une relation d'orientation avec la phase mère. Ces lattes présentent une grande diversité d'épaisseurs mais restent sub-micrométriques (cf. Figure 2a).

Un second traitement thermique, appelé revenu, est souvent appliqué à la martensite brute de trempe dans le but d'améliorer sa ténacité et sa ductilité, au détriment d'une perte en résistance. Ce traitement thermique est effectué à des températures, généralement comprises entre 170 °C (cuisson de la peinture des caisses automobiles) et 400 °C pour les aciers martensitiques mise en forme par roll-forming. Pendant le revenu, plusieurs phénomènes métallurgiques activés thermiquement se produisent, notamment la ségrégation du carbone sur les défauts cristallins, la précipitation de carbures de transition, la décomposition de l'austénite résiduelle et la formation de cémentite. La densité élevée de dislocations dans la martensite de la latte brute de trempe diminue au cours d'un traitement de revenu. Ce dernier phénomène est connu sous le nom de restauration.

Les propriétés mécaniques de la martensite ont été largement étudiées pour son importance technologique. Il est assez bien établi que la martensite à l'état trempé présente une résistance mécanique élevée, une limite d'élasticité conventionnelle élevée mais un faible allongement total. Elle est considérée comme une microstructure "fragile" dans ce sens. Cette observation trop rapide cache en fait une complexité importante car les propriétés des aciers martensitiques dépendent fortement de leur teneur en carbone ou de leur état de revenu. De plus, si l'on regarde de plus près leur comportement mécanique, on constate qu'ils présentent une faible limite de microplasticité et un très fort écrouissage initial, caractéristique que l'on retrouve paradoxalement dans les aciers multiphasés¹. Même si les aciers martensitiques sont connus et utilisés depuis des millénaires, l'origine de leur résistance et de leur écrouissage est restée une source de controverse. Un changement de paradigme s'est produit au cours des dernières années concernant leur compréhension. De nombreux chercheurs ont mis en évidence l'intérêt de décrire la martensite de latte non pas comme une phase « uniforme et homogène » mais plutôt comme un agrégat multiphasé. Cet agrégat serait le résultat de la nature séquentielle de la transformation de phase de la martensite, progressivement, de la température M_s à la température ambiante².

La Figure 1 représente schématiquement comment se forme progressivement la microstructure martensitique (microstructure et cinétique) et pourquoi il en résulterait une forte dispersion des grandeurs microstructurales (densités de dislocations, taille des structures, état de ségrégation du carbone) et mécaniques (contraintes internes), dans la microstructure finale à température ambiante.

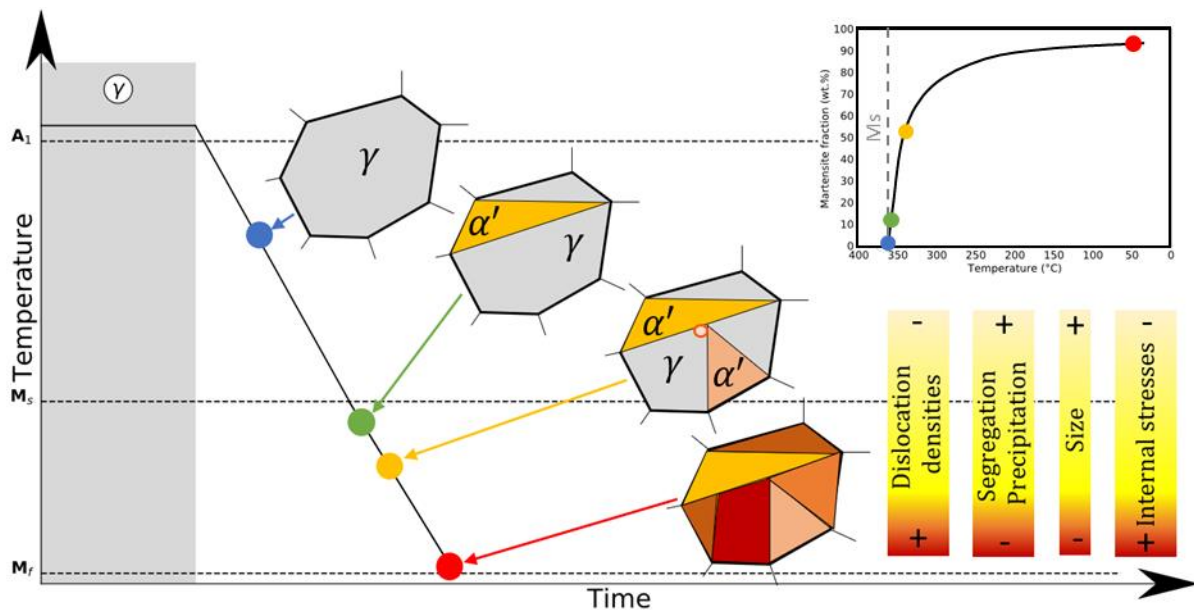


Figure 1: Représentation schématique de la nature séquentielle de la transformation martensitique montrant comment la distribution des densités de dislocations, de l'état de ségrégation/précipitation, de la taille caractéristique des lattes et les contraintes internes apparaissent à l'échelle de la microstructure tout au long du processus.

Dans ce nouveau cadre original, l'objectif principal de cette étude est d'améliorer la compréhension de la relation entre la nature séquentielle de la transformation martensitique, les distributions de microstructure associées (densités de dislocation, tailles de microstructure, états de carbone, contraintes internes) et le comportement mécanique final. Une autre originalité de ce travail est de montrer que les effets de la trempe et de revenu peuvent être traités dans le même cadre et un modèle unifié pour les aciers trempés/revenus est proposé. Ce travail est basé à la fois sur une approche expérimentale multi-échelle et sur la modélisation, ce qui permet de consolider et d'aborder les questions métallurgiques et mécaniques.

Chapitre 1 : Matériaux et Méthodes

Dans la présente étude, trois aciers avec des teneurs en carbone différentes (0.11, 0.21, et 0.31 % en poids) fournis par ArcelorMittal Maizières Research SA ont été utilisés. Il s'agit d'aciers bas carbone destinés à la fabrication de tôles minces, ce qui n'enlève rien à la généralité de l'étude.

La microtexture et les tailles résultantes des aciers sont étudiées par microscopie électronique à balayage et diffraction des électrons rétrodiffusés MEB-EBSD. L'évolution des densités de dislocation et leur distributions spatiales sont caractérisées par des expériences in situ de diffraction de rayons X à haute énergie (DRXHE). Des expériences de tomographie par sonde atomique tomographique 3D (3DSAT) ont été réalisées pour caractériser l'état de ségrégation du carbone à l'état trempé. La DRXHE in situ a également été appliquée pour étudier l'évolution de la séquence de précipitation et la restauration pendant le revenu. La taille des carbures a été mesurée post mortem par Microscopie Electronique à Transmission (MET). Le comportement mécanique en traction a été caractérisé post mortem pour les états trempés et revenus des trois aciers étudiés.

Chapitre 2

La Figure 2 a montre une cartographie en EBSD de la microstructure en lattes de l'échantillon 0.2C trempé. L'application de la méthode des intercepts sur ces cartographies permet de déterminer la taille moyenne des blocs, i.e. des groupes de lattes ayant une orientation cristalline similaire. Les joints entre les blocs semblent être en effet des obstacles majeurs au glissement plastique dans ces microstructures et donc leur taille joue nécessairement un rôle fondamental sur la limite d'élasticité locale d'un bloc. Après corrections stéréologiques, la distribution spatiale des tailles de ces blocs a également été obtenue. Une teneur en carbone plus élevée produit une diminution de leur taille moyenne et rétrécit la largeur de la distribution associée, comme observé sur la Figure 2 b.

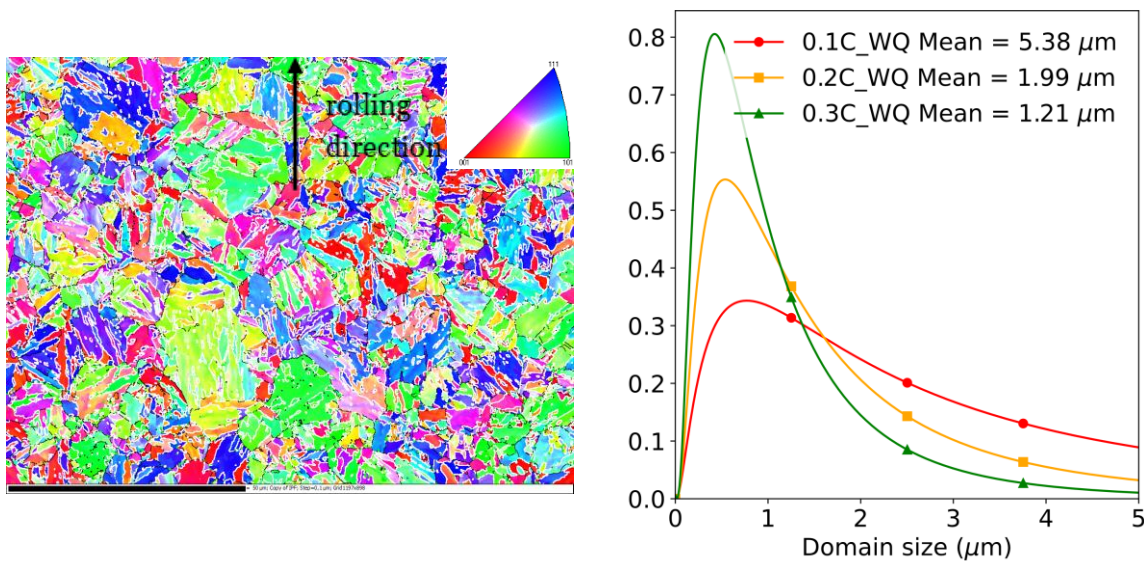


Figure 2: a) Cartographie EBSD de la microstructure en lattes de l'échantillon 0.2C trempé. b) Distribution de la densité de probabilité de taille (principalement des blocs) avec la correction stéréologique pour les trois aciers étudiés avec un angle de désorientation cristalline critique égal à 14°.

Dans un second temps, nous avons cherché à décrire la microstructure de dislocations. La méthode Williamson-Hall modifiée a été utilisée pour déterminer in situ lors d'expériences de DRXHE la densité de moyenne de dislocations au cours de la transformation martensitique. Les valeurs finales ont été confrontées à des déterminations en MET et EBSD sur des échantillons post mortem. Une nouvelle méthode a été développée pour déconvoluer l'effet de la tétragonalité sur les largeurs à mi-hauteur des pics de diffraction. Les valeurs "corrigées" ainsi obtenues sont en bon accord avec celles rapportées dans la littérature. Une nouvelle méthode est aussi proposée pour estimer la distribution spatiale de la densité de dislocations sur la base de l'évolution de la densité de dislocations moyenne avec la fraction transformée. Les distributions calculées des densités de dislocation locales s'élargissent avec la teneur en carbone comme le montre la Figure 3.

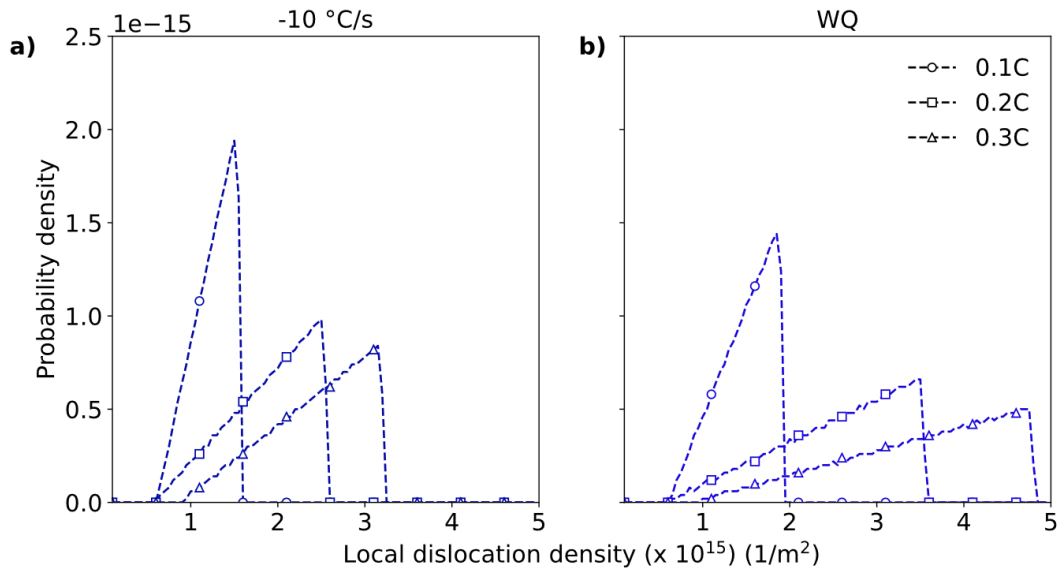


Figure 3: Distributions de densités de probabilité de la densité de dislocations locale pour les trois aciers utilisés après trempe à -10 °C/s (sous la température Ms) en a) et par trempe à l'eau (-1000 °C/s) en b).

L'évolution de la densité moyenne de dislocations due à la restauration lors du revenu a également été suivie par des expériences in situ pour les trois alliages étudiés et en utilisant de faibles températures de maintien (200, 300 et 400 °C). Comme attendu, la cinétique de restauration est bien thermiquement activée mais de façon surprenante une stagnation de la restauration est observée aux temps longs à 300 et 400 °C. Cette restauration a été modélisée par une loi empirique, qui sert de donnée d'entrée importante pour le modèle de revenu du chapitre 3. Ce modèle a permis en outre de déterminer l'évolution des distributions spatiales des dislocations, permettant de mettre en évidence un rétrécissement de la distribution avec la sévérité du revenu.

Chapitre 3

La martensite est une phase métastable qui a tendance à se décomposer en ferrite et en cémentite lors d'un traitement thermique. Avec la température et le temps, les atomes de carbone diffusent, ségrègent sur des défauts, forment des carbures de transition jusqu'à la formation de carbures de cémentite, plus stables. Classiquement, le processus de revenu peut être divisé en quatre stades. De la température ambiante à environ 100 °C, le "stade zéro", également appelé vieillissement, se produit avec la ségrégation du carbone dans les défauts et/ou avec de la décomposition spinodale. A température plus élevée, au cours du premier stade, la concentration en carbone dans la martensite diminue en raison de la formation de carbures de transition. Au cours du deuxième stade, l'austénite résiduelle se décompose. Enfin, la cémentite précipite au détriment des carbures de transition au cours du troisième stade.

La ségrégation du carbone au voisinage des dislocations a été caractérisée par des expériences de SAT3D et modélisée sur la base d'un modèle dérivé de la littérature. Ces travaux ont clairement permis de conclure que le carbone est déjà bien ségrégué sur les défauts dès la trempe (mécanisme d'auto-revenu).

La séquence de précipitation a été caractérisée par des expériences DRXHE in situ pour les trois aciers étudiés. Par exemple, la Figure 4 présente des diffractogrammes obtenus pendant le chauffage

à 400 °C de l'acier 0,3C, sur lesquels on peut observer la décomposition de l'austénite (pic gamma) ainsi que la formation du carbure de transition ϵ (300-375 °C) et la formation de cémentite θ (au-dessus de 375 °C). Il s'agit d'un agrandissement entre deux pics de diffraction majeur de la martensite (α).

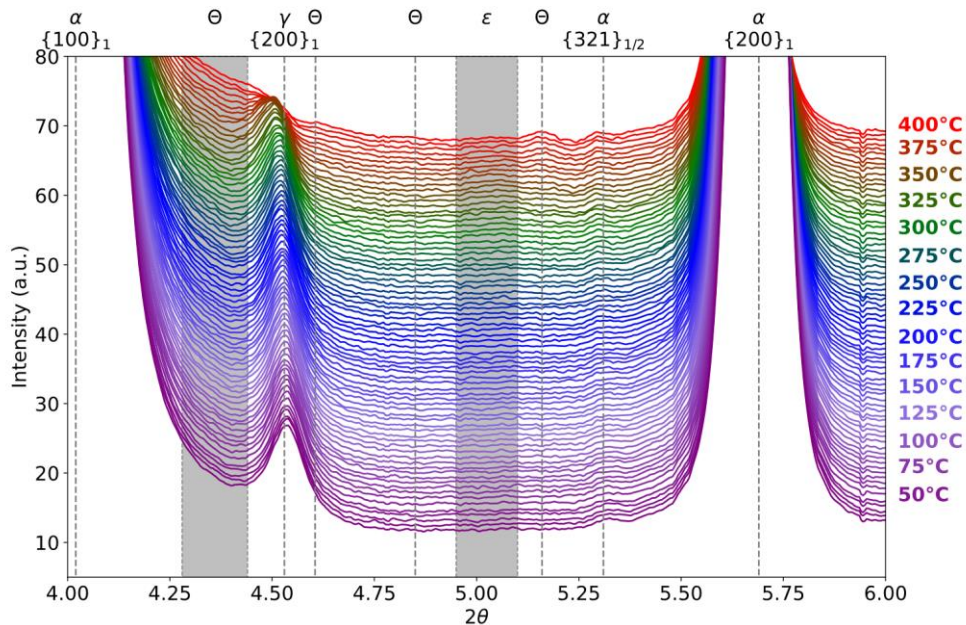


Figure 4: Diffractogrammes pendant le revenu jusqu'à 400 °C d'un échantillon à 0.3%C trempé.

L'un des résultats principaux de ce travail expérimental est que nous avons bien mis en évidence la présence de carbures epsilon lors du revenu de l'acier à 0.3C mais peu ou pas dans les aciers plus bas carbone. Dans tous les cas, la cémentite est par contre présente à la fin du chauffage, avec une fraction observée croissante avec la teneur en carbone et la sévérité du revenu (temps/température). La taille de ces carbures de cémentite caractérisée par MET augmente aussi en conséquence.

Un modèle de précipitation à base physique précédemment développé au laboratoire a été amélioré pour prendre en compte la ségrégation du carbone sur les dislocations. Il s'agit d'un modèle thermocinétique à champs moyen qui permet de décrire la germination, croissance et coalescence des différents carbures ainsi que leur compétition. Ce modèle permet de calculer la fraction, la distribution de tailles, et les densités volumiques de chaque type de carbure analysé³.

La ségrégation du carbone sur les dislocations a été modélisée par une approche thermocinétique de premier principe et calibré sur les données de SAT3D. Le modèle complet reproduit fidèlement les évolutions de fraction et de taille des carbures observés expérimentalement. Il permet en outre d'expliquer que dans le cas de l'acier à 0.1C, la ségrégation inhibe presque totalement la formation de carbures de transition en piégeant l'intégralité du carbone disponible, comme observé sur la Figure 5.a et que la densité de dislocation joue un rôle clé dans la séquence de précipitation (à des valeurs élevées, les carbures de transition sont désavantagés par rapport à la cémentite), comme le montre la Figure 5.b.

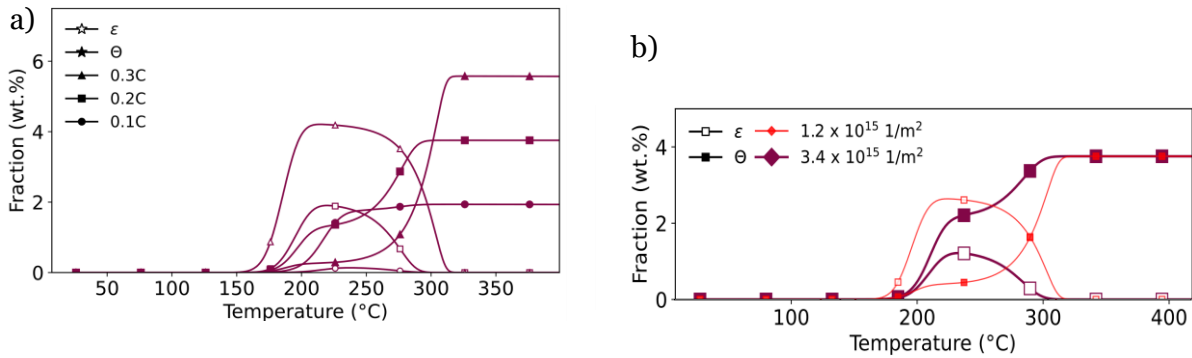


Figure 5: a) Evolution des fractions de carbures epsilon et de cémentite pendant le chauffage jusqu'à 400 °C pour les trois aciers étudiés. b) Similaire à a) en faisant varier la densité initiale de dislocations dans l'acier 0.2C.

Chapitre 4

L'approche micromécanique développée dans ces travaux est basée sur l'hypothèse que la martensite est un agrégat hétérogène avec différentes contraintes d'écoulement locales, hétérogénéités dues à la nature séquentielle de la transformation martensitique. Les contraintes d'écoulement locales sont dans ce cas la somme d'une limite d'élasticité locale liée à la microstructure et de contraintes internes déviatoriques⁴.

La distribution de la limite d'élasticité locale liée à la microstructure (appelée plus tard distribution YS de la microstructure) est prédite sur la base des observations expérimentales présentées dans les chapitres précédents. Les contributions des densités de dislocations, des tailles de microstructure, des précipités sont évaluées séparément et combinées judicieusement pour décrire les états trempé et revenu dans un cadre unique.

La Figure 6 est une représentation schématique du modèle micromécanique qui considère un assemblage d'éléments en interaction mécanique, soumis à un chargement macroscopique, assemblage présentant une distribution de la limite d'élasticité microstructurale (à gauche) et une distribution des contraintes internes (à droite). La limite élastique microstructurale de chaque élément dépend de sa densité des dislocations, sa taille de domaine microstructural et de l'état de son carbone (solution solide / ségrégré / précipité). Les contraintes internes pour chaque élément sont réparties de façon aléatoire et non corrélée. La distribution de ces dernières a été postulée empiriquement pour reproduire les résultats expérimentaux, en l'absence de données expérimentales évidentes ou de modèles dans la littérature. Il s'agit donc d'une approche stochastique à champs moyen pour décrire des chargement unidirectionnel monotone ou non (l'application du modèle selon des trajets Bauschinger a été présentée lors de la soutenance).

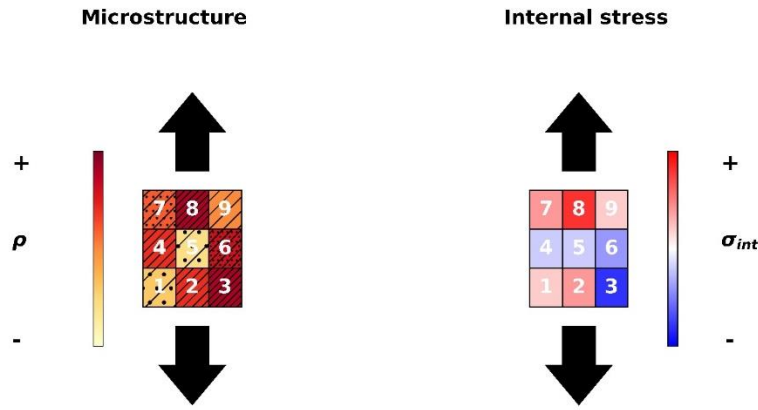


Figure 6: Schéma du modèle micromécanique considérant une distribution de la limite élastique de la microstructure (à gauche) et une distribution des contraintes internes (à droite). Les couleurs et densités de symboles sur la figure de gauche correspondent à des densités de dislocations, des tailles de domaines microstructuraux et des états de précipitations variables d'un composant à l'autre de la microstructure. De la même façon, les échelles de couleurs à gauche correspondent à des états de contraintes variables.

La Figure 7 a montre par exemple les probabilités cumulées de trouver un élément présentant un durcissement par effet de taille donné (F_{size}) et celle pour un durcissement structural (F_{dislo}) pour l'acier à 0.2C brute de trempe sur la base des distributions mesurées. Comme les deux mécanismes sont très probablement corrélés (Figure 1), la probabilité combinée F_{comb} peut être calculée par une approche que nous avons qualifié de soft-soft. $F_{comb+ss}$ tient compte en plus des effets de durcissement en solution solide (éléments substitutionnels et carbone). Les densités de probabilité correspondantes sont représentées sur la Figure 7 b. La densité de probabilité des effets combinés présente des valeurs comprises entre 575 MPa à 3700 MPa.

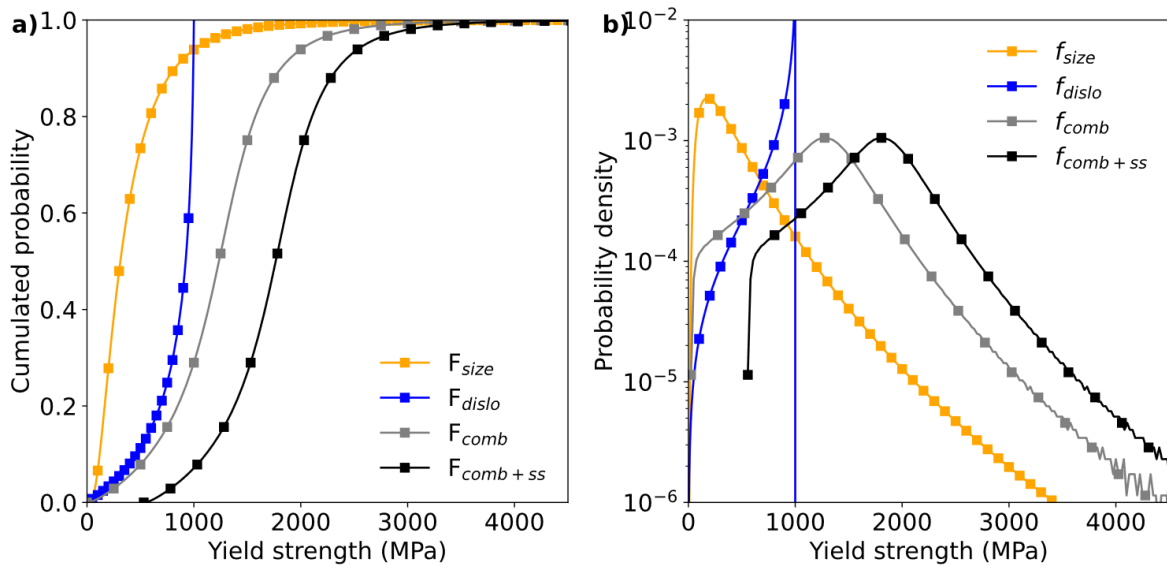


Figure 7: a) Probabilités cumulées de trouver un élément présentant un durcissement par effet de taille donné (F_{size} en orange) et celle pour un durcissement structural donné (F_{dislo} en bleu) indépendamment. Les effets combinés sont représentés par les courbes noire et grise respectivement. b) Densité de probabilité associée à a) avec le même code couleur.

À partir de la distribution des contraintes d'écoulement, le comportement macroscopique en traction est ensuite un simple modèle d'homogénéisation selon Hill et les interactions entre les différents éléments sont gérées par une loi de location simple à 1 paramètre. Les courbes de comportement expérimentales et modélisées pour les 3 aciers bruts de trempe sont présentées sur la Figure 8 a, et

les courbes d'érouissage correspondantes sur la Figure 8 b. Une bonne concordance est trouvée dans les trois cas, en particulier pour les aciers à 0,2C et 0,3C.

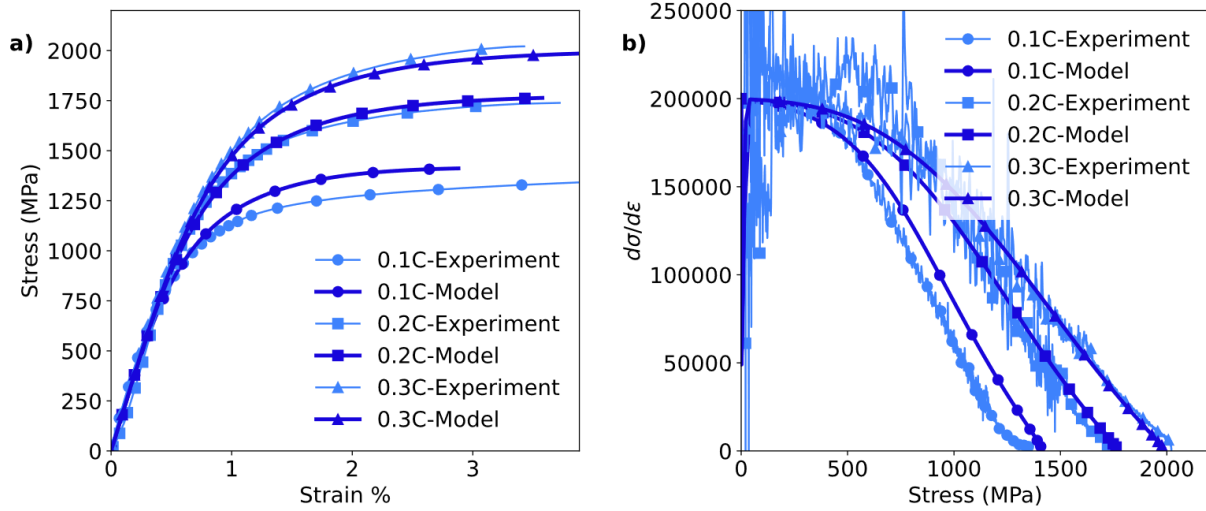


Figure 8: a) Courbes de comportement expérimentales et modélisées des trois aciers étudiés à l'état trempé (0.1C_WQ, 0.2C_WQ et 0.3C_WQ). b) Courbes d'érouissage obtenues à partir des courbes présentées en a).

A partir des même distributions de contraintes d'écoulement que dans les états trempés, les comportements en traction des états revenus peuvent être calculés en considérant les différents mécanismes se produisant pendant le revenu. La distribution des contraintes internes évolue par relaxation et celle des densités locales de dislocations par restauration. Le durcissement par précipitation se substitue progressivement au durcissement pas la solution solide selon le modèle présenté au chapitre 3. Le couplage entre précipitation et restauration a été considéré. Les Figures 9 montrent les courbes de comportement expérimentales (E) et modélisées (M) à titre d'exemple ; en a, il s'agit de l'effet de la température de revenu et en b l'effet de la durée de revenu. Globalement, le modèle micromécanique reproduit de façon très satisfaisant les effets du revenu selon le même cadre que pour les aciers bruts de trempe.

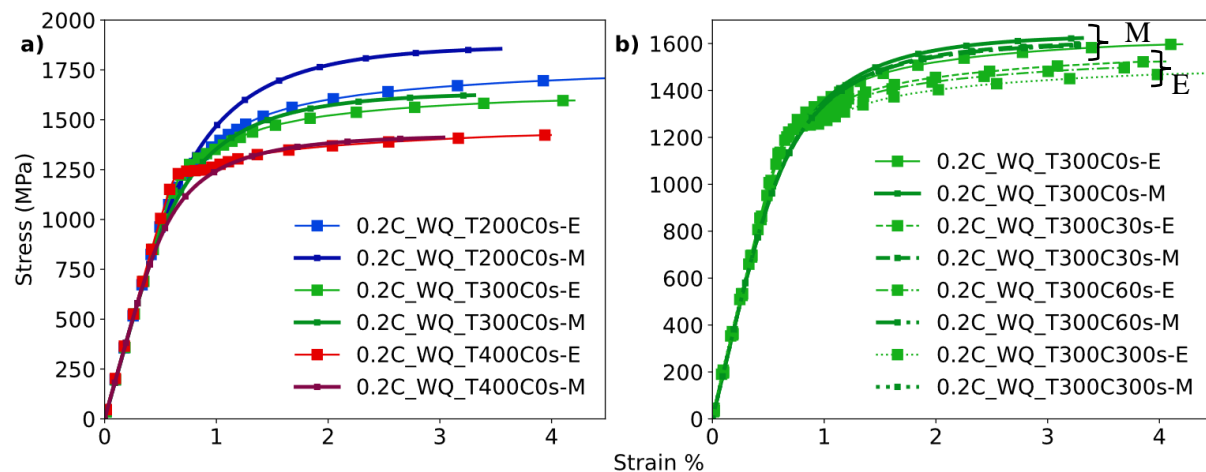


Figure 9: Evolution des comportements en traction expérimentaux (désignés par le suffixe E) et modélisés (désignés par le suffixe M) après différentes conditions de revenu pour l'acier 0.2C. a) L'effet de la température de revenu est présenté avec un temps de maintien constant (0s). b) L'effet du temps de maintien est présenté pour le revenu à 300 °C.

Conclusions

Pour conclure, ce travail est une étape supplémentaire vers une meilleure compréhension des aciers martensitiques à faible teneur en carbone, avec un accent particulier mis sur le rôle et l'importance des hétérogénéités de la microstructure et des contraintes internes pour expliquer leur comportement micromécanique.

Les hétérogénéités spatiales de la microstructure martensitique résultent de la nature séquentielle de la transformation et concernent les composants de la microtexture et leurs tailles respectives (organisation en lattes/blocs/paquets des variants), la densité des dislocations et l'état de ségrégation/précipitation du carbone. Les résultats expérimentaux présentés dans ce travail sont basés sur l'analyse systématique de l'ensemble de trois alliages avec des teneurs en carbone différentes de 0,1 à 0,3 % en poids de C, dans l'état trempé ou trempé et revenu, à différentes échelles.

La nature séquentielle de la transformation martensitique nous conduit à adopter une corrélation statistique entre les distributions spatiales des tailles et des densités de dislocations de la microstructure. La distribution résultante des limites d'élasticité locales à l'échelle de la microstructure est la principale entrée du modèle micromécanique basé sur la stochastique et la physique développé dans le présent travail.

Le comportement mécanique de la martensite est connu pour évoluer lors de l'application d'un traitement de revenu en raison de différents phénomènes thermiquement activés. Une étude multi-échelle du revenu (combinant les techniques 3DSAT / MET / DRXHE in situ) a été réalisée pour déterminer la ségrégation et la précipitation du carbone. La ségrégation et la précipitation des carbures ont également été modélisées par un modèle thermocinétique à champ moyen. Ce dernier a permis de prédire la suppression des carbures de transition à faible teneur en carbone en raison de la ségrégation du carbone en atmosphères de Cottrell au niveau des dislocations, ainsi que l'effet clé de la densité des dislocations sur la précipitation.

Le durcissement par précipitation (dépendant de la densité locale de dislocations), la restauration des dislocations et la relaxation des contraintes internes ont été intégrés dans le modèle micromécanique pour décrire le revenu, en plus des entrées déjà discutées. Par conséquent, nous sommes en mesure de comprendre et de prédire, dans un cadre unique, les principales caractéristiques du comportement mécanique des aciers martensitiques trempés, en particulier leur résistance et leur écrouissage plus faibles par rapport aux microstructures brutes de trempe.

[1] S. Allain, O. Bouaziz, M. Takahashi, Toward a New Interpretation of the Mechanical Behaviour of As-quenched Low Alloyed Martensitic Steels, *ISIJ Int.* 52 (2012) 717–722. <https://doi.org/10.2355/isijinternational.52.717>.

[2] L. Morsdorf, C.C. Tasan, D. Ponge, D. Raabe, 3D structural and atomic-scale analysis of lath martensite: Effect of the transformation sequence, *Acta Mater.* 95 (2015) 366–377. <https://doi.org/10.1016/j.actamat.2015.05.023>.

[3] S. Gaudez, Kinetics and microstructural evolutions during the tempering of martensitic and nano-bainitic low alloyed steel: in situ experimental study and modelling, PhD thesis, Université de Lorraine, 2021. <http://www.theses.fr/2021LORRO016> (accessed February 17, 2022).

[4] L.Y. Wang, Y.X. Wu, W.W. Sun, Y. Bréchet, L. Brassart, A. Arlazarov, C.R. Hutchinson, Strain hardening behaviour of as-quenched and tempered martensite, *Acta Mater.* (2020). <https://doi.org/10.1016/j.actamat.2020.08.067>.

Contents

Chapter I

I.1 Steel compositions.....	- 12 -
I.2 Heat treatments	- 12 -
I.3 Labeling system	- 14 -
I.4 Characterization technics	- 15 -
I.5 Conclusions of the chapter.....	- 30 -

Chapter II

II.1 Focused state of the art.....	- 32 -
II.2 Microstructure sizes	- 41 -
II.3 Dislocation density	- 46 -
II.4 Conclusions of the chapter	- 68 -

Chapter III

III.1 Focused state of the art.....	- 71 -
III.2 Experimental results	- 79 -
III.3 Modeling of tempering.....	- 102 -
III.4 Conclusions of the chapter.....	- 130 -

Chapter IV

IV.1 Focused state of the art.....	- 132 -
IV.2 Results: tensile behavior of the studied steels	- 145 -
IV.3 Tensile behavior model	- 149 -
IV.4 Results and discussion of tensile behavior model.....	- 166 -
IV.5 Conclusions of the chapter	- 180 -

Chapter V

V.1 Summary and key results	- 181 -
V.2 Future work.....	- 183 -

Appendix

Asymmetry	- 185 -
Comparison between gas-quenched and water-quenched 0.2C martensite	- 189 -
Influence of aging before tempering on precipitation	- 193 -
Influence of heating rate on the precipitation	- 195 -
In situ tensile test	- 197 -
Effect of the distribution of deviatoric internal stresses	- 201 -
Pedagogical example of the micromechanical model	- 203 -

Bibliography

General introduction

*"The greatest challenges humans face throw-out their lives are two:
1- the challenge of where to start*

-Sameh Elsayed

The martensite has been used by the humanity for millennia now, from the harden 'ignited iron' referred more than 3000 years ago in Homer's Odyssey (Homer, 900BC) [1], the archaeological findings in Jordan indicating that craftsmen were producing quench-hardened steel swords (ca. 1000 BC) [2] as well as some Celtic tools (400-100 BC) [3].

Applications and context of the study

Applications of martensitic steels are numerous and range from ancient elegantly crafted hand tools and swords [4] to current high-strength, high-fatigue resistant, high-wear resistant parts for machines, tools and dies [5], power transmission, gears and shafts, and demanding load-bearing structures such as aircraft landing gear [6] or body-in-white structures of light-duty vehicles [7,8]. The Oil and Gas industry is also demanding materials with properties that martensite can achieve, being used as pipelines, oil casing and perforating gun pipe which requires excellent impact toughness for safe applications in ultra-deep oil/gas well [9,10].

Martensite is one of the strongest phases in steels with both high yield strength (YS) and ultimate tensile strength (UTS). Such high mechanical properties allow to lighten structures made of steel. In fact, the thickness of a part made with a conventional steel can be reduced if made with a martensitic steel without modifying its mechanical performance. The lightening of structures is one of the key methods to reduce green-gas emissions of all transportation means.

This is why, for example, martensite has attracted the attention of steelmakers to manufacture new alloys, either 100 % martensitic or partially martensitic. Figure 1.a shows the main classes of steel concepts dedicated to automotive market and their relative performance in strength (UTS) and ductility (total elongation). Martensite is a main constituent in all the classes represented in red: Dual Phase (DP), Complex Phase (CP), Quench and Partitioning (Q&P), Martensitic (MART) and Press-Hardened Steels (PHS), i.e. in steels permitting to reach the highest strength, thus with the best lightening potential.

It must also be highlighted that martensite could also appear in steels during a mechanical loading. These latter take often benefit of this strain-induced transformation and show an improved work-hardening rate and superior strength. This particular hardening mechanism is called TRIP effect (Transformation-Induced Plasticity) and is solicited in the steel concepts represented in blue in Figure 1.a.

These martensite-containing steels have all critical importance from the socio-economic point of view.

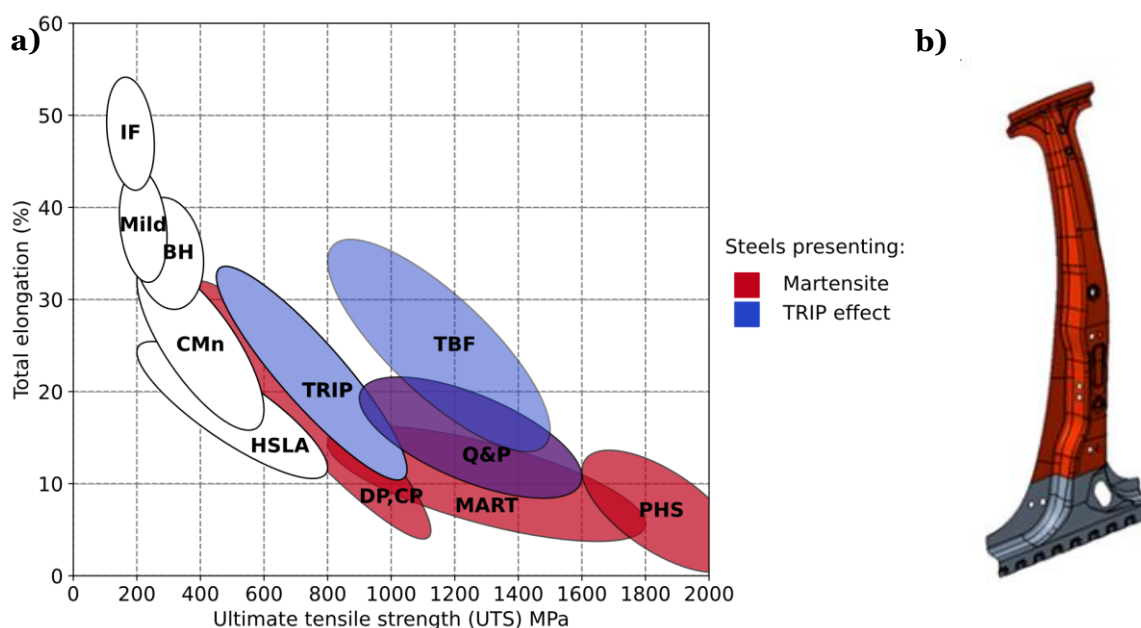


Figure 1: a) Elongation vs Ultimate Tensile Strength (UTS) of the different steel families for the automotive market (flat products). Product classes containing martensite are represented in red and the ones taking benefit from the TRIP effect are represented in blue. b) Example of a “B-pillar” used in automotive industry after [11].

One of the metallurgical concepts that has revolutionized the market and production methods of automotive parts over the past 20 years is undoubtedly hot stamping (also called press-hardening). This process consists mainly in stamping the workpiece at high temperature (in the austenitic state) and, then, quenching it between tools. This process makes it possible to benefit from the excellent hot formability of the steel and from the very high resistance obtained on the final part by quenching. This technology was therefore enabled by the exceptional properties of martensite. One example of parts (a so called “B-pillars”) now often produced by the car manufacturers by hot stamping is shown in Figure 1.b.

The press-hardening process itself requires a simple single-step heat treatment decreasing the cost and the carbon footprint of the production of the part. Hence, the study of PHS presents an industrial and environmental relevance. The importance of this issue prompted funding for their implementation in a fourth-generation industry. A Horizon2020 - Research Funds for Coal and Steel (RFCS) project named “Advanced metallurgical and micromechanical modelling to deploy the microstructural tailoring potential of press hardening” (MiPre) has been recently funded. The present study is not directly funded by the mentioned project but has contributed to the project.

The present study has been developed at the Institut Jean Lamour (IJL) funded by the i-Site Lorraine Université d’Excellence (LUE). It is framed on a larger collaboration with ArcelorMittal Maizières Research SA (AM) located at Maizières les Metz, also partner at the MiPre project.

In the present study, three steels with different carbon content provided by AM will be utilized. However, the methodologies and models developed in the present manuscript are more general and could be applied not only to those steels (belonging to a family of flat products) but to others martensitic steels (long and forged products as well).

Fundamentals about martensitic transformation

The martensite transformation in steels by a heat treatment is probably one of the earliest recognized examples of a phase transformation at the solid state [12]. Martensite is a body-centered cubic (BCC) phase from the crystalline point of view formed from the displacive transformation of the face centered cubic (FCC) phase austenite. This transformation is often obtained by a heat treatment as austenite is stable in carbon steels only at high temperature. The conventional process to obtain martensite consists, thus, of a full austenitization followed by a fast cooling, named “quench”, from the high temperature domain down to the room temperature. This fast cooling permits to avoid any time-dependent diffusive transformations, such as the pro-eutectoid ferritic or pearlitic transformations and even the bainite transformation. The martensite transformation starts at a threshold temperature, called M_s for martensite start, which depends mainly on the chemical composition of the alloy and on the prior austenite grain size (PAGS). The transformation is progressive below M_s but does not depend on time, but solely on the temperature.

The M_s temperature can be experimentally determined [13,14] as well predicted based on the steel composition and the prior austenitic grain (PAG) size [15–17]. In the following, an example of an expression to calculate the M_s temperature based only on the chemical composition is presented as well as another in which the effect of the PAGS is accounted for:

$$M_s (^{\circ}C) = 545 - 470.4 \times C - 6.96 \times Si - 37.7 \times Mn - 21.5 \times Cr + 38.9 \times Mo \quad \text{Equation 1 [15]}$$

$$M_s (^{\circ}C) = T_1 - \frac{\left(1015 + W_{\mu} + 370 \times \exp\left(-6 * \frac{D_{\gamma}}{11}\right) + 350/\sqrt{D_{\gamma}}\right)}{7.22} \quad \text{Equation 2 [17]}$$

$$\text{with } T_1 = 718.3 - 291 \times C - 1.8 \times Si - 24 \times Mn - 5.6 \times Cr - 18.4 \times Ni + 3.5 \times Mo$$

$$W_{\mu} = 670 \times \sqrt{C} + \sqrt{\frac{195 \times \sqrt{Mn} + 140 \times \sqrt{Si} + 170 \times \sqrt{Cr}}{+5 \times \sqrt{Ni} + 205 \times \sqrt{Mo}}}$$

with the elements fractions in weight.

The product phase obtained has, therefore, the same chemical composition as the parent phase. From the thermodynamic point of view, martensite is thus metastable and its resulting supersaturation in carbon leads to a distortion of the crystalline lattice, which is not strictly cubic as a consequence. Zener’s seminal work show that the interstitial carbon atoms would produce a tetragonal lattice (Body-Centered Tetragonal, BCT) by allocating octahedral voids in a favorized direction [18].

The martensite, its mechanical properties and evolutions upon thermal treatment has been the subject of study of several works, some of them presented in the following reviews [9,19,20] or in books [12,21,22].

It is not the aim of the present introduction to enter in a detailed description but to introduce some general fundamentals which will allow to introduce the goals and strategy of the present work.

A more detailed focused state of the art will be presented at the beginning of the following chapters. Each focused state of the art presents the different process and phenomena discussed in the chapter.

Structure at room temperature

The mechanisms of the martensitic transformation have been the subject of study of different works starting from the seminal work of Bain [23]. In the mentioned study the formation of the BCT structure is described by a compression and dilatation of the FCC matrix. The orientation relationship (OR) predicted by Bain has not however been experimentally observed and more complex transformation mechanisms have been later proposed. The latter considers an invariant plane, a volume change and a shear and other ORs are proposed. Some of the most often identified are the Kurdjumov-Sachs (KS) [24], the Nishiyama-Wassermann (NW) [25], and the Greninger-Troiano (GT) [26].

The transformation from the austenite, face centered cubic phase, into the martensite, tetragonal centered phase, thus produces a volume change and a shear deformation. The volume change is known to be function of the nominal carbon content [27].

The mentioned volume change and shear produce a stress state during the transformation itself which is partially relaxed by different mechanisms such as the plastic deformation of both phases (martensite and austenite) by dislocation gliding or twinning but also by the formation of new martensite unit with specific crystalline orientations with respect to the already formed units. This latter process is called variant selection and often leads to the formation of self-accommodating variants [28,29].

This relaxation is only partial and it is well known that the martensitic microstructure has a high level of internal stresses at the phase scale after transformation [30–32]. Chapter IV will give a description of those internal stresses and their particular role on the tensile behavior of these steels.

The different plasticity mechanisms produce different martensitic morphologies, lath type when dislocation plasticity occurs and plate when it is twinning. It has been shown that the fraction of each kind depends on the nominal carbon content of the steel as presented in Figure 2.

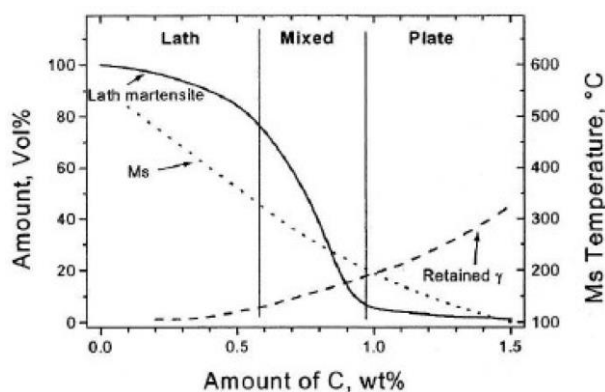


Figure 2: Fraction of the lath and plate morphologies as function of the carbon content. From [33].

The lath martensite, in which in the present study will focus, is composed by laths as it names specifies. A lath is a single unit of martensite with a lamellar morphology. A parallel group of them with a same variant of the Kurdjumov-Sachs OR compose a block, while a group of blocks with a same habit plane compose a packet [34]. It can be observed that the lath martensite presents a hierarchical microstructure which has a high density of boundaries with high and low angle disorientations.

These particular microstructure organizations can be revealed by crystalline-sensitive techniques such as SEM-EBSD. If one just etches chemically a martensitic steel, one can also reveal this lamellar structure as we can see in Figure 3.

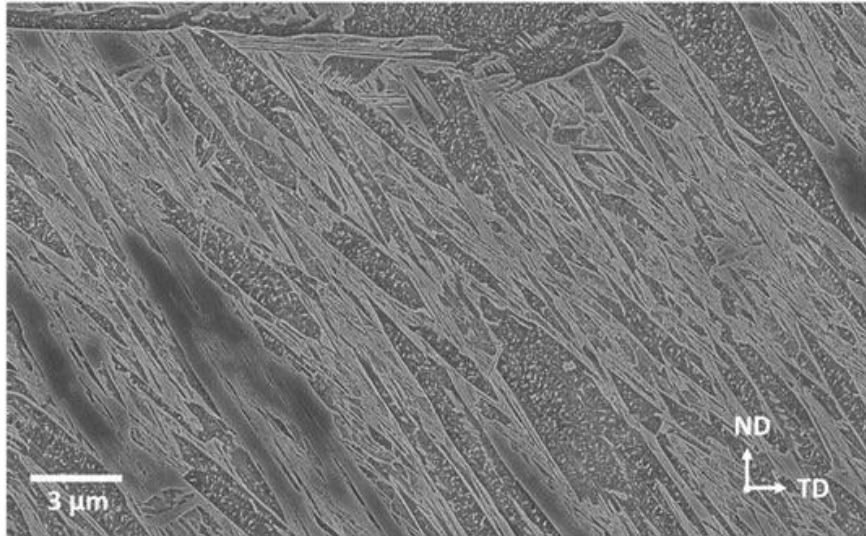


Figure 3: Lath martensitic microstructure observed by SEM after a chemical etching with a 2% nital solution. The presence of a lamellar microstructure can be observed as well as the presence of carbides inside some coarse domains. From [35].

We will of course return to this specific organization of the martensitic microstructure in Chapter II.

“Kinetics” of the transformation

As the martensitic transformation is displacive and time-independent, the martensitic transformation kinetics is often described in the literature by the famous Koistinen-Marburger (KM) equation [36]:

$$f_{\alpha'} = 1 - \exp(-A(M_s - T)) \quad \text{Equation 3}$$

where $f_{\alpha'}$ is the transformed volume fraction, A a rate parameter, M_s the martensite starts temperature and T the temperature. An improvement of this equation has been proposed by [17,37] by considering the alloying elements and the mean Prior Austenitic Grain Size (PAGS) on the kinetics rate parameter (A), keeping in mind that M_s is already function of those features.

A new full thermo-mechanic framework to predict the martensitic transformation kinetics has been developed by the author and others. This work permits to revise the seminal work of KM and understand

better the so-called spread of the transformation. Nevertheless, it will not be further discussed to maintain a reasonable length for this manuscript.

Tempering

A second heat treatment, named tempering, is usually applied to the as-quenched martensite with the aim of improving the tensile behavior, specially increase its limited toughness. This heat treatment is performed in the ferritic domain temperatures, usually from 170 °C (paint baking) up to 400 °C in automotive martensitic steels (higher temperatures are used in more alloyed steels).

During the tempering several thermally activated metallurgical phenomena occur. As with martensitic transformation itself, tempering processes have been studied and classified for a long time [20,38]. The classification of the different stages is now well accepted in the literature.

During the “zeroth stage”, trapped carbon segregates into defects (dislocations) and/or a spinodal decomposition occurs. In the “first stage”, transition carbides may form (usually in steels with carbon content higher than 0.2 wt.%). Then, the retained austenite decomposes in the ferrite and cementite in the “second stage”. Finally, during the “third stage” transition carbides dissolves and cementite forms in the martensite. The described precipitation sequence has been presented in several works as [19,20,39]. A more detailed description of the different stages as well as their modeling are presented in Chapter III.

The high dislocation density in the as-quenched lath martensite will decrease during a tempering treatment. The phenomenon known as recovery will be described and modeled in Chapter II as well as the relaxation of internal stresses resulting from the transformation.

Mechanical properties

The mechanical properties of the martensite have been widely investigated due to their structural importance. It is rather well established that as-quenched martensite shows high ultimate yield strength, a high conventional yield strength and a low total elongation [9]. It is seen as a “brittle” microstructure in that sense.

This rapid observation in fact conceals an important complexity because the properties of the martensitic steels depend heavily on their carbon content or their tempering state. Moreover, if we take a closer look at their mechanical behavior, we see that they generally have a low microplastic yield strength and a very strong work hardening [40], a characteristic found in multi-phase steels. Figure 4 presents a series of normalized true stress-true strain tensile curves of as-quenched martensitic steels with a carbon content ranging between 0.05 wt.% C and 0.4 wt.% C, from [40]. A relatively constant low microplastic yield strength is observed as well as an increase of the work-hardening with the carbon content.

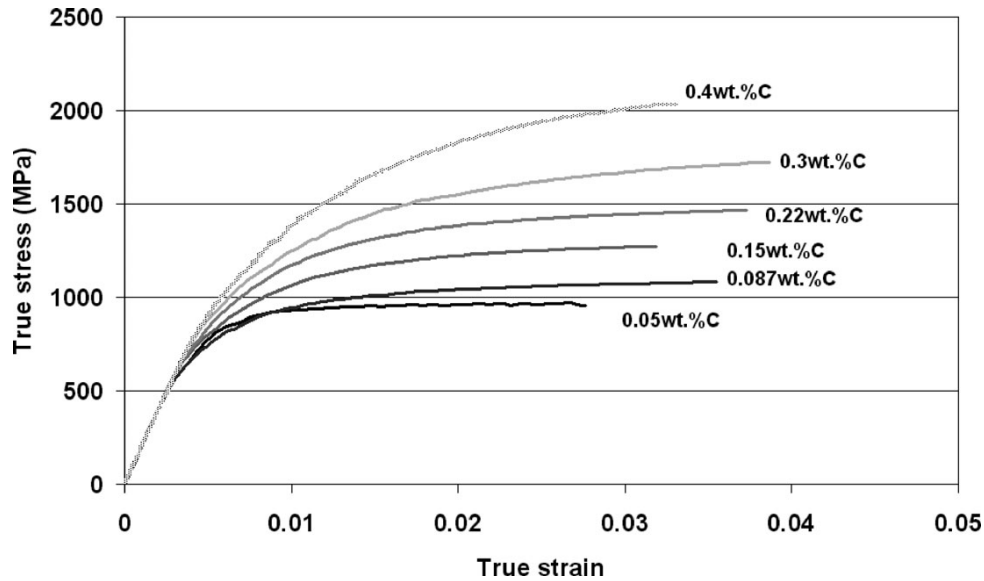


Figure 4: Tensile curves (true stress-true strain) varying the carbon content of different as-quenched martensitic steels. From [40].

One of the challenges of this thesis will be to investigate this complexity and explain the underlying mechanism. This discussion will be lead in Chapter IV.

Stakes of the study

Even if martensitic steels have been known and used for millennia now, the origins of their strength and work-hardening have remained a source of controversy. A change of paradigm has been occurring during the last few years regarding the understanding of them. Many researchers have put into evidence the interest of describing the lath martensite not as an homogenous phase but as a multiphase aggregate [40–44]. This multiphase aggregate is the result of the sequential nature of the phase transformation of the martensite at low temperature.

In fact, as explained above, martensite transformation does not follow a kinetics *stricto sensu* and it does not occur abruptly at M_s . It is thus gradually formed over time during the cooling process and as a consequence, the first martensite lath at M_s is formed in a non-deformed matrix. This matrix will have its original size (PAG) and will be relatively free of internal stresses. The volume change and the shear will produce high internal stresses in the formed martensite and in the austenitic matrix which will be partially plastically relaxed.

The martensite formed lately (at lower temperature) will form in smaller domain (the PAG are progressively fragmented by the martensitic transformation), in a deformed and stressed austenite matrix. Note that the first formed martensite will follow the whole cooling path while the ones formed latter only a fraction of it. As a consequence, the microstructural characteristics of the constituents appear at different temperature will be different.

A schematic representation of the sequential nature of the martensitic transformation showing how the distributions of dislocation densities, segregation/precipitation state, size and internal stress appear at the microstructure scale all along the process is presented in Figure 5.

Morsdorf et al. [45] have quantified this process by coupling multiple techniques. They concluded that the first formed lath (exemplified with the green dot on Figure 5) would be the largest one with a low dislocation density and a higher segregation/precipitation state. The ones formed later (orange and red dots) would present a higher dislocation density, a smaller width and a lower higher segregation/precipitation state.

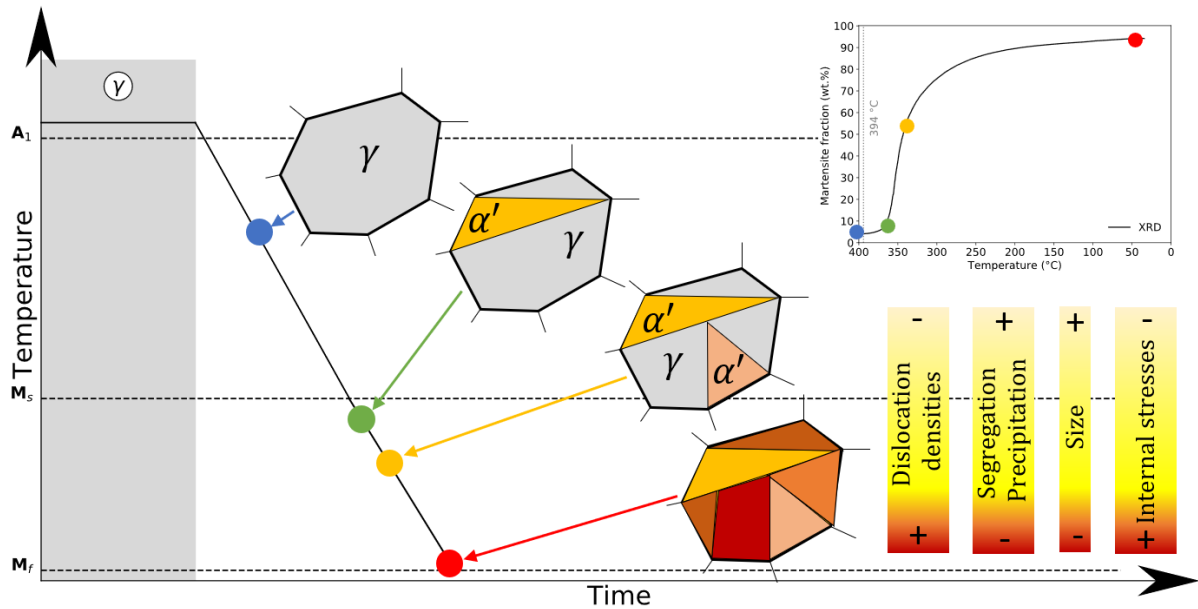


Figure 5: Schematic representation of the sequential nature of the martensitic transformation showing how the distribution of dislocation densities, segregation/precipitation state, size and internal stress appears at the microstructure scale all along the process. Based on the work of Morsdorf et al. [45].

Hence, from the micromechanical point of view, martensite is far from being a homogeneous phase. This implies a complete overhaul of our approaches to the mechanical behavior of this phase. To do so, recent studies such the one of Allain et al [40] based on the seminal works [41,46] succeed in predicting the tensile behavior based on a presupposed distribution of local yielding strengths [40,43] at the microstructure scale to describe the aggregate. In all the mentioned studies, the required distribution of mechanical properties are obtained by probability distribution function without relationship with the microstructure.

The main goal of the present study is thus to increase the understanding of the relationship between the sequential nature of the martensitic transformation and its associated microstructure distributions (dislocation densities, microstructure sizes, states of carbon, internal stresses) and the final mechanical behavior for the transformed microstructure. Another originality of this work is to show that the effects of tempering can be included in the same framework and a unified model for quenched/tempered steels is proposed.

This work is based both on a multiscale experimental approach and on modelling, which makes it possible to consolidate and address metallurgical and mechanical issues.

A schematic summary of the thesis is presented in Figure 6.

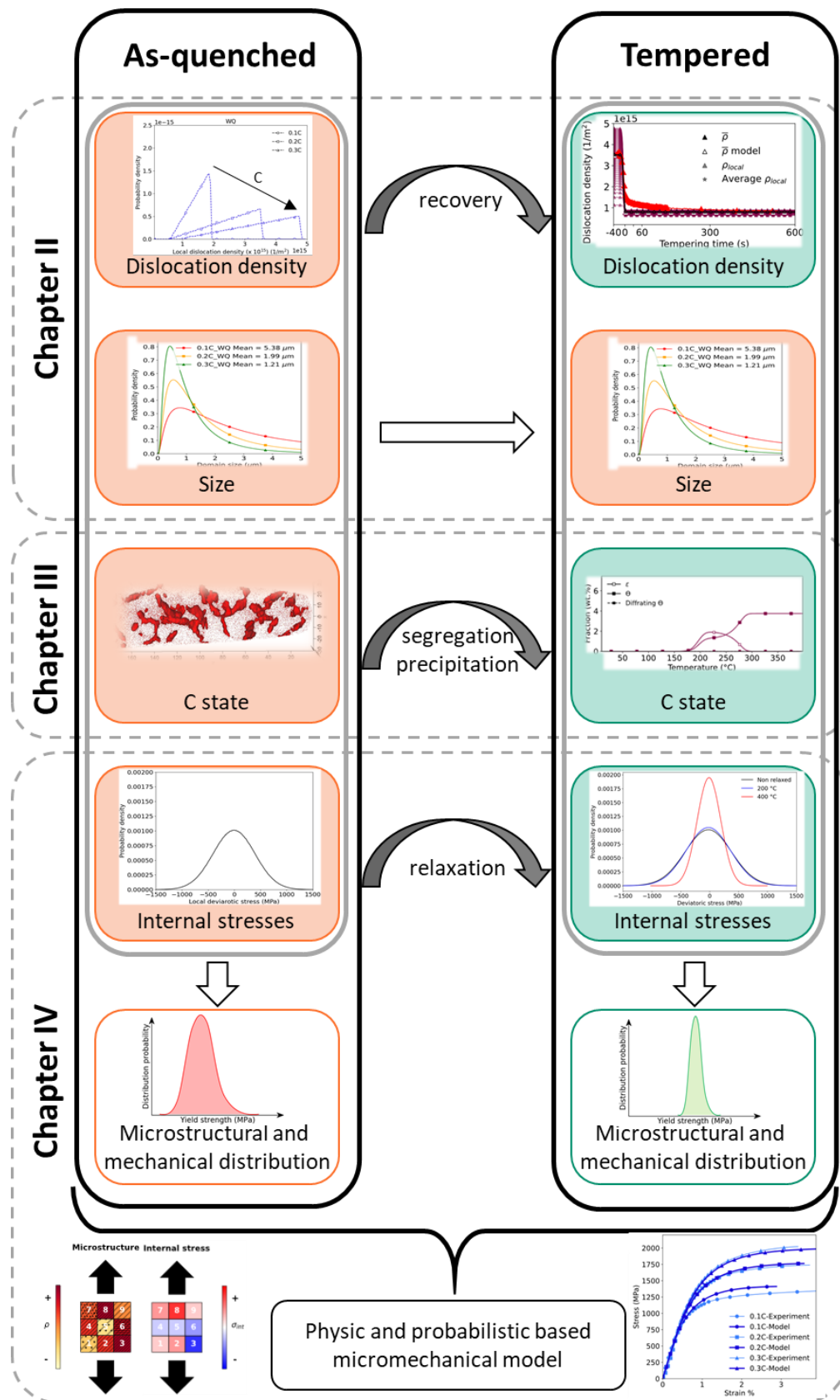


Figure 6: Schematic representation of the different phenomena studied for as-quenched and tempered martensite. The respective contents of the different chapters are indicated as well.

Manuscript organization

The following of the present manuscript is composed by four chapters. The first one presents the studied steels, the thermal treatments as well as the characterization technics. These technics relate to the in situ characterization of microstructures (HEXRD) during quenching or tempering or ex situ at room temperature (SEM, EBSD, 3DATP) or to the mechanical characterization (HV, tensile tests). As said above, the same three steels with different carbon contents will be used to build our experimental database. These data will be used to directly feed our micromechanical approach, either to calibrate intermediate models such as the one modeling the tempering coupling segregation and precipitation.

The second one is dedicated to the study of the microtexture of the martensitic microstructures, focusing on size distributions of the different constituents. In the same chapter, we are interested in the evolution of the dislocation density in the studied steels. Their formation will be studied in situ by HEXRD during the quenching and tempering processes. This in situ study is also supported by more conventional TEM/EBSD observations. An original method is presented to estimate the spatial distribution of these dislocations. Finally, the recovery phenomenon encountered during tempering is discussed and a model for this latter mechanism is proposed in the last section of the chapter.

The segregation and precipitation of the carbon in the low-carbon martensitic steels is the subject of the third chapter. The carbon segregation into dislocations was specially characterized by 3DAPT and modeled. The precipitation of carbides during the tempering of the three low-carbon steels was characterized by in situ HEXRD experiments as well as by TEM. The calibrated segregation model was coupled to a precipitation model able to predict the phase fractions as well as the precipitation size, two key characteristics which are compulsory to estimate the precipitation hardening induced by tempering.

In the fourth chapter, the experimental tensile behaviors of the as-quenched and tempered martensitic steels are presented. Then, our micromechanical framework based on a stochastic description of the aggregate is explained. It is based on the strengthening contributions discussed in the previous chapters (size distribution of the microstructure components, spatial distribution of dislocations) as well as a distribution of deviatoric internal stresses. The same micromechanical model is then used to predict the tensile behavior of the tempered martensite by considering the effects of the recovery, relaxation and carbide precipitation.

Finally, the main conclusions of the present study are summarized and some of the perspectives are enumerated.

Chapter I

Materials and methods

I.1 Steel compositions.....	- 12 -
I.2 Heat treatments	- 12 -
I.2.A Dilatometer.....	- 12 -
I.2.B Resistance furnace.....	- 13 -
I.2.C Salt and oil bath.....	- 14 -
I.3 Labeling system	- 14 -
I.4 Characterization technics	- 15 -
I.4.A In situ high energy X-ray diffraction (HEXRD).....	- 15 -
I.4.B Transmission Electron Microscopy.....	- 24 -
I.4.C 3D Atom Probe Tomography.....	- 26 -
I.4.D Electron BackScattered Diffraction in SEM.....	- 28 -
I.4.E Mechanical testing.....	- 28 -
I.5 Conclusions of the chapter.....	- 30 -

As disclosed in the introduction, the microstructure evolutions in the studied steel were investigated in situ by HEXRD (i.e during the heat treatments) and also post mortem (i.e. after the heat treatments) by coupling different technics at different scales (3DAPT, TEM, SEM). The mechanical properties of the microstructures were also characterized thanks to hardness measurements and tensile tests. This Chapter aims at presenting these different experimental set-ups and also how the results have been post-treated.

I.1 Steel compositions

In the present study three different industrial low-carbon alloy steels were provided by ArcelorMittal Maizières Research SA, presenting as main difference a variation of the carbon content. Their denomination as well as their compositions are presented in Table 1. In all the cases their boron content is lower than 5 ppm. The samples were received in the form of a plate after the cold-rolling stage, with a thickness of c.a. 1.5 mm.

Table 1: Denomination and composition of the three steel grades used in the present study.

Steel name	C (wt.%)	Mn (wt.%)	Si (wt.%)	Cr (wt.%)	Fe
0.1C steel	0.108	2.10	0.22	0.03	balance
0.2C steel	0.210	1.82	0.25	0.18	balance
0.3C steel	0.310	0.71	0.35	0.51	balance

The calculated Ae_3 (full austenitizing temperature at equilibrium) temperatures of the steel are 807, 791 and 802 °C for the 0.1C, 0.2C and 0.3C steel respectively and the M_s temperatures measured by dilatometry with the method presented by Yang et al. [13] are 432, 407 and 382 °C respectively.

I.2 Heat treatments

The heat treatments used in the present study consist mainly of an austenitization soaking (heating and holding), a quenching followed or not by a tempering. Different equipment were used to simulate these processes depending on the required control on the cooling rate or on the size of the samples. As the purpose of this work is not to reproduce an industrial process, the thermal schedules have been designed to understand the physical mechanisms and must be considered as model heat treatments.

I.2.A Dilatometer

The heat treatments permitting in situ High Energy X-Ray Diffraction (HEXRD) experiments were conducted in a Bähr DIL805 A/D dilatometer available at the Deutsches Elektronen Synchrotron (DESY) in Hamburg, Germany. Such device heats the samples by induction and allows cooling rates higher than -200 °C/s for thin flat samples. The austenitization consisted of a heating at 20 °C/s rate until 880 °C. The duration of the isothermal holding at high temperature was fixed at 300 s to prevent an exaggerate growth of the austenite grain size.

The same dilatometer is also available at IJL. It has served to duplicate some experiments and produce samples for post mortem examinations.

The quench was performed by He gas injection (in the following mentioned as GQ Gas cooling). Four different cooling paths were designed, all of them including a -100 °C/s segment until 20 °C above the M_s temperature of the considered alloy (in order to avoid any diffusive transformation at high temperatures). Then, the cooling rates applied were -10 , -50 and -100 °C/s and a “natural” cooling. This latter cycle was simulated with a mean rate of -20 °C/s between the M_s and 200 °C followed by lower rate. In Figure 7.a only the measured temperature-time curves are presented for clarity (the maximum difference between the measured values and the programmed ones is always lower than 25 °C). The temperature is measured with a thermocouple welded in the center of the sample on the edge. This thermocouple also serves to drive the heating/cooling devices.

The dilatometer was also used to simulate tempering treatments on samples previously water-quenched (prepared with a tubular furnace – see below). The tempering consisted of a heating, at 10 °C/s rate, up to the tempering temperature (200 , 300 and 400 °C) is reached, a holding during different durations (0 , 30 , 60 , 300 and 600 s) and a fast gas quench.

The samples heat treated by dilatometer had the following dimensions: $10\text{ mm} \times 4\text{ mm}$, with a thickness of 1.5 mm . For the gas quench at -100 °C/s cooling rate below M_s , the samples were machined to ca. 1 mm in order to be able to reach the imposed cooling rate.

I.2.B Resistance furnace

In order to obtain a microstructure with a lower state of self-tempering (i.e. a tempering state acquired during the quenching process itself), samples were also quenched in water (referred as WQ in the following). The water-quench required to heat the sample in a tubular furnace heated by resistance. In such device, the heating rate is 0.1 °C/s . The duration of the soaking was fixed at 300 s . The sample is then ejected and directly quenched in a water container. The measured cooling path is presented in Figure 7.a. The corresponding samples are called as WQ - IJL.

Tensile tests cannot be carried out on dilatometer samples. As a consequence, some plates of the steels have been heat-treated by salt baths at ArcelorMittal Research, Maizières les Metz, France (AM in the following) in order to reproduce at best the dilatometer treatments. The plates are then machined to prepare tensile samples.

In this case the heating rate to reach the full austenitization is not linear. It can be described roughly as a stepped heating; from room temperature up to 618 °C with a heating rate of 16 °C/s , followed by a segment at 1 °C/s up to 740 °C and last one at 0.5 °C/s up to 880 °C . The holding time in this case was only 105 s . The samples are then water-quenched (so called WQ – AM samples).

During the WQ experiments at IJL and AM and the tempering experiments at AM, the temperature of the plates is tracked with a welded thermocouple.

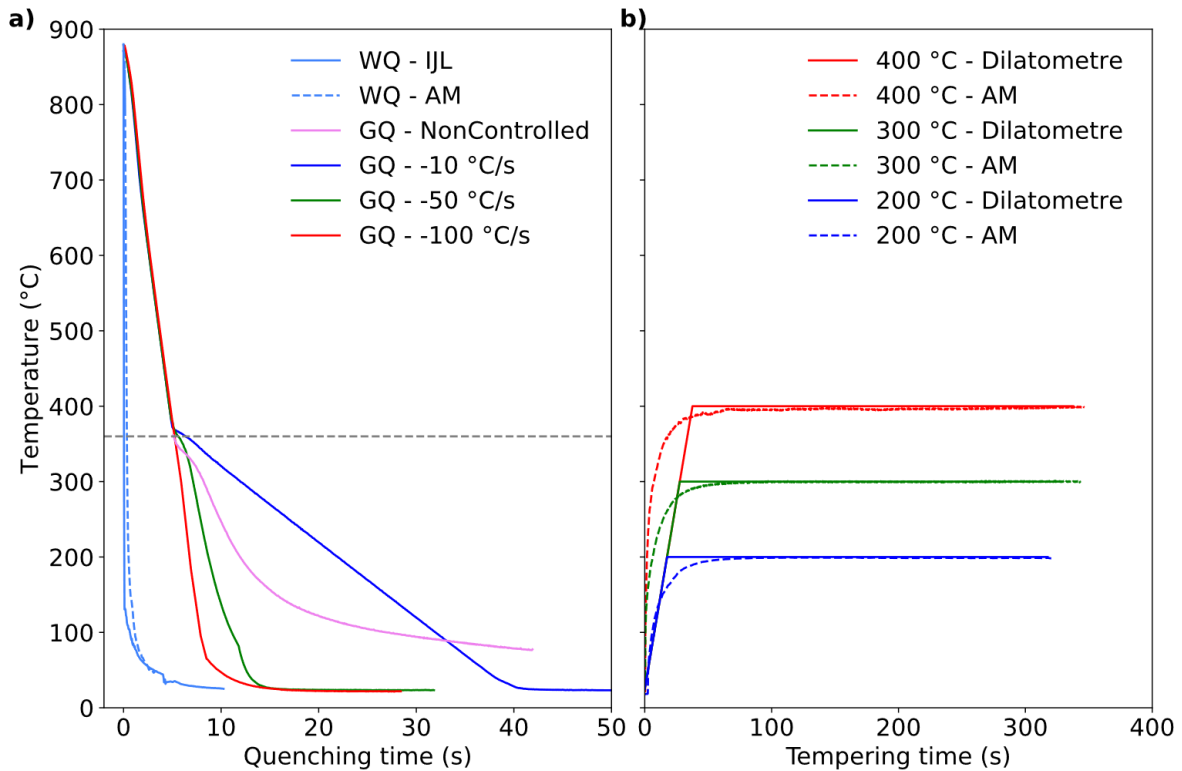


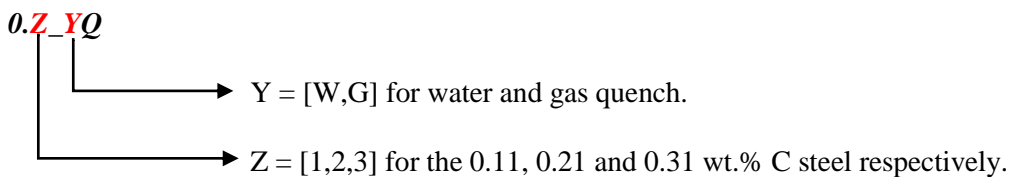
Figure 7 : a) Cooling paths applied to the 0.2C steel, WQ (in light blue) refers to water quench while GQ to gas quench with controlled temperature schedules (-10 °C/s in blue, -50 °C/s in green and -100 °C/s in red) and without temperature control (natural cooling in light violet). b) Tempering treatments applied in the present study, the continuous line refers to dilatometer trials while the dashed ones to the bath heat treatments applied at AM. Red lines refer to 400 °C tempering, while green ones to 300 °C and blue ones to 200 °C respectively.

I.2.C Salt and oil bath

The tempering treatments performed at AM on the plates (WQ-AM) were performed by oil bath for 200 °C treatments and salt bath for higher temperatures. The holding times were 0, 30, 60 and 300 s. The time-temperature curves showing the tempering heat treatments are presented in Figure 7.b. As explained above, the main differences between the tempering trials concern the heating stage. Baths are more efficient for the initial heat transfer.

I.3 Labeling system

In the following section the system used in the present work for naming the samples indicating alloy and heat treatment is presented. For quenched samples the names are composed as:



The samples named 0.Z_GQ refer to non-controlled gas-quench, a suffix is added for the controlled cooling-rate gas quenched samples:

0.Z_GQ_WWWCs

└───┬───> WWW = [10,50,100] for the -10, -50 and -100 °C/s cooling rate
 └───> respectively.

For illustrating the system a 0.11 wt.% C water quenched sample will be referred as 0.1C_WQ and a 0.31 wt.% C sample gas quenched at a -50 °C/s cooling rate will be named as 0.3C_GQ_50Cs.

For the tempered samples, the initial state was the water quenched one and the heat treatment is detailed as the following:

0.Z_WQ_TVVCUUUs

└───┬───┬───> UUU = [0,30,60,300] for holding times of 0, 30, 60 and
 └───┬───> 300 s.
 └───> VVV = [200,300,400] for 200, 300 and 400 °C tempering
 temperature.

A 0.21 wt.% C sample tempered at 200 °C with a holding time of 0s is referred as 0.2C_WQ_T200C0s for example.

A labeling system is also proposed for the figures presented in this work. In all the cases, if it is not applied, it will be highlighted.

The results of the 3 steels will be indicated by different symbols, 0.1C steel by ●, 0.2C steel by ▲ and 0.3C steel by ■. The color of the lines will indicate the tempering temperature and the linestyle the holding time, all the studied combinations are summarized in Table 2. Different colors will be used to present the experimental data (color experiment) and the simulation results (color model). Nevertheless, the colors are close to ease the readability.

I.4 Characterization technics

I.4.A In situ high energy X-ray diffraction (HEXRD)

High energy X-ray diffraction allows to perform X-ray diffraction characterization not only on the surface of a steel sample but in bulk, i.e. in a transmission mode, with a high acquisition rate.

The analyzed volumes (ca. 0.4 mm³) are more representative and provide an average information on the microstructure. The experiments conducted in transmission minimize the effect of possible surface heterogeneities (decarburization, oxides).

However, the beam size should not be too large to avoid possible thermal gradients (to avoid measured volumes too far from the thermocouple).

Table 2: Labeling system for identification of presented data depending on alloy, heat treatment (quenching/tempering, temperature and time) and nature of result (experimental/modelled).

Quenching

Type	Cooling rate (°C/s)	Color experiment	Color experiment	Linestyle	Color model	Color model
WQ	Non controlled	dodger blue		-	ultramarine blue	
GQ	Non controlled	darkviolet		-	purple	
GQ	-10	blue		-	-	-
GQ	-50	green		-	-	-
GQ	-100	red		-	-	-

Tempering

Temperature (°C)	Time (s)	Color experiment	Color experiment	Linestyle	Color model	Color model
200	0	blue		-	cobalt blue	
200	30	blue		--	cobalt blue	
200	60	blue		.-	cobalt blue	
200	300	blue		:	cobalt blue	
300	0	green		-	emerald green	
300	30	green		--	emerald green	
300	60	green		.-	emerald green	
300	300	green		:	emerald green	
400	0	red		-	red purple	
400	30	red		--	red purple	
400	60	red		.-	red purple	
400	300	red		:	red purple	

As the experiments presented in this manuscript were performed in situ, it was possible to follow the transformation kinetics, the Full Width at Half Maximum of the diffraction peaks and the phase's cell parameters during the experiments. Two campaigns were realized at PETRA III P07 beamline at the Deutsches Elektronen Synchrotron (DESY) in Hamburg, Germany in May 2019 and December 2021.

I.4.A.1 Synchrotron set-up

In the present section, only the specificity of our experimental set-up will be described. A description of a synchrotron operation can be found in [47]. The Figure 8 represents a schematic view of the set-up.

As previously said, a transmission configuration was used, with an incident beam size of $500 \times 500 \mu\text{m}^2$, leading to an analyzed volume of 0.375 mm^3 . A monochromatic beam with an energy of 87.1 keV, i.e. $\lambda = 0.014235 \text{ nm}$, was set using a monochromator. The sample ($4 \text{ mm} \times 10 \text{ mm} \times (1.5 \text{ or } 1) \text{ mm}$) was introduced in a modified Bähr DIL805 A/D dilatometer. The main modifications with respect to the commercial dilatometer used at IJL are the in/out windows for the X-rays and the inductor (copper coil) whose shape is designed to not interfere with the X-rays beam (incident and diffracted). As already said, the temperature was controlled and recorded thanks to a S type thermocouple spot welded at the half length of the sample, just above the probed volume (perpendicular to the main thermal gradient induced by the jaws). As a consequence, the temperature differences are minimized between the two measuring points.

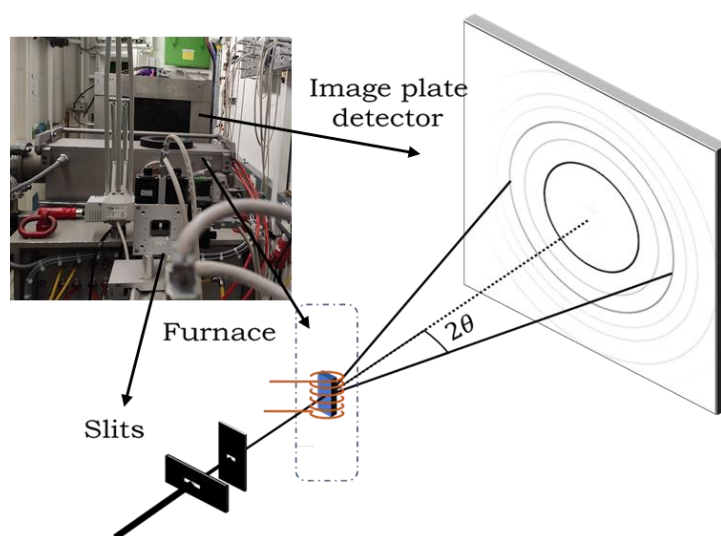


Figure 8: Schematic representation and photography of the HERD set-up used during the experimental campaigns at PETRA III P07 beamline at DESY.

The 2D Debye Scherrer diffracted rings were collected by a Perkin-Elmer XRD 1621 Flat Panel detector with a 2048×2048 pixel matrix and a pixel size of $200 \times 200 \mu\text{m}^2$ [48] set at ca. 1.5 m distance from the sample. During the quenching heat treatments, the end of the austenitization holding and the cooling section were registered at a 10 Hz acquisition rate with an exposure time of 0.1 s. The same acquisition rate was used during the heating and beginning of isothermal holding of the tempering heat treatments. While during the rest of the tempering holding time and the heating and holding of the austenitization a ca. 0.3 Hz acquisition rate was applied. A “dark” image (image of the electronic noise of the detector) used for correction is obtained before each 2D diffractogram when the acquisition rate is 0.3 Hz. In the

case of acquisitions at a 10 Hz rate, only one dark image is used for the correction of all the required batch of images (typically 1500–2000 images in the case of the present work).

I.4.A.2 X-ray data analysis

The 2D images with Debye Scherrer rings were azimuthally integrated with the Python library pyFAI [49] into 1D diffractograms, intensity vs diffraction angle. Figure 9.a presents a 2D diffractogram where martensite and austenite diffraction rings are visible while in Figure 9.b the classical 1D diffractogram after integration is shown. Only the angular window comprised between 3 and 11° in the 2θ axis was used in the present study. The working distance permits to record 5 full Debye-Scherrer rings for the ferritic and austenitic phases on the square screen.

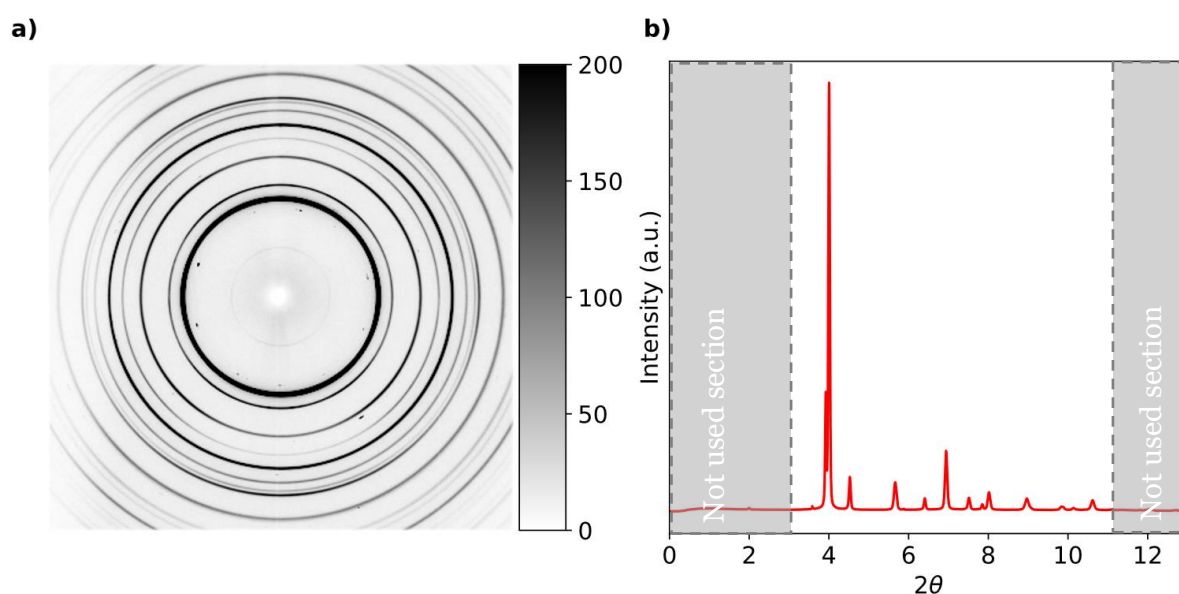


Figure 9: a) 2D Debye Scherrer diffracted rings during a quenching experiment. b) 1D diffractogram obtained after azimuthal integration of Figure 9.a.

The experimental set-up utilized during the experiments allows to obtain 1 diffractogram per degree Celsius during the heating of the tempering and during the quenching heat treatments at -10 °C 1 diffractogram each 1 °C, at -50 °C/s each 5 °C, and at -100 °C/s one diffractogram each 10 °C.

The 1D spectrums were also scrutinized qualitatively to detect the presence of low fraction of carbides. The qualitative analysis was applied for the determination of the presence of carbides (transition kind and cementite) at the quench state as well as during the tempering (focusing on the heating segment). The selected zone of the 1D diffractograms was between 4 and 6° in the 2θ axis. In the mentioned sector, two BCC/BCT peaks are present (at ca. 4° the {110} peak, while at 5.67° the {200} peak) and one FCC peak at 4.55° of the {200} reflection. Multiple cementite diffraction peaks should be visible in the selected angular window [39] as well as the distinctive diffraction peak of transition carbides between 4.95 and 5.15° 2θ [39,50–52]. The main cementite peaks should be visible at 4.6, 4.82, 4.8 and 5.16° 2θ. An angular window in which several cementite low intensity peaks are expected is also present between 4.28 and 4.46° 2θ.

A diffractogram obtained during the tempering of the 0.3C steel presenting the peaks of transition carbides is shown in Figure 10.a along with another one presenting cementite diffraction peaks (Figure 10.b). Note that not all the cementite theoretical diffraction peaks are present, only a composed peak formed by the $\{310\}$ and $\{231\}$ reflections and the one corresponding to the $\{131\}$ are visible. This may be due to the fact that the carbides are in an early precipitation state in which their shape is not spherical and, in some directions, more atomic planes are cumulated giving a deviation from the theoretical powder diffraction pattern.

The monochromators used to obtain a beam with a single wavelength may not be perfect. In the present work a $\lambda=1/2$ contamination was detected. The signal fraction of this beam component is lower than 1 % in intensity but it leads to the occurrence of weak additional artefact peaks, that can be misinterpreted as an additional phase.

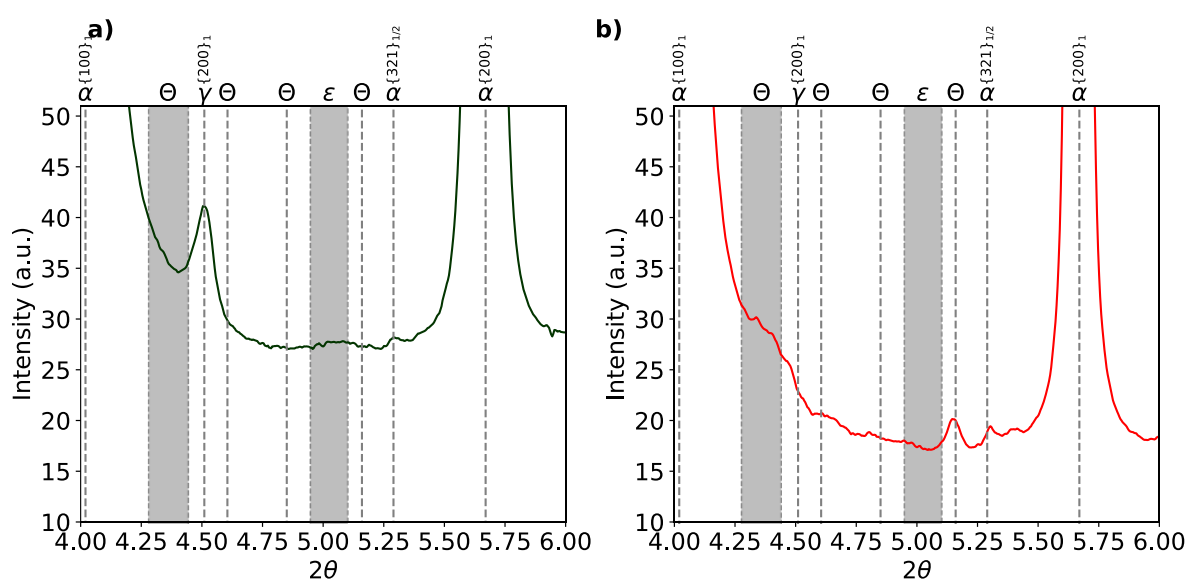


Figure 10: a) Diffractogram obtained at 325°C during the heating segment of the tempering at 400 °C of the 0.3C steel. b) Diffractogram obtained at the end of the isothermal segment (600 s) of the tempering at 400 °C of the 0.3C steel. The sub-indexes refer to primary diffraction or to contamination of $\lambda=1/2$.

The 1D diffractograms were then post-treated using two different quantitative technics:

- Rietveld refinement: for lattice parameters and phase fractions determination.
- Peak to peak analysis: for dislocation density and asymmetry determination.

I.4.A.2.a Rietveld refinement

A systematical analysis of the 1D diffractograms was performed by Rietveld refinement [53]. It consists in simulating a full experimental diffractogram with a theoretical one knowing the crystalline characteristics of the phases in presence (assuming a perfect random polycrystalline arrangement) and calibrating the background noise (due to the instrumental/set-up noise and amorphous volumes). This model accounts for the factor structure of each phase, the Lorentz factors and for the thermal scattering.

Only two phases were considered during the analysis of the quenching process (GQ experiments): austenite with a face centered cubic structure (Fm-3m) and martensite with a body centered tetragonal

structure (I/4mmm). In practice, it has been implemented with FullProf software [53]. The background was fitted with a fourth order polynomial function and the diffraction peaks were modeled with pseudo-Voigt functions.

The determination of the body-centered phase, in the following denoted as martensite (α'), and of the austenite (γ) (face centered) was performed in a sequential mode from a carefully manually refined diffractogram. During tempering treatments, when cementite (Θ) was detectable, individual diffractograms were refined manually. Table 3 present the three crystalline characteristics of the phases used during the Rietveld refinements.

Table 3: Crystallographic data used for the Rietveld refinement [39].

Symbol	Space group	Cell chemical	Nature	x	y	z	Atom occupancy
α'	I4/mmm	Fe	Fe	0	0	0	1
γ	Fm-3m	Fe	Fe	0	0	0	1
Θ	Pnma	Fe ₃ C	Fe	0.181	0.063	0.337	1
			Fe	0.034	0.250	0.840	0.5
			C	0.894	0.250	0.449	0.5

The respective phase fractions of the phases are estimated knowing their average composition (ATZ parameter of FullProf) and their respective X-Ray scattering. When comparing the integral breaths of the corresponding diffraction peaks, FullProf provides a measure of the respective weight fraction of the phases with an absolute uncertainty estimated around ± 1 %.

I.4.A.2.b Peak to peak analysis

As previously mentioned, the dislocation density has a crucial role in the behavior of martensite. For this reason, we analyzed our diffraction pattern even more closely and carried out a detailed peak-to-peak analysis to determine in situ or post mortem the density of dislocations in our samples, and more precisely in the martensite.

This analysis has been conducted following the seminal work of Williamson & Hall showing that dislocations by perturbing elastically the crystal lattices affect the width on the diffraction peaks on polycrystals [54]. Their method allows to separate the contribution of the crystallite size (perfect diffracting domains) from the contribution of the dislocations (crystal defects) on the Full-Width at Half Maximum (FWHM) of the diffraction peaks acquired on isotropic materials.

In the present study, two different methods were utilized to model the diffracting peaks of the martensite phase, therefore to obtain their respective FWHM. In the first one, a single mathematical function is used to model each diffracting peak, called “1Peak-1Function” in the following. In the second one, a set of functions is used for each diffraction peak in order to correct the possible broadening due to

tetragonality. This second method is called “1Peak-MultipleFunction method”. Both methods and their origins are described below.

These methods break away from the Rietveld approach, which predicts all the diffraction peaks of a perfectly random isotropic polycrystal at the same time. In these two alternative methods, each of the diffraction peaks is described individually.

I.4.A.2.b.i 1Peak-1Function

In our approach, we analyzed the {200}, {211}, {220} and {321} diffraction peaks of martensite and the {200}, {220}, {311} and {420} for austenite.

They are individually modeled with different single symmetric Pearson VII functions. As a result, the angular position and the FWHM are obtained for each of them. The modified Williamson-Hall method proposed by Ungar et al. [55–57] (called mWH in the following) allows to determine the crystallite size and dislocation density on anisotropic materials with the following equation:

$$\Delta K = \frac{\zeta}{D} + \left(\left(\frac{\pi M b^2}{2} \right)^{1/2} \bar{\rho}^{1/2} \right) * K \overline{C_{hkl}}^{1/2} + O K^2 \overline{C_{hkl}} \quad \text{Equation 4}$$

where $\Delta K = \text{FWHM}(\theta) * 2 \cos(\theta) / \lambda$, ζ was set to 0.9 as done in [54], D is the crystallite size, M is a parameter that depends on the dislocation density, b is the Burgers vector (0.25 nm for both the martensite and the austenite), $\bar{\rho}$ is the mean dislocation density, K is the scattering vector defined by $K = 2 \sin(\theta) / \lambda$ and $\overline{C_{hkl}}$ is the average contrast factor of dislocations for the specific reflection. The last term of the equation, $O K^2 \overline{C_{hkl}}$, is a higher order term with no meaning defined [56] and in which O is much smaller than the coefficient before $K \overline{C_{hkl}}^{1/2}$, as consequence this term was not considered [58,59].

The parameter M , related to the cut-off radius of the dislocations and their arrangement, can be evaluated with the Warren-Averbach method [60]. Recently Borbély [59] showed the relevance of performing the Warren-Averbach method without this M parameter which is related to the arrangement and orientation of the dislocation’s Burgers vectors.

However, the mentioned analysis method was not used in the present work and as a consequence M was set as a constant during all heat treatments. The retained value is 2.2 corresponding to an average of the values proposed by [61]. Saliez et al. present a dislocation density study where M was considered as a variable, varying between 3 and 1.5 [62].

The average contrast factor of dislocations for the specific reflection ($\overline{C_{hkl}}$) depends on the elastic constants of the material, slip systems considered and type of dislocations. The elastic constants (C_{11} , C_{12} and C_{44}) are temperature dependent and as a consequence $\overline{C_{hkl}}$ as well. For the body-centered phase anisotropic elastic constants were available in the literature [63–65], however this was not the case for the austenite (they were thus considered as constants [66]).

The considered slip system for the body-centered phase is $\langle 111 \rangle \{ 110 \}$ and for the austenite (FCC) is $\langle 110 \rangle \{ 111 \}$. A 50%-50% mix of edge and screw dislocations was considered in this study for both

phases. With all the required data the \overline{C}_{hkl} were calculated with the AZNIC software [67] and are presented in Table 4 for room temperature. The \overline{C}_{hkl} were calculated up to 700 °C and then fitted with a second order polynomial function ($a + bT + cT^2$ with T in K). For the {200} reflection, the fitted parameters are, $a=0.277$, $b=4.854 \times 10^{-5}$ and $c=1.73 \times 10^{-7}$ while for the three other reflections used in this work ({211}{220}{321}) $a=0.1408$, $b=7.042 \times 10^{-7}$ and $c=2.266 \times 10^{-8}$. To the author's knowledge, the work presented here and published already in [14] is the first one to use thermal dependent contrast factors.

Table 4: Dislocation average contrast factor at room temperature, considering a 50%-50% ratio between edge and screw dislocations for the body-centered phase and for the face-centered phase.

Martensite	{200}	{211}	{220}	{321}
\overline{C}_{hkl}	0.278	0.141	0.141	0.141
Austenite	{200}	{220}	{311}	{420}
\overline{C}_{hkl}	0.299	0.148	0.204	0.202

As shown in Equation 4, the determination of ΔK and K is related to a proper description of the diffracting peaks (positions and FWHMs). The procedure described above is developed for the description of perfectly cubic lattice. However, our martensitic microstructures are probably not cubic, but slightly tetragonal in a very limited extent. The tetragonality will lead to the weak dissociation (degeneration outbreak) of certain peaks from the cubic lattice and to a specific enlargement of these peaks even if a splitting is not observed strictly. As a consequence, the determination procedure based on the FWHM could be affected. This is the reason why, in the present work a new method (multiple function peak fitting) is proposed to deconvolute the contribution of a possible tetragonality by combining an analysis of the full diffractogram (Rietveld refinement) and of each peak individually.

I.4.A.2.b.ii 1Peak-MultipleFunctions

The method explained in the following has been developed in the frame of the present study and has been published already in [68].

The multiple function peak fitting consists in modeling each experimental diffracting peak not by a single mathematical function but as the sum of different symmetric functions whose number corresponds to the different reticular spacings associated with a degenerated family of planes. In the case of the family {200}, if the lattice is tetragonal, the (002) and the (200)/(020) planes have indeed two different reticular spaces and as a consequence two functions will be used to represent the whole family (Figure 11.a). In the case of the family {321}, three mathematical functions will be used in the modeling (Figure 11.b) procedure. The red lines represent the experimental data, the yellow, green and pink are the different fitting functions used and the black ones are the sum of them.

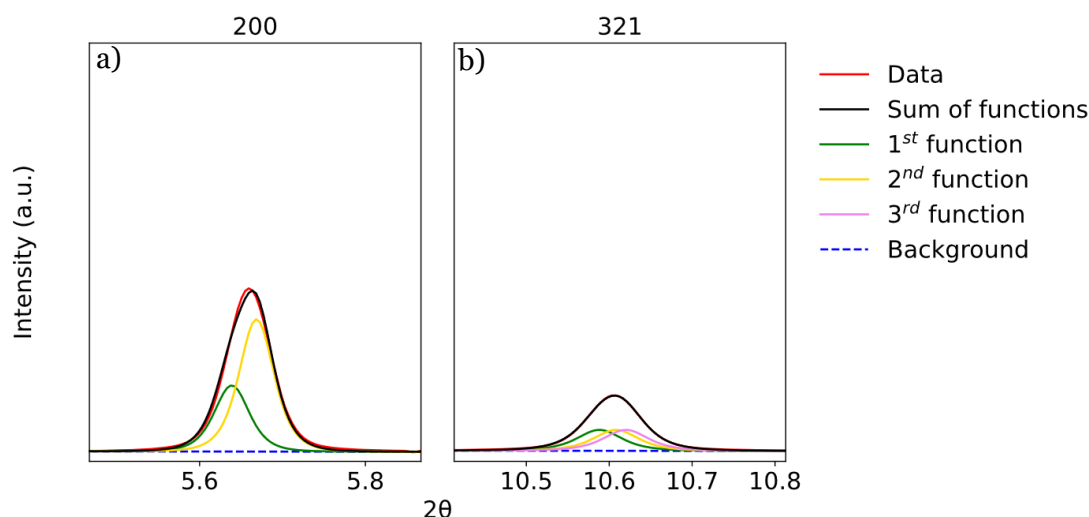


Figure 11: Multiple function modeling of the diffraction peaks {200} in a) and of the {321} in b).

To perform the multiple function peak fitting, the peak positions of respective contributions and their respective intensity ratio have to be determined. To achieve this, a two-step procedure has been implemented to minimize the degrees of freedom.

Firstly, the c/a ratio is determined by the Rietveld refinement with a body centered tetragonal structure ($I4/mmm$), then the reflection positions are calculated for each peak (i.e. in the case of {200}, the (002) and the (200)/(020) positions, while for the {321} three positions are calculated (321)/(231), (312)/(132) and (213)/(123)) with the Bragg's law. The angular separations, i.e. the difference between the mentioned positions, are then calculated a priori.

Secondly, each diffraction peak (c.a. {200} or {321}) is individually modeled with the number of Pearson VII functions determined by the number of previously calculated positions (as for the single peak fitting method). The intensity ratio between Pearson VII functions used for each peak is obtained with the Bragg's analysis. In the case of {200} planes two functions are used, one twice intense than the other one corresponding to the (002) plane reflection. In this last step, the functions are forced to have the same FWHM and shape, and their position is restrained by the previously calculated angular separation. Finally, the obtained FWHM is used instead of the one-function-per-peak one. For the modified Williamson-Hall method, the mean angular position of the family is chosen as the intensity weighted average of the reflection positions.

The FWHM obtained by the mentioned different peak fitting methods is finally corrected by suppressing the instrumental contribution (measured with calibrants Si, LaB_6) by considering a square additive law [13]. The instrumental contribution was considered constant during the experiments considering the beam stability and apart from of the temperature no other changes were performed in the set-up.

It has to be pointed out that the present dislocation density determination method only considers the crystallite size and the dislocation density as contributions to the FWHM. However, it is known that surface effect (minimized when working in transmission mode), composition distribution and internal stress distribution may affect the FWHM. Although no substitutional diffusion is expected due to the fast quenching and low tempering temperature, some banded co-segregation Mn-C was evidenced by

the steel supplier. Regarding the distribution of internal stress at the sample scale, no characterization was performed in the present work.

With the corrected FWHM and position determined by the peak fitting, the ΔK and K were calculated for each peak. The following step consisted of a linear fit with the obtained points as presented in Figure 12. From the obtained slope, the dislocation density was deduced using Equation 4.

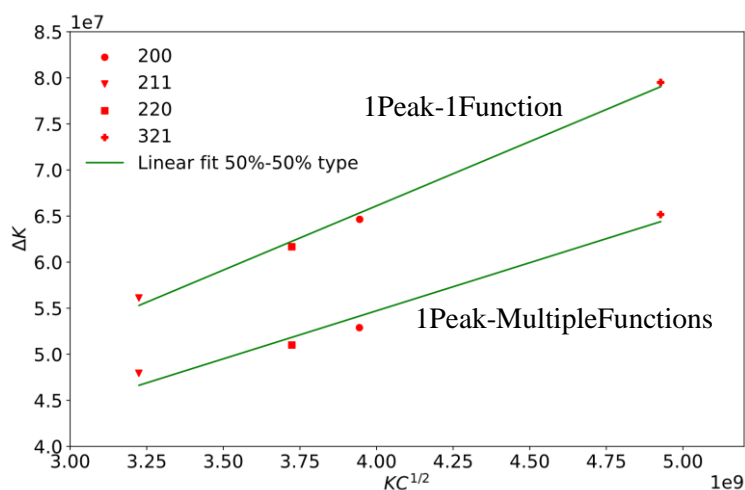


Figure 12: mWH graph from a diffractogram at the end of the 0.2C_T400C with the two methods used in the present study.

The design of the HEXRD experiments as well as the whole post-treatment was performed by the PhD candidate. In the experimental campaigns the co-participation of Clélia Couchet, Cécile Rampelberg and Guillaume Geandier has to be mentioned and thanked.

I.4.B Transmission Electron Microscopy

The HEXRD characterization allows to detect the presence of carbides but no information regarding their shape or size can be obtained with the set-up used in the frame of this work. As a consequence, some selected samples were characterized post-mortem by transmission electron microscopy (TEM). This technic was also used to determine the dislocation density of the 0.2C_WQ sample for the sake of comparison with HEXRD. As this method is time-consuming and not necessarily more accurate, a single state was studied.

A JEOL ACCEL-ARM200F microscope equipped with probe and image correctors in scanning mode was used to observe the dislocations and to perform EDS maps with a standard calibration.

Another JEOL ACCEL-ARM200F microscope equipped with probe corrector in classic bright field TEM mode was used for carbide characterization. In both cases, a cold FEG source working at an accelerating voltage of 200 keV was used.

I.4.B.1 TEM sample preparation

Samples were milled from their initial thickness, c.a. 1.5 mm, and polished mechanically down to a thickness around 100 μm . 3 mm diameter discs were then punched from the slices. The discs were

polished electrolytically with a solution of 2 butoxy-ethanol, methanol and perchloric acid with a Struers TecnuPol-5 twin-jet machine. The temperature of the solution was set between 10 and 14 °C and a voltage of 40 V was applied.

I.4.B.2 Carbide characterization

The size of the carbides during the tempering was determined manually by measuring the external shape of the detectable carbides. It was assumed that the carbides present a prolate ellipsoidal shape. The image analysis grants access to the minor and major axis (r_m and r_M respectively) of the 3D shape. Both values are then aggregated to estimate an equivalent sphere radius (r_{eq}). In order to obtain sufficient data which allows to calculate the size distribution, more than 300 carbides were measured at each studied condition (considering at least 5 zones of the samples). The procedure is illustrated in Figure 13.

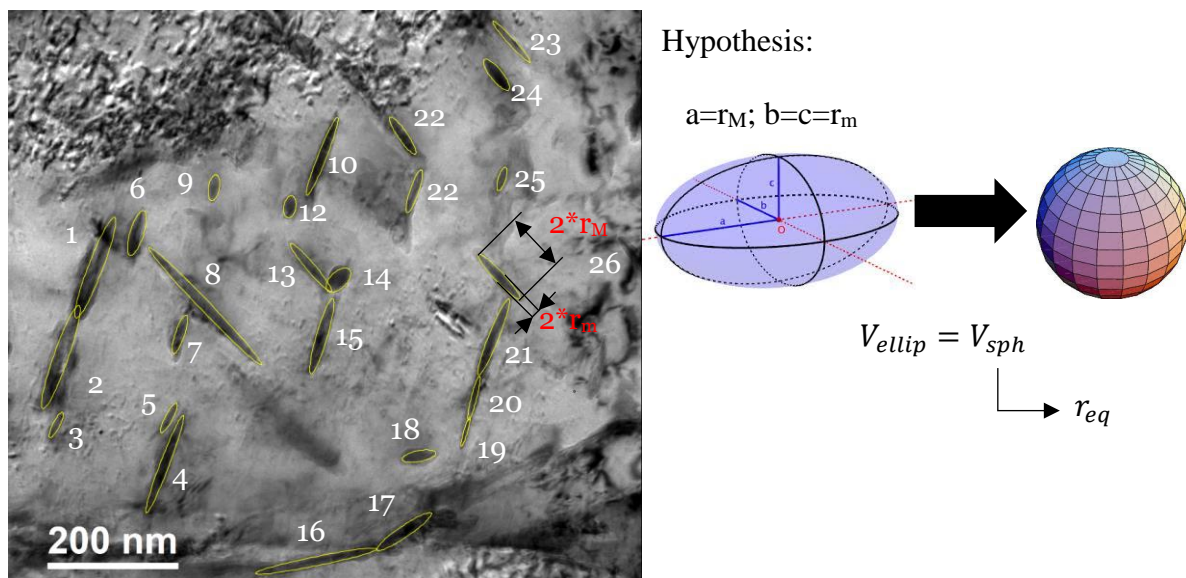


Figure 13: TEM image acquired on the 0.3C_T400C300s steel. Fe₃C carbides are measured with ellipsoids (in yellow). The schematic transformation of volumes to obtain the equivalent radius is presented on the left.

The nature of carbides was confirmed using ASTARTM/precession electron diffraction (NanoMEGAS) hardware and the associated software package. The zones of interest were mapped to obtain local diffraction patterns. The mentioned patterns are compared with a simulated pattern bank by a pattern matching method. This method allows to obtain the most probable phase (from the data bank introduced) and its orientation [69,70]. This section of the study was performed in close collaboration with AM.

The TEM images utilized for carbide size determination and ASTAR indexation were obtained by the PhD candidate in autonomy. The post-treatment of the data was also performed by the author.

I.4.B.3 Dislocation density

The dislocation microstructures in the studied steel were analyzed post-mortem by STEM with the aim of estimating the density of dislocations.

The dislocation density was estimated using a line intercept method as [27]:

$$\rho = \frac{2N}{Lt}$$

Equation 5

where N is the number of intercepts, L is the sum length of all the used lines and t is the thickness of the thin foil.

Six different sections were analyzed in order to avoid extremely localized values. The thickness of the sample was determined by Energy-Filtered Transmission Electron Microscopy (EFTEM), with a mean value of ca. 100 nm. The STEM characterization was performed by Ph.D. Jaafar Ghanbaja and Mélanie Emo while the analysis of the data was done by the PhD candidate.

I.4.C 3D Atom Probe Tomography

-60 °C is classically considered as the temperature above which carbon can diffuse in a reasonable time in steel. Carbon atoms are thus sufficiently mobile during quenching and even at room temperature to segregate onto certain microstructure defects, such as dislocations and boundaries [38,71,72] or to form carbides (self-tempering & tempering). The level of carbon segregations at microstructure scale thus depends strongly on the severity of the heat treatments.

In order to study the carbon atoms distribution in the microstructure, and thus the possible segregation state and kinetics, 3D Atom Probe Tomography (3DAPT) characterizations were performed on 0.2C_GQ and 0.2C_WQ samples. The experiments were performed after between 1 and 2 months of storage at room temperature. For the 0.2C_GQ condition 8 tips were characterized and analyzed while for the 0.2C_WQ condition 5 tips were studied.

The 3DAPT experiments were performed in collaboration with PhD. Frédéric Danoix, at the Université de Rouen. PhD. Frédéric Danoix performed the sample preparation (electrochemical preparation) and the tips tomographies, while the data analysis was performed by the author under PhD. Danoix supervision. The experiments were performed at 50 K with a CAMECA LEAP 4000 system operated in voltage pulse mode a pulse ratio of 20% and a repetition rate of 200kHz. The characterization technique is detailed in [73,74]. The 3D volumes were recreated and analyzed with IVAS 3.8 software, the k-factor used during the reconstruction was set to 4.1.

It has been reported [75,76] that in some cases, C atoms clusters arrived on the detector in the form of clusters of ions, producing extra peaks that must be considered and decomposed for a good composition determination. The total number of carbon atoms is calculated by the equation:

$$C_{total} = C_6 + C_{12} + 3C_{18} + 3C_{24} + 3C_{36}$$

Equation 6

where C_{total} is the total C atoms and C_x are the number of C atoms detected in carbon peaks at a ratio mass over charge of x [74].

Even if the tips were mostly analyzed searching for linear segregated regions (probably segregated dislocations), some planar segregated defects were found as well as segregated volumes (austenite). The linear segregations were detected by isosurfaces at 2.5 at. % C as shown in Figure 14.a, in which interior

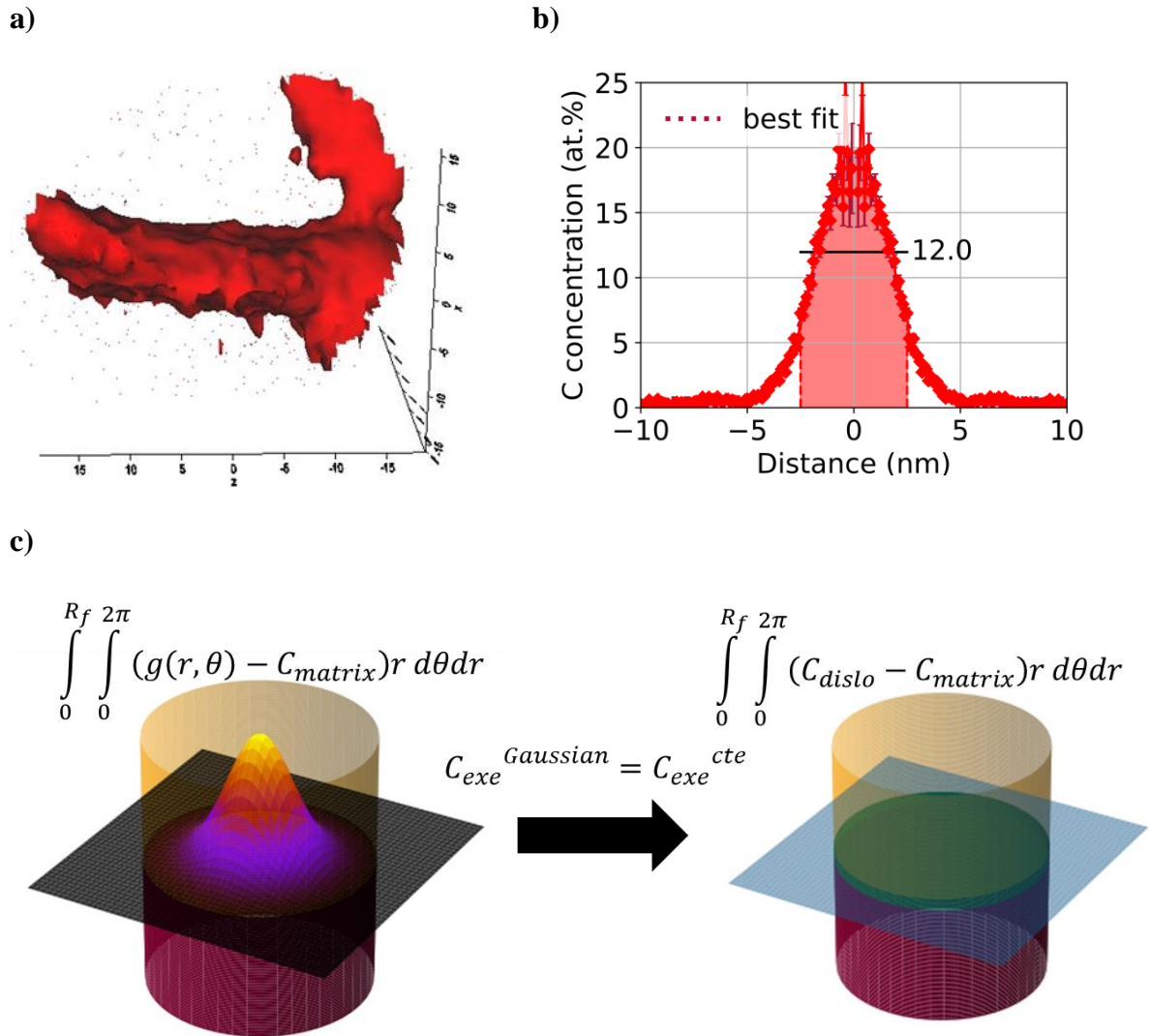


Figure 14: a) Isosurface of a linear segregation on a 0.2C_WQ tip. b) Reflected and centered proxigram obtained from the isosurface presented in a). c) Scheme of the calculation of the solute excess from the gaussian fitted function [77] (in b)) and the conversion into a constant value.

the carbon content was higher. From the created isosurface, a proxigram¹ was created and by reflecting it, it was possible to obtain the carbon profile, Figure 14.b. The proxigram was also used to show the carbon enrichment of the austenite film, in this case no reflection was used.

The excess of solute (C_{exc}) in the dislocation is calculated by circularly integrating the mentioned profile minus the C concentration measure far from the dislocation (C_{matrix}) [77]. A constant concentration (C_{dislo}) that gives the same C_{exc} was then calculated, this value will be used to compare and calibrate a segregation model (cf. Chapter III). Figure 14.c presents the described methodology.

¹ A proxigram is built by evaluating the minimum distance of each point in the selected volume to the isosurface. Once all the distances are calculated, the concentration are evaluated considering all the points between a given distance and the distance step selected.

I.4.D Electron BackScattered Diffraction in SEM

Some selected samples have also been characterized by SEM-EBSD (Scanning Electron Microscopy - Electron BackScattered Diffraction) to study the microstructure and the microtexture of martensite. It has been used to determine the PAGS for the three studied alloys, the microstructure size of the alloys (Chapter II) as well as the density of Geometrically Necessary Dislocations (GND).

The sample preparation and data acquisition was performed by Dr. Matthieu Salib, at AM. The sample preparation consisted of a classical sandpaper polishing until 4000 grit, then polishing with 6, 3 and 1 μm grain size diamond pastes, finishing with 30 minutes polishing with standard fumed silica suspension. The data acquisition was performed in a FEG-SEM JEOL 7001-F microscope equipped with a Bruker e Flash HR EBSD detector. The distance work was set at 12 mm and the accelerating voltage to 15 kV.

The Prior Austenitic Grain Sizes (PAGS) were determined by EBSD measurements and the use of the post-treatment software MERENGUE [78] for the three alloys (characterization and analysis made by AM). The PAGS for the 0.1C steel was measured to be 10.6 μm , for the 0.2C steel 6.54 μm and for the 0.3C steel 3.94 μm . For the 0.2C steel, the PAGS was also determined by thermal etching at the IJL. The austenitic grain boundaries were revealed during the austenitization treatment [79], then they were observed by optical microscopy (more than 500 grains were considered). In this case, the mean PAGS was measured to be 4.8 μm with a standard deviation of 2.3 μm (versus 6.54 μm determined by EBSD).

The microtexture and size analysis were performed with the HKL CHANNEL 5 software with the line intercept method after cleaning the EBSD maps (90 x 120 μm , step 0.1 μm) with a maximum starting zero solutions equal to 13 %. The noise reduction was applied with an iterating mode for extrapolating with 8, 7 and 6 neighbors. Then, manually repeatedly extrapolation with 5 neighbors until reaching 1 % zero solution. Finally, the wild spike were extrapolated.

An intercept line method was used to determine the distribution and mean size of domains. This method was performed with different misorientation angles as thresholds to define the domain limits with 200 lines (number of lines determined after carrying out a sensibility study to this parameter). For each condition both, vertical and horizontal, sets of lines were used.

The GND determination was performed by using the equation proposed by Liu et al. [80] with the Kernel Average Misorientation (KAM), considering a square shape Kernel of 5 x 5 pixels, the Burgers vector equal to 0.25 nm and the alpha parameter set to 3. Five different zones were used for the present determination (60 x 45 μm), with a total surface of around 13500 μm^2 . The EBSD data was post-processed using AZtec Crystal Software. The GND determination was performed by Dr. Matthieu Salib, at AM.

I.4.E Mechanical testing

The tensile behavior and the microhardness are the selected mechanical behaviors of the martensitic steel to be characterized.

I.4.E.1 Tensile testing

The tensile tests were performed at AM with a Zwick machine and under the standard NF EN ISO 6892-1. The samples shape followed the ISO 12.5x50 specifications. A constant loading rate was followed at low strain followed by a displacement controlled stage. The engineering stress and strain were transformed into true stress and true strain a in later treatment to be compared to behavior models.

The mechanical trials were performed by AM staff while the treatment of the obtained engineering stress and strain curves was performed by the author.

I.4.E.2 Micro-hardness

Hardness values were measured by micro-indentation Vickers tests carried out using a Presi HZ50-4 machine with a load of 0.1 kgf, leading to indentation size of about 15 to 25 μm . For each condition at least 50 indents were produced. The incertitude envelopes 80% of results.

A first evidence of the microstructural evolution with the different heat treatments can be obtained by measuring their microhardness as presented in Figure 15. It can be observed that the GQ (average - 20 $^{\circ}\text{C}/\text{s}$ between 400 $^{\circ}\text{C}$ and 200 $^{\circ}\text{C}$) state presented a lower hardness than the WQ state. The microhardness values for the low-time low-temperature tempering conditions are higher than WQ and then the values decrease with time and temperature. It is remarkable that the microhardness of the GQ state is similar to the ones presented at long-time 300 $^{\circ}\text{C}$ and all holding times at 400 $^{\circ}\text{C}$.

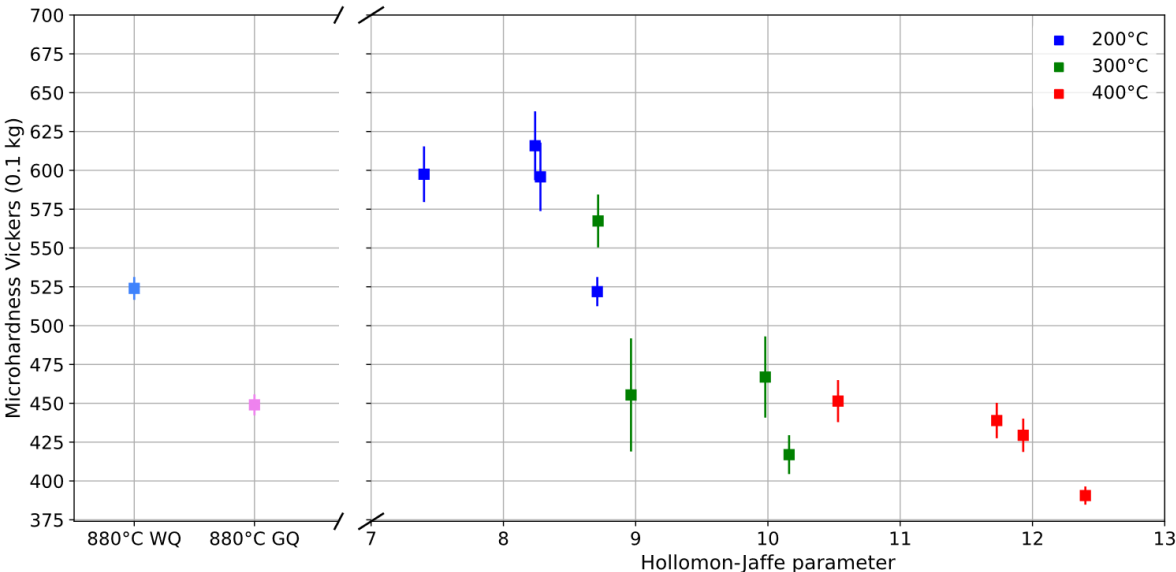


Figure 15: Evolution of the Vickers microhardness (0.1 kg) in the WQ state and GQ natural cooling state as well as function of the Hollomon-Jaffe parameter on the tempered conditions for the 0.2C steel.

I.5 Conclusions of the chapter

- 1) Although the characterization technics proposed in the present study are often utilized in metallurgical studies, their use in combination is rarer, especially when applied to martensitic steels.
- 2) The present set of characterization technics will allow to describe the martensitic microstructure at a multiscale (from a few nanometers in the case of the 3DAPT to a few microns in the case of the PAGS, or even at the scale of the part when considering the mechanical tests). A special attention will be paid to also analyze the microstructure distributions at the different scales.
- 3) The characterization of the three studied steels at the different states (from as-quenched to different tempering states) has been a collaborative work produced with the help of AM, of Groupe de Physique des Matériaux (GPM) at Rouen and the CC3M at IJL.

Chapter II

Microstructure of martensitic steels: Structures, defects and sizes

- II.1 Focused state of the art - 32 -
 - II.1.A Microtexture of lath martensite - 32 -
 - II.1.B Dislocation density - 36 -
- II.2 Microstructure sizes - 41 -
 - II.2.A Average domain sizes - 41 -
 - II.2.B Domain size distributions - 44 -
- II.3 Dislocation density - 46 -
 - II.3.A Dislocation densities during martensite transformation - 46 -
 - II.3.B Evolution during tempering - 61 -
- II.4 Conclusions of the chapter - 68 -

Industrial steels are far from being structures without defects in the crystalline sense of the term, and these defects are even responsible for their mechanical properties. The microstructural “crystalline defects” such as grain boundaries, twins, dislocations, vacancies act as obstacles to dislocation gliding. As a consequence, they have a key role on their mechanical behavior and contribute to harden the material. It is now well established that this hardening effect is partially controlled by the relative strength of the obstacles but more interestingly to their spatial distributions, meaning that the hardening effect is extremely size-sensitive [81–83]. Two classical examples of such sensitivity are the forest hardening (related to the mean distance between mobile and obstacle dislocations) or the famous Hall-Petch effect (grain size effect). The dislocation interactions and the detailed plasticity mechanisms leading to such sensitivity are out of the scope of this thesis but will we will use in the present Chapter general laws taken from the literature permitting to draw a link between the microstructure description and the mechanical properties.

This is the reason why it is absolutely fundamental to characterize finely these microstructure defects in the studied steels but also their spatial distributions. In this Chapter, we will focus our attention mainly on the microtexture of the martensite steels (laths/block/packet structure and associated sizes) and on the dislocations spatial distribution. The dislocation density affects not only the yield strength but also the plastic hardening in ferritic steels. This dislocation density also involves a certain stored elastic energy that is the driving force for possible recovery mechanisms, in the case of tempering heat treatments.

The present Chapter is divided in three main sections, the first one aiming to introduce a bibliographic research focusing on the prior work related to the martensite structure and defects. The second section will present our experimental size measurements on microstructure (mean values and distributions) of the as-quenched steels. The third one gathers our results on the measurements of the dislocation densities during the martensite transformation and further tempering treatments.

II.1 Focused state of the art

II.1.A Microtexture of lath martensite

As explained in the introduction, martensite is a metastable BCT product of the transformation from the FCC austenite. This transformation occurs at low temperature by a displacive diffusionless mechanism. In low carbon steels, the BCC structure appears in the form of small ellipsoidal prolate volumes of a few micrometers in length and a few hundreds of nanometers in diameter, called laths.

Due to the displacive nature of the transformation, the BCC structure presents a certain Orientation Relationship (OR) with the parent austenite. It has been proven that martensite does not respect strictly the Bain process and few possible OR have been identified in the literature experimentally, as the Kurdjumov-Sachs orientation relationship ($\{111\}_{\gamma} // \{011\}_{\alpha} \& (110)_{\gamma} // (111)_{\alpha}$), the Nishiyama-Wasserman ($\{111\}_{\gamma} // \{011\}_{\alpha} \& (10\bar{1})_{\gamma} // (100)_{\alpha}$) or the Grenier-Troiano ones [84]. It is nevertheless difficult to state about the real nature of the process [85]. From a single PAG orientation, depending on the chosen process, different possible BCT orientations can appear, which are called variants. The laths, however, do not appear in the PAG with a random variant.

The lath martensite presents a multiscale and hierarchical microstructure composed of packets, blocks, sub-blocks and laths inside the PAG as presented in Figure 16.a. In a single PAG, there are 24 possible variants. A packet is defined as a group of laths with similar habit planes and the same close-packed plane parallel relationship with the PAG (former $\{111\}$ planes), and 4 orientations of packets are possible in a given PAG [28]. The disorientation between packets can reach misorientation angles higher than 30° . Each packet can be composed by three types of blocks with a block defined as a group of laths with similar crystal orientation (between 3 to 6 possible variants depending on the OR). Following the KS OR, the blocks can also sometimes be decomposed in two kinds of variants with a misorientation angle lower than 10.5° [28,86]. These two groups are known as sub-blocks. The smallest microstructural domains are the laths whose boundaries present misorientation angles of only a few degrees between them inside a given sub-block. A set of SEM-EBSD micrographs presenting PAG boundaries as well as packet boundaries and laths are shown in Figure 16.b and Figure 16.c. As observed in Figure 16.c a group of laths in a block are aligned presenting a morphological texture at the submicrometric scale.

The characterization of the microstructure size can be performed by optical microscopy, after a thermal etching. At a smaller scale, EBSD characterization has been widely used to study the microstructural size as function of the critical misorientation size while applying the intercept method [87].

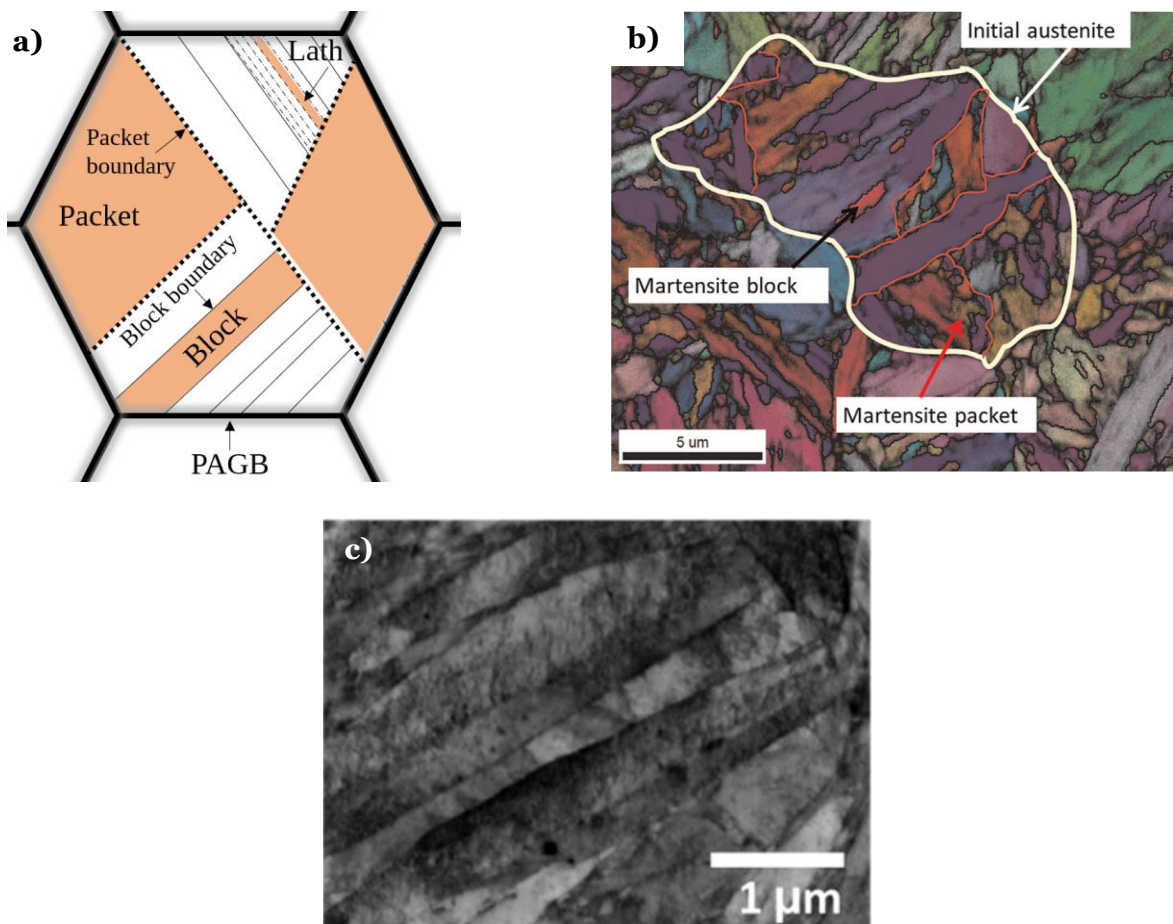


Figure 16: a) Hierarchical microstructure of lath martensite, highlighting the concepts of packets, blocks, sub-blocks and laths inside a Prior Austenitic Grain (PAG). b) SEM-EBSD micrograph of an as-quenched martensite presenting a set of PAG boundaries as well as packet boundaries. The thin aligned boundaries are laths boundaries shown in detailed in c) by backscattered electron contrast imaging . b) from [88] and c) from [89].

EBSD characterization allows to perform reconstruction of the microstructure up to the PAG by using the previously established orientation relationships [86,89]. Finally, at an even smaller scale, the lath width can be characterized by TEM [89,90]. In this last case the drawbacks are that no distinction of the boundary kind can be performed. The analyzed volume is also limited and the statistical representativeness of such observation must be often questioned.

Hutchinson et al. performed a systematic study of the effect of the carbon content on the martensite microstructure size by applying the intercept method on EBSD maps [87], as the one presented in Figure 17.a. The evolutions of the microstructural size as function of the considered critical misorientation angle for different steels are shown in Figure 17.b.

The measured mean size increases with the threshold chosen to make the measurement, first rapidly between 2° and 10° and then slowly. This evolution is explained as different microstructural features are in fact characterized. The lath width is mostly measured at few degrees misorientation, when the threshold is placed over a few degrees. Close to 10° , mostly the sub-blocks are identified. When the threshold angle is higher than 10° , for example 14° , then most of the highly disoriented boundaries are characterized including PAG boundaries, packets and blocks. These curves give a good overview of the sizes of all microstructure components at a glance.

When now comparing the different steels, it clearly appears that the microstructures are finer when the steels contain higher carbon content [87]. The low-carbon steels (steels A and B) in [87] presented a smaller PAGS.

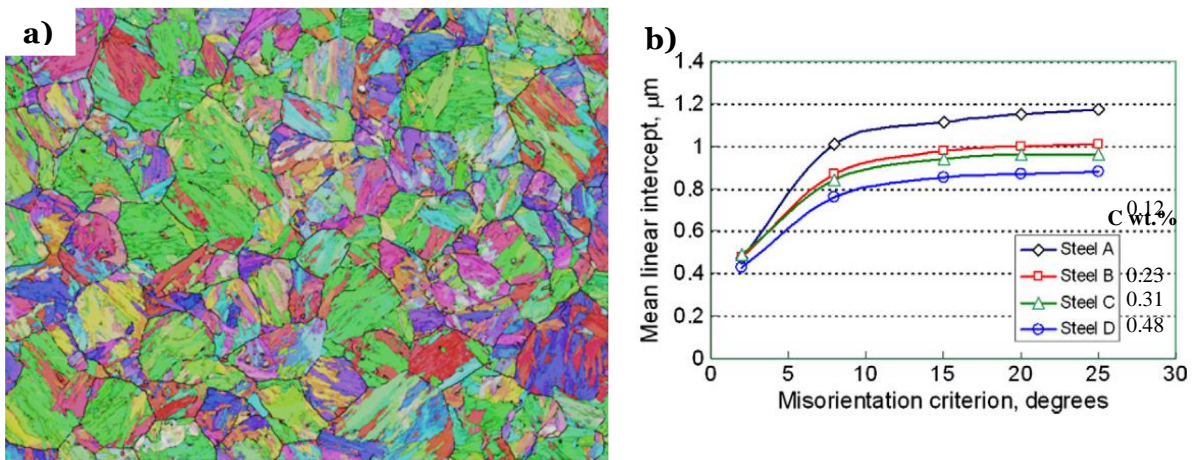


Figure 17: a) EBSD map of a 0.23 wt.% steel. b) Evolution of the microstructural size obtained by the line intercept as a function of the carbon content. From [87], image width is 100 μm .

The diversity of the characterization methods and of the types of boundaries that they are likely to reveal make comparisons between literature publications very difficult. This is a point that will be discussed at length in the present Chapter.

Maki et al. showed the linear correlation between the packet size and the PAGS [91]. This correlation was later confirmed by Galindo-Nava et al. [92] combining the results of [10,86,93]. A linear correlation between the block size and the PAGS is proposed for PAGS lower than 75 μm . However, a decreasing correlation for the mean lath width is proposed versus the carbon content of the alloy and not with the

PAGS as for the other two microstructural features. This particular correlation of lath width with the carbon content is based on the works of [87,94–96].

The size of lath martensite has also been the subject of scientific work from the late 1960s and 1970s until nowadays, mainly by TEM analysis. Krauss [94,97,98] showed that in a 0.2 wt.% C steel the most frequent lath widths ranges between 0.15 and 0.2 μm (a similar average lath width was reported by Speich and Warlimont [99], 0.25 μm) with a log-normal distribution from 0.1 to several micrometers. Even if in the mentioned studies the distribution of lath width were reported, in more recent work usually only the mean values of lath, block and/or packet width are reported. One recent study presenting the block diameter distribution of a 0.3 wt.% carbon steel was performed by HajyAkbari et al. [88]. Shamsujjoha presented the distribution of lath width and block diameters for three different steels with varying the carbon content [89].

The distribution of the lath width has been related to the martensite transformation sequence. Apple et al. [94] suggested that first the large laths are formed and then the finer ones in the constrained austenite. In a much more recent work, Morsdorf et al. [45] studied the effect of the transformation sequence on different microstructural features (size, carbon segregation/precipitation, dislocation density) by a combination of characterization techniques and showed evidence of the mentioned sequence.

From the presented results, it can be concluded that the microstructure size of the martensite decreases with the carbon content of steel. A correlation with the PAGS is also presented due to the hierarchical nature of the martensite. The distribution of sizes present a log-normal shape in which the wider sizes are related to the first formed martensite.

Moreover, the size distribution of domains and their mean values are susceptible to evolve during tempering. This evolution has been documented in high temperature tempering but not at temperatures lower than 600 °C [100]. Garcia-Mateo et al. showed that tempering at temperatures lower than 550 °C does not affect bainite thickness [101]. As all the tempering heat treatments performed in this work are at least 150 °C lower than the two cited temperatures, it will be considered that no changes on the as quenched domain size distribution occurs during tempering.

The size of the microstructure domains has important effect on the mechanical properties, for example on the yield strength. As rule of thumb, the finer the microstructure, the higher the flow stress is. As this evolution follows an inverse power law (Hall & Petch like), the relative hardening in ferrite becomes highly sensitive to the size when it reaches micron or submicron values as observed in Figure 18. This Figure thus shows the importance of a careful determination of the domain sizes in the case of martensitic steels. Note that the steels studied in [82] were produced by power metallurgical which may affect the mechanical properties.

In the present work, the mean domain size will be studied as function of the critical misorientation angle for the three considered alloys in the water quenched state as proposed by Hutchinson et al. [87], with a special attention dedicated to the obtained distributions.

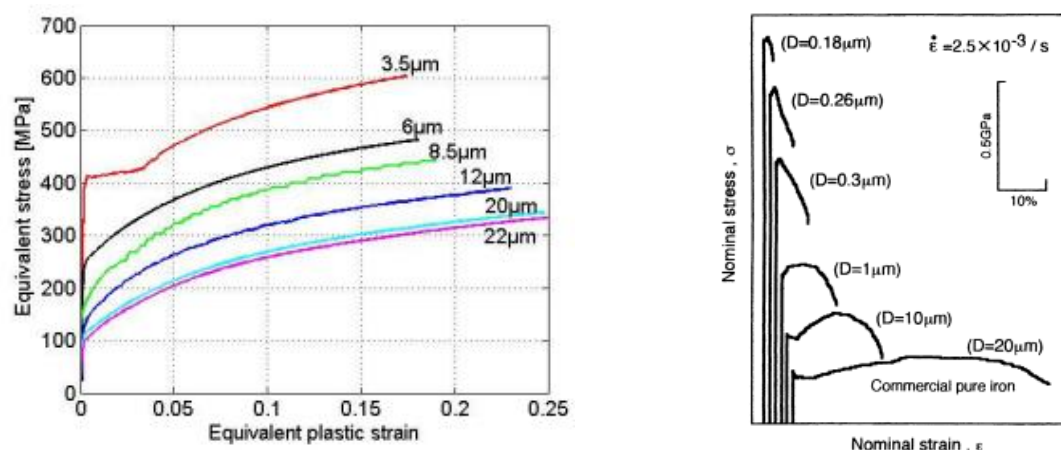


Figure 18: a) Tensile behavior of ferritic steels with different grain sizes, after [81]. b) Tensile tests on ultrafine grain ferritic steels (manufactured by powder metallurgy, after [82]).

II.1.B Dislocation density

Although it is well established that the mean dislocation density has an important effect on the strengthening of metals [102], it also affects other metallurgical mechanisms. As example, dislocations are known to trap carbon atoms and could act as nucleation sites for carbide precipitation [38,103–105]. As a consequence, it is crucial when studying martensitic steels and their tempering to have a proper idea of the dislocation density, nature and spatial distributions.

In the rest of this work, we will be interested in the different categories of dislocations that are generally found in the microstructure of steels and their spatial distributions. When possible, we will try to distinguish systematically the Geometrically Necessary Dislocations (GNDs) which contribute to the plastic accommodation in between microstructure components and generate long range internal stresses from the Statistically Stored Dislocations (SSDs) which are debris from the plastic deformation process and thus solely contribute to an isotropic hardening. The low angle boundaries in between the laths often correspond to walls of GNDs for instance. Dislocations cells encountered inside the laths are on the contrary often made with SSDs. Figure 19 shows some examples of TEM observations of such defects in martensitic microstructures.

The dislocation density can be determined by a large variety of characterization techniques; XRD (Williamson-Hall method [54], modified Williamson-Hall method [55–57] and Warren-Averbach [60]), TEM [27], Electron Channeling Contrast Imaging (ECCI) [83,106], Small-Angle Neutron Scattering (SANS) [17], neutron diffraction (ND) [42] and by EBSD [80] without being exhaustive. Even dilatometry has been used to estimate the dislocation density [107]. Most of the technics put into evidence all the dislocations (SSD and GND) while only the geometrically necessary dislocations (GND) can be detected by EBSD as it is based on the Kernel disorientation angle.

The following section will deal successively with the available literature on dislocations in as quenched martensite and on their evolution during tempering.

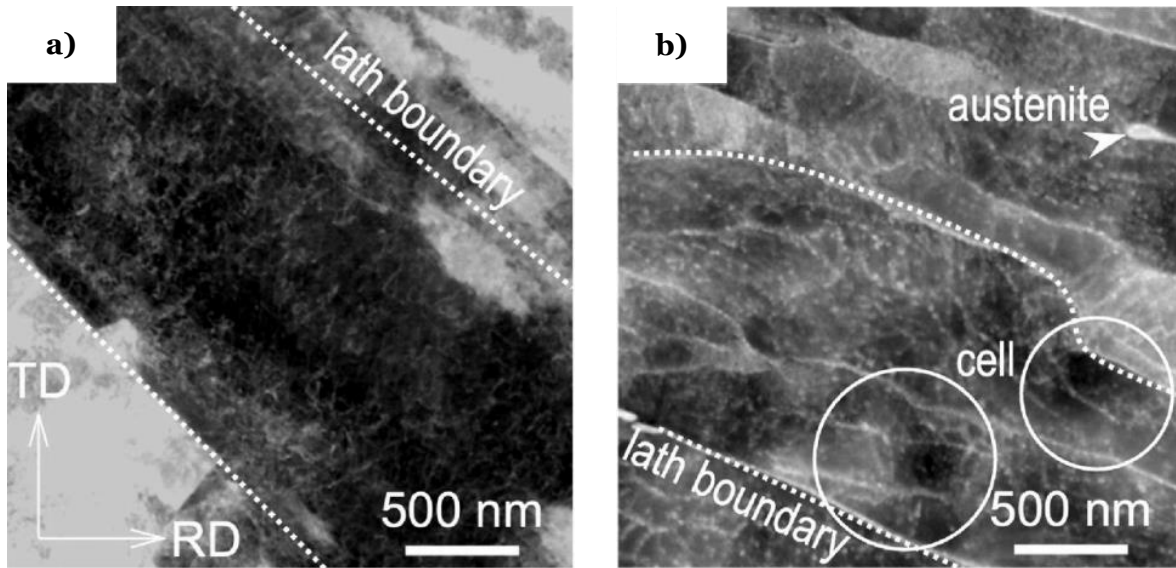


Figure 19: Electron channeling contrast images of dislocation structures presenting in a) homogenous distribution within the lath and in b) the presence of cells with its concentrated and depleted regions. From [83].

II.1.B.1 Dislocation density in as quenched martensite

It has been often reported in the literature that dislocation density in the martensite increases with the carbon content of the steel [27,92]. This trend is related to the higher transformation strain. Figure 20 presents a summary of mean dislocation density values measured in martensite as a function of carbon content (up to 0.38 wt.% C) obtained from the bibliography [17,27,42,61,88,89,108–110]. From 0 to 0.22 wt.% C a linear correlation is visible, for higher carbon contents this correlation becomes more scattered.

In the frame of our study, an equation is proposed to represent mathematically the mentioned correlation:

$$\bar{\rho} = 1 \times 10^{14} + 1 \times 10^{16} \times \text{wt. \% C} \pm 1 \times 10^{15} \text{ 1/m}^2 \quad \text{Equation 7}$$

where $\bar{\rho}$ is the mean dislocation density.

The presented dislocation densities are considerably high for metals. For instance, similar magnitudes are usually obtained in metals which have undergone severe plastic deformation [111,112]. The specific contribution to the 0.2 yield strength can be estimated up to 900 MPa [88,89] which can be compared with the size strengthening observed in defect-free sub-micrometric microstructures.

All the dislocation densities presented in Figure 20 were determined at room temperature after quenching. The determination of the dislocation density during the martensitic transformation itself requires a more specific in situ experimental set-up with a high acquisition rate, as the transformation is fast below Ms.

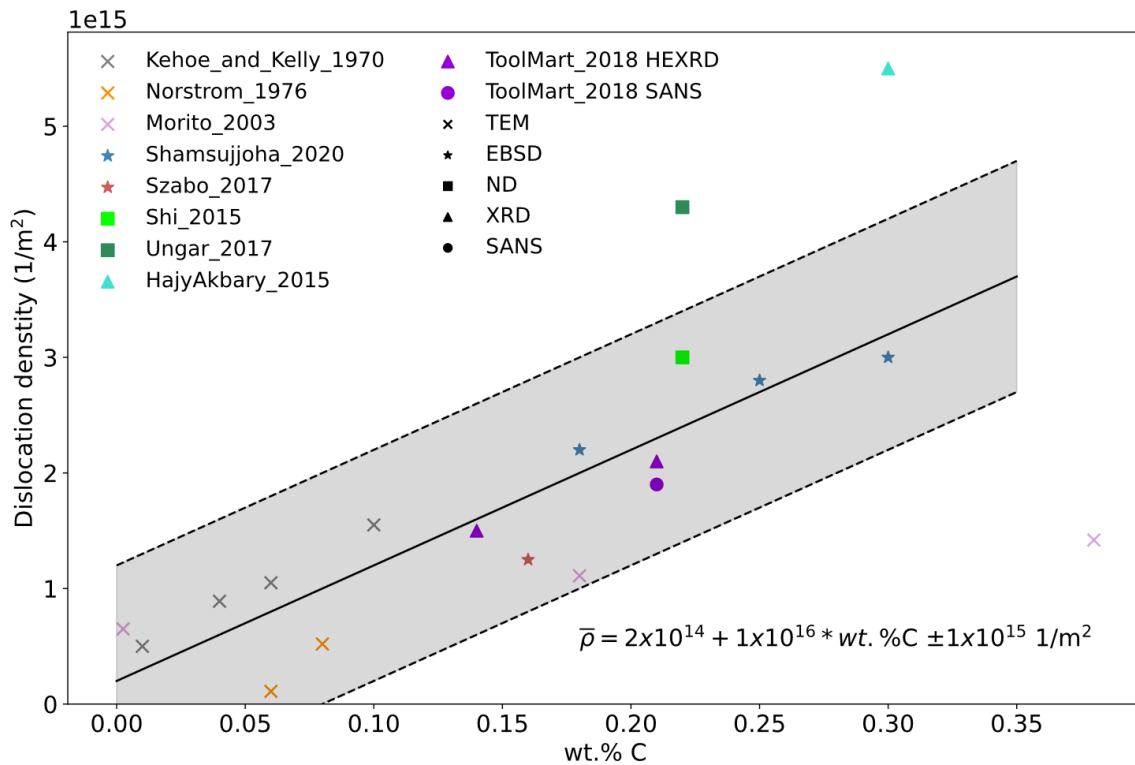


Figure 20: Mean dislocation density in low carbon martensitic steels as function of the C content [17,27,42,61,88,89,108–110]. The values determined by TEM are indicated with a cross, those by EBSD by a star, those by neutron diffraction (ND) with a square, those by XRD by a triangle and the one by Small-Angle Neutron Scattering (SANS) with a circle. An empirical equation is proposed for the mentioned correlation.

Christien et al. studied the evolution of the dislocation density in the martensite and in the austenite along the martensitic transformation in a stainless steel using in situ neutron diffraction [113]. In a more recent work Yonemura et al. utilized an X Ray free-electron laser (XFEL) [114]. However, in this latter study the dislocation density evolution as a function of the transformation was not obtained from a single sample but from the juxtaposition of 11 independent experiences. In a recent project funded by the Research Fund for Coal and Steel of the European Union (ToolMart project), the dislocation density curve (of the martensite and of the austenite) as a function of the temperature is determined from one single in situ HEXRD synchrotron experience [17]. In this last mentioned report, no correlation was made however between the mean dislocation densities in the martensite and the transformed fraction.

The dislocation densities in martensite and in austenite increase with the transformation (sometimes only indicated by the decrease of the temperature) during quenching according to these three works [17,113,114]. This phenomenon can be related to the sequence of the transformation, in which the transforming martensite forms from an austenite that becomes harder due the transformation strain and a size effect (progressive fragmentation of parent austenite). The martensite inherits progressively more dislocations from the austenitic matrix.

The dislocations present within laths are shown to be distributed homogeneously at the as quenched state as reported by [83,89], this may evolve during a tensile test [89,115] and during tempering [83]. In lath martensitic steels, it has been found that a higher proportion (ca. 75 %) of screw dislocations are present in the as-quenched state and that tempering at 500 °C may decrease this proportion [83]. Tensile deformation was found to not affect significantly the 75% screw proportion [83,89].

A steel with high dislocation densities is unstable as it contains a high amount of stored elastic energy. As a consequence, if the system is reheated, recovery of the dislocation structure can take place.

II.1.B.2 Recovery and tempering

The recovery corresponds to the decrease in the dislocation density mainly by annihilation and recombination of dislocations as well as their rearrangement at the microstructural scale. Both mechanisms are thermally activated (as based on the iron self-diffusion) and their driving force is the decrease in the elastic stored energy (as for the recrystallization process which generally occurs at higher temperatures).

From an experimental point of view, the evolution of the dislocation density during a tempering is usually deduced by indirect measurements, though the evolution of the mechanical properties: hardness [116,117], or tensile test curves [118]. Pesicka et al. characterized post mortem the effect of tempering at 750 °C on the SSDs and GNDs by combining TEM and XRD measurements, showing that for high dislocation densities XRD characterization is more suited [119]. Sallez et al. followed the recovery of a oxide dispersion-strengthened ferritic powder at 600 °C by in situ HEXRD synchrotron experiments [62] as shown in Figure 21. Below 400 °C, a slow change of the dislocation density is observed. From 400 °C to higher temperatures a fast diminution of the dislocation density is reported, followed by a plateau. Similar conclusions regarding the heating section were presented by Moreno et al. by an in situ HEXRD synchrotron experiment on a cold rolled steel [120].

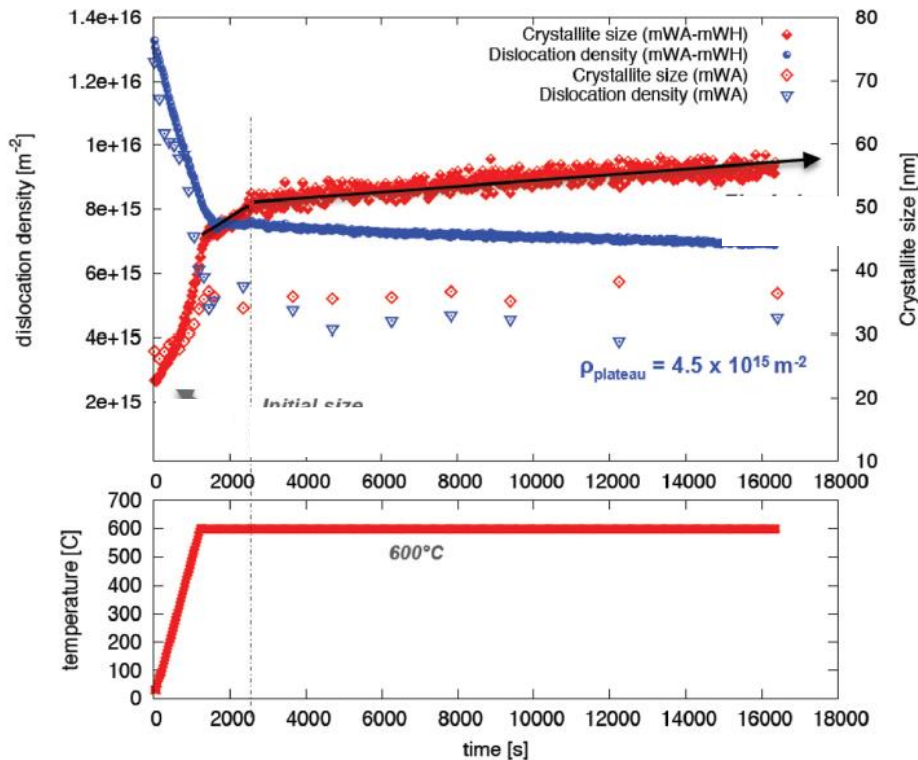


Figure 21: Dislocation density evolution during tempering at 600 °C of a ferritic powder taken from [62]. mWA standing for modified Warren-Avenbach method.

In situ studies of recovery at low temperatures are rare in the literature. Shi et al. tracked the dislocation density by in situ neutron diffraction in a temperature range from 100 °C to 700 °C on a low-carbon martensitic steel [61]. However, in their work, the authors only inform the final values indicating that from 100 °C to 200 °C no major changes are observed.

From a modeling point of view, two main families of recovery models are found in the bibliography; physically based and empirical models. The first family aims to obtain a good understanding of the underlying physical mechanism even if the description of the experimental results is not perfect. Few models falling into this category can be cited: Friedel's model based on the mechanical relaxation [121], Humphreys' model based on dislocation microstructure rearrangement [122], or Nes' model combining both mentioned theories [123].

For instance, the evolution of the mean dislocation density predicted by Friedel according to the short-range annihilation of dislocations by a thermally activated cross-slip mechanism follows the equation:

$$\frac{d\bar{\rho}}{dt} = -K_F \frac{2(\alpha C_T \mu b \bar{\rho})^2}{k_B T} \exp\left(\frac{-U_0 - V \alpha C_T \mu b \sqrt{\bar{\rho}}}{k_B T}\right) \quad \text{Equation 8}$$

where K_F is a constant ($J/(GPa^2 s^1)$), α is a geometrical constant with values typically between 0.25 and 0.5, C_T is the Taylor constant (can be considered as 3), μ is the shear modulus, b is the Burgers vector and $\bar{\rho}$ has been previously defined. U_0 is the apparent activation energy (kJ/mol) with values typically between 150 and 174 kJ/mol for iron self-diffusion in ferrite [123,124], V is the apparent activation volume, k_B is the Boltzmann constant and T is the temperature in K. An example of a recovery experiment with the modeled recovery by the Friedel's model as well as by the Nes' one is presented in Figure 22.a.

In the second family of models, i.e. empirical ones, logarithmic mathematical functions are often proposed [125,126] (with no good description neither at the beginning of the tempering nor at long times) as well as some more complex mathematical expressions [127]. The following model introduces a threshold dislocation density in order to capture the experimentally observed saturation and is expressed as:

$$\frac{d\rho}{dt} = -\frac{2\mu b^3 D_{\text{eff}} C_{\text{rec}}}{k_B T} (\rho^2 - \rho_{\text{sat}}^2) \quad \text{Equation 9}$$

where D_{eff} refers to the effective diffusion coefficient for substitutional elements (m^2/s), C_{rec} is a material-dependent parameter which has to be calibrated, ρ_{sat} is the temperature-dependent "saturation" dislocation density ($1/m^2$) and the other terms have the already established meaning. A similar formulation is proposed by Wedberg [128]. Such formulations could serve to describe experimental data at constant temperatures but are less suitable to predict evolutions along non-isothermal holdings, contrary to physically-based models. Figure 22.b presents one example from the literature in which this kind of empirical model was applied.

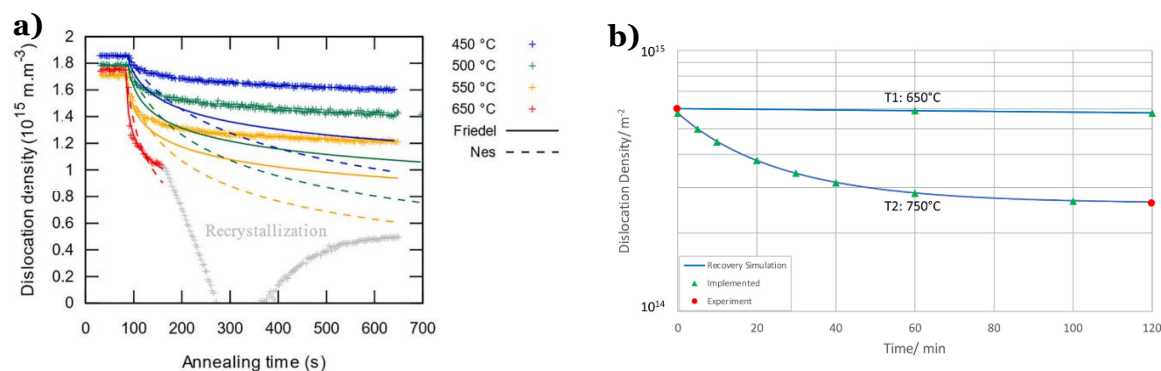


Figure 22: a) experimental and modeled evolution of the dislocation densities when annealing a cold-rolled steel at different temperatures, from [129]. b) experimental and modeled evolution of the dislocation densities when tempering a chromium-alloyed ultra-low-carbon martensitic steel, from [130].

The present work will focus on the systematic characterization of the evolution of the mean dislocation density during the martensite formation, considering the effect of the nominal carbon content of the alloy as well as the effect of the cooling rate. From the evolution of mean dislocation density, the spatial distribution after quenching will be predicted. The recovery of the dislocation densities (mean and distribution) at low temperatures tempering will then be characterized and modeled.

II.2 Microstructure sizes

Our experimental study of the microstructure in the studied steels will be divided in two sections. The first one will focus on the average domain size and its evolution as function of the carbon content. A special emphasis will be done on the choice of the threshold misorientation angle permitting to define boundaries in the microstructure and thus what we called domains of interest delimited by these boundaries or more simply “domains”. The second section will be dedicated to the analysis of the obtained size distributions of these domains.

II.2.A Average domain sizes

The EBSD maps of the studied steels are presented in Figure 23, a) for the 0.1C_WQ steel, b) for the 0.2C_WQ steel, and c) for the 0.3C_WQ steel. The black lines represent all boundaries with a disorientation higher than 10° , while the white ones refer to the boundaries higher than 50° . For the different alloys some PAG with two or more clear different orientations (for instance one close to 111 and one close to 001) can be observed indicating the presence of different variants. Some of these “multivariant” PAGs are highlighted with black dashed ellipses. The PAG size of the 0.2C_WQ steel seems visually smaller than the 0.1C_WQ, while the 0.3C_WQ is visually the one presenting the smallest PAG size.

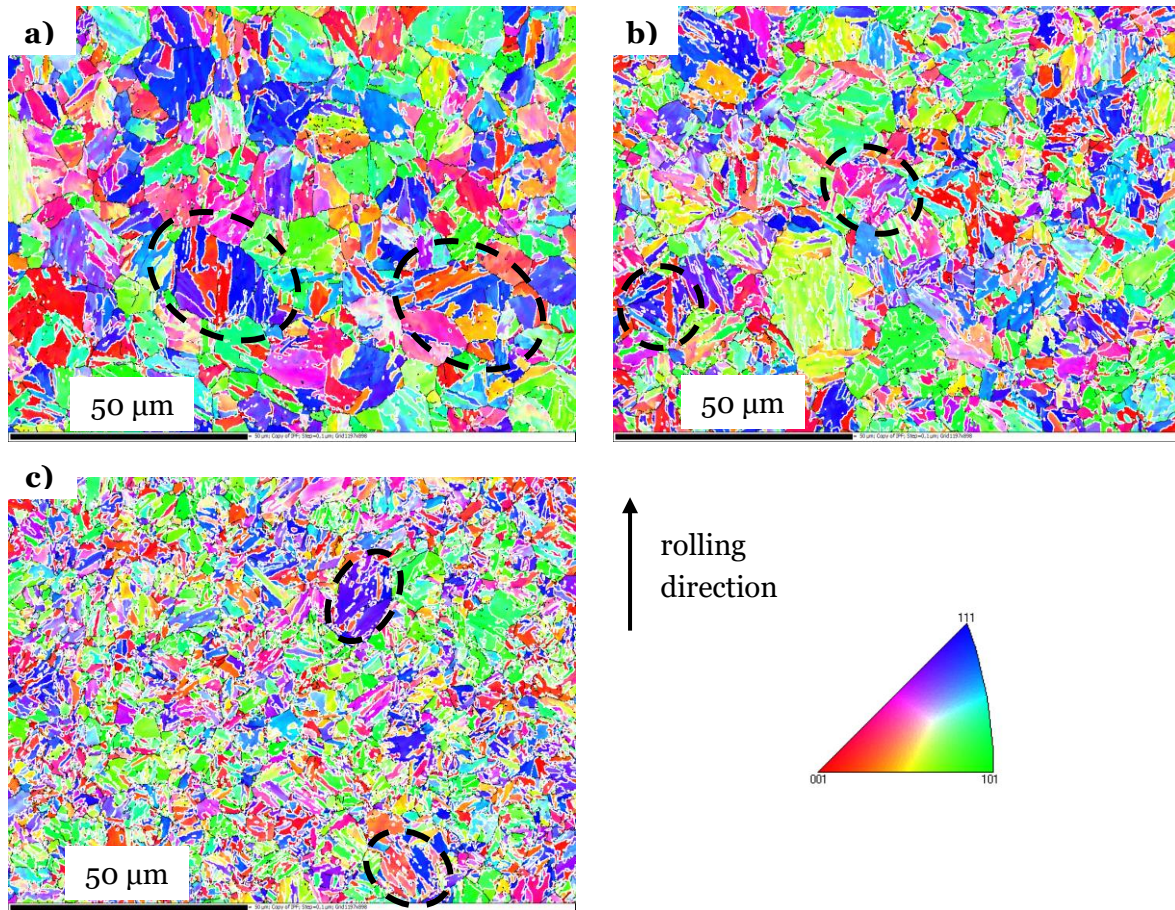


Figure 23: SEM-EBSD maps (Inverse Pole Figure representation) a) of the 0.1C_WQ steel, b) of the 0.2C_WQ steel, and c) of the 0.3C_WQ steel. The black lines represents misorientations $\geq 10^\circ$, while white ones $\geq 50^\circ$. The black ellipses highlight some PAGs

The domain sizes in the water quenched state for the three studied steels were first measured by the line intercept. As explained in the state of the art (Section II.I.A), this procedure require to define a critical misorientation angle to be able to detect the expected boundaries on the maps. Varying the threshold misorientation angle would allow to get insights on the low disoriented joints as well as on the highly disoriented ones. This is the reason why the line intercept has been conducted on each map with different thresholds and the results will be presented as a function of this latter critical angle (from 2° to 45°).

Two sets of lines were used for each map, a horizontal one and a vertical one (400 lines in total). The lowest number of segments measured, 7680, was reached at the highest threshold value (45°) on the 0.1C steel (largest PAG). On the other hand, using a critical angle of 2.5° on the 0.3C steel leads to more than 50000 segments. From the total number of segments, only the ones identified as BCC phase and longer than $0.15 \mu\text{m}$ (1.5 times the probe step) were considered. Then, the average value was calculated and stereologically corrected (multiplied by a 0.32 factor as proposed in [131]).

Figure 24 presents the results for the three alloys including results obtained with the vertical and the horizontal sets of lines. The mean value is also reported (considering the two set of lines). The minimal average values are 0.28, 0.24 and $0.2 \mu\text{m}$ for 0.1C, 0.2C and 0.3C steels respectively, while the maximum ones, at the highest misorientation angle, are 0.7, 0.45 and $0.35 \mu\text{m}$. The difference in sizes between the three alloys increases with the misorientation angle.

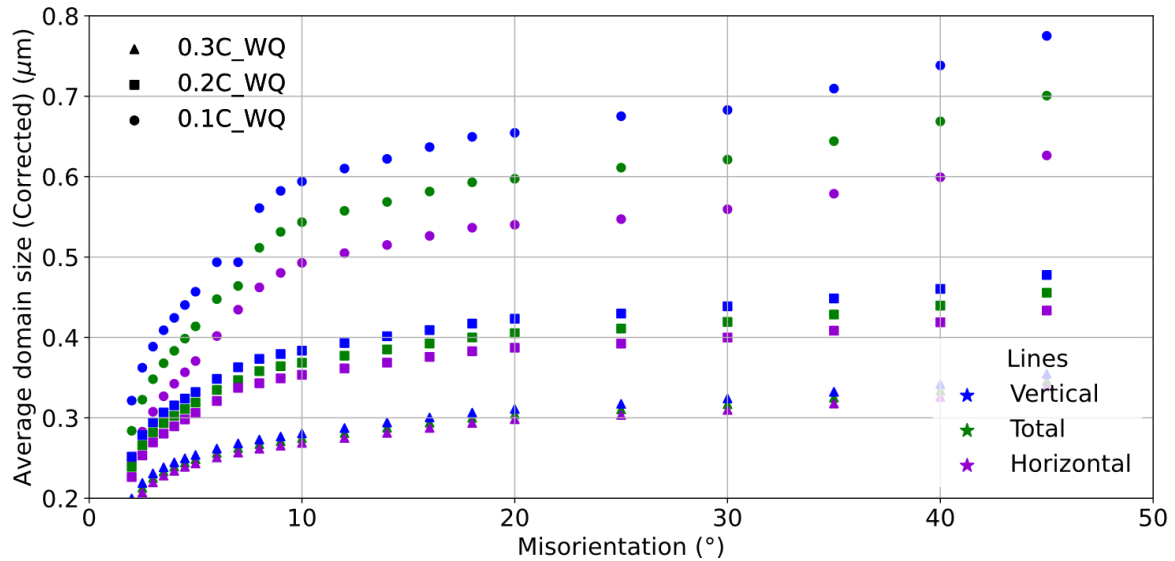


Figure 24: Average domain size as function of the threshold misorientation angle. The alloys are identified by the marker type as presented in Section I.3. The color code corresponds to the orientation of the intercept: vertical lines in blue, horizontal ones in violet and mean in green.

In Figure 24 three main tendencies can be appreciated.

As expected, the mean domain size increases with the threshold angle; first quickly below 10° and then at a slower rate. A similar evolution of the size with the misorientation has been reported by [87,132]. It is related to the hierarchical lath martensite structure. The low critical misorientation angles put into evidence the laths and sub-blocks and, therefore, the mean size is controlled by these features [28]. Above, the mean size is more controlled by the block, packet and PAG structure and, thus, increase with the critical angle. The 60° corresponds especially to the angle found between self-accommodating variants and are usually related to block boundaries [133]. Although several block boundaries are observed in Figure 23 in white lines ($\geq 55^\circ$), by considering this threshold many high disoriented PAG boundaries are not detected. As a consequence, no determination higher than 45° was performed.

Then, the higher the carbon content of the steel, the lower the domain size as reported by [87]. As shown in Chapter I, the PAGS are 10.6, 6.54 and $3.94 \mu\text{m}$ for 0.1C, 0.2C and 0.3C steels respectively. It obviously decreases with the carbon content, in contrast with [87]. The packet size is related to the PAGS and the block size to the packet size [91,92]. The observed trend can be thus explained and inherited from the austenitic state. Another reasonable explanation is related to the transformation temperatures as in bainitic steels [132]. The lower the carbon content of the steel, the higher the M_s temperature is.

For the three studied EBSD maps studied (one per alloy), the analysis using vertical lines gives higher average domain sizes than one using horizontal lines. A possible hypothesis explaining this phenomenon is that the three maps has been obtained in the same direction versus the rolling axis, with the vertical direction parallel to the rolling axis. The systematic difference put into evidence could be explained by a weak morphological texture of the austenitization due to a memory effect.

The EBSD characterization allows to determine the mean microstructural size as function of the choice of the critical misorientation angle. It can be concluded that the microstructure becomes finer with the

carbon content in the studied steels. However, our measurement can be further exploited to determine also the statistical and special distributions of these sizes.

II.2.B Domain size distributions

In the analysis conducted above, for each threshold angle, the length of each intercept is recorded allowing to exploit and analyze further their statistical distribution. However, the occurrence of a certain length in the distribution does not represent the probability to find a certain feature size at a given point in the microstructure. The purely statistical distribution of the measured lengths must be corrected by a stereological approach to account for:

- The measure in a cutting plane neglecting the inclination of the lath below the surface
- The measure is not made perpendicular to the boundaries
- The volume distribution

A strong assumption is made is that the laths of martensite are thin lamellas in the microstructure. The first parameters have been taken into account when considering the stereological correction of the mean value (0.32 parameter).

The volume-fraction distribution of the true spacing can be calculated as by Cahn and Fullman [134]:

$$P_{v(l)} = 3lN(l) + l^2 \frac{dN(l)}{dl} \quad \text{Equation 10}$$

where the l is the intercept spacing (not multiplied by 0.32) and $N(l)$ is the occurrence of the segments with a length l (occurrence distribution discussed above). $P_{v(l)}$ will be called spatial distribution of size in the following.

Figure 25.a presents the spatial distribution as well as the stereological corrected one (in the following named “spatial” distribution) for a 14° critical misorientation angle.

For some intercept sizes the Cahn and Fullman correction predicts negative probability density when applying directly to the sparse experimental data (due to the derivative term of Equation 10). As a consequence, the spatial distribution will be first modelled with log-normal distributions and not used directly.

The log-normal distribution function is defined as:

$$PSD = \frac{1}{x\varpi\sqrt{2\pi}} \exp\left(-\frac{(\ln(x) - \Pi)^2}{2\varpi^2}\right) \quad \text{Equation 11}$$

where x refers to the variable, ϖ and Π the parameters related to the spread and the position.

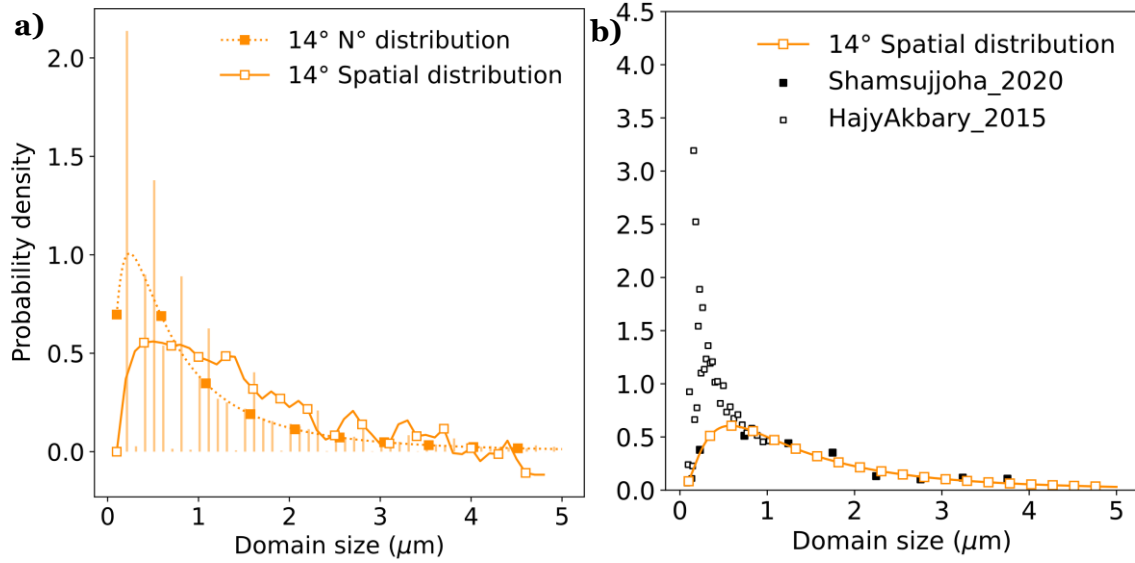


Figure 25: a) Occurrence and spatial distribution determined on the 0.2C_WQ EBSD map applying a 14° threshold angle. b) Comparison between the 14° here founded spatial distribution (represented with a log-normal equation) and the distributions reported by [88,89]. The colors used in the present figure do not follow the chart presented in Section I.3.

From the log-normal distribution the mean is given by:

$$\text{mean} = \exp\left(\mu + \frac{\sigma^2}{2}\right) \quad \text{Equation 12}$$

The spatial distribution, represented with a log-normal distribution, obtained by applying 14° as threshold angle is presented in Figure 25.b. The mentioned angle is higher than the misorientation between sub-blocks and the ones between laths and, therefore, would include only high angle boundaries (HAB) as blocks, packets and PAG. As the packet boundaries and the PAG are also physical boundaries of the composing blocks it can be concluded 14° would reveal the block boundaries.

The herein determined distribution is compared with block size distributions reported in the literature [88,89]. HajyAkbery et al. performed their characterization by ECCI and no stereological correction is mentioned [88]. Shamsujjoha determined the size distribution by EBSD with a 50 nm step, no stereological correction mentioned [89]. The distribution determined in the present study show a good agreement with the one reported by Shamsujjoha [89] while the one reported by HajyAkbery et al. [88] presents a narrower dispersion highly concentrated in submicron sizes. The difference between the herein determined distribution and the one reported by HajyAkbery et al. may be due to a difference in the PAGS (which affect the block size [92]).

The effect of the carbon content in the spatial size distributions is presented in Figure 26. For each of the three studied steels the spatial distributions were obtained applying a 14° threshold.

The mean values presented in Figure 26 differ from the one presented in Figure 24. Two main explanations can be postulated. Firstly, the stereological corrections methodologies are different in both analyses. Secondly and more important, in Figure 24 the average is based on number of occurrences while in Figure 26 a volume analysis is presented.

Although, all three alloys present segments with the minimal considered length, the lower the nominal carbon of the steel, the higher is the proportion of blocks with longer dimension. As a consequence, the 0.1C steel has a larger size distribution than the 0.2C steel and both are widely spread compared to the 0.3C steel.

The domain size study (average, number and size weighted distributions) was done at the water quench state for the three alloys. As all the tempering temperatures are lower than the ones in which evolution of the microstructure size have been reported [100,101], no change of these distributions are considered to happen with further tempering heat treatments.

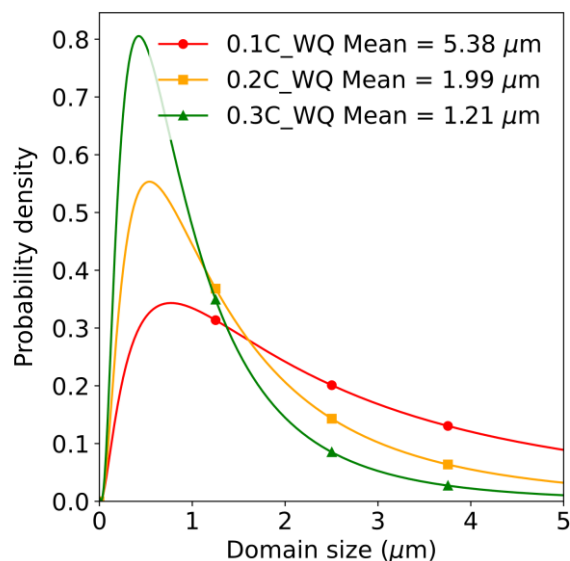


Figure 26: Probability density distribution of domain size (with stereological correction applied) for the three studied steels using as threshold angle of 14° . The colors used in the present figure do not follow the chart presented in Section I.3.

II.3 Dislocation density

The study of the dislocation density will be separated into two sections. The first one focuses on the evolution of the dislocation density (mean and local values) during the martensitic transformation itself while the second one is dedicated to the evolution of the dislocation density (mean and local values) during tempering by recovery. The methods (HEXRD, TEM and EBSD) and the studied alloys and conditions are presented in the dedicated Chapter I.

II.3.A Dislocation densities during martensite transformation

The results of the present section have been in large extent published in two publications during the PhD. [14,68].

The effect of two main parameters were systematically studied, the nominal carbon content of the alloys and the cooling rate under M_s temperature. Four different cooling rates were applied during quenching, 3 controlled gas quenches at -10, -50 and -100 °C/s respectively and water quench (cooling rate between

-1000 and -5000 °C/s). The characterization of the gas quench heat treatments were performed in situ (HEXRD) allowing to acquire data during the whole transformation while the water quenched samples were only characterized at room temperature (HEXRD). Some samples have also been studied post mortem at room temperature by EBSD and TEM.

II.3.A.1 Mean dislocation density

In the following subsection a detailed analysis of 0.2C_GQ_10Cs in situ HEXRD experiment is presented. The objective of this subsection is to introduce the applied methodology. Then, in a latter subsection only the results will be discussed.

II.3.A.1.a 0.2C_GQ_10Cs in situ HEXRD experiment

The data (temperature, sample elongation, diffractograms) obtained from the considered experiment (0.2C steel, martensite transformation at -10 °C/s below Ms) are presented in Figure 27.

The evolution of the temperature during cooling is presented in Figure 27.a. Some small deviations from the linearity are observed at the beginning of the cooling, then a small change is observed due to the exothermic nature of the martensitic transformation and, finally, close to room temperature the rate deviates from the programmed one due to a lower temperature difference between the sample and the cooling gas.

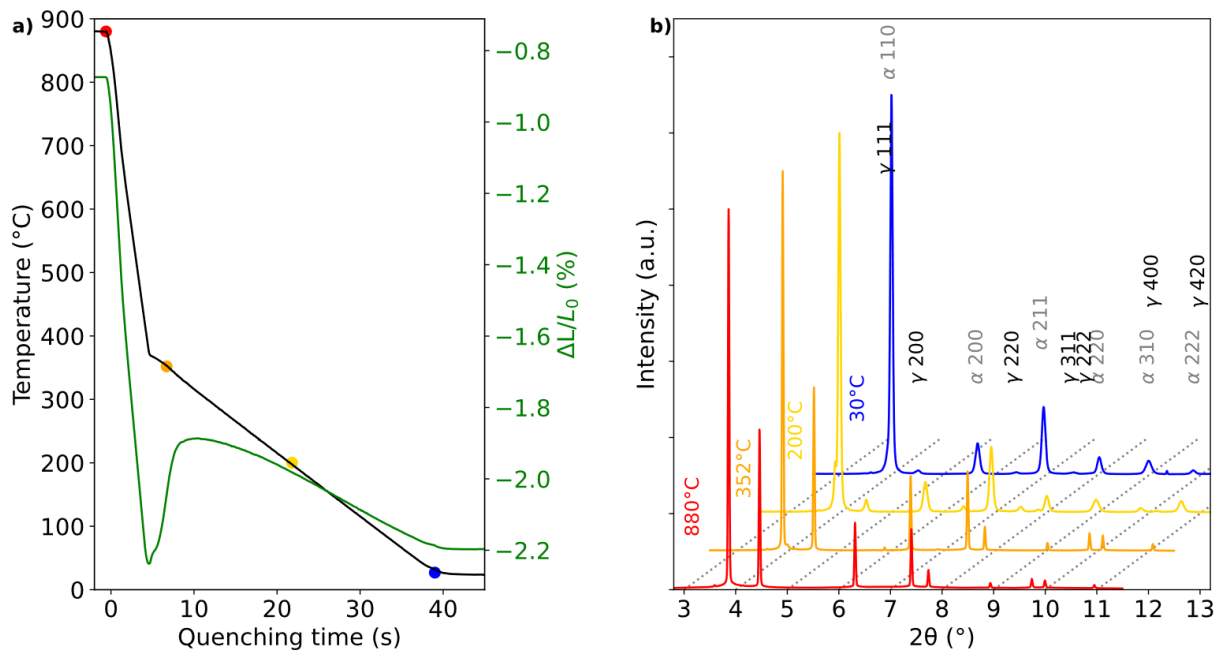


Figure 27: a) Evolution of the temperature during the quenching at -10 °C/s rate during one of the in situ experiments as well as the dilatometric signal. b) Selected diffractograms at the points shown in a) with the peak positions of the austenite and the martensite. The diffractograms have been shifted in 2θ and in intensity to facilitate the reading.

The martensitic transformation can be confirmed by the dilatometric data which shows a clear volume expansion below Ms temperature. Above this critical temperature, no deviation from the linear thermal contraction is observed meaning that no pro-eutectoid or bainite is formed during cooling.

These results are confirmed by some selected diffractograms shown in Figure 27.b. In these diffractograms, the alloy remains fully austenitic down to the M_s . The diffractogram obtained at 200 °C shows the diffraction peaks of both phases, austenite and martensite while at room temperature, at the present scale, all the diffraction peaks correspond to the martensite and only a weak {200} austenitic peak are observable.

In order to be able to determine the dislocation density as function of the martensite fraction, two different analyses of each dataset have been performed. The phase fraction evolution was measured firstly by Rietveld refinement using all the peaks simultaneously (the whole angular-window) while the second one is based on peak-by-peak analysis (using restricted angular-windows around selected diffraction peaks) to determine the dislocation densities for each diffractogram, as explained in Chapter I.

For the selected experiment, the evolution of the phase fractions and of the Full-Width at Half Maximum of the {200}, {211}, {220} and {321} martensitic peaks as well as {200}, {220}, {311} and {420} austenitic peaks are plotted in Figure 28.

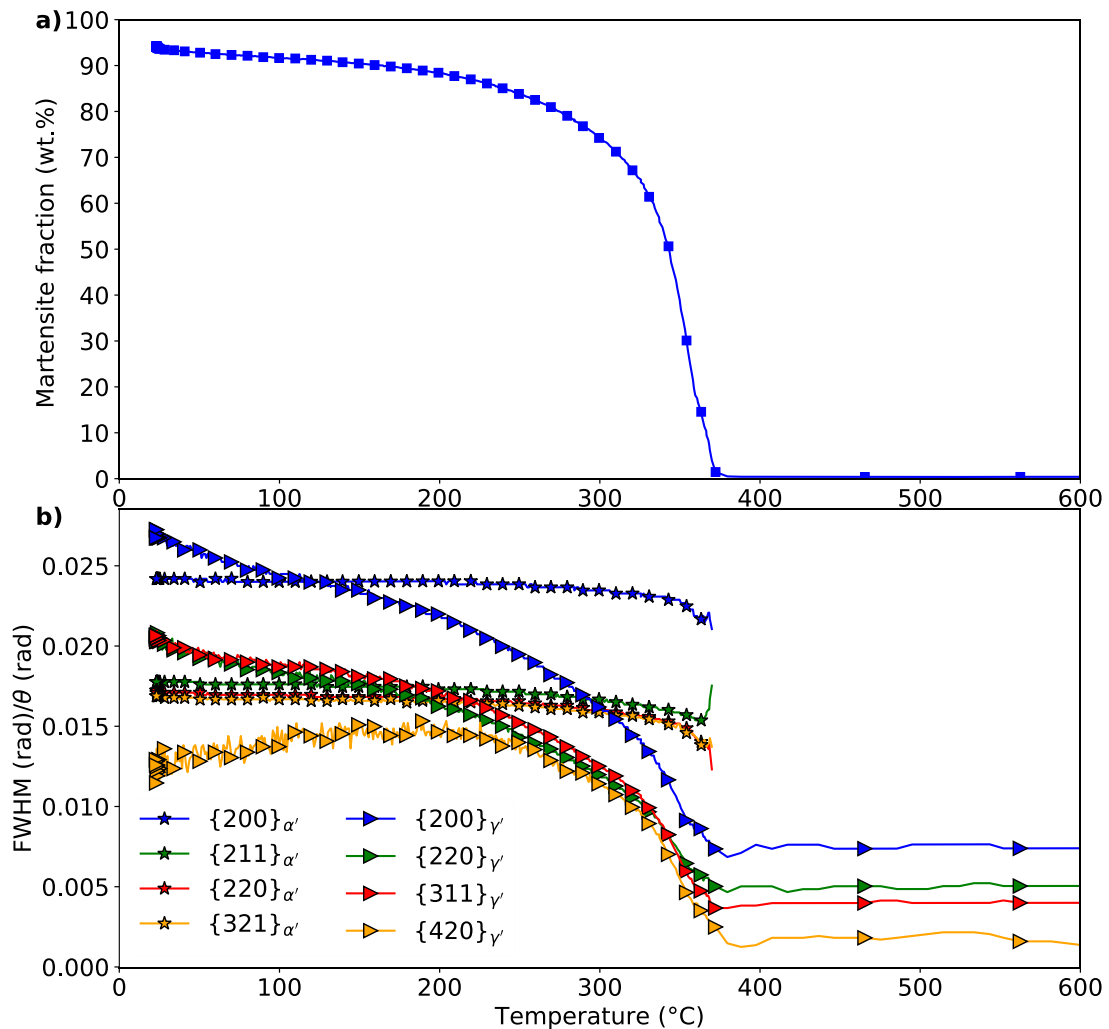


Figure 28: a) Martensite transformation kinetics (0.2C_GQ_10Cs experiment). b) Evolution of the FWHM divided by the position of the diffraction peaks used for the dislocation density determination in the martensite (stars) and in the austenite (triangles). The curves presented in b) does not follow the chart presented in Section I.3.

The transformation kinetics during the quench is shown in Figure 28.a. At temperatures above 400 °C no BCC or BCT phase was detectable, i.e. the microstructure is fully austenitic as expected after annealing at 880 °C followed by a fast cooling. The transformation starts sluggishly at ca. 390 °C followed by a rapid change of the transformation rate at 372 °C. The first segment, between 390 and 372 °C, may be due to some chemical heterogeneities, thermal gradients, decarburization of the surface, PAGS distribution [37,135]. The temperature at which the transformation speeds up agrees well with the theoretical M_s temperature of the investigated steel (369°C) accounting for the nominal steel composition and the prior austenite grain size (PAGS) [16,136]. At room temperature all the austenite is not transformed into martensite, the weight fraction of retained austenite is equal to 5 wt.%.

Figure 28.b presents the evolution of the normalized FWHM values (FWHM divided by the peak position) of the austenite and martensite peaks. These peaks will serve to determine the dislocation densities according to the mWH method.

Between 880 °C down to the 372 °C, the normalized FWHM values of the austenite are almost constant as expected, meaning no change in the defect density and in the crystallite size, the absence of phase transformation and plastic events, consistently with [113,137]. Then, a fast increase is observed for the four austenitic peaks. The positive evolution with decreasing temperature continues for the three peaks with higher diffracting intensity {200}, {220} and {311}, while the normalized FWHM value of the {420} peak starts to decrease around 200 °C. The decrease in the {420}'s FWHM is probably due to the low intensity of the mentioned peak at low austenite fraction (<20 wt.%). The ratio maximal intensity over background is 0.41 at the mentioned temperature while at room temperature it decreases down to 0.31.

The normalized FWHM values of the four martensitic peaks followed successive stages. During the first one a relatively fast increase is observed, followed by a saturation. When martensite first appears its normalized FWHM values are ca. 5 times higher than the ones of the austenite, while that at the end of the transformation the normalized FWHM values are similar for both phases.

The mWH method (Section II.4.2.C) allows to determine the mean dislocation density (average of dislocation density in the whole phase's volume) in martensite and in austenite from the peak positions and their measured FWHM values. The main hypothesis of this method is that the measured FWHM values are a direct consequence of the crystallite size and dislocation density only. We will show that this vision is probably reductive in Section I.3.A.1.c, and we will introduce in particular the effect of a possible tetragonality. However, in the absence of any quantitative data, we will neglect the possible heterogeneities of hydrostatic stresses that could also affect FWHM. The internal stresses due to the phase transformation deformation and its accommodation during the martensitic transformation are present at different scales and their precise determination is still an open question. At a phase scale, mean hydrostatic stress leading to a shift of the diffraction peaks have been evidenced by HEXRD experiments [137–139]. The heterogeneities of internal stresses inducing peak broadening are relatively little addressed in literature unfortunately. SEM-FIB ring-core method have been applied to report an anisotropic strain distribution at the scale of martensite variants [30,140]. Nevertheless, it is difficult to extrapolate their findings.

The evolutions of the mean dislocation density in the austenite and in the martensite as function of the martensite fraction are presented in Figure 29. The mean dislocation density in austenite at less than

30 wt.% of martensite was lower than $1 \times 10^{13} \text{ 1/m}^2$ followed by a fast increase up to $7 \times 10^{14} \text{ 1/m}^2$. When the martensite fraction is higher than 80 wt.%, a stagnation is found related to the decrease of the $\{420\}$'s normalized FWHM. At martensite fractions higher than 90 wt.% the austenitic dislocation density determination was no more possible (negative values of the slope in the mWH equation). The increase of the dislocation density during the martensitic transformation can be explained by the plastic deformation observed by Miyamoto et al. in parent austenite adjacent to the forming martensite lath [141].

The austenitic high dislocation density at high martensite fraction indicates that this phase is not a “soft” component of the as quenched martensitic microstructure, confirming the results of [17]. Retained austenite is in fact already intensively plasticized at room temperature due to the transformations strain and thus is also a hard phase of the microstructure (dislocation strengthening higher than 500 MPa). As a consequence, the plastic behavior of the martensitic microstructures cannot be strongly related to the residual austenite as claimed by [142] assuming a localized plastic deformation between laths.

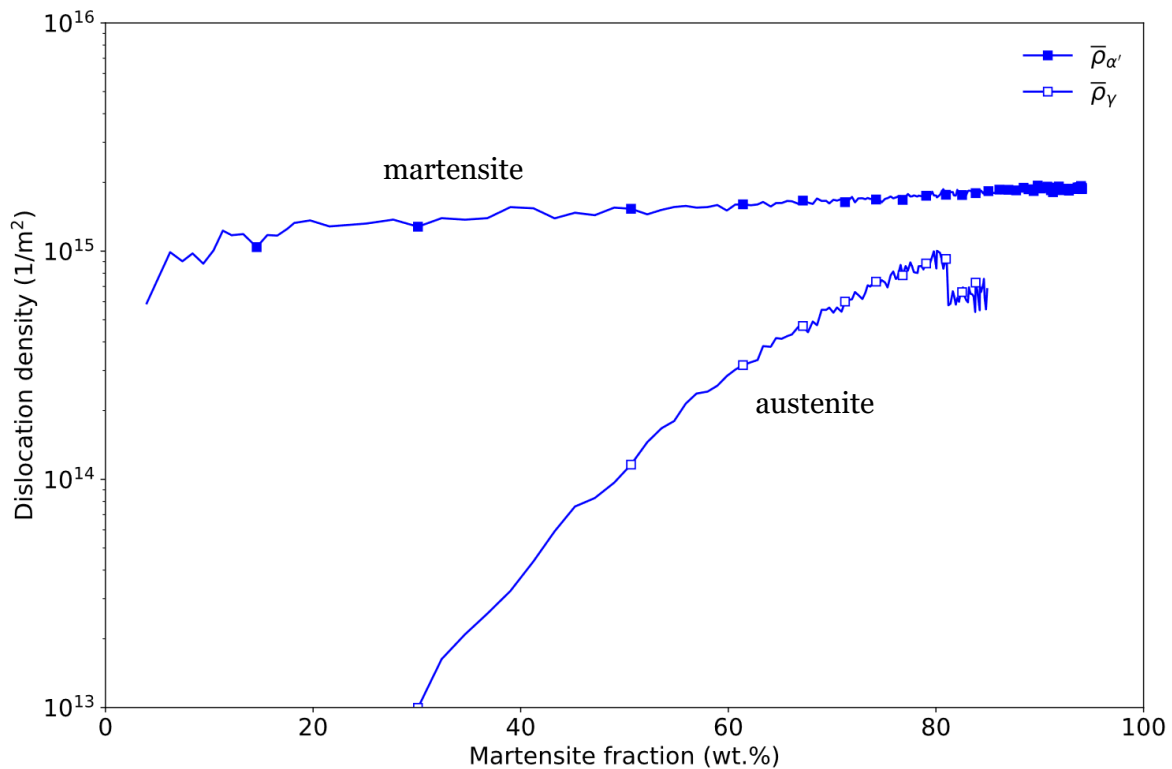


Figure 29: Mean dislocation densities evolution in the martensite (full colored markers) and in the austenite (white-center marker) as function of the martensite weight fraction.

The dislocation density in the martensite showed a relatively fast increase in the first ca 20 wt.% from 5×10^{14} to $1.5 \times 10^{15} \text{ 1/m}^2$. This stage is followed by a more constant and low increase with ca $2 \times 10^{15} \text{ 1/m}^2$ dislocation density at the end of the transformation.

II.3.A.1.b Effect of the nominal carbon content and cooling rate

The evolution of the mean dislocation density in martensite during the phase transformation was characterized in situ by HEXRD for the three studied steels at the three cooling rates. The experimental

results are shown in Figure 30; a) for the 0.1C steel, in c) for the 0.2C steel and in e) for the 0.3C steel while in b) the three steels are compared at $-10\text{ }^{\circ}\text{C/s}$ cooling rate, in d) at $-50\text{ }^{\circ}\text{C/s}$ and in f) at $-100\text{ }^{\circ}\text{C/s}$.

From three gas quench heat treatments for the 0.2C steel and the 0.3C steel (Figure 30.c and Figure 30.e), it can be inferred that the mean dislocation density in martensite increases with the cooling rate; a similar correlation was previously found in [17]. This tendency is not clear for the lower carbon content steel as the differences between the mean dislocation densities at the different cooling rates falls into the uncertainty of the measurement. The increase of mean dislocation density with the cooling rate is however confirmed by the post mortem characterization of the water quench samples.

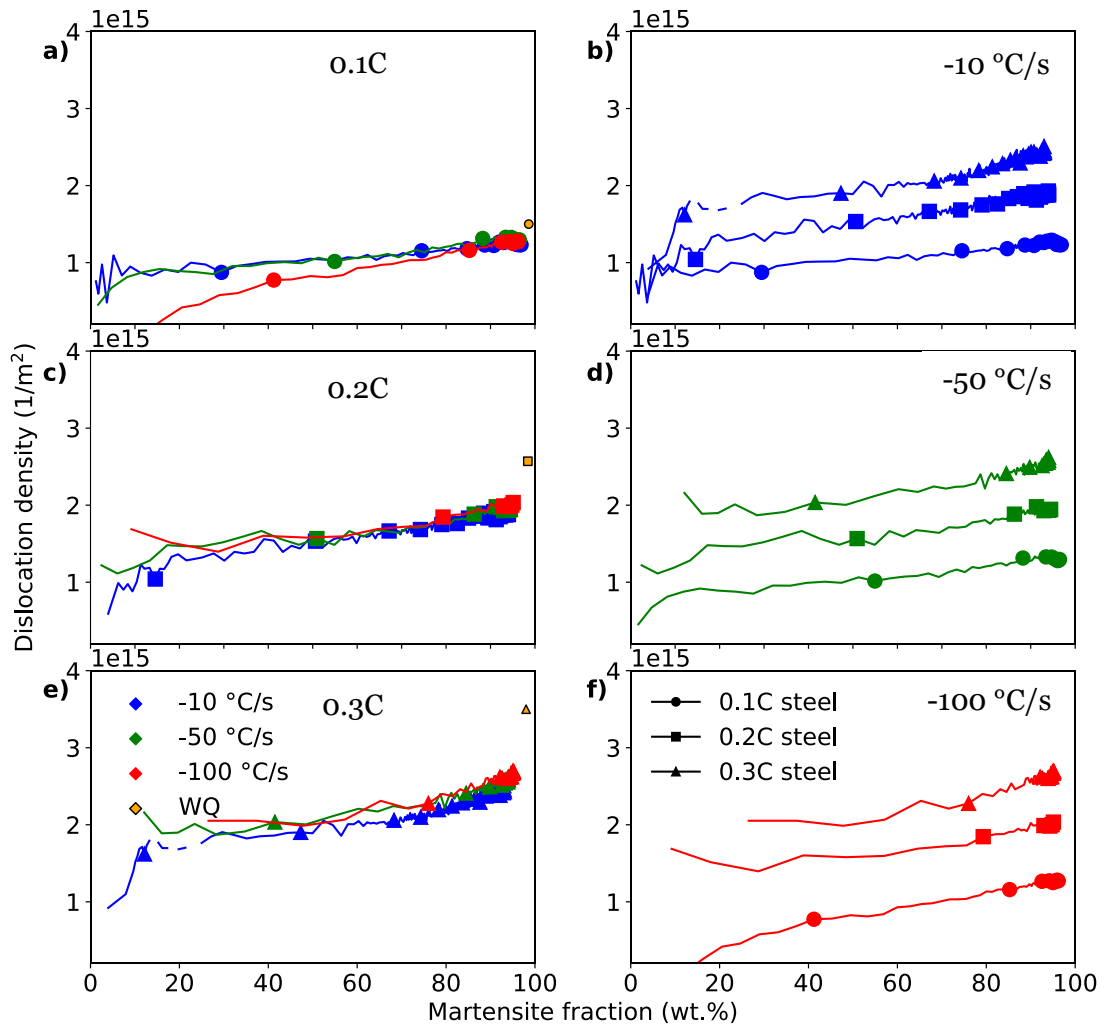


Figure 30: Evolution of the mean dislocation density in martensite as function of the transformed fraction. a), c) and e) present the effect of the cooling rate for the 0.1C steel, the 0.2C steel and 0.3C steel respectively while b), d) and f) compare the effect of carbon content at the three studied cooling rates.

Figure 30.b , Figure 30.d and Figure 30.f) shows obviously that the higher the carbon content the higher mean dislocation density is for a given cooling rate. The increase of the final dislocation density with the carbon content has been related to a higher volume change of the matrix during the transformation as proposed by Morito et al. [27].

II.3.A.1.c Effect of the tetragonality

In the preceding section, the evolutions of FWHM were linked only to the evolutions of dislocation densities and crystallite sizes in both phases as supposed by the mWH method. The FWHM are of course corrected using a calibrant to remove the experimental broadening. Nevertheless, this approach neglects a specificity of martensitic steels. In fact, it is well admitted that above a certain carbon content, the lattice of martensite could be BCT instead of BCC. As a consequence, the tetragonality could introduce a peak broadening not related to the defect density as some BCC peaks are slightly split. This tetragonality and its related effect on the FWHM is assumed to increase intuitively with a nominal carbon content and with the cooling rate as the self-tempering is reduced.

The Rietveld procedure reveals that the quality of the refinement is always better on the studied diffractograms using a BCT lattice than a BCC one. The difference is sufficiently high to claim that a tetragonality ($c/a > 1$) can be measured in all combinations of cooling rates and carbon contents at room temperature.

The c/a ratios at room temperature for the three studied steels for all the cooling conditions are presented Table 5.

Table 5: Tetragonality ratio at room temperature for the three steels studied at the four cooling rate during the quenching as well as the calculated carbon content in martensite (2 empirical equations).

Steel	Cooling rate	c/a ratio	C in matrix [22] - [143]
0.1C	-10 °C/s	1.0051	0.11-0.16
	-50 °C/s	1.0052	0.12-0.17
	-100 °C/s	1.0051	0.11-0.16
	WQ	1.0058	0.13-0.16
0.2C	-10 °C/s	1.0066	0.15-0.21
	-50 °C/s	1.0068	0.15-0.22
	-100 °C/s	1.0069	0.15-0.22
	WQ	1.0071	0.16-0.23
0.3C	-10 °C/s	1.0076	0.17-0.23
	-50 °C/s	1.0082	0.18-0.26
	-100 °C/s	1.0082	0.18-0.26
	WQ	1.0089	0.20-0.29

From the c/a ratios, the estimated carbon contents of the matrix, were calculated with the equations [22,143]:

$$c/a = 1 + 0.045 * wt. \%C \quad \text{Equation 13 [22]}$$

$$c/a = 1 + 0.031 * wt. \%C \quad \text{Equation 14 [143]}$$

The results of the calculation using the equations presented in [143] are higher than the nominal composition for the 0.1C steel and for the others two steels is very close to it. If the classical equation [22] is used instead, for the cooling conditions of the 0.1C steel the carbon content in the matrix is close to the nominal one while for the 0.2C and 0.3C steels some carbon seems to be missing in solid solution. As in the water quench condition no carbides were detected by TEM, it can be supposed that not all the carbon in the martensite contributes to the tetragonality in the same way (ca. carbon trapped in dislocations) also that some carbon is partitioned into the austenite. Also, an overestimation of the c/a ratio may be raised from the Rietveld refinement. The hypothesis of carbon partitioning into the austenite seems to be sustained for gas-quenched samples by the presence of carbon enriched regions which have been detected by 3DAPT and presented in Section III.2.A. Another element proving carbon partitioning is the higher retained austenite fractions measured in the experiments at lower cooling rates. These results are presented in Section IV.2.B. The simple applicability of these equations to low-carbon steels is also doubtful.

Even if their meaning is not fully clear, the tetragonality ratios summarized in Table 6 were used in order to perform a correction on the dislocation density determination procedure.

Table 6: Mean dislocation density without (1Peak-1Function method) and with tetragonality correction (1Peak-MultipleFunction method) and the difference between both values are presented for all the quenching conditions studied.

Steel	Cooling rate	$\bar{\rho}$ ($\times 10^{15} \text{ 1/m}^2$)	$\bar{\rho}_{c/a \text{ corrected}}$ ($\times 10^{15} \text{ 1/m}^2$)	$\Delta\bar{\rho}$ ($\times 10^{15} \text{ 1/m}^2$)
0.1C	-10 °C/s	1.31	0.98	0.33
	-50 °C/s	1.37	1.10	0.27
	-100 °C/s	1.41	1.28	0.13
	WQ	1.54	1.25	0.29
0.2C	-10 °C/s	2.06	1.76	0.3
	-50 °C/s	2.12	1.74	0.38
	-100 °C/s	2.14	1.76	0.38
	WQ	2.49	2.13	0.36
0.3C	-10 °C/s	2.73	2.21	0.52
	-50 °C/s	2.91	2.28	0.63
	-100 °C/s	2.94	2.31	0.63
	WQ	3.51	2.43	1.08

To do so, the c/a ratio was used to first calculate the diffraction peak splitting. Then, the individual peaks derived from a given splitting are adjusted individually while considering that they should present same FWHM (same density of dislocations) in order to reproduce the experimental signal (sum of the respective contributions). This methodology is detailed Section I.4.B.3 as well as in [68].

Figure 31 presents the results of both methods; in a) the 1Peak-1Function and in b) the 1Peak-MultipleFunction. {200} peak is better described with the first method while the shape of the {211} at low intensity is better with the second method. Small differences can be detected in the two remaining fitted peaks, in both cases the 1Peak-MultipleFunction gives a slightly better description.

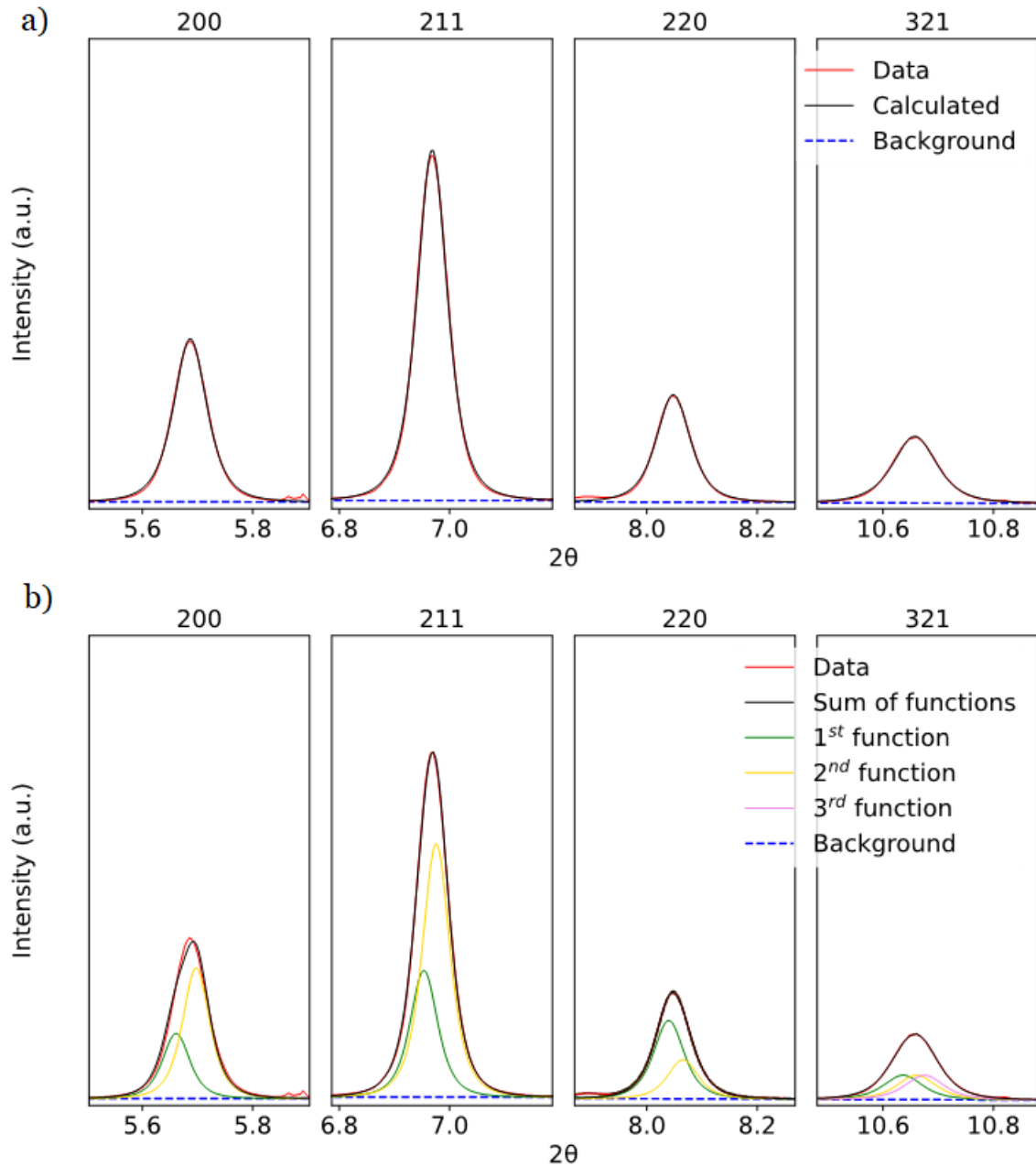


Figure 31: a) Diffraction peaks fitted by the 1Peak-1Function method. b) Same diffraction peaks fitted by the 1Peak-MultipleFunction method developed in the present work.

The mean dislocation density without and with tetragonality correction for each quenching conditions are presented in Table 6. The difference between both mentioned methods is also presented.

As expected, the mean dislocation densities with tetragonality correction are always lower than the ones without the correction. The higher the estimated tetragonality is the higher the difference between the methods is.

The uncertainty due to the M constant choice in the mWH method is $0.47 \times 10^{15} \text{ 1/m}^2$ between M set to 2 and to 3 for the 0.1C_GQ_10Cs condition while for the 0.3C_WQ one the uncertainty is $1.28 \times 10^{15} \text{ 1/m}^2$. In both extreme cases the difference due to the tetragonality correction is lower than the uncertainty due to the M choice.

In conclusion, the tetragonality correction does not play a significant role on the dislocation density determination in comparison with other parameters involved. This result is sustained by the fact that the diffraction peaks are highly symmetrical meaning that the possible tetragonality put into evidence by the Rietveld analysis is probably an upper bound. Appendix A is dedicated to present the asymmetry of the diffracting peaks, and why the c/a ratio determined by the Rietveld refinement is probably an overestimation.

II.3.A.1.c Additional post-mortem measurements by TEM and EBSD

The mean dislocation density was determined on the 0.2C_WQ sample by TEM using the intercept method used by Morito et al. [27], and detailed in II.5.C Dislocation density. The total length of the lines was $2158 \mu\text{m}$ with a total number of intercepts of 77. The thickness of the sample determined by EFTEM was 90 nm ($\pm 10 \%$). The mean dislocation density was estimated around $0.95 \times 10^{15} \text{ 1/m}^2$. The mean GND density determined by EBSD analysis is $1.32 \times 10^{15} \text{ 1/m}^2$.

Regarding the consistency between the values obtained by the different methods, the higher dislocation density estimated by HEXRD ($2. \times 10^{15} \text{ 1/m}^2$) might be due to the lattice perturbations induced by other microstructures defects as twins, lath boundaries, small carbon heterogeneities producing different lattice parameter. The dislocation density determined by EBSD is low compared to the value obtained by HEXRD, but it only takes into account the GNDs, which represent only a fraction of the total density of defects (between 60 and 90 % in martensitic steels [89]).

The relative low dislocation density measured by TEM can be justified by the sample preparation, some relaxation/recovery may occur in thin samples (image forces due to the proximity of free surface), as well as by a bias in the measurement. The determinations have been done in regions in which the dislocations can be identified individually, however some other regions might present higher dislocation densities which we were not able to quantify. The boundaries rich in dislocations may have been also not fully considered by this last technic while HEXRD characterizations do not present this limitation.

These additional experiments thus sustain our HEXRD measurements, even if the absolute values must be always considered with care accounting the choice of the empirical M factor in the mWH method and others possible contributions put aside (internal stresses, tetragonality).

II.3.A.1.e Discussions

Comparison with the literature

The mean dislocation densities of the water quench conditions of the three C contents determined by the mWH method (without and with tetragonality correction) as well as by EBSD and by TEM for the 0.2C_WQ condition are presented in Figure 32 with the values from the literature (cf. Figure 20). The mean dislocation densities determined by the mWH method without tetragonality correction follows the main identified tendency. The ones with the tetragonality corrections deviate with the increase in carbon even if all the values are in the predicted trend. GND density measured by EBSD are in the low limit of the predicted zone, while the mean dislocation density measured by TEM is slightly below the scattering zone (probably due to the selection of regions of interest for the analysis).

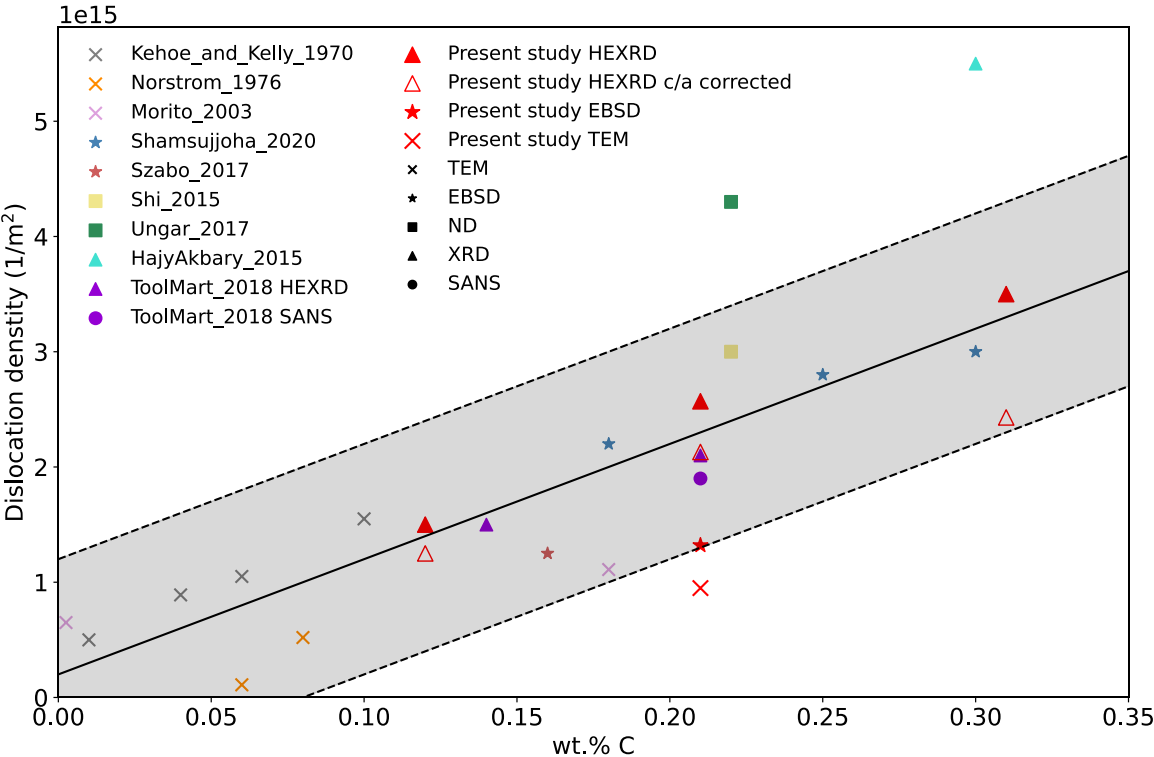


Figure 32: Comparison between mean dislocation densities obtained from the literature and the ones obtained in the present study (red symbols). Symbols correspond to the characterization technics.

Relations between lath structure & GNDs

Even if in the present Chapter, the discussion about the microtexture components and the dislocation density analysis are separated, there exists a strong connection between both. In fact, the low angle boundaries defining the laths are in fact made of GNDs.

A first estimation of the GNDs density stored in the lath boundaries can be calculated from the lath width and the misorientation between laths. The misorientation produced by a barrier of dislocations can be calculated as [144]:

$$\sin\left(\frac{\theta_{\text{misorientation}}}{2}\right) = \frac{b}{2h} \quad \text{Equation 15}$$

where $\theta_{\text{misorientation}}$ is the misorientation between the two sides of the dislocation wall, b is the Burgers vector and h is the distance between the dislocations. The density of GNDs can be, then, calculated by knowing the fraction of surfaces in a volume which in a simplified model can be calculated as one over the distance between the walls, i.e. laths width. The density of GNDs can be then calculated as:

$$\rho_{\text{GND}} = \frac{1}{d \times b} \times 2 \sin\left(\frac{\theta_{\text{misorientation}}}{2}\right) \quad \text{Equation 16}$$

where d is the lath width.

Therefore, the GNDs density required for producing a 4° misorientation between lath with a mean lath width of 250 nm (close to the mean of the TEM determined spatial distribution) is equal to $1.2 \times 10^{15} \text{ 1/m}^2$. The present value is in good agreement with the one measured by EBSD, confirming the consistencies of our coupled analysis at different scales.

II.3.A.2 Spatial distribution of dislocations

In this section, we will try to estimate the spatial distribution of dislocations on the basis of metallurgical assumptions and using the in situ measurements discussed in the preceding section.

The starting point for this reasoning is the martensitic microstructure is the result of a continuous transformation. The sequential nature of the martensitic transformation induces a dispersion of microstructural features as domain sizes, carbon segregation/precipitation states, residual stresses, and also dislocation densities [45]. As a consequence, the measured dislocation density discussed above is an average over the analyzed volume.

The observed evolution of the dislocation densities along with the martensite transformation can be explained either by an average increase of a uniform dislocation density or by the progressive formation of martensite with higher dislocation densities, while the previously formed martensite keeps its dislocation density constant. Intermediate scenario can also be considered.

The first hypothesis seems unlikely due to two reasons. The first one is that plastic accommodation due to the martensitic transformation should occur mainly in the austenite, i.e. the softest phase. This can be corroborated by the drastic increase in the austenite dislocation density. The second one is that after the percolation of the martensite structure (20-30% of transformation) a higher degree of plastic interactions is expected [145,146], but the results showed a decrease in the creation rate of dislocations.

In the present work, the second hypothesis will be assumed in the case of the martensite transformation. It is supported by different experimental observations, in particular by the work of Morsdorf et al. [20]. The progressive increase in the mean dislocation density is a direct consequence of the nucleation of new laths with higher local dislocation density. With the present assumption, the local dislocation density (in the following denominated ρ_{local}) in each new formed martensite increment can be calculated.

For a given formed martensite fraction (F), the mean dislocation density ($\bar{\rho}$) (the measured value) is equal to the average of the local dislocation densities that appeared in all previously formed martensite laths. This local dislocation density will be called ρ_{local} in the following. In other words, each formed martensite fraction (f) has a local dislocation density (ρ_{local}) giving at a given total formed martensite fraction (F) an average dislocation density ($\bar{\rho}$) that is the value measured. As a consequence, the mean density can be calculated by the Equation 17:

$$\bar{\rho}(F) = \frac{1}{F} \int_0^F \rho_{local}(f) df \quad \text{Equation 17}$$

The derivative form of the Equation 17 allows to calculate the local dislocation density at a given transformed fraction:

$$\rho_{local}(F) = \frac{d\bar{\rho}(F)F}{df} \quad \text{Equation 18}$$

As shown by Equation 17 and Equation 18, the only input required to calculate ρ_{local} is the mean dislocation density as function of the martensite fraction.

Such calculations on the raw experimental values lead to unexploitable results as the curves can be jerky (cf. Figure 30). Hence, in order to be able to plot the result the results of Equation 18, the mean density was first modeled empirically ($\bar{\rho}$ as function of F)

The proposed equation is a parametrized square root formula:

$$\bar{\rho}(F) = A_{dislo} + B_{dislo}\sqrt{F} \quad \text{Equation 19}$$

where A_{dislo} and B_{dislo} are constants to be calibrated on the experimental data (Figure 30) for each studied condition (steel, cooling rate).

Even if the proposed equation as no direct physical ground except that describing the experimental data, a first interpretation of the parameters A_{dislo} and B_{dislo} can be proposed. The parameter A_{dislo} can be related to the minimum dislocation density required to partially relax the internal stresses caused by the volume change during the martensitic transformation. The parameter B_{dislo} can be related to the slope of the evolution of the dislocation density with the martensite formed fraction, it might be affected by the carbon content (affecting the volume change [27]) and others factors as a possible recovery during the quench (these effect may be ruled out at high cooling rates).

The experimental mean dislocation density as function of the martensite fraction for the three studied compositions were modeled with Equation 19 in order to obtain the required parameters (only the lowest cooling rate data were analyzed as they are the best time resolved ones). The found values for parameter A_{dislo} are 6.3×10^{14} , 6.0×10^{14} and 9.0×10^{14} $1/m^2$ for 0.1C, 0.2C and 0.3C steel respectively and the values for parameter B_{dislo} are 6.32×10^{14} , 1.28×10^{15} and 1.50×10^{15} $1/m^2$ respectively. The experimental points as well as the calibrated curves are shown in Figure 33.a.

The empirical modeled curves for the 0.1C and the 0.2C steels presents a good agreement with the measured values while for the 0.3C steel the description of the evolution of the measured values is poorer particularly when the martensite fraction is lower than 20 wt.%. In this first fraction the experimental incertitude is higher as the diffraction peaks are poorly defined.

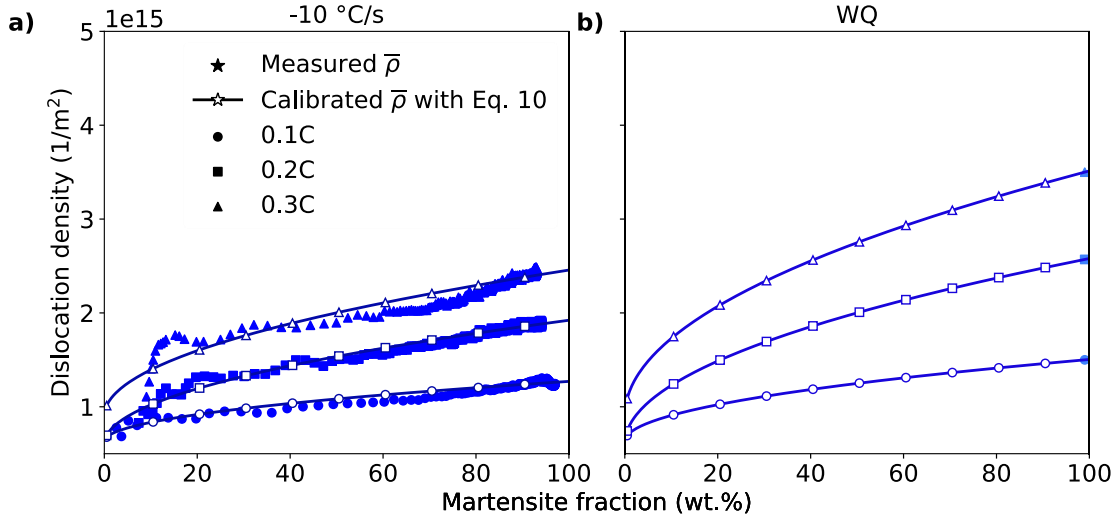


Figure 33: Evolution of the experimental dislocation density with the transformed fraction as well as the curves obtained by calibrating Equation 19 for the three studied steels at the lowest cooling rate (-10 °C/s) in a) and by water quench b).

For the water quenched conditions, the only available data is the mean dislocation density at room temperature. It has been assumed that they have the same origin (A_{dislo}) as for the -10 °C/s cooling rate conditions but the slope (B_{dislo}) is calculated in order to provide the experimental value. The mean dislocation density curves and the local dislocation density ones for the water quenched conditions are shown in Figure 33.a. The B_{dislo} values are in this case 8.7×10^{14} , 1.98×10^{15} and 2.61×10^{15} $1/m^2$ for the 0.1C, 0.2C and 0.3C steel respectively.

The derivative form of the previous Equation allows to calculate the local dislocation density at a given transformed fraction:

$$\rho_{local}(F) = A_{dislo} + \frac{3}{2}B_{dislo}\sqrt{F} \quad \text{Equation 20}$$

The lower local dislocation densities are equal to 7×10^{14} $1/m^2$, equal to 7.5×10^{14} $1/m^2$ and equal to 1.05×10^{15} $1/m^2$ for the 0.1C, 0.2C and 0.3C steels respectively. The maximal local dislocation densities at the end of the -10 °C/s quench are 1.58×10^{15} , 2.58×10^{15} and 3.23×10^{15} $1/m^2$ respectively. The result of the local dislocation density as function of the transformed fraction are shown in Figure 34.

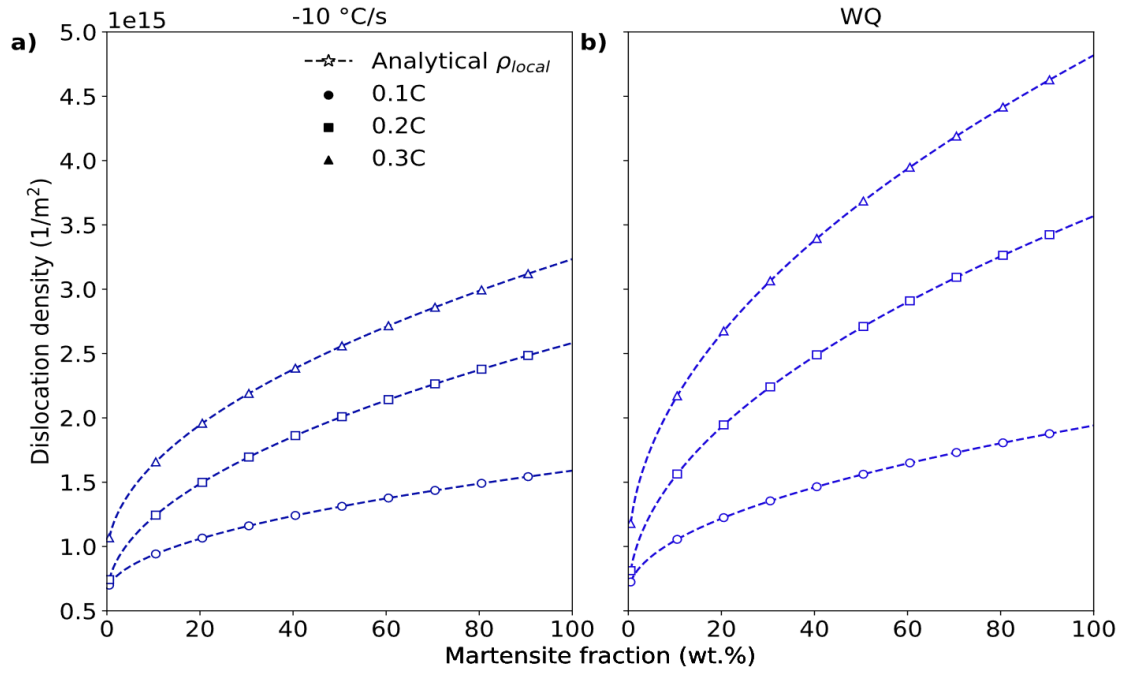


Figure 34: Evolution of the calibrated local dislocation densities with the transformed fraction for the three studied steels at the lowest cooling rate (-10 °C/s) in a) and by water quench b).

As the mean dislocation density at the end of the transformation is higher for the water quench conditions, the local values for the water quench conditions are higher than the ones for the lower cooling rate. For example, the local dislocation density for the 0.2C steel for a totally transformed martensite at -10 °C/s cooling rate is $2.58 \times 10^{15} \text{ 1/m}^2$ while that for the water quench condition it is $3.57 \times 10^{15} \text{ 1/m}^2$.

Once calculated the local density of dislocations of each martensite increment, the volumetric (spatial) density of probability to find a position where the density of dislocation is comprised between ρ_{local} and $\rho_{local} + d\rho_{local}$ can be calculated. The corresponding distributions of the local dislocation densities are presented in Figure 35 for the three carbon contents and for the two quenching conditions. The ρ_{local} was calculated each 0.5 wt.% with Equation 20 and the previously presented A_{dislo} and B_{dislo} . Then, the obtained ρ_{local} were binned each $1 \times 10^{14} \text{ 1/m}^2$. Finally, the integral of the obtained histogram was normalized to 1 to obtain a probability density function.

Figure 35.a presents the mentioned distributions for the -10 °C/s cooling rate while the distributions of local dislocation density for the water quench conditions are shown in Figure 35.b. The distributions widen with the carbon content and that for a given steel the distribution is wider for the water quench condition, i.e. for the highest studied cooling rate. The widening with the carbon content revealed in the present study contradicts ones of the hypothesis proposed by Badinier [74].

In conclusion, a new method to estimate the local dislocation density and its distribution has been proposed. This method is based on a metallurgical hypothesis considering the main characteristics of the martensitic transformation. The distribution of the local dislocation densities widens with the carbon content of the steel as well as with the cooling rate. The distributions would produce a distribution of local yield strength; consequence that will be discussed in Chapter IV.

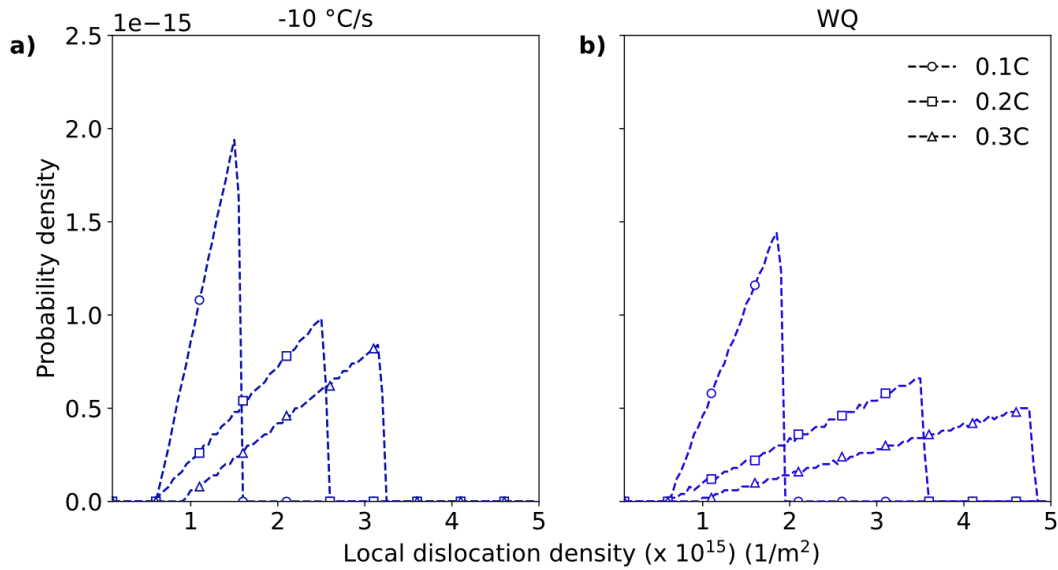


Figure 35: The probability density distributions of the local dislocation density for the three steels used in the present study after quenching at -10 °C/s (under the M_s temperature) in a) and by water quenching in b).

II.3.B Evolution during tempering

The following section aims at studying the recovery of three studied water quenched martensitic steels. The associated decrease in the dislocation densities will affect in fact the carbide precipitation but also their related hardening effect. We will show in particular how the spatial distribution of dislocation density is presumably affected.

The studied tempering heat treatments consist of a linear heating at 10 °C/s followed by an isothermal holding (200, 300 and 400 °C) of 600s (10 minutes) and a fast cooling. Such model heat treatments are often encountered in the literature and could serve as a basis to calibrate a recovery model.

II.3.B.1 Mean dislocation density

II.3.B.1.a Results

The evolution of the mean dislocation density was followed during the tempering heat treatments and the results are presented in Figure 36 using the same methodology as in the previous section, i.e. by conducting in situ HEXRD experiments.

The results are shown in Figure 36.a, in Figure 36.c, and in Figure 36.e for the 0.1C, 0.2C and 0.3C steels respectively. Figure 36.b, Figure 36.d and Figure 36.f, presents the results for the three steels at the different holding temperatures, 200, 300, and 400 °C respectively. The reference time ($t=0s$) is set at the start of the isothermal holding by convention to be able to compare more easily the behaviors.

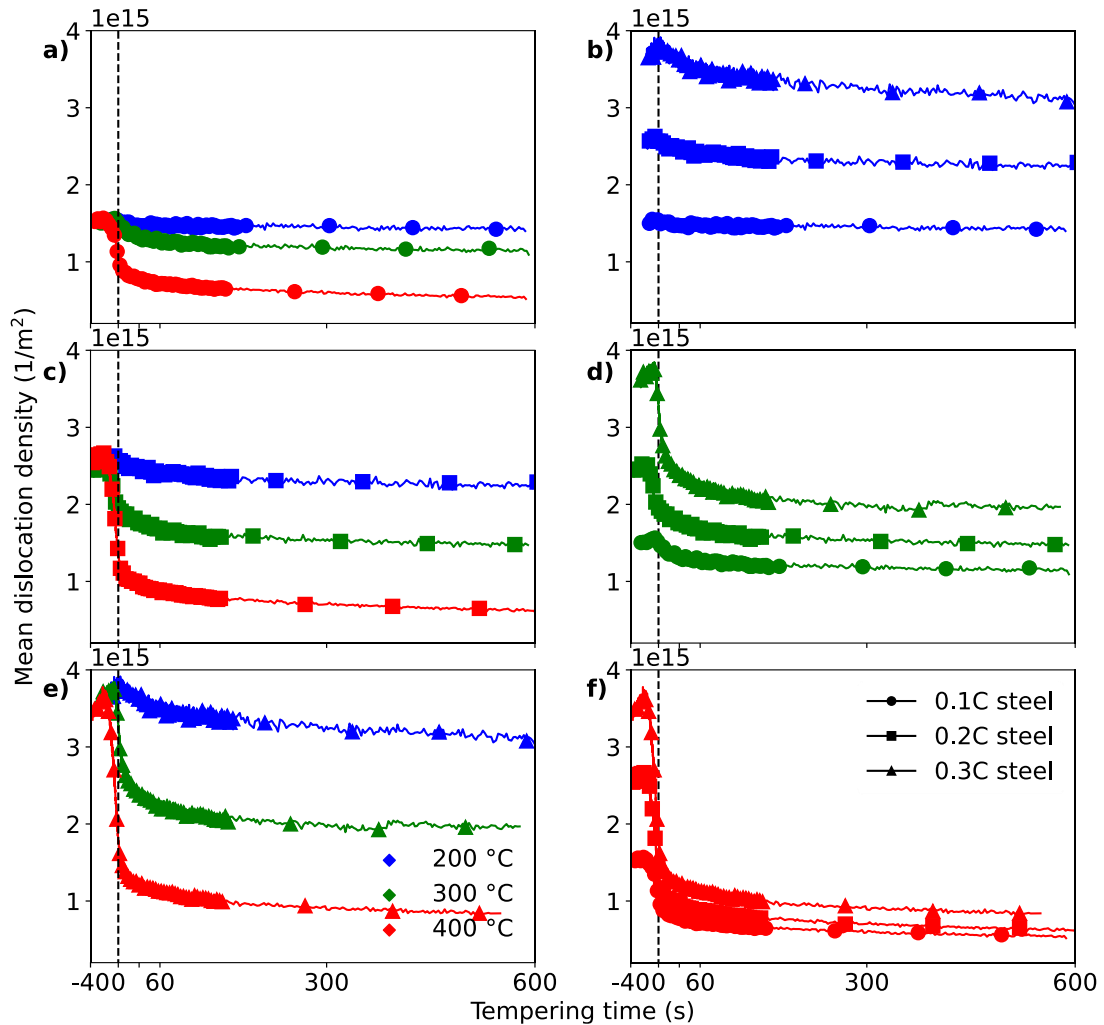


Figure 36: Evolution of the martensitic mean dislocation density during tempering as function of the holding time. a), c) and e) effect of the holding temperature for the 0.1C, 0.2C and 0.3C steels respectively and b), d) and f) effect of C content at the three studied holding temperature.

All the curves present the same trends. Most of the recovery occurs at the end of the heating stage and during the first 30s of the holding, followed by a much slower recovery kinetics. The fast recovery is followed by a saturation has been previously reported [129]. In the mentioned work, the two stages recovery is explained by a fast annihilation of ‘free’ dislocations followed by slower reorganization of entangled dislocations forming cell boundaries.

The low recovery of the three studied steels at 200 °C, almost negligible and the intensification of this phenomenon at 300 °C and 400 °C are in agreement with the work of Shi et al. [61] in which only the values at the end of the tempering treatments were presented.

The recovery of the mean dislocation density of the three studied steels at 200 °C, shown in Figure 36.b, shows that the dislocation density at the saturation (in the following denominated saturation dislocation density, ρ_{sat}) depends not only of the temperature but also of the initial dislocation density and consequently of the carbon content. The higher the initial dislocation density the higher the “equilibrium” dislocation density. A similar tendency is observed at 400 °C (Figure 36.f). However, the difference between the three dislocation densities at saturation decreases with the temperature.

II.3.B.1.b Discussions

Possible effect of the tetragonality

During tempering, the mean dislocation density obviously decreases but carbon atoms trapped will also segregate and precipitate (this subject is discussed in detailed in the following Chapter). As a consequence, the tetragonality associated with the carbon in the matrix is supposed to decrease as well. It can be thus questioned if the observed decrease of the FWHM attributed to the decrease in dislocation density could be or not related to the evolution of the tetragonality.

In Figure 37.a the evolution of tetragonality of the three tempering conditions of the 0.3C_WQ steel is presented. Figure 37.b presents the evolution of the mean dislocation density determined without (1Peak-1Function), full markers, and with (1Peak-MultipleFunction) tetragonality correction, empty markers.

The first feature to be mentioned is that the recovery of the non-corrected mean dislocation density presents the same kinetics as the evolution of the tetragonality ratio. This tendency is present for the three holding temperatures. The coincident kinetics can be rationalized as both precipitation and recovery are thermally activated phenomena whose kinetics are related to the self-diffusion of iron [39,127].

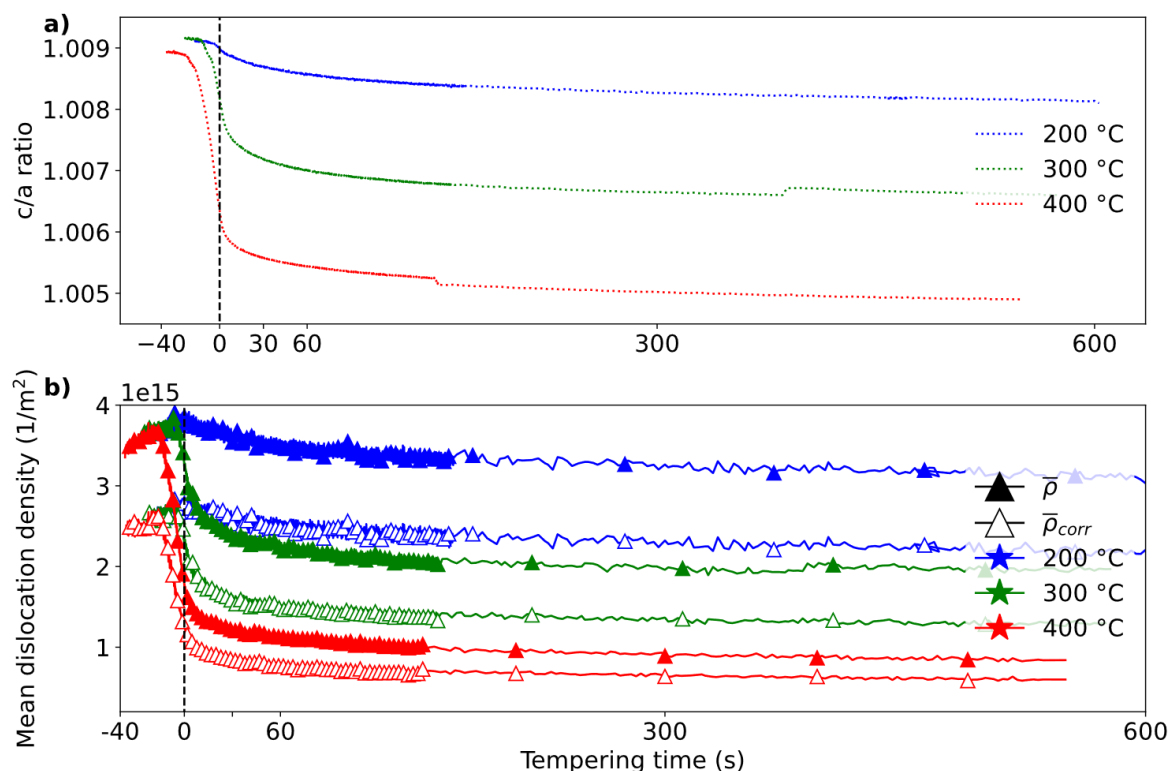


Figure 37: a) Evolution of the tetragonality ratio (c/a ratio), for the three tempering heat treatments of the 0.3C_WQ steel. b) Evolution of the mean dislocation density determined without (1Peak-1Function method) and with (1Peak-MultipleFunction method) for the three holding temperatures .

Regarding the difference between dislocation densities determined by the two methods, at 200 °C the difference falls into the resolution of the method. At 300 °C, even if the recovery kinetics seem similar for both determination methods the initial difference between the two methods, is lower at the end of the tempering ($1.0 \times 10^{15} \text{ 1/m}^2$ versus $6.7 \times 10^{14} \text{ 1/m}^2$). Finally, at 400 °C the gap between the both methods is clearly reduced (from $1.0 \times 10^{15} \text{ 1/m}^2$ to $2.4 \times 10^{14} \text{ 1/m}^2$). It can be concluded that when the tetragonality correction is not used a slightly higher recovery is determined (lower saturation value) but the kinetics are rather similar.

The gap between the two methods is however lower than uncertainty due to the choice of the parameter M as mentioned above. In the following only the 1Peak-1Function method was used even if it has been proved that the tetragonality evolves during tempering and could affect the measurements.

Recovery modelling

The recovery for the nine presented conditions has been modeled with Equation 9 (empirical model derived from the work of Kozeschnik [127]). C_{rec} was set to 6×10^{-4} as in [127] for all the conditions. The diffusion as a function of the temperature was calculated as in [147] while the shear modulus was calculated using the work of Ghosh and Olson [148]. The Burgers vector is set constant equal to $2.5 \times 10^{-10} \text{ m}$. Only ρ_{sat} has been calibrated for each curve individually to reproduce the last value.

Figure 38 presents the experimental recovery values as well as the ones obtained using the recovery model. The same subgraph structure that the one used in Figure 36 is applied.

For the recovery at 200 °C, the calculated kinetics for the three steels are slower than the experimental values. On the other hand, the recovery at 400 °C presents a fast decrease of the dislocation density in good agreement with the experimental values. The model presents also a good agreement with the experimental values for the tempering at 300 °C. The discrepancies between the model and the experiments may be partially due to the use of a fixed C_{rec} . A better adjustment could have been obtained by considering C_{rec} as a free parameter but at the cost of a loss in physical meaning.

The adjusted saturation dislocation densities used for the calculations presented in Figure 38 are summarized in Table 7. The saturation values are in the order of the GNDs (cf. previous discussion), meaning that the recovery probably affect more the SSDs than the GNDs defining the lath (stable with the temperature).

In order to be able to develop a fully predictive equation of the recovery, a linear extrapolation of the dislocation density at saturation is proposed as function of the initial dislocation density and of the tempering holding temperature. Therefore, the dislocation density at saturation can be estimated as:

$$\rho_{sat} = 5.5 \times 10^{14} + (-3.064 \times 10^{-3} T + 1.2963) \times \rho_0 \quad \text{Equation 21}$$

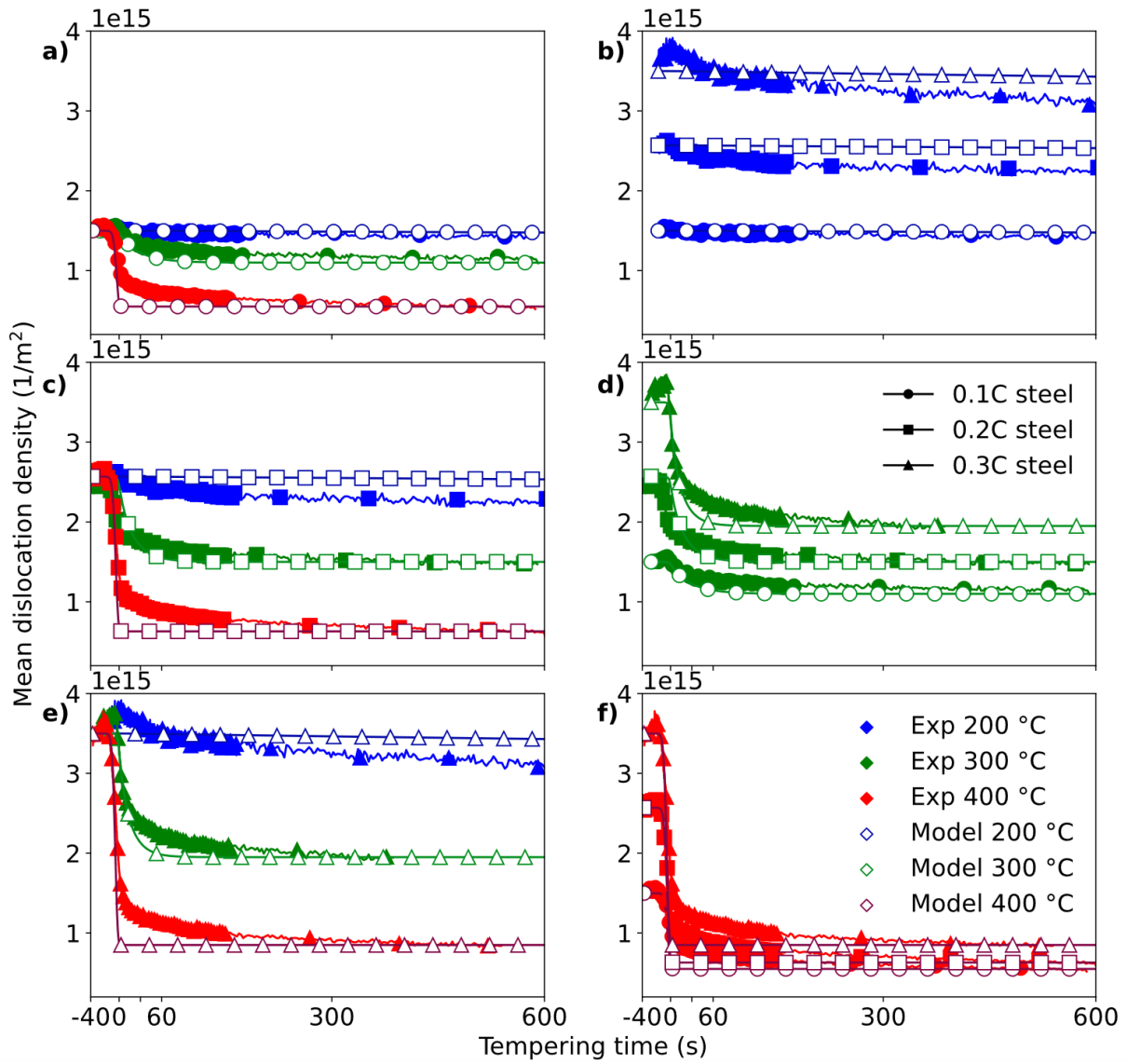


Figure 38: Evolution of the experimental and simulated mean dislocation densities during tempering as function of the holding time. a), c) and e) effect of the holding temperature for the 0.1C, 0.2C and 0.3C steels respectively and b), d) and f) effect of carbon content at the three studied holding temperature.

Table 7: Saturation dislocation densities for the nine studied tempering conditions (200, 300 and 400 °C holding temperatures for the 0.1C_WQ, 0.2C_WQ and 0.3C_WQ steels).

Steel name	$\rho_{\text{sat}} \text{ (x } 10^{15} \text{ 1/m}^2\text{)}$			
	ρ_0 (x 10^{15} 1/m^2)	200 °C	300 °C	400 °C
0.1C steel	1.50	1.20	1.10	0.55
0.2C steel	2.50	2.30	1.50	0.63
0.3C steel	3.50	3.10	1.95	0.85

Equation 60 can be rewritten taking into consideration the relation between the nominal carbon content and the initial dislocation density as:

$$\rho_{sat} = 5.5 \times 10^{14} + (-3.064 \times 10^{-3} T + 1.2963) \times (2 \times 10^{14} + 1 \times 10^{16} \text{ wt. \%C}) \quad \text{Equation 22}$$

Equation 22 will be useful to design the coupled recovery/segregation/precipitation model presented in Chapter III.

The recovery of the mean dislocation density has been determined by in situ HEXRD experiments for the nine tempering conditions. Two stages were observed; a fast one followed a stagnant stage. The obtained results were modeled with an empirical model obtaining the required parameter (ρ_{sat}). By obtaining the parameters as function of the temperature, the empirical recovery model now is suitable to describe non-isothermal heat treatments including the heating section. The calibrated model will be used to calculate the recovery as function of the local dislocation density and the temperature in the following chapters.

II.3.B.2 Local dislocation density distribution

The recovery of the dislocation densities discussed in the previous section correspond in fact to a mean evolution which encompasses a spatial distribution of local dislocation densities.

The method developed in this work grant access to the distribution of the local dislocation density at the initial state, i.e. as-quenched martensite. It is also possible to estimate the individual recovery kinetics in each martensite domains (with their own local dislocation density). To do so, we have to couple our estimation of the spatial distribution of dislocations (cf. Figure 35) and our model presented just above. The recovery model is applied with C_{rec} , set to 6×10^{-4} , and ρ_{sat} calculated by applying Equation 60, i.e. with $\rho_0 = \rho_{local}$ instead of assuming $\rho_0 = \bar{\rho}$.

This approach is of course an extrapolation assuming that the model is correct also at a local scale.

The evolution of local dislocation densities due to recovery is shown in Figure 39 for the 0.3C steel. Figure 39.a, Figure 39.c and Figure 39.e show the evolution of the experimentally determined mean dislocation density and the recovery model results as in Figure 38 with the evolution of the local dislocation density (each line represents 2 wt.% of martensite). At each step, the average of all local dislocation densities is calculated and is shown as an ‘average ρ_{local} ’.

As expected, the fraction of martensite containing higher densities of dislocations recovers faster than the one with densities lower than the average. Nevertheless, the average of the recovered local dislocation densities is almost juxtaposed with the results of the mean recovered dislocation density. This point validates in some extent the methodology.

As soon as the local densities of each martensite increment can be tracked individually, the spatial distribution of the local dislocation densities can be calculated all along the tempering treatment. The spatial distribution of the local dislocation densities at the water quenched state (already presented in

Figure 35) and at different holding times (0, 30, 30 and 300s) for the three studied tempering temperatures are presented in Figure 39.b, Figure 39.d and Figure 39.f. These figures shows that the tempering obviously leads to a global decrease in the mean density as already discussed but also reduces the width of the distribution. For the 200 °C tempering (Figure 39.b), the only observable change is at 300s. In the case of the 300 °C tempering, the process seems finished after 60s. Finally, even at 0s of holding in the tempering heat treatment at 400 °C the distribution of local dislocation densities is already narrower than the one in the as-quenched condition.

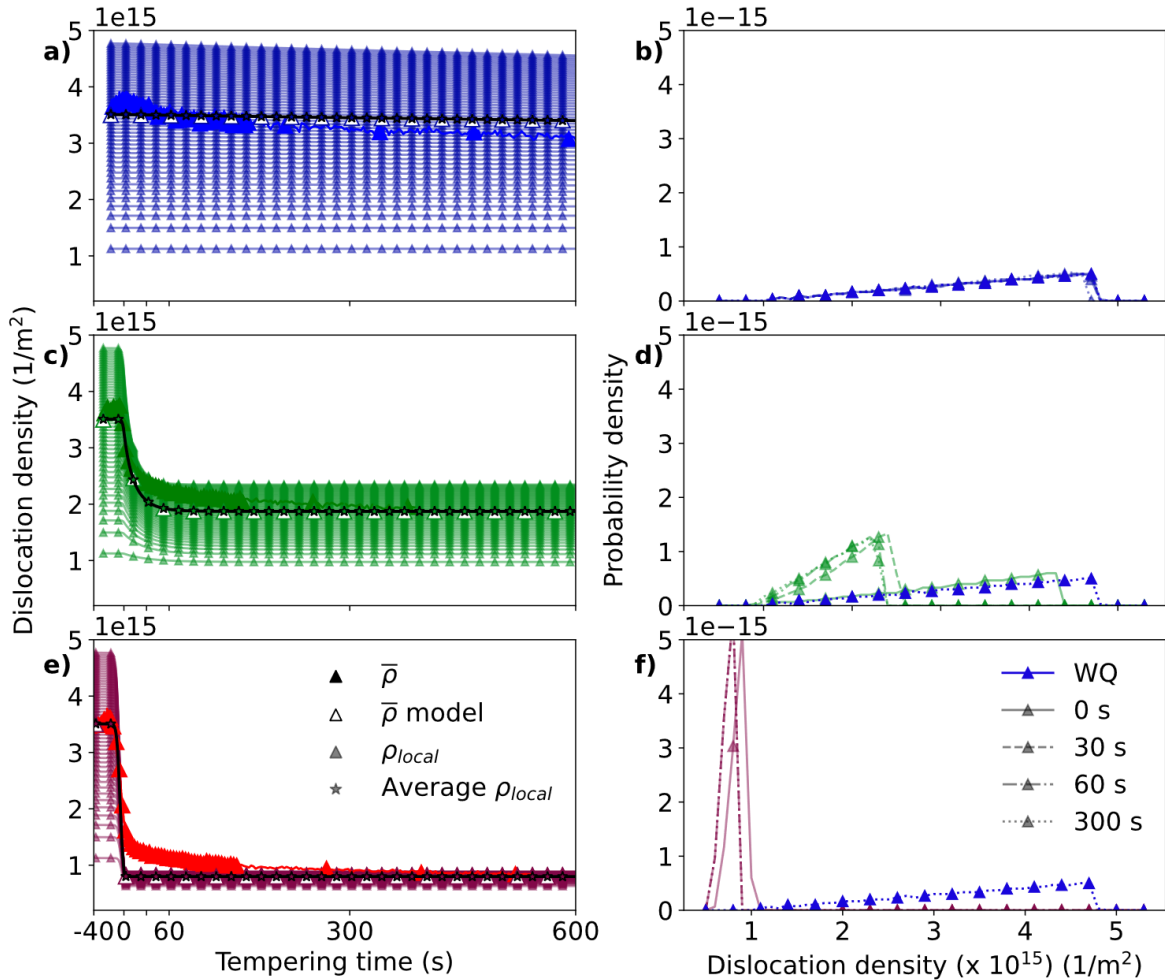


Figure 39: Evolution of the mean dislocation density (bold symbol), the modeled dislocation density (bold empty symbol), the modeled local dislocation densities (small symbol) and the average value of the modeled local dislocation densities (star) for the 0.3C alloy during tempering at 200 °C in a), at 300 °C in c) and at 400 °C in e). The corresponding distributions of local dislocation densities at the water quench state and during the tempering after 0s, 30s, 60 and 300s are presented in b), d) and f) for the treatments at 200, 300 and 400 °C respectively.

The methodology presented in the present work allow to estimate by reasonable extrapolation the evolution of the spatial distribution of dislocation densities during the tempering heat treatments. A clear narrowing of the distributions is observed for the 300 °C and the 400 °C tempering treatments while this phenomenon is less pronounced for the 200 °C tempering. As a consequence, a decrease in the distribution of local yield strength at the microstructure scale is expected when tempering a martensitic steel.

II.4 Conclusions of the chapter

This Chapter has shown that important metallurgical characteristics (density of dislocations, sizes of microtexture components) for the mechanical behavior of martensitic steels may exhibit large dispersion on a given microstructure. The width of these distributions depends on the carbon content of the steels but also on the manufacturing conditions (hardening or tempering speed).

- 1) The application of the line intercept method on EBSD maps allows to determine the mean domain size as a function of a threshold angle for the three studied steels. After stereological corrections, the spatial distribution of the block sizes has been also obtained. Higher carbon content produces a decrease in the mean size and narrows the associated distribution.
- 2) The mWH method (for the 0.1C, 0.2C and 0.3C steels) as well as TEM and EBSD (for the 0.2C steel) were used to characterize water-quenched samples at room temperature. The measured densities of dislocations are in good agreement with the literature. A new method was developed to deconvolute the tetragonality effect on the FWHM. The obtained 'corrected' values are in the dispersion reported in the literature.
- 3) A new method is proposed to calculate the spatial distribution of the local dislocation density based on the evolution of the mean dislocation density with the transformed fraction. The calculated distributions of local dislocation densities widen with the C content.
- 4) The evolution of the mean dislocation density due to recovery during tempering was also tracked by in situ experiments for the three studied alloys and using low holding temperatures (200, 300 and 400 °C). The kinetics fastens with the temperature. The heat treatments at 300 and 400 °C present a stagnation of the recovery. The recovery was modeled using an empirical law, and the stagnation dislocation density was parametrized allowing to calculate the recovery as function of the holding temperature and the initial dislocation density (or carbon content).
- 5) The recovery of local dislocation densities was calculated with the parametrized recovery model. The distribution of local dislocation densities was found to vary with the tempering narrowing in more severe tempering conditions.

Chapter III

Segregation and carbide precipitation

III.1 Focused state of the art.....	- 71 -
III.1.A Tempering sequence	- 71 -
III.1.B Tempering models	- 77 -
III.2 Experimental results	- 79 -
III.2.A Carbon segregation.....	- 80 -
III.2.B Precipitation sequence.....	- 85 -
III.2.C Summary of the microstructural characterization of tempering	- 101 -
III.3 Modeling of tempering.....	- 102 -
III.3.A Carbon segregation model.....	- 103 -
III.3.B Precipitation model	- 111 -
III.3.C Conclusions of the segregation and precipitation models.....	- 128 -
III.4 Conclusions of the chapter.....	- 130 -

This Chapter is part of an understanding of the formation and tempering mechanisms of martensitic microstructures, in order to be able to better predict their mechanical behavior. In this Chapter, particular attention will be paid to the state of carbon during tempering (including a possible autotempering), keeping in mind that this process also affects dislocation densities as seen in Chapter 2 and internal stresses, as we shall see in Chapter IV.

As shown in the General Introduction, the precipitation of carbides during the tempering of martensitic steels has been extensively studied in the literature. The nature of the carbides formed, their size, shape and their sequence of formation could be established, as well as the evolutions of the matrix phases (decomposition of austenite, recovery of dislocations, distribution of carbon). However, most previous studies considered relatively high carbon steels, usually above 0.4 wt.% C, and usually high temperatures of tempering, above 400 °C. This facilitates the characterization of carbides, because of the higher fraction. The lower M_s temperature also reduces the autotempering, which simplifies the study of first stages of the precipitation sequence. Considering high tempering temperature also enhances the growth and coarsening phenomena, thereby increasing the radius of carbides, facilitating their characterization by TEM and their detection by XRD. As a consequence, few studies in the literature combined experiments and modelling on low-carbon steels [149,150].

As the present study focuses on three industrial steels with carbon content lower than 0.3wt.%C, the literature provides a limited basis to interpret the microstructural evolutions which take place upon tempering of these steels. Some questions regarding low-carbon steels have not been fully answered yet. The segregation of carbon into defects has a critical importance in these steels, as a large part of the carbon is consumed by this process. Even if some segregation models have been developed in the literature, the consequences of carbon segregation on the precipitation sequence upon tempering have almost not been addressed, apart in a study by Shan et al. [127]. However, in this latter study, the only carbide phase considered was cementite, whereas we want to consider also the transition carbides. Indeed, it has been reported [38,103] that the segregation of carbon may enter in competition with the formation of these carbides. In this Chapter, we will combine experiments and modeling to study the competition between the carbon segregation and the formation of transition carbides, and its consequences on subsequent formation of cementite, by combining experiments and simulations.

The experimental part of this work will raise some difficulties.

The characterization of tempering in low-carbon steels is limited by the low fraction of the carbides, but also by the number of scales at which the different phenomena occur. This implies the use of different characterization techniques, which have specific limitations. The carbon segregation into microstructure defects occurs at a nanometric scale, while the sizes of the carbides range between 1 and 100 nm. A much higher volume has to be sampled to measure the fraction of the carbides. In this work, we will combine three different techniques, 3D atom probe tomography (3DAPT), TEM and in situ HEXRD, to characterize the microstructural evolutions upon tempering. 3DAPT has a spatial resolution at the nanometric scale and it allows chemical identification to study the segregation of carbon [50,71,151], but the volume sampled is small (dimensions ca. $200 \times 60 \times 60 \text{ nm}^3$) and it is usually not statistically representative. To overcome this drawback, several samples will be studied for each condition. Although TEM allows to study the microstructure at an upper scale and, therefore, to characterize the size and nature of the carbides [149,152], it remains too local to determine the fraction of the carbides. HEXRD

experiments performed in synchrotron beamlines will allow to sample a volume of about 1 mm³ and to track in situ the mass fraction of the carbides and of the matrix phases (ferrite/martensite, austenite), as well as the chemical composition of the latter.

In order to address specifically the segregation and precipitation phenomena and to understand their interaction, two characterization steps will be conducted. The segregation after quenching and aging at room temperature will be investigated by 3DAPT, by considering two cooling rates (gas quench, water quench). The precipitation of transition and cementite carbides will be studied by TEM and HEXRD, in water quenched samples, considering tempering treatments which include a heating at 10 °C/s followed by isothermal holding. The effects of the tempering temperature (200, 300 or 400 °C) as well as of the carbon content of the alloy (0.1, 0.2 or 0.3 wt.% C) will be investigated. It will be seen that the characterization techniques employed will not be sufficient to provide a comprehensive overview on the phenomena. This is why a modeling approach will be developed in order to go further in our analysis.

A model for carbon segregation from the literature [153] will be coupled to a precipitation model previously developed in the laboratory, which predicts the kinetics of nucleation, growth and coarsening of epsilon and cementite carbides successively [39,154]. The main purpose of this modeling study will be to investigate by the simulation the consequences of the carbon segregation (heterogenous carbon concentration in the matrix) on the precipitation sequence. After calibration of model parameters on the basis of the experiments and assessment of its predictions, the model will also serve to estimate the influence of important parameters for our study: the dislocation density, which shows a high dispersion inside the investigated martensitic microstructures, but also the heating rate. Besides, this model will be necessary for our modeling study on the tensile behavior of these steels (Chapter IV), which will consider a large range of tempering conditions (time, temperature), that we could not examine all experimentally.

The present chapter is composed of three sections. A focused state of the art on the tempering, followed by the experiments, and then the modeling.

III.1 Focused state of the art

The tempering of martensite has been an active subject in the metallurgical community which has produced several works related to it, with some complete reviews as [19,20]. The present state of the art will focus on following the carbon movement within and between phases during the tempering of low carbon martensitic steels at low temperature (not exceeding 500 °C).

The different steps of the tempering sequence are detailed in the first section of this bibliographic state-of-the-art, while the second one is dedicated to the modeling of the carbide precipitation as well as of the carbon segregation. The effect of the carbon segregation on the precipitation in low carbon steels will also be addressed in the first section.

III.1.A Tempering sequence

When obtained in low alloy low carbon steels, martensite is a metastable phase which tends to transform to more stable phases (ferrite and cementite) when heat is applied. With temperature and time carbon

atoms diffuse producing different structures and transition precipitates until the more stable carbide is formed.

The tempering process can be separated in at least four different stages which usually can partially overlap. From room temperature up to ca. 100 °C the ‘zeroth stage’, also known as aging, occurs with carbon segregation into microstructural defects or/and spinodal decomposition. During the first stage, carbon concentration in the martensite decreases due to the formation of transition carbides. During the second stage, the retained austenite decomposes into ferrite and cementite. Finally, cementite precipitates at the expense of transition carbides during the third stage.

It has to be mentioned that carbon redistribution and even carbide precipitation may occur during quenching if M_s is high enough [38]. This phenomenon known as auto tempering is enhanced by slow cooling rates. Appendix B is dedicated to the comparison between the uncontrolled gas-quenched martensite and the water quenched one, from both, experimental and modelling, points of view.

III.1.A.1 Zeroth stage of tempering (aging)

Substantial changes in as-quenched martensite held at room temperature and up to 100 °C have been reported regarding mechanical properties (cf. Chapter IV for examples) and microstructural evolutions. A concomitant increase in electrical resistivity and of hardness when martensite is aged from -60 °C up to 100 °C has been reported by Winchell and Cohen [155] in 1962. An increase in electrical resistivity occurs during aging at even lower temperature (-196 °C), as has been described by Olson and Cohen [147] in 1983. Two different phenomena have been postulated as the main explanations of these increases, the first is a decrease in the degree of order in the martensite solid solution and the second one is a very first initial stage of precipitation [155]. A third explanation is postulated and discredited, the growth or spreading of stacking faults.

During this stage, different phenomena might occur: spinodal decomposition, carbon segregation into microstructural defects as well as carbon clustering. Each of them will be discussed in the following.

Spinodal decomposition consists of the formation of a modulated superstructure with carbon rich regions, with a local composition of ca. 10 at.%, and the corresponding carbon depleted regions. A variety of characterization technics have been employed to determine the spinodal decomposition: TEM [156–158], XRD [159], Mössbauer spectroscopy [160], differential scanning calorimetry (DSC) [161], electrical resistimetry [147,155], and recently atom probe tomography (APT) [20,72].

The modulated superstructure has an initial wavelength in the order of 1 to 5 nm depending on the alloy carbon concentration [157]. Cluster formation is also commonly reported during this stage [72,162]. The formation of both structures have been reported to be controlled by carbon diffusion by DSC and Mössbauer spectroscopy [163,164].

The presence of C segregation into clusters and/or spinodal decomposition can be visually determined by TEM, as shown in Figure 40.a, and by the study of the diffraction patterns, as presented in Figure 40.b. 3DAPT reconstructions can also be used to visually assert the presence of clusters and/or spinodal decomposition, as observed in Figure 40.c. Linear profile analysis of carbon concentration on linear segments, as shown in Figure 40.d, can evidence the modulated structure. From an experimental point

of view, carbon segregation into defects (planar and linear) has been recently well characterized by different APT studies [87,151,162,165,166]. The local carbon concentration, in so called ‘Cottrell atmospheres’ is found to be between 7 and 10 at.%.

The formation of modulated microstructures has been mostly reported in low Ms steels (high carbon and high Ni concentration steels). On the other hand, for steels with high martensite start temperature, carbon segregation into defects may occur before the modulation and, therefore, carbon atoms are trapped and no modulated structure is obtained.

The carbon segregation into defects, its kinetics and some of their consequences such as the inhibition of transition carbide precipitation (discussed in more detail later in the present section) has been a subject of study for at least 70 years from the pioneer work of Cottrell and Bilby [167] regarding the segregation kinetics.

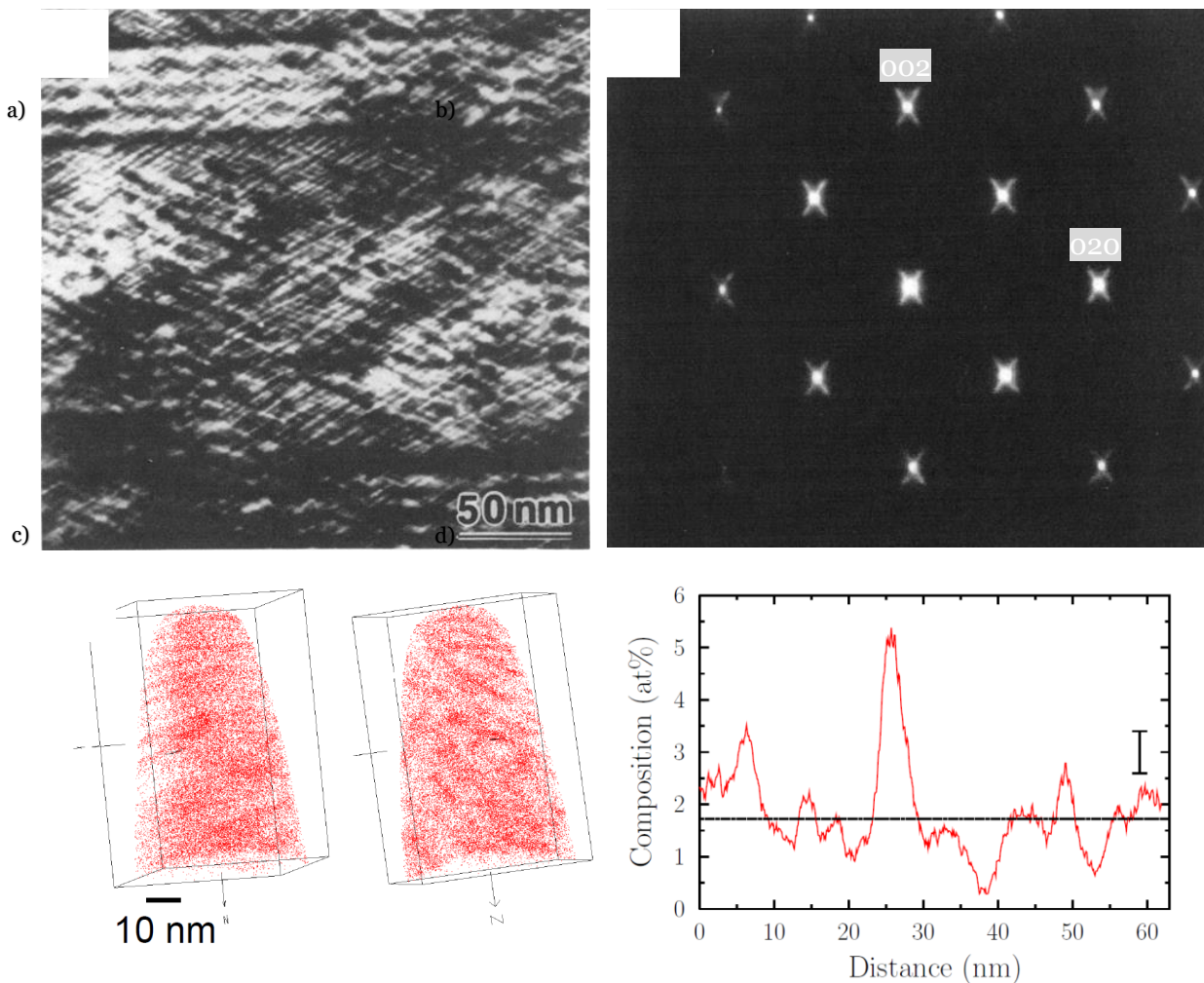


Figure 40: a) TEM dark field obtained on a Fe-15Ni-1C steel after room temperature aging for 5 hours, showing modulated structure. b) Diffraction pattern (axis [100]) obtained on Fe-15Ni-1C steel after room temperature aging for 26 min with spikes form the diffraction spots, revealing the modulated carbon concentration. c) Three-dimensional 3DAPT reconstruction of a 0.39 wt.% C steel after quench by helium presenting a segregated structure. d) Linear profile of the carbon composition along a selected region of c). a) and b) taken from [158]. c) and d) taken from [74].

Cottrell and Bilby [167] developed a model for the carbon segregation to a dislocation for short aging times described by:

$$f_{\text{seg}} = 3 \left(\frac{\pi}{2} \right)^{1/2} \rho \left(\frac{ADt}{k_B T} \right)^{2/3} \quad \text{Equation 23}$$

where f_{seg} is the fraction of steel's carbon content that is segregated, ρ is the dislocation density, D is the diffusion coefficient of carbon, t is the segregation time, T is the absolute temperature, k_B is the Boltzmann constant and A is a parameter related to the interaction between the dislocation and the carbon atoms. More recently, Zhao et al. developed a model based on the same physical principle but considering a saturation [168].

In a recent work, the segregation kinetics into linear and planar defects has been modeled using the thermodynamic extremal principle by Svoboda et al. [153]. In this study, the authors calculated the total Gibbs free energy of the system by taking into account the carbon segregation into defects, which decreases it. Then, a derivation with respect of time is proposed, to estimate the rate of decrease of the Gibbs energy by knowing the rate of carbon diffusion and its energy of attachment with the defects. The kinetics of the carbon segregation can then be deduced. This model also predicts the concentration of carbon at saturation of the defects atmospheres (differently than in the Cottrell and Bilby model).

As previously mentioned, the segregation of carbon on defects may suppress the formation of a spinodal structure but also the formation of transition carbides (first stage of tempering) [38]. This segregation can even prevent the formation of cementite (third stage of tempering) or induce its dissolution [105]. The possibility of inhibiting precipitation of transition carbides and/or of cementite has been analyzed in the pioneer work of Kalish and Roberts [103]. In the mentioned work, it is shown that a dislocation density of $2 \times 10^{16} \text{ 1/m}^2$ can inhibit the precipitation of transition carbides for a 0.2 wt.% C steel. The third stage of tempering is suppressed for steels with lower carbon content and dislocation density higher than $5 \times 10^{15} \text{ 1/m}^2$. These dislocation densities are higher than the ones usually reported for the carbon compositions of the steels used in the present study (cf. Chapter II).

Morsdorf et al. [162] showed that the formation of carbon segregations in the dislocations atmospheres occurs in the same precipitation stage as the formation of carbon clusters/transition carbides. A competition between cluster and Cottrell atmospheres forming can then be expected. The clusters may act as nucleation facilitator of the transition carbides.

Morsdorf et al. [162] interpreted as clusters the presence of local segregations with composition ca 9 at.%, but in other studies the same identified "clusters" were interpreted as transition carbides [150].

Even if in low carbon steels the presence of transition carbides can be suppressed by carbon trapped by segregation, it is commonly reported that for carbon contents higher than 0.2 wt.% the precipitation of transition carbides occurs [38,103,169]. The precipitation of those carbides is discussed in the following.

III.1.A.2 First stage of tempering

The precipitation of fine transition carbides (metastable) is the phenomenon that characterizes this tempering stage which usually occurs at temperatures between 100 °C and 200 °C. The nature and composition of the transition carbides is a subject of debate in the literature.

Jack observed the presence of epsilon (ϵ) carbide (hexagonal, $\text{Fe}_{2.4}\text{C}$) in high carbon martensitic steels [170]. This carbide presents a needle-shaped morphology with a high aspect ratio. Figure 41.a presents a TEM micrograph of a 0.8 wt.% C steel after a one hour holding at 200 °C in which epsilon carbides are observable [171]. The epsilon carbide is coherent with the matrix and its growth is in the minimum misfit direction $[01\bar{1}0]_{\epsilon} \parallel \langle 211 \rangle_{\alpha}$ [172]. Hirotsu and Nagakura [173] discovered another type of transition carbide named eta (η) with orthorhombic structure and with Fe_2C stoichiometry. This carbide was detected in high carbon steels as well as in steels with 0.3 and 0.5 wt.% C [174,175].

A third kind of transition carbide is the Hägg (χ) carbide (monoclinic, Fe_5C_2). This carbide may form as an intermediate step in the transition between ϵ/η and cementite (θ) [176,177].

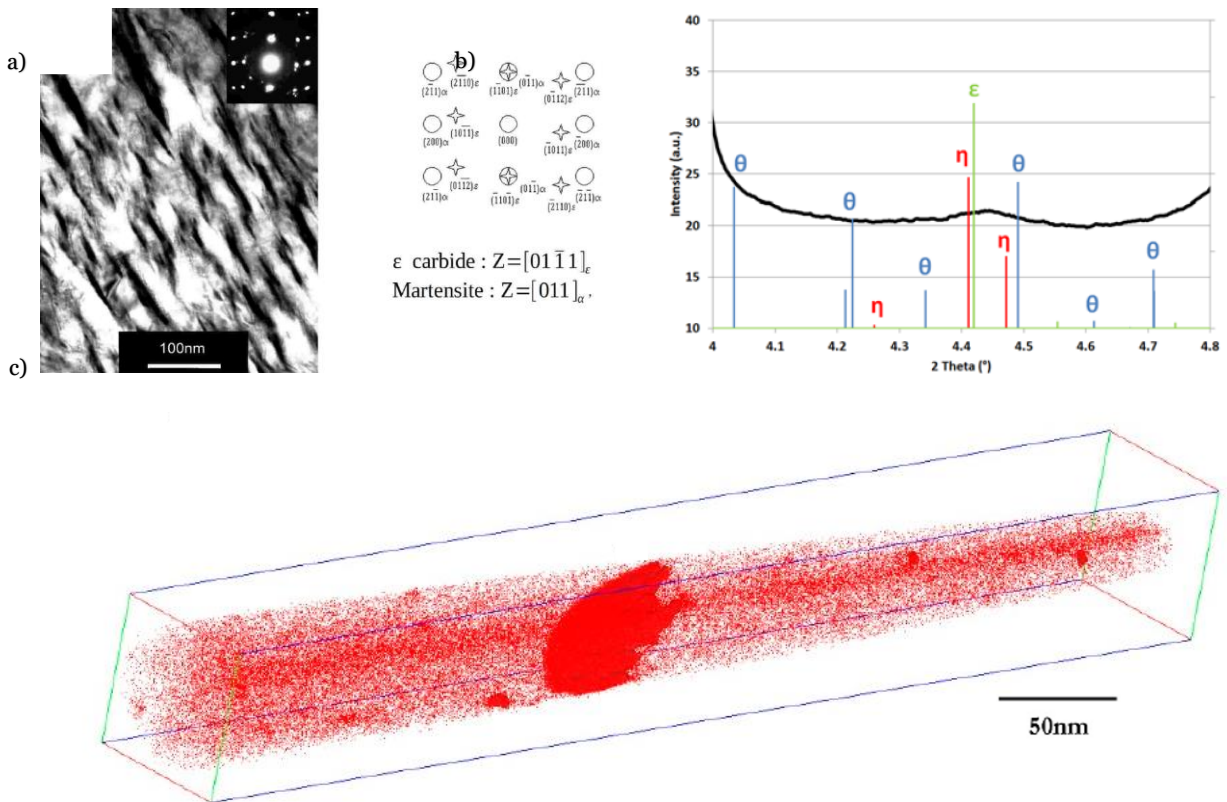


Figure 41: a) TEM micrograph and diffraction pattern of epsilon carbide in a 0.8 wt.% C steel after tempering 1 hour at 250 °C from [171]. b) HEXRD diffractogram showing the presence of a transition carbide and the expected position for the different possible carbides reproduced from [51]. c) 3D reconstruction of a 3DAPT tip showing the presence of a carbide, extracted from [178].

It has been proved difficult to clearly determine the crystallography, stoichiometry and as a consequence the nature of the transition carbides. The difference in crystallographic structure is small enough to be in the error of TEM and XRD characterization [51,179,180], as shown in Figure 41.b. The 3DAPT composition measurements cannot conclude on the stoichiometry of the carbide due to the error and low difference between Fe_2C and Fe_3C [178] (a reconstructed 3DAPT tip presenting a carbide is shown in Figure 41.c). Some 3DAPT measurements provided local carbon content lower than the expected ones for transition carbides. This is the case of Ning et al. who observed the presence of transition carbides in coarse lath after quenching by TEM and their characterization by 3DAPT results in a carbon content between 10 and 15 at.% [150]. The presence of transition carbides and its concurrence with the formation of carbon clusters has been discussed by Morsdorf et al. [162]. The authors postulate that the carbon clusters might act as precursors of the transition carbides.

The nucleation of transition carbides is also a subject that is not totally set in the metallurgical community, some authors claimed that it is heterogenous [181] while others that it is homogenous [158]. As previously mentioned, the evolution of carbon clusters into transition carbides have been also postulated [162].

In the following of this Chapter, the transition carbide will be treated as epsilon carbide, especially in the model development.

Let us mention that during the first stage of tempering, the carbon content of the matrix decreases with a decrease in the tetragonality of the matrix allowing to follow the transformation kinetics by in situ HEXRD [182]. It also can be followed by resistometry and by dilatometry [183] if carbon content is high enough.

III.1.A.3 Second stage of tempering

The martensite transformation is by nature incomplete, with a retained austenite fraction depending on the M_s temperature (which depends on the composition of the steel and on the PAGS [15,17,37,184]). The fraction of retained austenite also depends on the cooling rate below the M_s temperature [185,186]. For low-carbon lath martensitic steels, the retained austenite is found as thin films along the martensite laths.

During the second stage of tempering the retained austenite decomposes into ferrite and cementite. The kinetics of this transformation can be followed by dilatometry [183,187], by resistometry [183], Mössbauer spectroscopy [188], by DSC [161,189] and by in situ HEXRD [166,178,182].

III.1.A.4 Third stage of tempering

This stage, from 200 °C to 450 °C, is characterized by the dissolution of the transition carbide (if present) and the precipitation of the cementite (Θ) carbide (orthorhombic, Fe_3C). Cementite carbides present the often called ‘Bagaryatski’ orientation relationships: $[001]_{\Theta} \parallel [\bar{1}01]_{\alpha'}$, $[100]_{\Theta} \parallel [111]_{\alpha'}$ and $[010]_{\Theta} \parallel [\bar{1}2\bar{1}]_{\alpha'}$ [22].

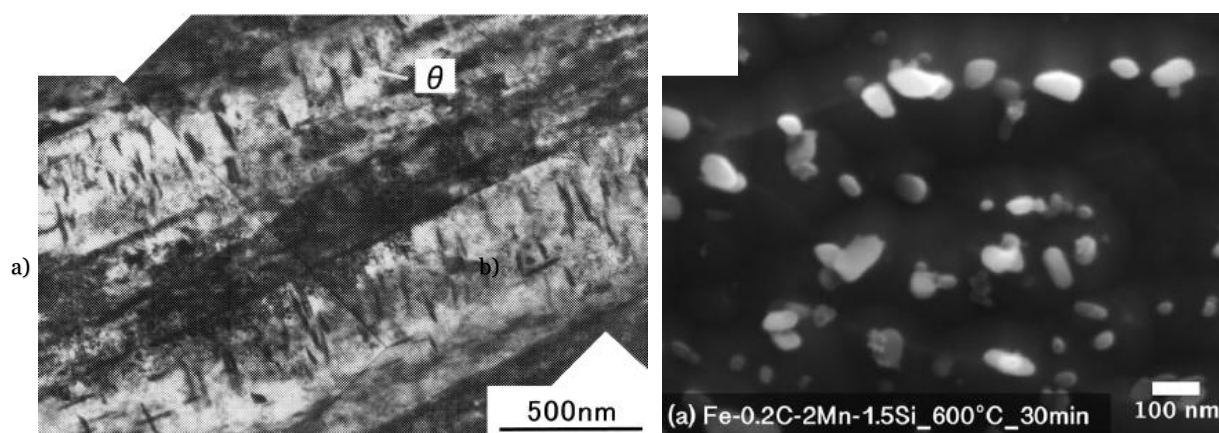


Figure 42: a) TEM micrograph presenting long-needle shaped cementite carbides after a fast heating (100 °C/s) up to 550 °C, from [190]. b) TEM micrograph presenting more spheroidal cementite carbides after a 30 minutes holding at 600 °C taken from [191].

The nucleation mechanism is not totally resolved, in situ transformation of ϵ carbide on cementite is proposed by [179] while the hypothesis of independent nucleation of cementite and subsequent dissolution of the ϵ carbide/cluster is sustained by [162,171,190]. The cementite particles show an elongated shape at the beginning of their formation [190] followed by a spheroidization at higher time/temperature tempering heat treatments as shown by Wu et al. [191] and summarized in Figure 42.

The cementite precipitation induces a third decrease of the carbon concentration in the matrix due to a lower solubility limit of carbon than the one presented by the ϵ carbide. However, it has been shown that at the early stages of the cementite precipitation the same composition among substitutional elements (u-fraction) is present in the matrix and in the carbides [39,192]. One frequently assumes that the cementite carbides grow under paraequilibrium regime. At high temperatures (i.e. 600 °C) and long holding times, substitutional elements partition from the carbides (e.g. Si, Al) and to the particles (e.g. Mn, Cr, etc.) [191,193].

III.1.B Tempering models

The tempering sequence detailed in the previous section has a critical effect on the mechanical properties of the martensitic steels and, as a consequence, numerous models have been proposed in the literature. A recent review regarding the different approaches and their main goals has been performed by Deschamps and Hutchinson [194].

In all the models, the system which is out of equilibrium (carbon supersaturation in the matrix) follows a sequence of metastable equilibrium states related to the stages of tempering. In the following a classification of the models based on the different scales, from more local to more global, is introduced.

- **Atomic scale:** The nucleation stage of precipitates can be described by Monte Carlo simulations, by cluster dynamics methods (used e.g. in the Al-Li system) [195]. Ab initio calculations have been used to simulate carbon segregation [196]. However, due to limitations on the size neither carbide growth nor complex interactions can be simulated. Another limitation is that multicomponent systems are highly complex to model by these methods.

- Mesosopic scale: Two main subfamilies of models are found at this scale, phase field method models and nucleation-growth models.

The phase field method focuses on a good description of the interfaces as well as the description of the complex evolutions of the chemical compositions without any *a priori* assumption of the precipitate shape. These models, coupled with reliable databases, are able to describe growth and coarsening. Nucleation has been using the Langevin noise method (detailed in [197]) or the classical nucleation equation as mentioned by [198]. The detailed simulations and flexibility are related to a very high simulation cost. Dedicated reviews [199,200] regarding this simulation method present few results obtained with precipitation model results.

Another approach is to describe the nucleation, growth and coarsening using assumed precipitates shape and some composition simplifications. These metallurgical and physical assumptions and simplifications allow to highly reduce the computational cost. The so-called nucleation-growth or mean field models predict several microstructural features including the fraction, the number density, the distribution and the mean size of the carbides. The composition changes of the matrix and of the carbides can be also tracked. The sequence nucleation-growth-coarsening can be described by this group of models even for coexisting precipitate types [39,154,201,202]. Lately, even carbon segregation into dislocations has been introduced into one model of this family [127].

For example, the precipitation of B2 precipitates in a high chromium-nickel martensitic steel have been simulated in [202]. The composition of the nuclei was calculated depending on the matrix composition, the fraction of carbides was also determined (function of the number of nuclei and their radius, considering growth kinetics).

- Macroscopic scale: This last group of models aims to predict the global phase transformation kinetics with a low computational cost mainly by using the Johnson-Mehl-Avrami-Kolmogorov (JMAK) approach [189,203]. Only the volume fractions of the phases are computed with neither physical description nor information regarding the size and number density of the precipitate as main drawbacks.

As in this work the aim is to obtain a physical based model (crossing out the macroscopic models) but with a relatively small computational cost (one of the main drawbacks of the phase field model), the choice was between a very local model or a nucleation-growth one. We selected the last kind as it can consider a larger number of particles and also the interactions between them and the matrix (including dislocations).

To the author knowledge two main commercial precipitation software are available for simulating tempering heat treatments with the nucleation-growth approach. TC-PRISMA, which is coupled to the ThermoCalc suite, has been recently published [204]. Some recent studies using this software are [205–207]. The other commercial software is MatCalc [208] which is based on thermodynamic extremal principle (total description of the Gibbs energy and its deriviate with time). Some of the recent works using this latter model are [90,127,149]. Evolution of the cementite composition at high tempering temperature has been achieved in [149], while the segregation of carbon into dislocations before precipitation in [127].

Nucleation-growth models are also developed in different laboratories. The “in-house” models allows to control to all the hypothesis considered for the calculations, the numerical implementation and the physical parameters used [39,154,209].

One of the main accomplishments of the mean field models is the prediction of the particle size distribution (PSD) by the utilization of the Kampmann-Wagner scheme. Computing the PSD allows to predict the sequence of nucleation-growth-coalescence in particle size and carbide number density. The PSD of each precipitate type can be followed independently. One drawback that has to be mentioned is that the use of the Kampmann-Wagner scheme and the classical coarsening theory produces a left-skewed distribution while experimental PSDs are right-skewed.

A model developed “in-house” in the laboratory will be used in the present work. The nucleation-growth model is mainly modified by coupling a segregation submodel, by changing the cementite precipitation environment and by modifying the dislocation recovery submodel implemented (with the one presented in Chapter II). The previously developed model [39,154] and the present modifications are presented in detail in Section III.3.B.

To summarize the present state of the art and guide the rest of the present chapter, the main points to be kept in mind are:

- In low carbon steels, as the ones studied in the present work, the carbon segregation into microstructure defects affects the precipitation sequence. If the carbon content is low and the dislocation density is high enough the precipitation of transition carbides might be inhibited.
- In low carbon steels the experimental characterization is more complex than in the case of higher carbon content steels due to a lower precipitate fraction and, therefore, a lower signal. In some characterization technics the low temperature of the aimed tempering also affects the intensity of the signal. To overcome this problem and be able to characterize different scale phenomena, a triple-scale characterization will be performed. 3DAPT will be utilized to measure the segregation state, TEM the size of the carbides and in situ HEXRD the precipitation temperature range and fraction.
- The kinetics of the carbon segregation into microstructural defects has been modeled in the literature [153,167] by different models. However, the coupling between this phenomenon and nucleation-growth model is almost inexistent in the literature. This point will be achieved in the present chapter.

III.2 Experimental results

As discussed above, the experimental description of the precipitation requires a set of characterization technics that allows to observe local phenomena such as carbon segregation and more global ones to observe the phase fraction evolution.

The carbon segregation was characterized by 3DAPT and its results are presented in the next section. Then the determination by HEXRD of the carbides presence as well as the determination of the cementite fraction are introduced. The precipitation characterization section finishes with the carbide

size measurement performed by TEM. These different experimental technics have been detailed in Chapter II.

III.2.A Carbon segregation

As previously mentioned in Chapter I, 3D Atom Probe Tomography characterization was performed in order to observe the distribution of the carbon in the microstructure at the quenched state. Even if the main objective of the 3DAPT characterization was to establish the segregation state especially around the dislocations, the carbon enrichment of an austenitic film was also observed (presented in Figure 43.a).

Two quenching conditions were analyzed for the 0.2C steel, “natural” gas quench (8 tips were studied) and water quench (5 tips were studied). The time between the heat treatment and the characterization was around 2 months.

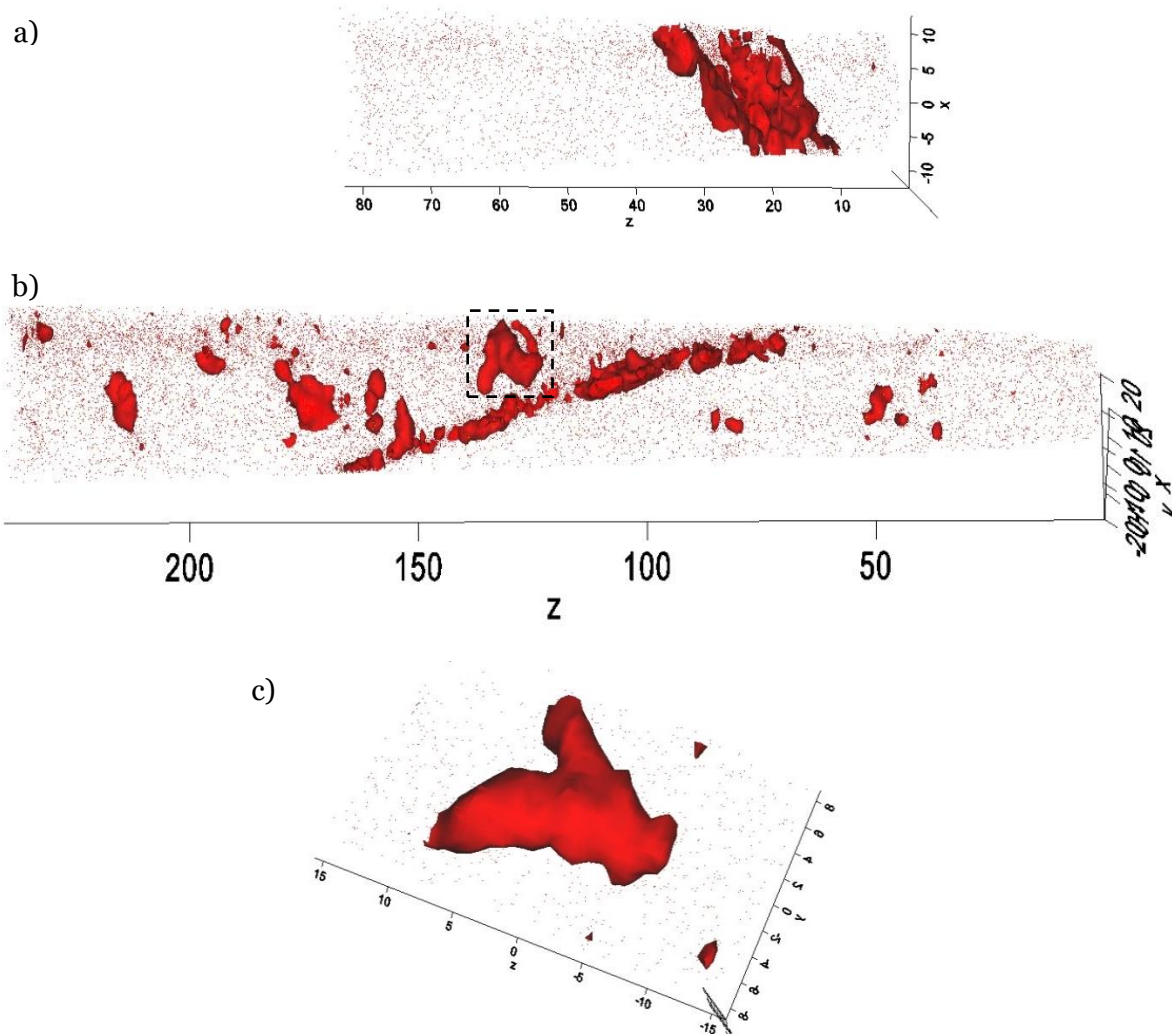


Figure 43: a) Reconstruction of a 3DAPT tip of a 0.2C_GQ sample presenting a carbon rich film, probably austenite. b) Reconstruction of another 3DAPT tip of the same 0.2C_GQ sample with a planar defect and a dislocation (marked zone with dashed lines). c) Closer reconstruction of the region marked in b). For all the cases 4 at.% C isosurfaces are shown, and the axes are in nanometers.

Two reconstructed tips of the 0.2C_GQ condition are shown in Figure 43. Carbon atoms are represented by red dots and isosurfaces of 4 at.% C are shown. In Figure 43.a, a carbon rich film is present between Z coordinates 40 and 10 nm and diagonal to the tip. In Figure 43.b a planar segregated region is observed (also diagonal to the tip between 175 and 75 nm in Z). A linear segregation is found in the same tip (marked with a dashed rectangle), a rotated close up is shown in Figure 43.c. Some globular volumes are found in the tip presented in Figure 43.b. If the carbon concentration selected to create the isosurfaces is increased over 10 at.% C these volumes are no more observable.

Even if 8 tips have been characterized for the GQ condition, only in two of them the presence of dislocations has been established for sure. The reason behind this can be the local nature of the characterization technic coupled with a lower dislocation density than in the case of the WQ condition.

A proxigram calculated using the isosurface of the carbon segregated film shown in Figure 43 is presented in Figure 44 (the definition of the proxigram is given in Chapter I). The carbon concentration far from the isosurface (distance equal to 0) in the matrix is ca. 1 at.%. It evolves near the isosurface, with values in the carbon rich region ranges between 6 and 8 at.% (1.25-1.5 wt.%). The latter values show a high dispersion and errorbar due to the low number of detected atoms at those distances. This carbon concentration is even higher than the one expected in a stabilized austenite by a quenching and partitioning heat treatment [210–212], the difference may be explained by the different martensite/austenite fraction ratio. No variations of the substitutional elements (Mn and Si) are observable between the carbon rich and carbon depleted regions. The Cr concentrations are not presented as their values are even smaller than the ones of the Si, for which no partition was observable either. Substitutional diffusion is much slower than the carbon diffusion and the time at high temperature during cooling may be not enough to produce a substitutional partitioning profile.

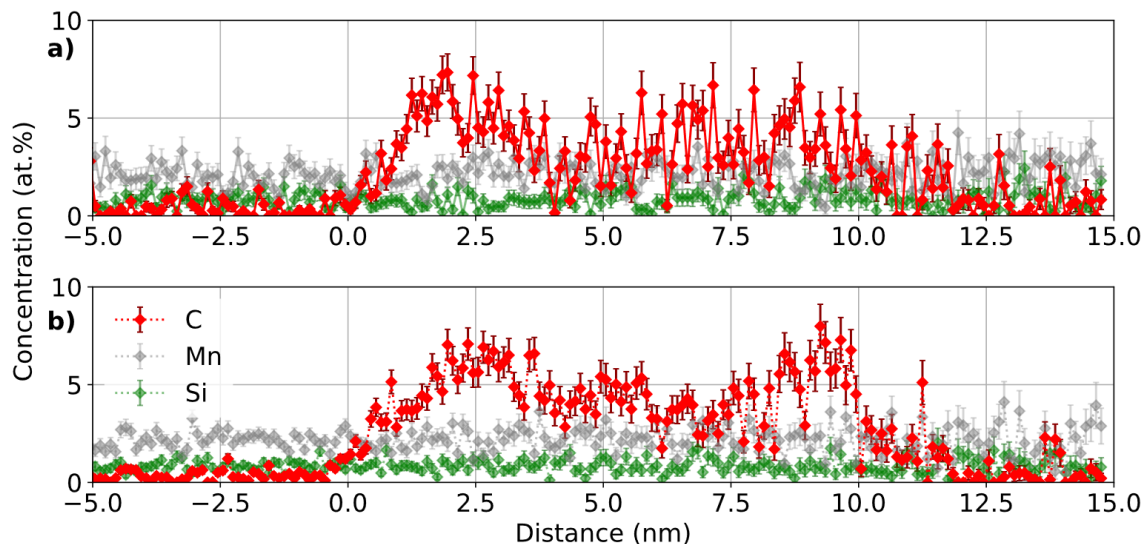


Figure 44: a) Proxigram of C, Mn and Si calculated from the left isosurface limiting the rich carbon region in Figure 43.a. b) Same as in a) but using the right isosurface. Colors used in the present graph do not follow the chart presented in Section I.3.

Some of the 3DAPT results of the water quenched condition are presented in Figure 45. The results presented are representative of the five observed tips. For this condition no planar segregation was detected and few small isolated globular isosurfaces are observed. Indeed, for the gas quenched sample,

only three dislocations were found while for the water quenched sample, 19 dislocations were found. Two tangles of two dislocations were clearly observed in the water quenched condition, (their observation is easier in three dimensions). Even if the number of linear segregations, related to the number of dislocations, was found higher in the water quenched condition no quantification of the dislocation density could be performed due to the local nature of this characterization technic.

Proxigrams of one linear segregation observed in a tip from the GQ and WQ conditions are presented in Figure 46.a and Figure 46.b respectively. In both cases the segregation profile can be well described by a gaussian distribution. It can be observed that most of the carbon excess is between -2.5 and 2.5 nm,

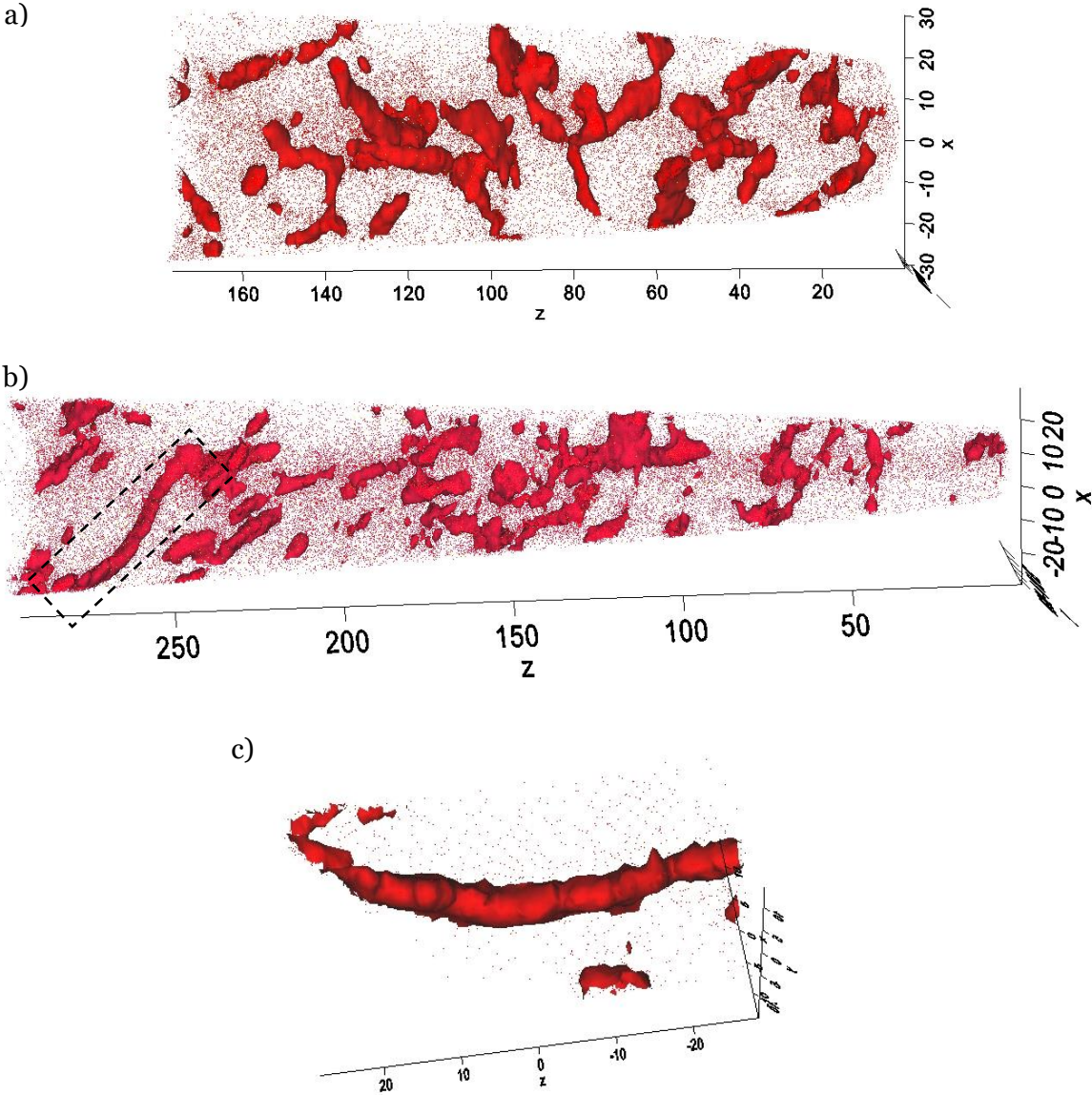


Figure 45: a) Reconstruction of a 3DAPT tip of a 0.2C_WQ sample. b) Reconstruction of another 3DAPT tip extracted from the same 0.2C_WQ sample with several linear segregations. c) Close-up reconstruction of the region marked in b). For all the cases 4 at.% carbon isosurfaces are shown, and the axes are in nanometers.

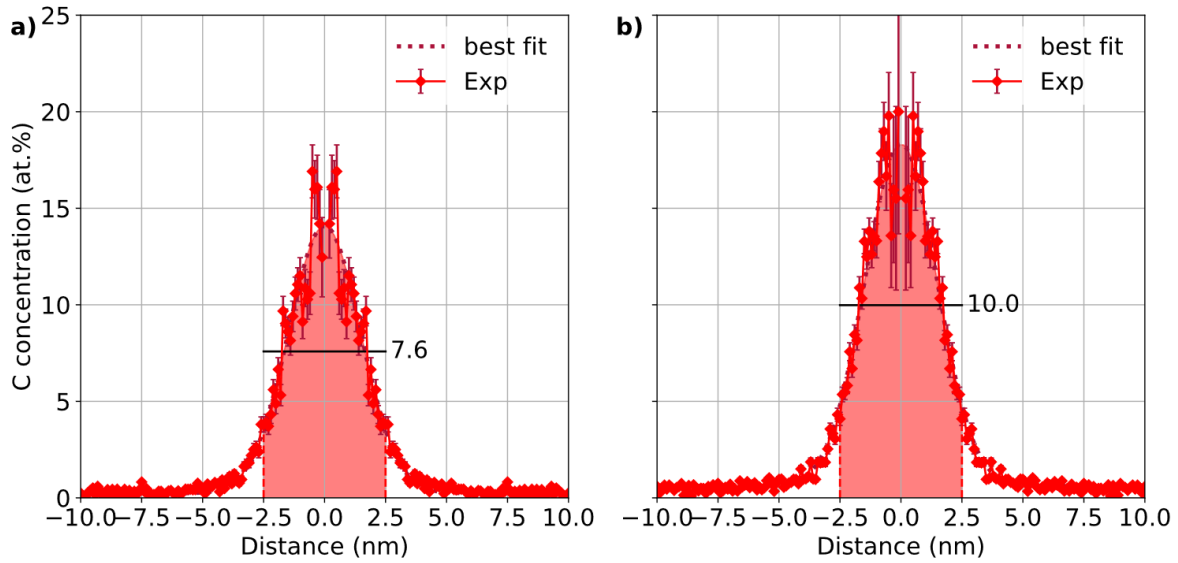


Figure 46: Proxigram of a linear segregation and its gaussian best fit in a) GQ tip b) WQ tip. In both cases the equivalent carbon in excess is indicated.

with a residual carbon excess up to 5 nm from the center. The influence radius of the dislocation seems to not change between both quenching conditions (and after aging at room temperature for two months). Similar profiles were found in all the detected linear segregations.

For each linear segregation the excess carbon was calculated as explained in Section I.6. Table 8 presents the results for each 0.2C_GQ tip in which linear segregations were detected. For each sample the number of detected dislocations is presented as well as the carbon concentration far from the defect (C_{matrix}), the carbon excess using as limits 7.5 and 2.5 nm. Finally, the constant carbon concentrations that will give a carbon concentrations equivalent to the ones calculated using a gaussian distribution ($R_f=2.5$ nm) are presented ($C_{equivalent}$). In an analogous table (Table 9), the results for the water quench condition are presented.

Table 8: Gas quenched condition of the 0.2C steel: number of linear segregations analyzed per sample (in which at least one linear segregation is present). Average value per sample as well as total average of the carbon content in the matrix, excess of carbon calculated as in [77] using a gaussian profile and equivalent concentration using a uniform profile (Section I.6).

Sample	Number of linear defects	C_{matrix} (at.%)	C_{excess} (at./nm)		$C_{equivalent}$ (at.%)
			7.5 nm	2.5 nm	
0.2C_GQ 1	2	1.2	180.0	86.4	8.2
0.2C_GQ 2	1	0.8	77.1	67.9	6.3
Average	-	1.1	145.7	80.2	7.6

The average values of carbon in excess in the dislocation atmospheres for both conditions are in the same range, with slightly higher values in the water quenched condition (the difference may be in the errorbar). The 0.2C_WQ condition presents an excess of 99 at/nm and 156 at/nm with 2.5 nm and 7.5 nm limits respectively, while the average obtained values for the 0.2C_GQ condition are 80 and 146 at/nm

respectively. As a consequence, the equivalent carbon concentration for both quenching conditions are similar. The values of water quenched condition being slightly higher (7.6 for the gas quenched sample and 8.4 for the water quenched one with radius set at with 2.5 nm). These values are in good accordance with the Cottrell atmospheres reported in the literature [41,151,213], between 7 and 10 at.%. Table 8 and Table 9 also show the carbon concentration in the matrix. Despite the experimental uncertainty, it is lower in the water quenched condition than in the gas quenched one.

Table 9: Analogous to Table 8 but for the water quenched condition (0.2C_WQ).

Sample	Number of linear defects	C_{matrix} (at.%)	C_{excess} (at/nm)		$C_{\text{equivalent}}$ (at.%)
			7.5 nm	2.5 nm	
0.2C_WQ 1	2	0.4	115.8	88.8	7.6
0.2C_WQ 2	7	0.2	118.4	83.4	7.0
0.2C_WQ 3	4	0.4	184.5	111.3	9.4
0.2C_WQ 4	1	0.3	244.3	125.8	10.5
0.2C_WQ 5	3	0.4	204.5	118.5	10.0
Average	-	0.3	156.3	99.3	8.4

Main outcomes of the 3DAPT characterization in the as-quenched states are:

- Linear segregations, related to Cottrell atmospheres near dislocations were found in both quenching conditions (0.2C_GQ and 0.2C_WQ) with a similar segregation state.
- The observed dislocation density is higher in the water-quenched sample than in the GQ one, in accordance with HEXRD results (cf. Chapter II).
- The segregation radius is estimated at 10 times the Burgers vector (2.5×10^{-9} m), it was used to calculate the equivalent carbon content.
- Both quenching conditions presented high segregation values, close to the Cottrell atmospheres usually reported in the literature, between 7 and 10 at.% [4,85,86].

Surprisingly, the carbon concentration inside the segregated zones is similar in both GQ and WQ conditions, despite the difference in cooling rate. This may signify that the carbon segregation is extremely fast even during water quenching (between -1000 °C/s and -5000 °C/s) or that carbon atoms firstly segregated during quenching and then they continued segregating at room temperature during the two months between the heat treatment and the characterization. This hypothesis will be evaluated by modeling the carbon segregation in III.3.A Carbon segregation model.

The presence of small globular segregated volumes with carbon concentration lower than 10 at.% was observed, in a higher proportion in the GQ condition than in the WQ one. Their presence probably indicates the presence of carbon clusters in view of the size (thickness ca. 5 nm) which is in accordance with [162]. However, the presence of transition carbides in addition cannot be totally ruled out. Ning et al. proposed that similar globular concentrated carbon regions corresponded to the presence of transition

carbides [150]. The possible presence of transition carbides is also supported by the TEM characterization of the GQ condition (cf. Section III.2.B.1).

An austenitic film was found in a 0.2C_GQ tip showing carbon partition from martensite to austenite and the absence of partition of elements Mn and Si. It can be concluded that some carbon partition may occur even during a not extreme quench. To the authors knowledge no previous evidence of this stabilization obtained by 3DAPT characterization is present in the literature.

III.2.B Precipitation sequence

The precipitation sequence during the tempering heat treatments is studied in the present section. In order to better understand the evolutions during the tempering, the initial state has to be characterized. The characterization of the initial state by HEXRD and TEM will compose a first subsection. Secondly, the precipitation kinetics during tempering will be tracked by in situ HEXRD experiments. Finally, the evolutions of the cementite size determined by TEM analysis will be presented.

III.2.B.1 Initial state

The initial states, i.e. quenched states, are analyzed in a first time by HEXRD. The diffractograms obtained for the three alloys (0.1C, 0.2C and 0.3C) quenched at the different cooling rates (-10, -50, -100 °C/s and water quench) are presented in Figure 47. The positions of the usual martensitic peaks are indicated as well as the {321} diffraction peak due to the harmonic contamination [214]. The only peak observable of austenite, {200}, is also indicated. The diffraction positions expected for cementite are indicated as well as an angular window (areas in grey) in which several low intensity peaks are expected. The same representation is used for the epsilon carbides.

Retained austenite is present in all the samples. The {200} austenitic diffraction peaks intensity varies with the cooling rate: the higher the cooling rate, the lower the intensity, which indicates a variation of the austenite fraction at the end of the quench. The retained austenite weight fractions obtained by the Rietveld refinement are shown in Table 10.

Table 10: Retained austenite weight fractions for the three studied steel compositions and different cooling rates.

Steel	Cooling rate			
	-10 °C/s	-50 °C/s	-100 °C/s	WQ
0.1C	2.6	3.1	3.4	1.4
0.2C	5.6	4.9	4.1	1.8
0.3C	6.7	5.3	4.5	2.0

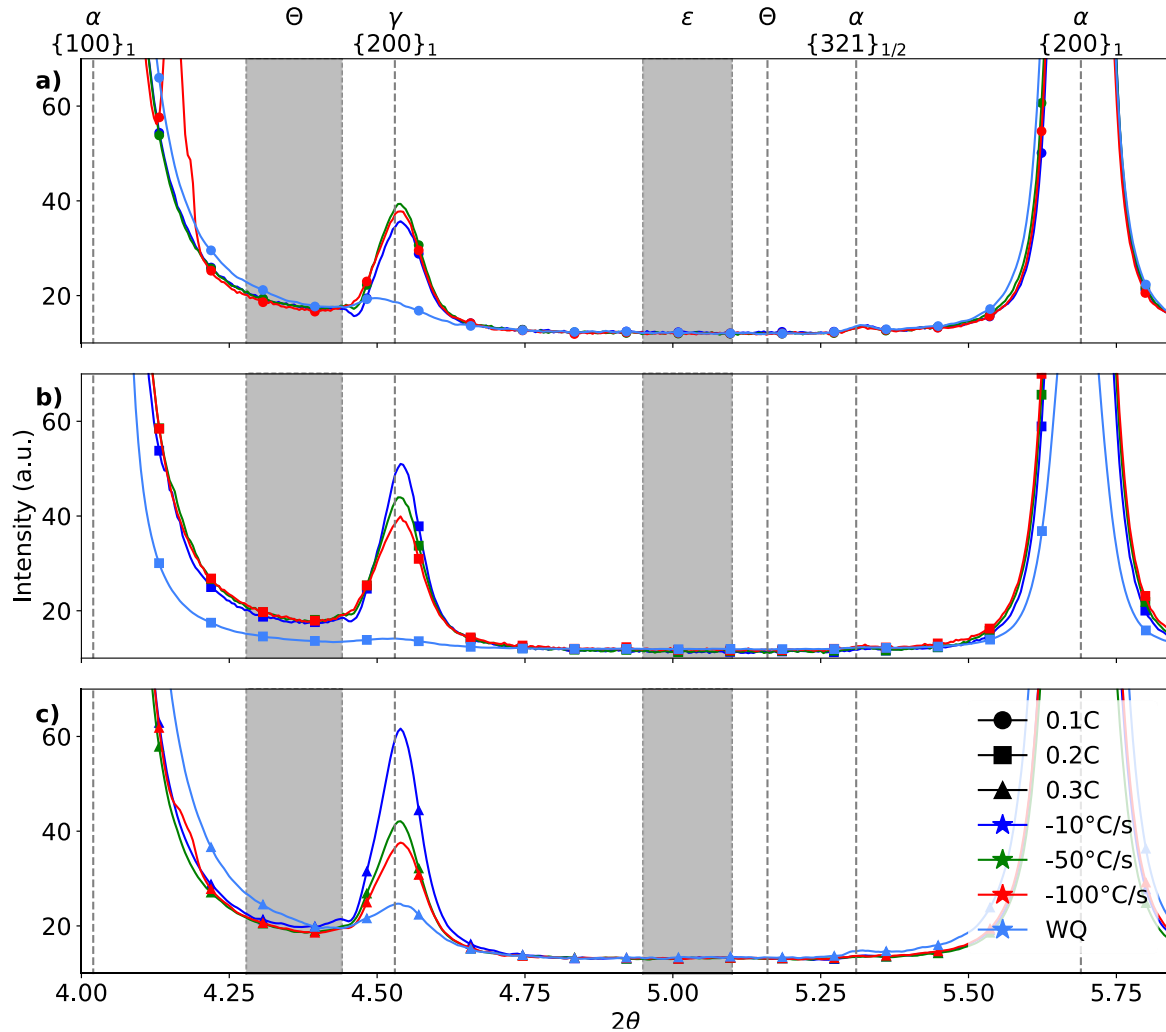


Figure 47: Diffractograms in the angular window used for the carbide detection for the four quenching rates (controlled gas quench at -10, -50 and -100 °C/s and water quench) in the steel 0.1C in a), 0.2C in b) and 0.3C in c). The index $\frac{1}{2}$ refers to the harmonic wavelength ($\lambda/2$).

For a given cooling rate, the increase of carbon content leads to an increase in the retained austenite fraction. This effect is well known and is mostly due to the decrease of the M_s temperature with the carbon content [37]. A second observation from Table 10 is the decrease of the fraction of austenite with increasing cooling rate. This effect has been previously reported in [185,186] and two main phenomena may be responsible, a lower autocatalytic effect at lower cooling rate and a higher chemical stabilization of the austenite, due to a higher carbon diffusion, at the lower cooling rates as proposed by [185]. This last point seems to be confirmed by the 3DAPT observations previously presented on the 0.2C_GQ sample.

Neither transition carbides nor cementite are detected in any of the studied conditions as no changes in the expected diffraction positions are visible. The 0.1C_GQ_100Cs diffractogram shows a spike at ca. 4.15 2θ , which can be due to a partial diffraction of the thermocouple (platinum) or of the inductor of the dilatometer (copper). Regarding the non-detection of carbides at the quenched state, it has to be kept in mind that the presence of carbides can be confirmed by HEXRD only if the diffraction peaks of the precipitates are actually detectable, while the non-detection does not rule out the presence of the phases. If the volumes of the precipitates are too small to diffract or if there is a high density of defects the

diffraction may be limited. Other characterization techniques as dilatometry may detect global changes before the carbides are detectable by HEXRD as has been evidenced by Gaudez [39] during tempering, in the case of transition carbides. However, dilatometric analysis carried out in the steels of the present study did not show exploitable results during quenching probably due to a lower carbon content than in [39] (about 0.7 wt.% C).

The 0.2C_GQ (“natural” gas quench, cooling rate ca. $-20\text{ }^{\circ}\text{C/s}$) and the 0.2C_WQ conditions were also characterized by TEM and the results are shown in Figure 48. The gas quenched condition presents an abundant precipitation (Figure 48.a) while no carbides are observable for the water quenched sample with the same magnification (Figure 48.b) or even higher (500 000 X). Combining the present results and the results from APT, it is concluded that no carbides are present in the 0.2C_WQ condition.

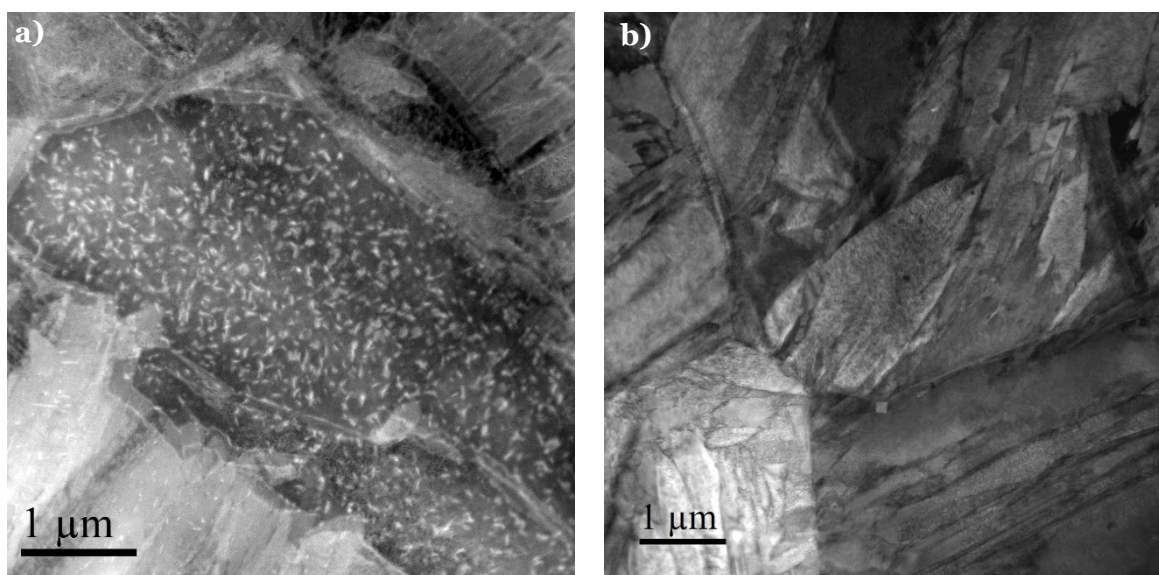


Figure 48: a) TEM micrograph of the 0.2C steel after a “natural” gas quench (between -10 and $-50\text{ }^{\circ}\text{C/s}$), precipitates are observable in lighter grey level. b) Similar to a) for a water quenched sample, no precipitates are observable.

The chemical composition of the carbides detected in 0.2C_GQ was characterized firstly by composition maps showing the carbon and substitutional elements distributions (Figure 49). The precipitates are thicker than the surrounding matrix as can be observed from the Fe map, due to a preferential chemical attack of the matrix during the preparation of the sample. The chemical composition of the precipitate marked with the yellow circle was calculated without considering the interstitial atoms (u -fractions) giving $u_{\text{Mn}} = 2.1\%$, $u_{\text{Si}} = 0.24\%$ and $u_{\text{Cr}} = 0.25\%$. Four additional carbides were analyzed with same results. These concentrations are close to those of the nominal composition of the steel. This indicates that at the quenched state no partition of substitutional elements occurred between the matrix and the precipitates. The absence of substitutional elements partition has also been previously observed during the cementite precipitation at low temperature tempering heat treatments [39,192,215]. It was ascribed to a growth regime under paraequilibrium mode.

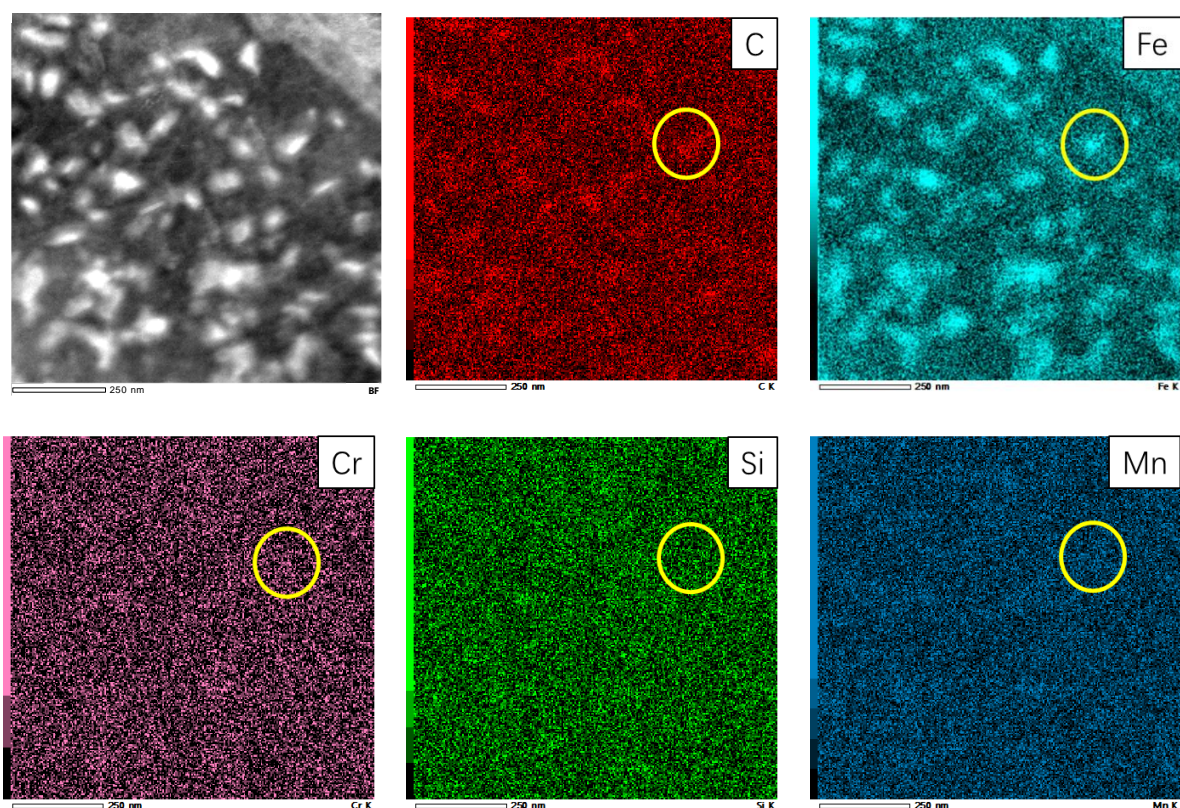


Figure 49: On top left a close up of the Figure 48.a is presented. The other figures present the element distributions (C, Fe, Cr, Si, Mn). The colors used in the present figure do not follow the chart presented in Section I.3.

The water quenched condition (in which at least for the 0.2C steel no carbides are observable by TEM) was the initial state chosen for the characterization of precipitation during tempering. Indeed, one expects that the precipitation sequence will be made visible if more carbon is in solid solution in the initial state. The results are presented in the next section.

III.2.B.2 In situ tracking of precipitation kinetics during tempering by HEXRD

The analysis of the tempering heat treatments will be separated in two parts, on the heating and on the isothermal holding. The constant heating rate of all the presented heat treatments was 10 °C/s and the maximum holding time was 600 s at the three selected tempering temperatures, 200, 300 and 400 °C. The three steel compositions were considered; 0.1C, 0.2C and 0.3C.

III.2.B.2.a Heating stage

The diffractograms obtained during the heating part of the tempering of the 0.1C, 0.2C and 0.3C steels are shown in Figure 50, Figure 51 and Figure 52 respectively. Each diffractogram is shifted in intensity from the previous one to facilitate the interpretation. The diffraction positions shown for the martensitic and austenitic peaks correspond to the lattice parameters at room temperature while the ones for carbides were calculated on the basis of the lattice parameters presented by [39].

The diffractograms of the 0.1C_WQ steel show small variations from room temperature up to 400 °C. The main change is the decomposition of the retained austenite starting around 225 °C and accelerates above 350 °C. No variations in the epsilon window are visible and a small change from the background is observable for the cementite diffraction peak at ca. 5.15 2 θ at the end of the heating (better observed in Figure 53). The 0.2C_WQ sample presents a better-defined cementite peak at the latter mentioned position at the end of the heating. The retained austenite decomposition starts at 250 °C and shows fast decomposition from 325 °C. The 0.3C_WQ sample shows a similar temperature range for the austenite decomposition and an even better definition of the cementite diffraction peaks, as expected due its higher carbon content.

The determination of the presence of epsilon in the 0.2C_WQ and 0.3C_WQ conditions by observation of the diffractograms is more difficult. It seems that some serrations in the epsilon angular window are present for the 0.3C_WQ condition from 300 °C up to 400 °C. A close-up is presented in Figure 53 for easier observation. All the diffractograms shown in this figure have been shifted in intensity to have the same intensity at the lower end of the angular window in order to facilitate the observations. Only one diffractogram each 25 °C is presented for better visibility.

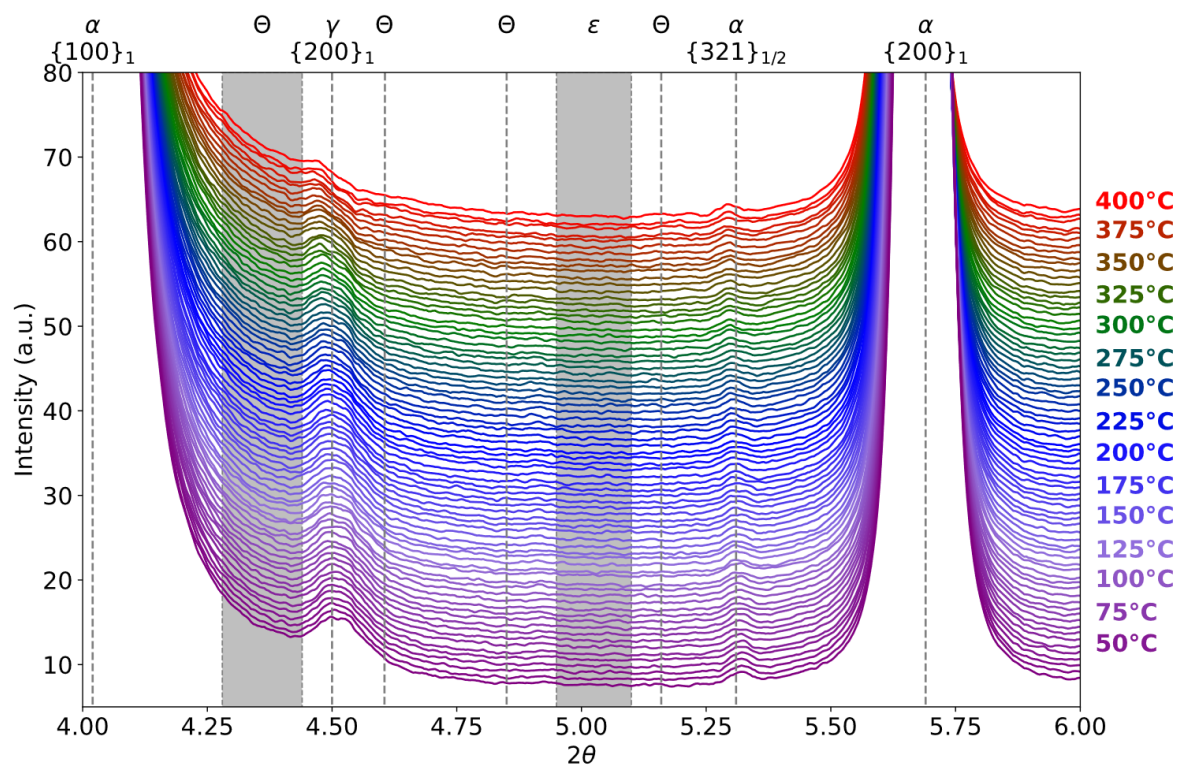


Figure 50: Diffractograms during the heating section of tempering until 400 °C of a 0.1C_WQ sample.

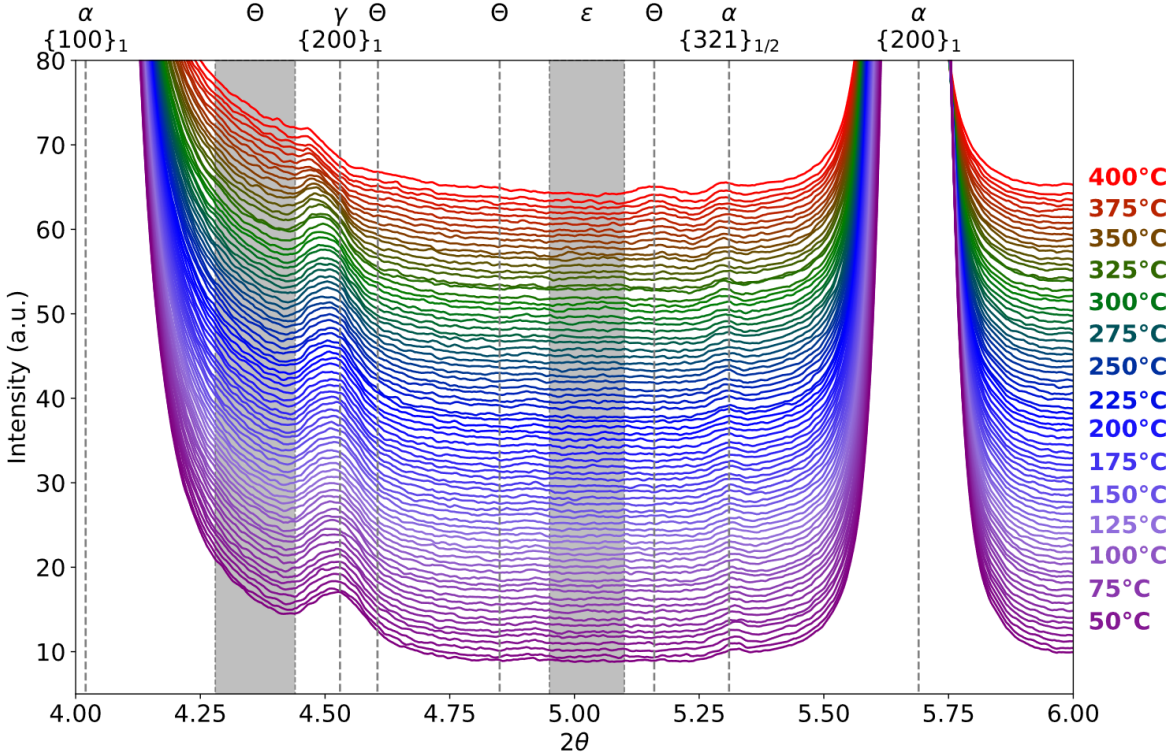


Figure 51: Diffractograms during the heating section of tempering until 400 °C of a 0.2C_WQ sample.

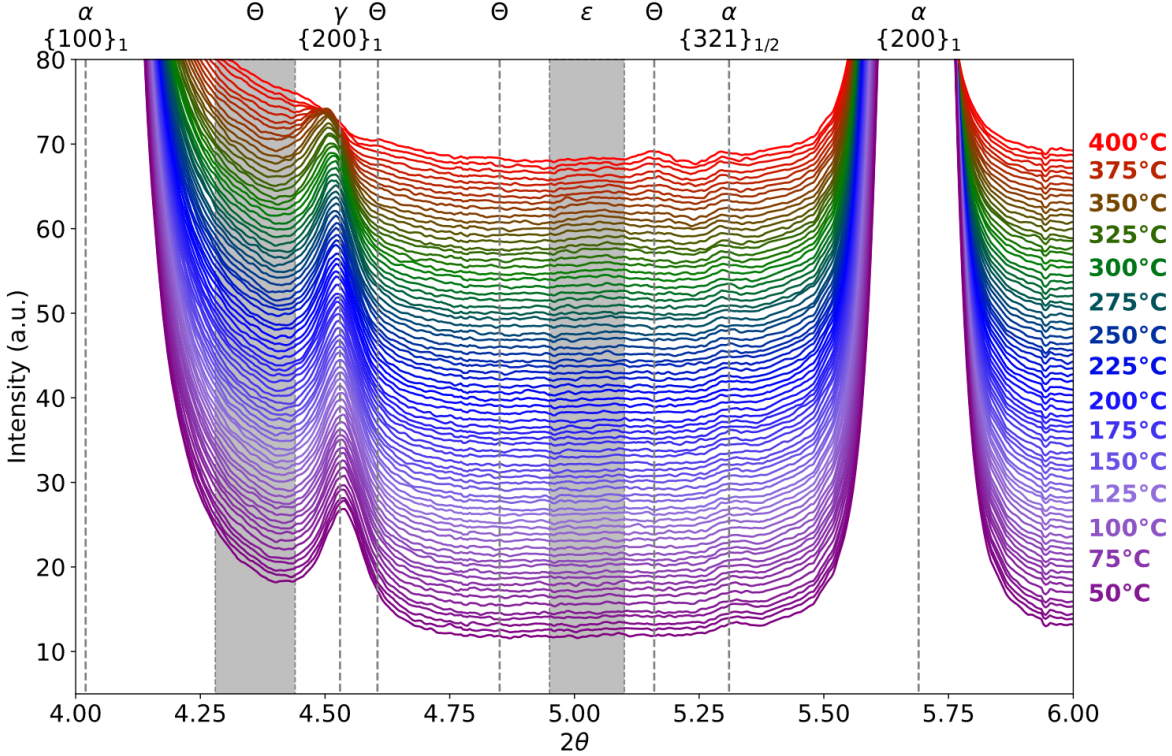


Figure 52: Diffractograms during the heating section of tempering until 400 °C of a 0.3C_WQ sample.

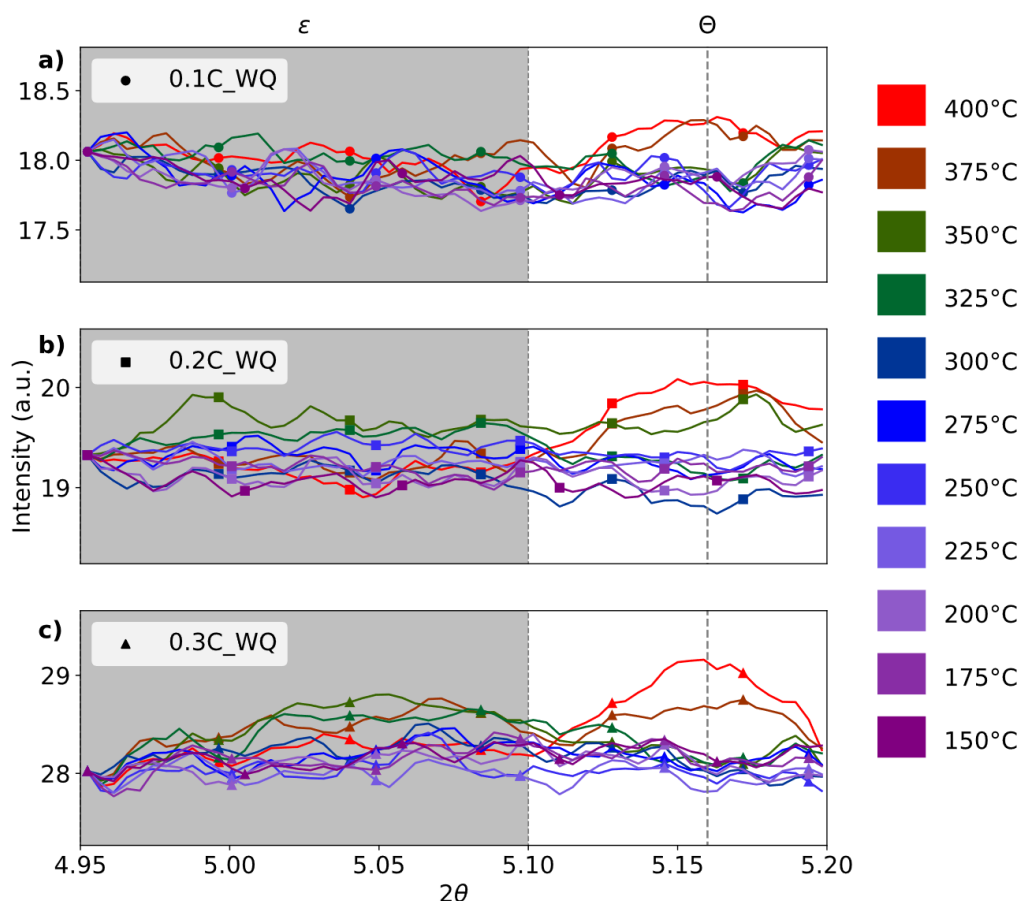


Figure 53: Different diffractograms (one each 25 °C) during the heating section of tempering of the 0.1C_WQ condition in a), of the 0.2C_WQ condition in b) and of the 0.3C_WQ condition in c).

The 0.1C_WQ does not show any clear formation of epsilon as previously mentioned and the formation of cementite is observable from the 400 °C diffractogram.

Although the 0.2C steel also presents the expected cementite peak after 350 °C, the diffractogram acquired at 325 °C present a lower intensity in the epsilon angular window. It could indicate the formation of the transition carbide.

The presence of epsilon in 0.3C_WQ sample can be observed in Figure 53.c, for the diffractograms corresponding to 300, 325, 350 and 375 °C. At 375 °C a first disturbance at the cementite position is present. At the next shown diffractogram, 400 °C, no epsilon is observed and a better defined cementite peak is detected.

Hence, to summarize, the epsilon carbides are not detected in the 0.1C steel. They are probably present in the 0.2C steel and their presence is clearly observable in the 0.3C steel. In both latter steels, the sequence of transition carbides formation followed by the formation of cementite which replaces the transition carbides (probably formed in the 0.2C steel) is visible by HEXRD. Conversely, in the 0.1C steel the cementite precipitates directly without a detectable prior stage of transition carbides.

As presented in Section III.1.A.3, the presence of transition carbides in steels with carbon content lower than 0.2C may be canceled due to segregation into dislocations [103]. However, it is worth to recall that this calculation considers a dislocation density almost 10 times higher than those reported in the previous

Chapter (2×10^{16} $1/m^2$ in [103] versus 2.5×10^{15} $1/m^2$ in the present study). Thus, the presence of epsilon in small fraction during the tempering of the 0.2C_WQ condition seems consistent with the segregation of carbon with the determined dislocation density. In the 0.1C steel, all the carbon would be segregated, which would prevent the formation of the transition carbides. For the 0.3C_WQ, epsilon precipitation would be suppressed if the dislocation density was equal to or higher than 3×10^{16} $1/m^2$ which is also far higher than the measured dislocation density. Therefore, the presence of epsilon in this alloy is also in accordance with the literature [103].

Regarding the temperature range in which the transition carbide is detected, from 300 °C to 400 °C, it can be stated that it is higher than the epsilon precipitation temperature ranges usually reported in the literature (100-250 °C) [170,171]. The presence of epsilon up to 500 °C was observed by HEXRD in situ experiments in [39]. The fact to start detecting the transition carbides at a higher temperature range than the usual one is probably due to their small size. The epsilon carbides might be too small to be detected during the nucleation stage and the first moments of the growth stage. On the other hand, their detection up to 400 °C is a new outcome from HEXRD.

III.2.B.2.b Holding stage

In the following, the diffractograms for the isothermal section of the heat treatment on the 0.3C_WQ are presented. For the sake of clarity, only one diffractogram every 25 seconds is shown. The diffractograms corresponding to holding temperatures 200 °C, 300 °C and 400 °C are presented in Figure 54, Figure 55 and Figure 56 respectively. In some of the diffractograms, before 200s of holding, some spikes of the background are observable (as at $5.41^\circ 2\theta$ in the 400 °C holding). These spikes are due to an excessive correction of the collected image by the detector during the fast acquisition mode.

During the 200 °C holding, no evidence of epsilon nor of cementite precipitation is observable in the HEXRD diffractograms. The retained austenite peak's intensity remains constant, i.e. no austenite decomposition occurs. The evolutions during the holding at 300 °C present some differences. The retained austenite decomposes between the start of the isothermal holding and the first 50 seconds. Cementite precipitation can be observed after 125 seconds and presents a slow increase of the associated peaks' intensities. At the end of the holding at 300 °C, the peaks are not enough defined to properly quantify this phase by the Rietveld refinement.

The cementite precipitation is more clearly observable during the holding at 400 °C. The cementite diffraction peak at $5.14 2\theta$ is already observable at start of the isotherm and it intensifies during the holding. Although in the cementite angular window between 4.28 and $4.48 2\theta$ no cementite peaks are visible at the time 0, at the end of the holding some serrations are observable in this section of the diffractogram. At the beginning of the isotherm, no austenite peak is detectable as can be also observed in Figure 52 at the end of the heating.

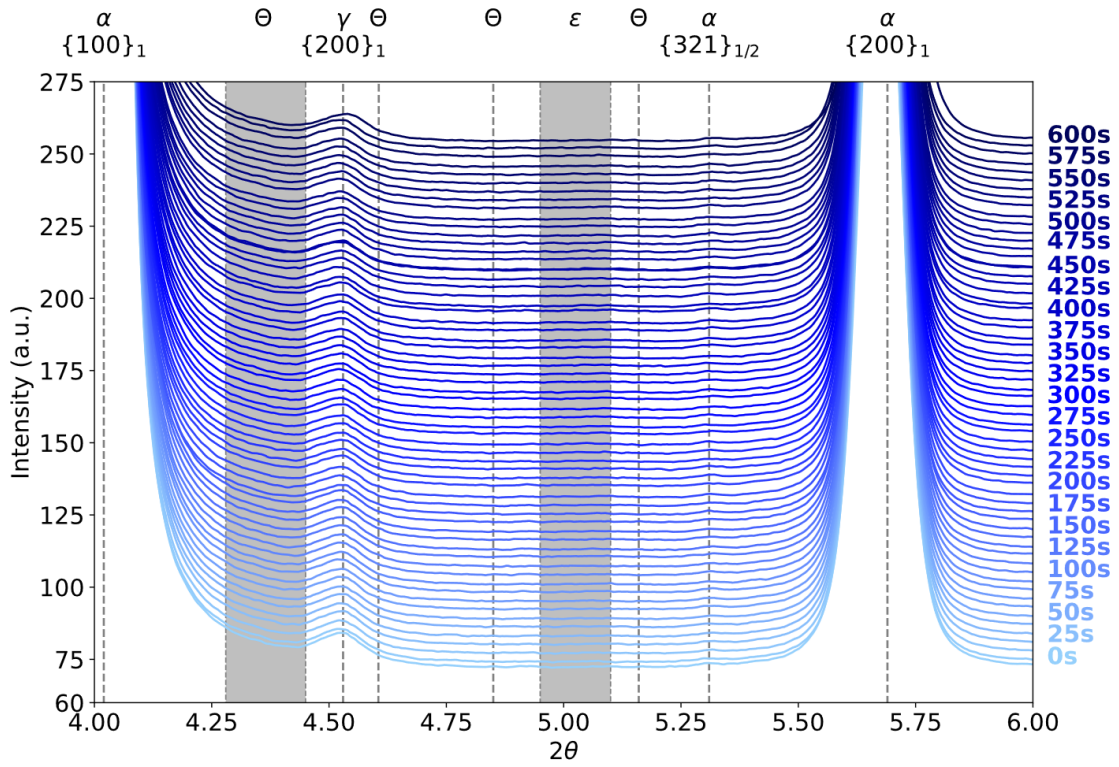


Figure 54: Diffractograms during the isothermal section of tempering at 200 °C of a 0.3C_WQ sample.

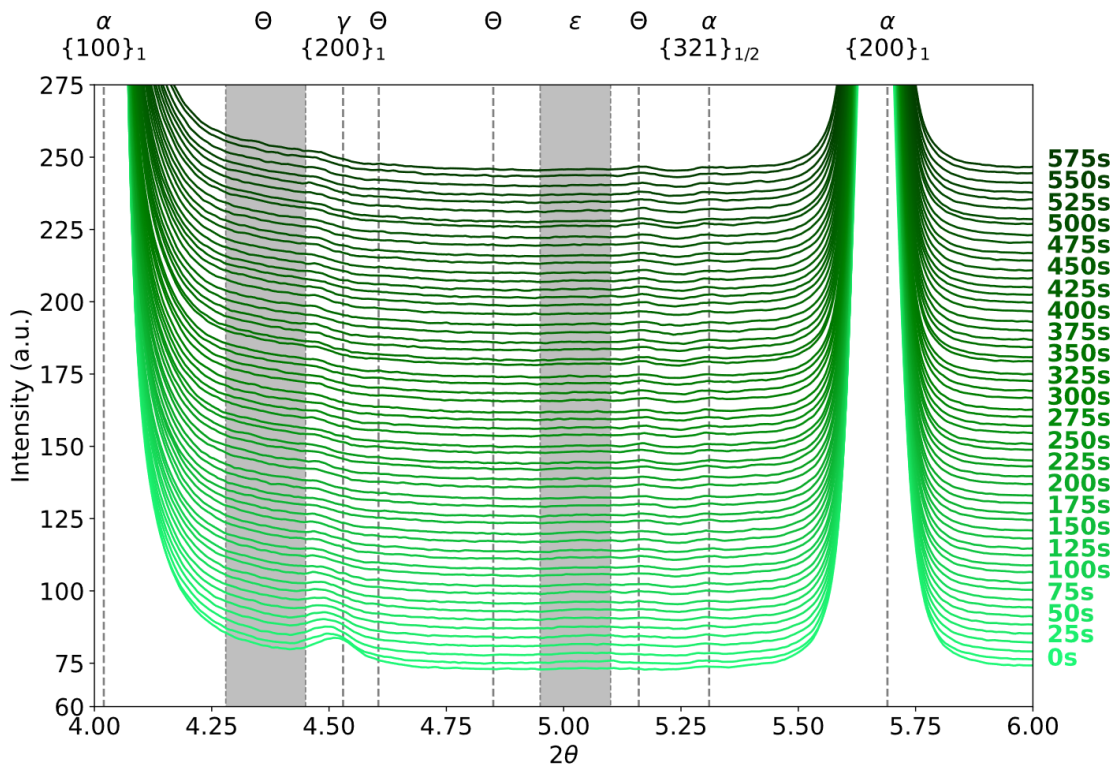


Figure 55: Diffractograms during the isothermal section of tempering at 300 °C of a 0.3C_WQ sample.

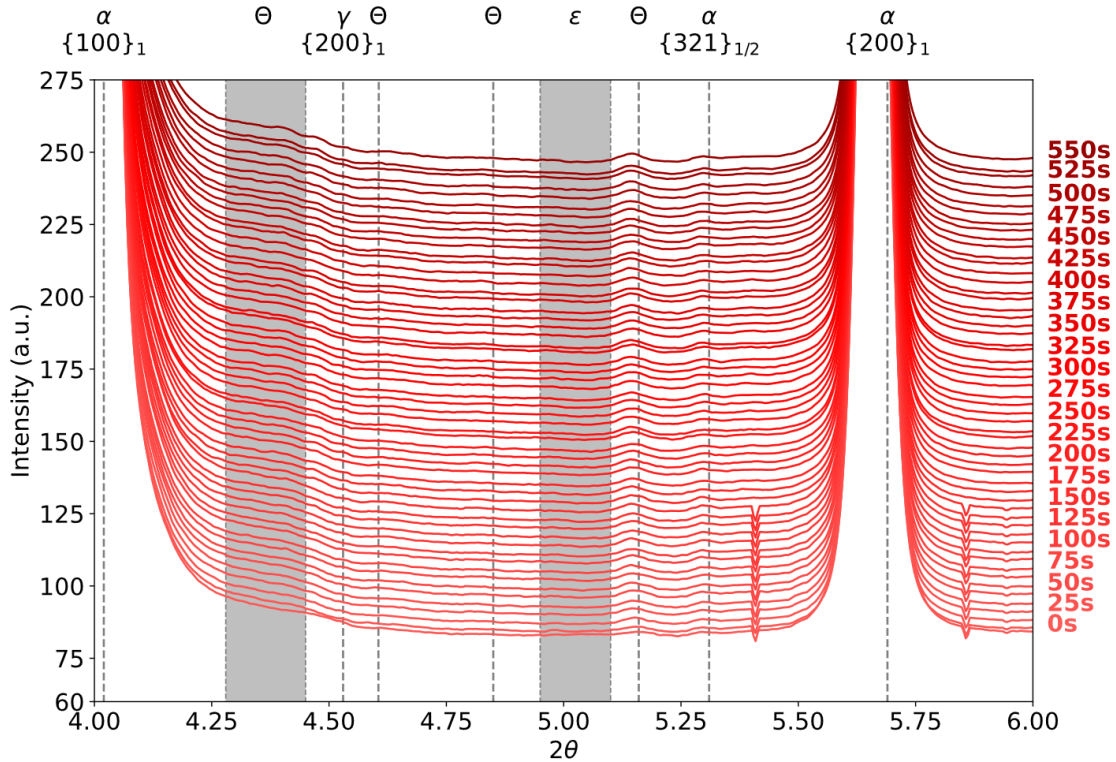


Figure 56: Diffractograms during the isothermal section of tempering at 400 °C of a 0.3C_WQ sample.

The shape of the cementite carbides may explain the higher intensity of the diffraction peak at one position (5.14° 2θ) than in other diffracting positions (4.28-4.48° 2θ angular window, and 4.61 and 4.85° 2θ). As will be shown in Section III.2.B.3 with TEM observations, the cementite carbides present a high aspect ratio up to ca. 9. Cementite growth is anisotropic due to anisotropic constants [216] and interface energies [217]. However, one should mention that with temperature and time, the cementite tends to decrease its aspect ratio, i.e. to spheroidize. Spheroidization was observed in [190,191] while the anisotropic growth rate decreases with the temperature, as was modeled by [218].

The effect of the carbon content on the cementite precipitation is presented in Figure 57, by comparing the three studied steels at 0s of holding at 400 °C (end of the heating section, Figure 57.a) and at the end of holding (Figure 57.b). At the start of the isothermal holding, the presence of cementite is clear in the 0.2C and in the 0.3C steels while in the 0.1C some noise is observed around the expected diffracting positions but it is not conclusive. Contrarily, at the end of the holding, the presence of cementite can be confirmed for all three alloys with higher intensities of the diffraction peaks with increasing carbon content of the steel.

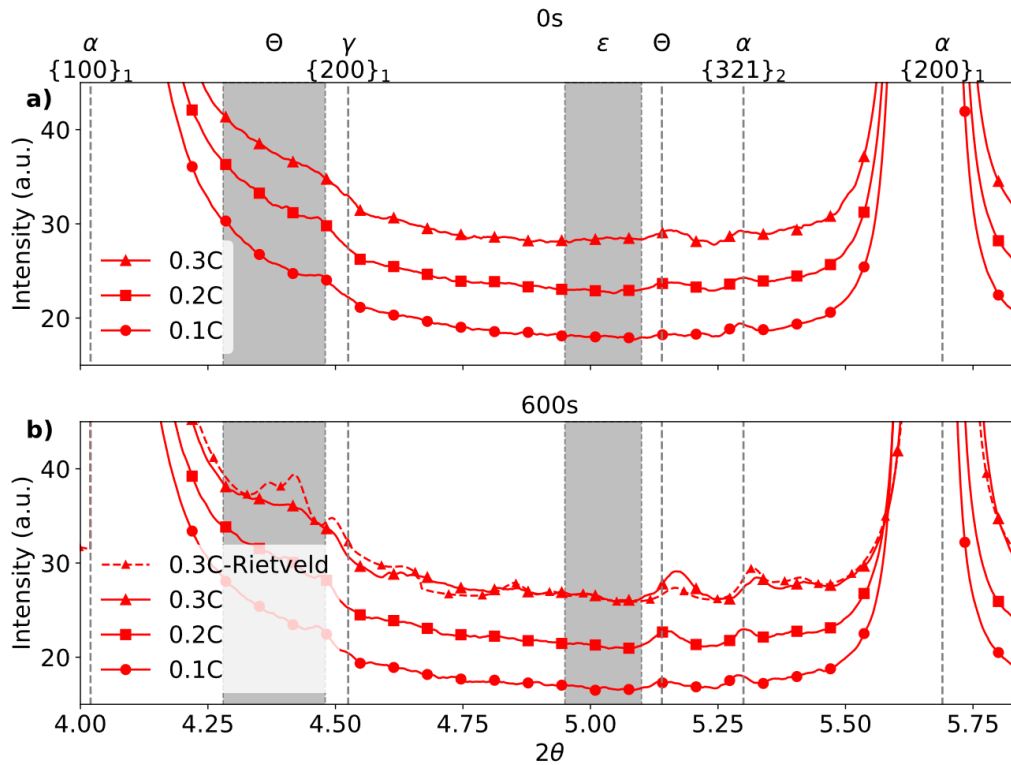


Figure 57: Diffraction patterns of the 0.1C, 0.2C and 0.3C steel at the start of the 400 °C holding in a) and at the end of the 600s holding in b).

The cementite fraction in the 0.3C steel was estimated by performing the Rietveld refinement in a manual mode, i.e. by changing the phase parameters until observing a reasonable agreement between the calculated diffraction pattern and the experimental one. Two main difficulties have to be mentioned, the first one is the low intensity of the cementite diffraction peaks and the second one is that not all the expected cementite diffraction peaks are present in the experimental diffraction patterns. One of the obtained modeled diffraction patterns is presented in Figure 57.b for the 0.3C steel. The results of this analysis are shown in Figure 58. For each time at which the cementite fraction was estimated two points are plotted, corresponding to the lower and to the higher fraction at which the calculated diffraction pattern was considered similar to the experimental one.

The cementite fraction at 0s of the isothermal holding is around 1 wt.% and a fast increase is observed between 25s and 50s up to 2 wt.%. Then, the fraction continues to increase but at a slower rate. At the end of the holding the estimated fraction is between 3 and 3.5 wt.% which is lower than the fraction that would be expected if all the carbon of the steel was used to form cementite (4.7 wt.%). Although the usual error estimated in the Rietveld refinement is 1 wt.%, it can be considered much higher in the present case as the refinement was performed manually and not all the expected diffracting peaks are observed as previously mentioned. If the difference between the measured cementite fraction and the one expected is not caused by the characterization uncertainty, the two main hypotheses can be postulated: some carbon still remains in the matrix or that not all the carbides are diffracting and, thus, the measured fraction only corresponds to the diffracting fraction. This latter hypothesis is supported by the fact that, for example, the precipitates which were observable by TEM at the 0.2C_GQ condition were not

detected by HEXRD. The detection of carbides by 3DAPT and TEM and not by HEXRD has been also reported by [219].

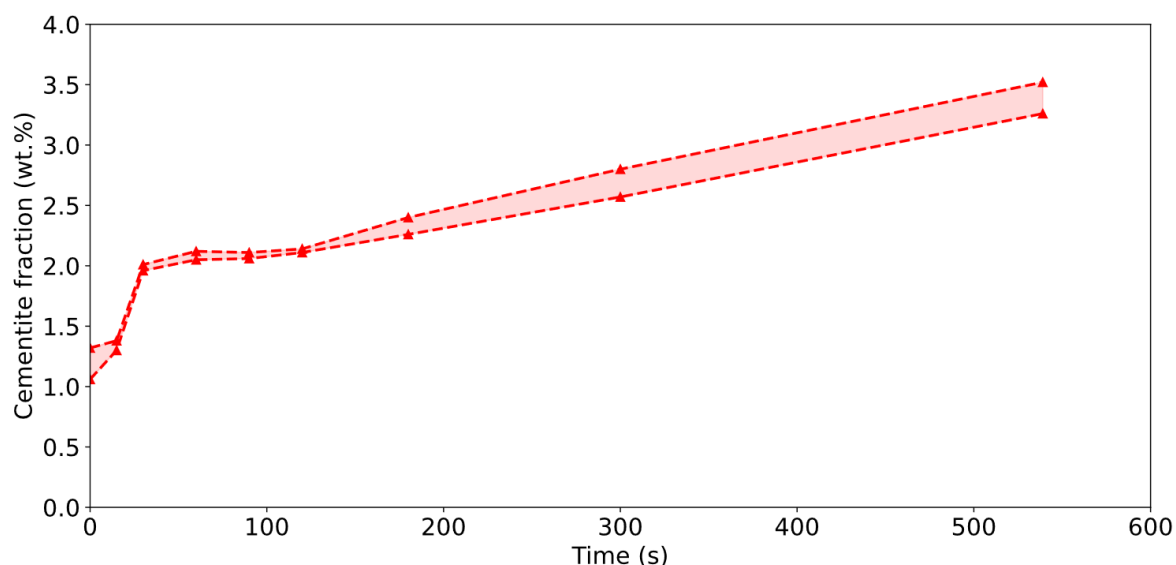


Figure 58: Cementite weight fraction as function of the holding time during the 400 °C holding of a 0.3C_WQ sample.

An indirect and complementary analysis of the precipitation could be performed by following the evolution of the tetragonality ratio during the tempering. However, the final c/a ratio determined by the Rietveld refinement at the end of the 400 °C holding is too high: it would indicate that more than 50 % of the carbon content in solid solution, which is unrealistic. The validity of the tetragonality determined by the Rietveld refinement is questioned in Appendix A.

III.2.B.3 Cementite carbide size evolutions

To determine the size of the cementite carbides, a statistical study by TEM has been performed at each condition (size distributions and mean values). As more than 300 carbides were measured at each studied condition (with ellipsoidal shapes as explained in Section I.5.B), any mixture of carbide populations (epsilon, cementite) must be avoided. It is for that reason that the cementite carbide size analysis was performed only in tempering conditions in which epsilon carbides were not present: different holding times during the tempering at 400 °C and at the end of the isotherm at 300 °C. As an example, a set of bright field TEM micrographs showing evolution of the cementite carbides during the holding at 400 °C of the 0.3C steel (0.3C_WQ_T400C) is presented in Figure 59. One micrograph of the 0.3C_WQ_T300C is also presented.

In the following, the analysis of carbide size is presented in the 0.3C_WQ_T400C300s condition by showing the distributions as well as the obtained mean values for this particular treatment. This will be followed by the presentation of the evolution of the mean values for the other tempering conditions (influence of time, temperature and carbon content of the steel).

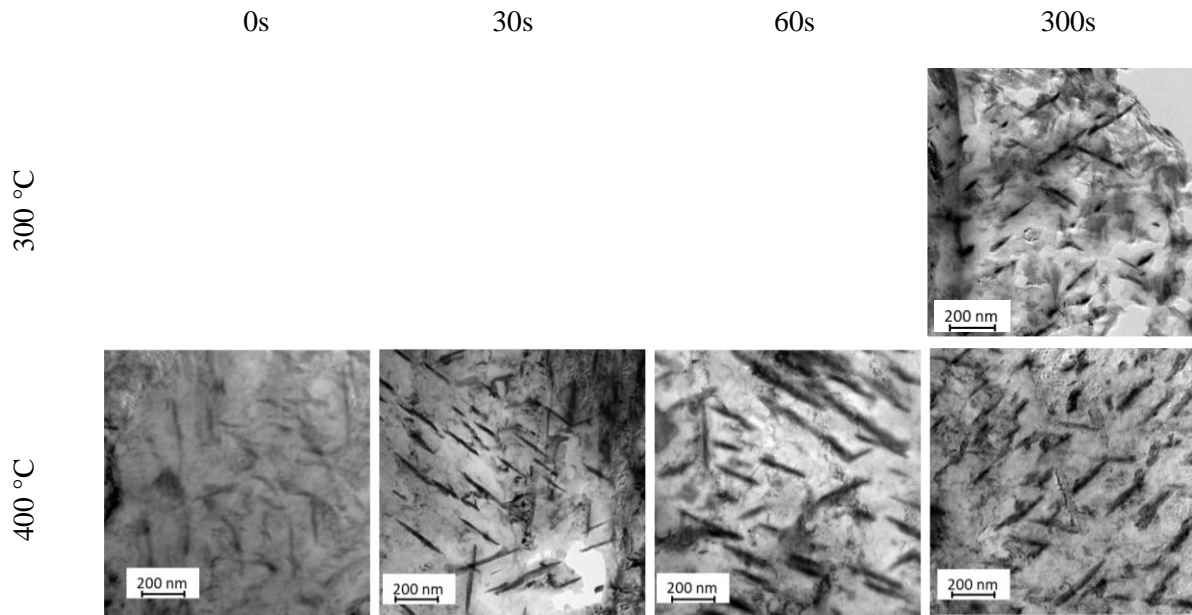


Figure 59: Bright field TEM micrographs showing the evolution of the cementite carbides in the 0.3C steel during holding at 400 °C at different holding times, 0, 30, 60 and 300 s from left to right. One bright field TEM micrograph of the 0.3C steel tempered for 300s at 300 °C is also presented.

Figure 60 presents the distribution of the minor and major radii. Both distributions have a log-normal shape and the dispersion (defined by the parameter ϖ in the Equation 11 in Chapter II) is higher for the major radius (0.54 ± 0.03) than for the minor radius (0.44 ± 0.03). The mean values obtained by modeling them with log-normal functions are 12.4 nm for the minor radius (with 68% interval from 6.9 to 17.8) and 51.9 nm for the major axis (with 68% interval from 27.8 to 75.8), the equivalent radius (r_{eq}) calculated from both mean values is 19.9 nm.

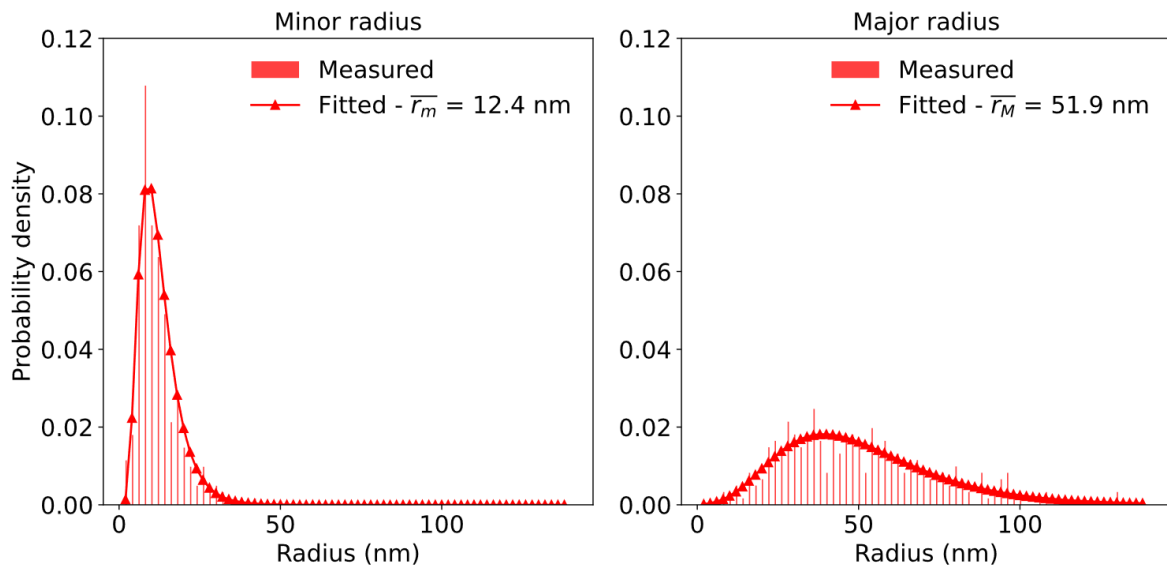


Figure 60: a) Distribution of a) the minor radius, b) the major radius of ellipsoidal cementite carbides in the 0.3C_WQ_T400C300s steel.

Another analysis consist in calculating the equivalent sphere radius for each precipitate and to fit the obtain distribution. The result is shown in Figure 61. The distribution of equivalent radii also follows a log-normal distribution, with a mean value equal to 19.4 nm and σ equal to 0.41 ± 0.01 , giving a 68% prediction interval between 11.4 and 27.1 nm. The dispersion parameter is thus lower than the ones obtained for the minor and major radius. The distribution shape is similar to the one presented by Gaudez et al. [39] and by [190,220,221].

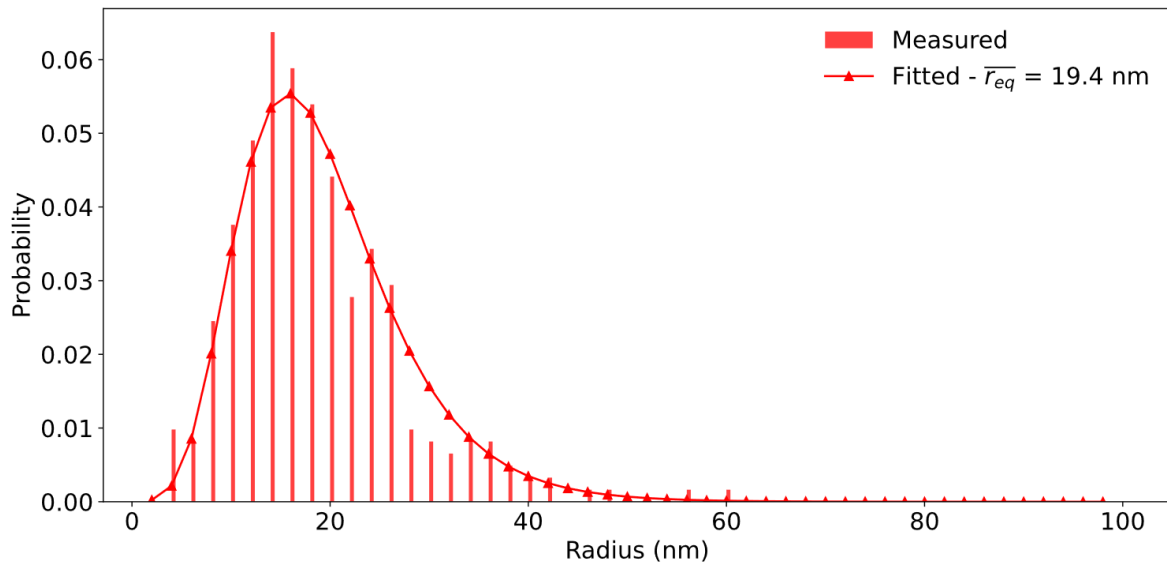


Figure 61: Distribution of the equivalent radius obtained by measuring the carbides in the 0.3C_WQ_T400C300s steel.

The mean equivalent radius obtained by the fit of the distribution of the equivalent radius is equal to the one calculated previously based on the means of the minor and major radius. Wu et al. [191] reported the average cementite radius obtained by a tempering at 400 °C and 300s holding time for a 0.1 wt.% C steel and a 0.4 wt.% C steel being ca. 16 nm and 24 nm respectively. The mean equivalent radius obtained in the present work is between both reported values giving confidence to the proposed method.

The same analysis was performed for tempering at 300 °C and 400 °C for different times and for 0.2C and 0.3C steels. The evolutions of the minor and major radius are presented in Figure 62.

The effect of the tempering temperature can be discussed by considering the results for the 0.2C steel as typical example. At 400 °C, the minor and the major radii increase with the holding time while at 300 °C both radii remain constant or even present a small decrease. After 300s holding, both minor and major radii are smaller at 300 °C than at 400 °C, but the difference is in the confidence interval (accounting 68% of the size distribution).

Considering the effect of the carbon content (0.2C vs. 0.3C steels), the minor radius is higher in the 0.3C steel than the ones determined in the 0.2C steel at both holding temperature and whatever the holding time. Regarding the major radius, it increases in the 0.2C steel during the holding at 400 °C, whereas it is nearly constant in the 0.3C steel (although it might be overestimated at holding time 0s). The final major radius is similar in the 0.2C and in the 0.3C steel at the end of both isothermal holdings (300 °C

and 400 °C). For all the mentioned comparisons, the differences are within the confidence interval, indicated by errorbars. The actual error of each measurement and their average is much lower.

Hence, for both steel compositions and both holding temperatures, the final major axis of the cementite carbides has a similar size, whereas the minor axis for the 0.2C steel is lower than for the 0.3C steel.

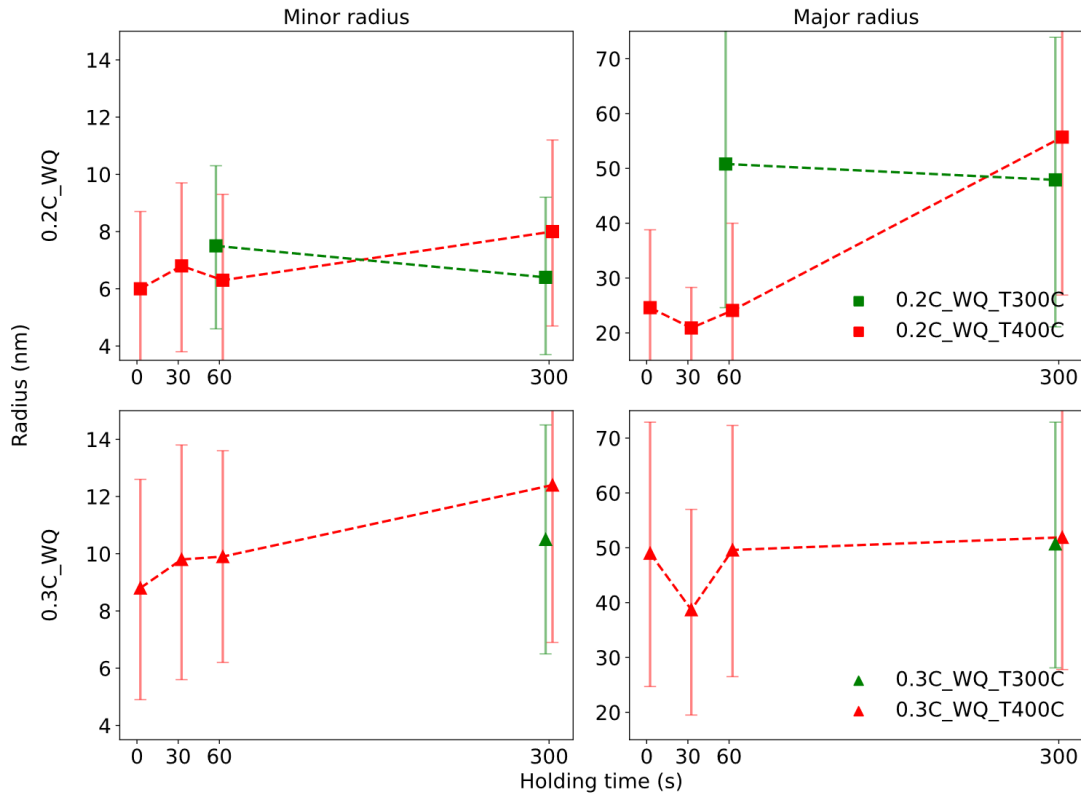


Figure 62: Evolution of the minor radius (first column) and major radius (second columns) as function of the holding time in tempering heat treatments applied to the 0.2C_WQ condition (first row) and to the 0.3C_WQ condition (second row). The points have been slightly displaced in the x axis to avoid juxtapositions.

As mentioned above, the evolution of the cementite mass fraction was estimated by HEXRD in the 0.3C steel and during the holding at 400 °C. It increased from ca. 1 wt. to 3 wt.% between 0s and 300s holding (cf. Figure 58). However, as shown above, the minor and major axes present small increasing variation for this treatment. Thus, the increase of the cementite mass fraction observed by HEXRD may be interpreted as an increase of the density of cementite carbides or by the increase of the thickness (evolution of the minor radius in the errorbar). If one considers that the point at 0s is the singular point in the curve (instead of the one at 30s), this means that the major axis clearly increases during holding at 400 °C in the 0.3C steel.

The evolution of the equivalent radius and aspect ratio are presented in Figure 63.

The equivalent radius is calculated as prolate carbides, the shape most frequently observable in the TEM images, which is also reported in low tempering conditions in literature [169,190,222]. As expected, these evolutions are in agreement with those obtained for the minor and major radii. The equivalent radius increases in the 0.2C steel during the holding at 400 °C, but it is nearly constant at 300 °C. For the 0.3C steel only a small increase is observed at 400 °C (which would be higher if the 0s holding was

considered as a singular point). At the end of the holdings at both temperatures, the equivalent radius is larger in the 0.3C steel than in the 0.2C steel, as in [191]. As seen above, this is due to the larger size of the minor axis (i.e. the cementite carbides are thicker but their length is similar).

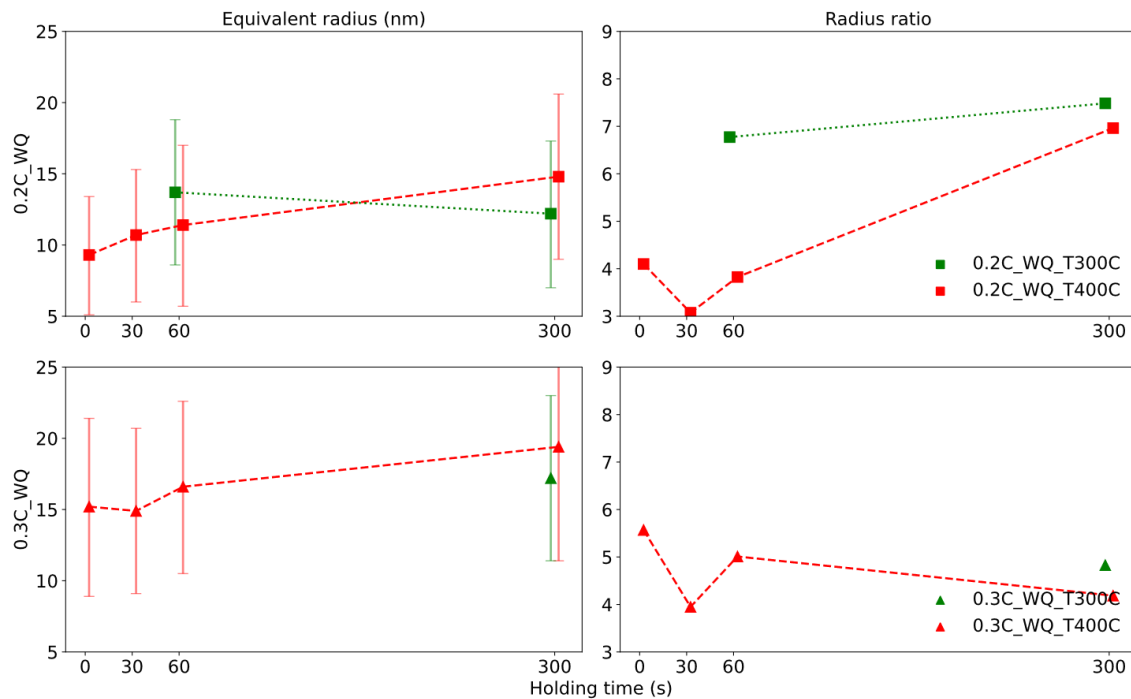


Figure 63: Evolutions of the cementite carbides equivalent radius and aspect ratio during the isothermal holdings at 300 °C and 400 °C in the 0.2C and 0.3C steels.

Regarding the tempering temperature effect, it can be observed that for both alloys the equivalent radius is higher at 400 °C than at 300 °C. The difference is clearly in the confidence interval, and higher than the actual error of the measurements.

The aspect ratio shows two different behaviors in the 0.2C and 0.3C steels. In the 0.2C steel, it clearly increases at 400 °C (and seems to have the same behavior at 300 °C), which suggest that cementite carbides are growing. In the 0.3C steel, the aspect ratio is lower than in the 0.2C steel, and it remains nearly constant.

Main outcomes of the cementite carbides sizes measurements are the following. As expected, the carbides are larger in the 0.3C steel, with higher carbon content than the 0.2C steel. They might be larger (more exactly thicker) after holding for 300s at 400 °C than at 300 °C, but the difference is inside the uncertainty of the measurements (defined as the standard deviation of the size distributions). Except for the 0.2C steel held at 400 °C, the length of the carbides is nearly constant (a small increase is observed also at 400 °C of the 0.3C if the 0s holding is considered as a singular point). This means that the carbides would have ready reached their final length at the end of the heating rate and that they mostly underwent thickening afterwards, during the isothermal hold.

III.2.C Summary of the microstructural characterization of tempering

Here is a summary of the microstructural characterizations by APT, HEXRD and TEM. The segregation of carbon of the 0.2C steel has been investigated by 3DAPT at the two quenched state, gas quenched (GQ) and water quenched (WQ) (after two months aging at room temperature), showing the segregation of carbon around the dislocations in both samples. In both conditions, the segregated zones have the same carbon concentration and the same size (radius of “influence” around the dislocations) despite the cooling rate. This may be ascribed to the segregation occurring at room temperature. The carbon concentration measured is in accordance with the literature (between 7 and 10 at.% [41,151,213]) and the radius of influence has been established to 10 times the Burgers vector (2.5 nm). The dislocation density is larger in the WQ condition than in the GQ state, which is in agreement with the HEXRD measurements. Some globular carbon enriched volumes were also observed, in larger number in the GQ state. These are probably due to carbon clusters [162] even if the presence of transition carbide nuclei cannot be ruled out [150]. In the GQ sample, an austenitic film enriched in carbon was also put in evidence by 3DAPT, showing that the carbon has time to partition during GQ.

The sequence of precipitation was partially established by combining in situ HEXRD experiments and TEM observations of the microstructure. At first, the initial state, corresponding to austenitization followed by cooling at different rates (WQ, -10, -50 and -100 °C/s) was characterized. No carbides could be put into evidence by HEXRD (whereas retained austenite is present) whatever the cooling rate. But an intense precipitation of (probably) transition carbides could be revealed by TEM after GQ (ca. -20 °C/s). No carbides were observed in the WQ state. The non-detection of the GQ carbides by HEXRD is ascribed to their small size and the presence of defects.

The WQ condition was chosen as the initial state to study the precipitation sequence, in order to enhance carbides precipitation during the tempering. Table 11 summarizes the detected carbides for the different alloys, the range of temperature in which they were observed and, if possible, an estimation of their fraction during the heating. As mentioned, the non-detection of carbides by HEXRD does not mean that these carbides are absent as they may be too small to be detected.

At the end of the holding at 400 °C, all the studied steels present evidence of the presence of cementite. During the holding at 300 °C, cementite is observed to form in the 0.2C and 0.3C steels. For all the steels, no carbides were detected during the holding at 200 °C.

The non-detection of transition carbides in the 0.1C steel is in accordance with the literature in which it is commonly stated that for nominal compositions lower than 0.2 wt.% no transition carbides precipitation occurs [20,103]. Indeed, the carbon would be segregated at defects, especially dislocations. Transition carbides are detected in the 0.2C and 0.3C steels. The temperature range in which the transition carbides were detected is higher than the usual range reported in literature (100-250 °C). This an outcome of the use of HEXRD. Indeed, in [39] the presence of epsilon up to high temperatures (500 °C) was also put in evidence. In fact, the transition carbides disappear only when the cementite precipitation occurs.

The formation of cementite was established for the three investigated steel compositions. It starts to form upon heating, at least in the 0.2C and 0.3C steels. The cementite fraction could be determined by the Rietveld refinement only in the latter steel. It was lower than the value expected by thermodynamic calculations at the end of the isothermal hold at 400 °C. The difference may be due to the uncertainty on the measured value (higher than 1 wt.%) and, once again, due to the fact that small precipitates are not detectable by HEXRD [219].

The evolutions of cementite carbides sizes were measured from TEM micrographs in the 0.2C and 0.3C steels, during isothermal hold at 300 °C and 400 °C. In all cases, the carbides show an elongated shape with an aspect ratio higher than 4. Except in the one case (0.2C steel, 400 °C hold), the length of the carbides is nearly constant, whereas the carbides thicken during the isothermal holds. The precipitates have higher equivalent radius in 0.3C than in 0.2C steel, and it may be slightly smaller at 300 °C than at 400 °C.

Put together, these results conform to the usual sequence of precipitation: segregation followed by transition carbides and the cementite. Newest outcome regards the characterization of the segregation at the initial state. Its impact on the sequence is significant, as the transition carbide are probably suppressed in the 0.1C steel. As mentioned before, we exploited the HEXRD method at its limits, in view of the low carbon content of the steels. Nevertheless, an

Table 11: Summary of the detected carbides, their temperature range and fraction for the three studied steels determined during tempering by in situ HEXRD experiments.

		0.1C	0.2C	0.3C
Epsilon	Temperature (°C)	-	300-350 (?)	300-375
	Fraction (wt.%)	-	-	-
Cementite	Temperature (°C)	400	330-400	350-400
	Fraction(wt.%) after holding at 400 °C for 600s	< 2	ca. 3	ca. 3.4

interesting outcome is the persistence of the transition carbides up to high temperatures. The trends regarding the sequence are those expected and, combined with TEM data, this provides a set of data that will be used in the calibration and validation of the models detailed in the following.

III.3 Modeling of tempering

As shown in the literature survey (Section III.1.A.1) and in the experimental study based on 3DAPT (III.2.A), the phenomenon of carbon segregation to dislocations makes the composition of the matrix in carbon highly heterogeneous. The experimental study on the precipitation sequence showed that the segregation of carbon inhibits the formation of transition carbides in the steel with the lowest carbon content. Our purpose in this part is to investigate by simulations the consequences of the segregation

phenomenon on the sequence of precipitation. To this aim, we will combine a model that predicts the kinetics of segregation to a model for the precipitation of transition and cementite carbides. In Section III.3.A, the model for segregation of Svoboda et al. [153] is presented and its parameters are selected on the basis of our experimental results and the literature. In Section III.3.B, this segregation model is coupled with an in-house precipitation model previously developed [39,154] and adapted for this purpose. Its predictions are also confronted to the experimental results (phase fractions, temperatures of formation and size of cementite), highlighting the impact of segregation on the precipitation sequence.

III.3.A Carbon segregation model

Different modeling approaches have been applied to understand the complex interactions between carbon atoms and the stress/strain fields around dislocation and the resulting segregation; from local ab-initio [196], embedded atom methods [223] and Monte Carlo [213] simulations to mean field calculations based on the thermodynamic extremal principle [153]. In the present work, the method developed by Svoboda et al. [153] has been chosen for its low number of parameters, low computational cost, but keeping a sound physical basis. Also, it is mean-field approach, which is well adapted to be coupled to the precipitation model which will be used in Section III.3.B. In the following, the segregation model is re-introduced briefly and its parameters are calibrated. The model is then used to simulate the segregation kinetics for the experimental conditions studied in this work.

III.3.A.1 Carbon segregation model implementation

The method proposed by Svoboda et al. [153] to predict the kinetics of segregation is based on the thermodynamic extremal principle [224]. The total Gibbs energy of the system is calculated as a function of the amount of carbon segregated at dislocations and of the carbon concentration remaining in the matrix, far from the defects. This calculation takes account of the trapping energy for carbon at dislocations (ΔE), which makes decrease the energy of the system, and which represents the driving force for the carbon diffusion from the matrix to the dislocations. The dissipation rate associated with the carbon diffusion in the matrix towards the dislocations is assumed to be equal to the rate of decrease of the total Gibbs energy of the system matrix + dislocations. The model is not fully re-introduced here, but the main equations and parameters are presented.

The mass balance of the system and the resulting conservation law are written as:

$$f_{dislo}x_{dislo} + (1 - f_{dislo})x_{matrix} = \bar{x} \quad \text{Equation 24}$$

$$f_{dislo}\dot{x}_{dislo} = -(1 - f_{dislo})\dot{x}_{matrix} \quad \text{Equation 25}$$

where f_{dislo} denotes the volume fraction of traps for the carbon. The latter are schematized as cylinders of a given radius around the dislocations, inside which the carbon segregates with a local uniform concentration. x_{dislo} is the carbon concentration in the traps, x_{matrix} the carbon concentration in the depleted matrix and \bar{x} is the overall carbon concentration in the system matrix + dislocations. The dots denote time derivatives.

The volume fraction of the traps (f_{dislo}) is expressed as:

$$f_{dislo} = \pi r_{disl}^2 \rho \quad \text{Equation 26}$$

The whole system (matrix + dislocations) is represented by a single dislocation surrounded by a cylinder which contains the matrix. The radius of this cylinder, r_{matrix} , is related to the dislocation density by the equation:

$$\pi r_{matrix}^2 = \frac{1}{\rho} \Rightarrow r_{matrix} = \frac{1}{\sqrt{\pi \rho}} \quad \text{Equation 27}$$

with ρ the dislocation density.

The total Gibbs energy of the system is written as:

$$G = G_0 + \frac{V}{H} \left(J_1 + J_2 - \frac{x_{dislo} \Delta E(x_{matrix}, x_{dislo})}{R_g T} \right) \quad \text{Equation 28}$$

$$J_1 = (1 - f_{dislo}) \left(R_g T (x_{matrix} \ln x_{matrix} + (1 - x_{matrix}) \ln (1 - x_{matrix})) \right)$$

$$J_2 = (f_{dislo}) \left(R_g T (x_{dislo} \ln x_{dislo} + (1 - x_{dislo}) \ln (1 - x_{dislo})) \right)$$

with G_0 being the Gibbs energy independent of the carbon distribution in the system, H is the molar volume, V the volume of the system, R_g the gas constant and T the absolute temperature. The molar trapping energy (ΔE) can be considered independent of the temperature, but it can depend on x_{matrix} and x_{dislo} due to carbon-carbon interactions [153]. Both the matrix and the segregation zones are assumed to be ideal solutions.

By calculating the rate of total dissipation by carbon diffusion in the system (thanks to the simplified geometrical representation mentioned above) and by deriving the total Gibbs energy, one obtains the rate of increase of the carbon concentration in the Cottrell atmospheres [153]. If the dependence of the trapping energy with the carbon concentration either in the matrix or in the dislocation is neglected, the rate of increase of the carbon concentration in the Cottrell atmospheres can be calculated as:

$$\dot{x}_{dislo} = \frac{2D}{r_{disl}^2 \left(\ln \left(\frac{r_{matrix}}{r_{disl}} \right) - \frac{3}{4} \right)} x_{matrix} \left(\ln \frac{x_{matrix}(1 - x_{dislo})}{x_{dislo}(1 - x_{matrix})} + \frac{\Delta E}{R_g T} \right) \quad \text{Equation 29}$$

with D being the diffusion coefficient of carbon in matrix.

In the previous equation, some parameters come from our experiments: the dislocation density (which determines the parameter r_{matrix}) and the “dislocation radius”, r_{disl} . The former was obtained from HEXRD experiments and the modified Williamson-Hall method (cf. Chapter II). The latter is set to $10 \times b$, b being the Burgers vector (2.5×10^{-10} m), on the basis of 3DAPT results presented above.

The carbon diffusion coefficient as a function of the temperature is calculated with D_0 set equal to 3.56×10^{-6} m²/s and the activation energy to 90.7 kJ/mol. These values were obtained from the thermodynamic and mobility databases TCFE9 and MOBFE2 from ThermoCalc for the ferrite with the composition of the 0.2C steel. Let us mention that other values for the diffusion coefficient can be found in the literature for the diffusion of carbon in ferrite [192,225] or in martensite. For the latter, carbon diffusivity is lower than in ferrite because of the tetragonal structure [18,226,227]. But the HEXRD study showed that the tetragonality is low in the investigated steels, because of their low carbon content. Moreover, if the tetragonality is accounted for, one should take account of its decrease upon tempering, as the matrix will be depleted in carbon. This is why the carbon diffusion coefficient in ferrite was chosen for the simulations. The value given by Thermocalc’s databases for bcc ferrite ranges between those reported by Tapasa et al. [225] and Ghosh and Olson [192].

The parameter related to the trapping energy (ΔE) is a determining factor for the kinetics of carbon segregation at dislocations and for the concentration inside the Cottrell atmospheres. Different values of ΔE have been obtained by simulations and/or experiments in the literature. Clouet et al. presented a summary of the reported values, which depend on the type of dislocation considered (edge/screw), along with the methods used for the estimations [223]. ΔE ranges between 0.41 and 0.78 eV.

As the segregation model presented above considers a unique value of trapping energy for all the dislocation affected volume (i.e. without dependence on the distance between the carbon atom and the dislocation, inside the denoted r_{disl}), an average value of ΔE has to be estimated.

In Figure 64, ΔE is plotted as function of the distance from the dislocation core according to [228].

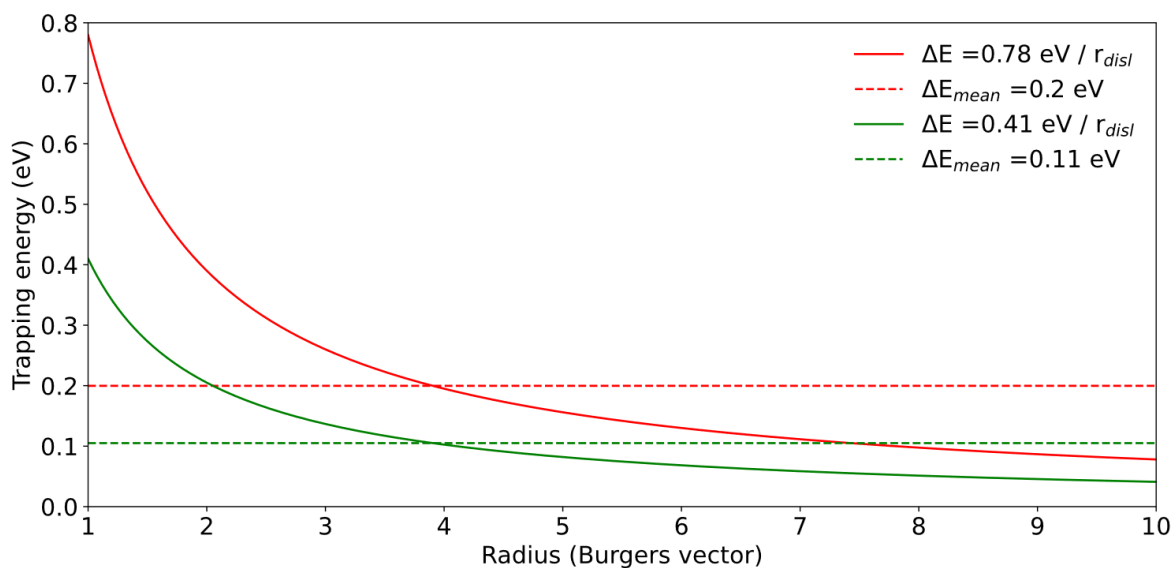


Figure 64: Trapping energy as a function of the distance from the dislocation core, according to the formula proposed by Kalish and Cohen [228] as well as the average calculated over a distance of 10 times the Burgers vector, considering the highest and lowest trapping energies presented in [223].

The formula proposed by Kalish and Cohen in [228], considers that ΔE decreases hyperbolically with the distance from the dislocation radius. Even if from the 3DAPT proxigram it is not possible to obtain the ΔE value and its dependence with the radius, a fast decrease has been observed justifying the use of the formulation proposed by Kalish and Cohen.

Two values of ΔE at the dislocation core (at radius $1b$) have been assumed: 0.78 eV or 0.41 eV, i.e. the highest and the lowest values reported in [223]. This allows to calculate an average value (represented by the dashed lines), of 0.20 eV and 0.11 eV respectively. The average is calculated over a distance of $10b$, the radius of influence of the dislocations (r_{disl}) which was estimated on the basis of our 3DAPT observations. These two values give the range inside which the average trapping energy ΔE should be selected.

Finally, the criterion to select the average value of ΔE is based on our 3DAPT experiments: the concentration of carbon segregated at the dislocations should be in agreement with the measurements. In order to select the appropriate value, a precipitation model parametrization study was performed. The segregation kinetics was calculated for different values of ΔE . The dislocation radius, r_{disl} , was set to $10 \times 2.5 \times 10^{-10}$ m, the dislocation density to 3.5×10^{15} $1/\text{m}^2$ and the simulations were performed at temperature 200 °C, taken as an example.

After some time, the carbon concentrations in the matrix (x_{matrix}) and at the dislocations (x_{dislo}) stabilize. The evolution of both concentrations varying average value of ΔE as function of time are shown in Figure 65. The kinetics of the carbon segregation are faster at higher ΔE and the stagnation values are higher as well.

Figure 66 shows both final concentrations as function of ΔE . Hereafter, these final concentrations will be termed as “equilibrium” concentration as these correspond to the minimum of the Gibbs energy of the system (matrix + dislocations).

x_{dislo} increases as the trapping energy increases while x_{matrix} decreases, as expected. For $\Delta E = 0.11$ eV, x_{dislo} is equal to 10.34 at.% and x_{matrix} equal to 0.76 at.%, while for $\Delta E = 0.2$ eV, $x_{\text{dislo}} = 18.58$ at.% and $x_{\text{matrix}} = 0.17$ at.%.

When increasing the trapping energy, x_{dislo} eventually stabilizes around 20 at.%. According to our 3DAPT measurements (III.2.A Carbon segregation) the carbon concentration in the Cottrell atmospheres ranges between 7.6 and 8.4 at.%, after 2 months tempering at ambient temperature. According to the literature, the dislocation carbon content of the Cottrell atmospheres is expected to be around 8 at.% [151,220] and even 10 at.% at 0 Kelvin [229]. On this basis, we have chosen the lower limit of the value range mentioned above for the average $\Delta E=0.11$ eV, which corresponds a maximum trapping energy of 0.41 eV at the dislocation core. Taking a higher value would lead to overestimate the amount of carbon which will segregate to dislocations.

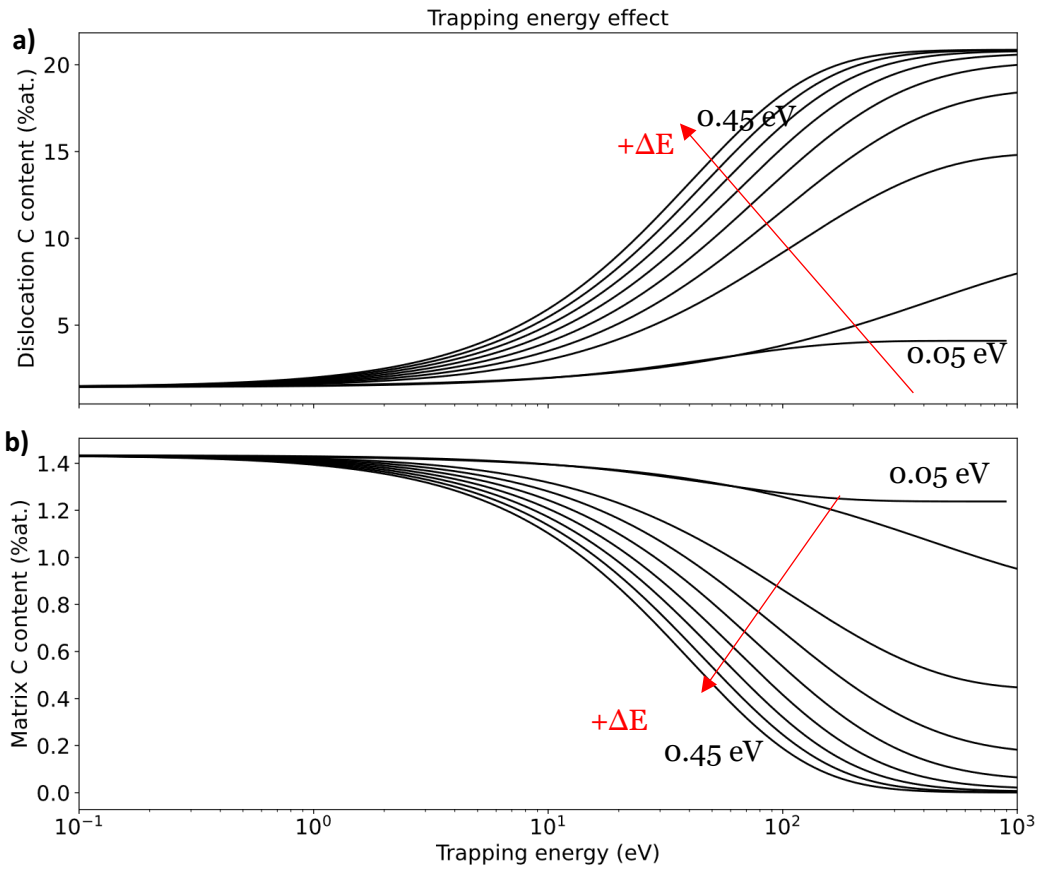


Figure 65: Carbon concentrations at the dislocations (x_{dislo}) (in a) and in the matrix (x_{matrix}) (in a) as function of the time during a holding at 200 °C varying the trapping energy (ΔE) at a 0.05 eV step.

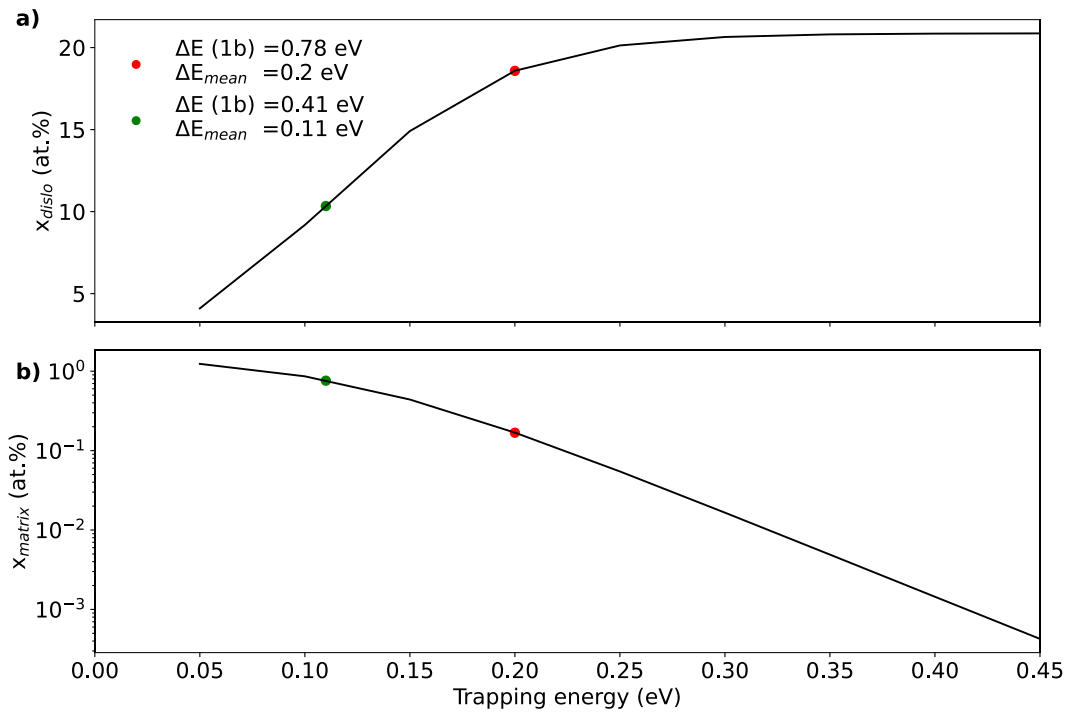


Figure 66: "Equilibrium" carbon concentration as function of the trapping energy at 200 °C in a) in the segregated dislocation atmosphere (x_{dislo}); b) the matrix (x_{matrix}). The green and red dots correspond to average trapping energies 0.11 and 0.20 eV.

As shown in Equation 27 and Equation 29, x_{dislo} and x_{matrix} also depend on the dislocation density. The effect of the dislocation density was thus investigated, as there is a large dispersion of this feature inside the martensitic microstructure (cf. Chapter II). As an example, the equilibrium values of x_{dislo} and x_{matrix} were calculated with the segregation model for the 0.3C steel with the average dislocation density at the water-quenched condition (3.5×10^{15} 1/m²) as well as with two times this value (7.0×10^{15} 1/m²). x_{dislo} and x_{matrix} are plotted in Figure 67. In a first time, it can be observed that x_{dislo} decreases with the temperature. This is expected, as the efficiency of the dislocations as traps for carbon decreases as the temperature increases. Indeed, as seen with Equation 10, the concentrations x_{dislo} and x_{matrix} converge, after sufficient time, to values related by the relationship below [153] (similar to McLean equation [230]):

$$\frac{x_{matrix}}{1 - x_{matrix}} = \frac{x_{dislo}}{1 - x_{dislo}} \times \exp\left(-\frac{\Delta E}{R_g T}\right) \quad \text{Equation 30}$$

A higher dislocation density leads to a lower value of x_{matrix} , as more carbon traps are present (this can be deduced from Equation 24 and Equation 30). The concentration of carbon inside the segregated atmospheres (x_{dislo}) decreases also, as the carbon is distributed among more dislocations. These trends are reproduced by the simulations.

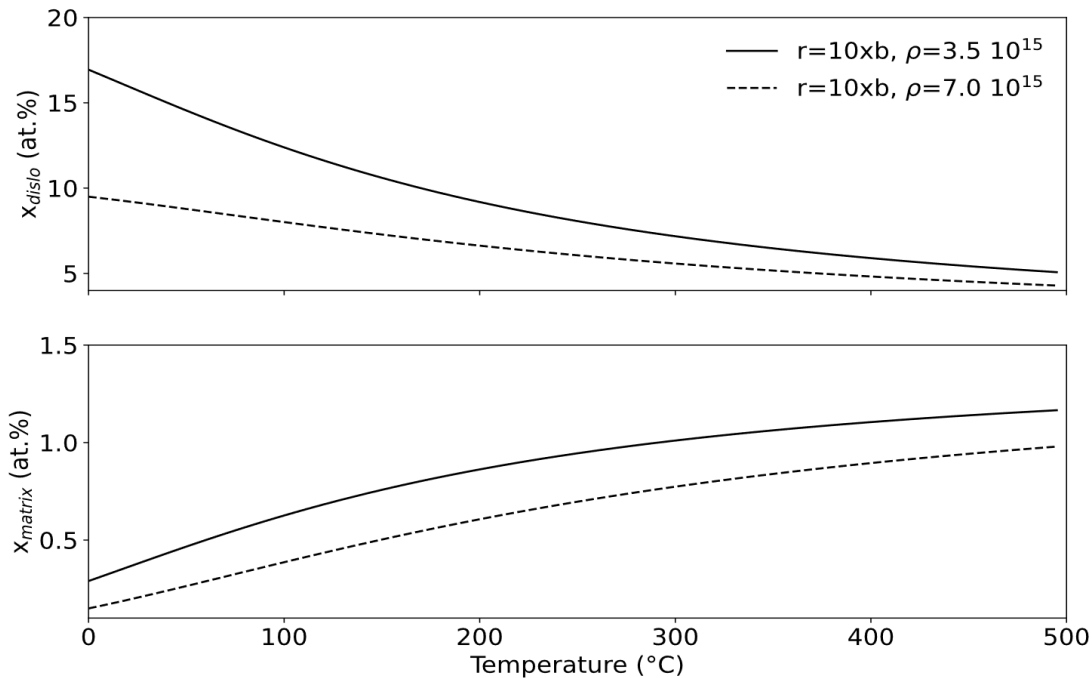


Figure 67: x_{dislo} (a) and x_{matrix} (b) at equilibrium as a function of the temperature for the 0.3C steel with low (continuous line) and high (dashed line) dislocation density.

Finally, it remains to discuss the effect of the martensite composition (with thus different initial dislocation densities). The equilibrium carbon concentration in the matrix (x_{matrix}) was calculated for the three studied steels (0.1C: 0.1 wt.% C and $\rho = 1.5 \times 10^{15}$ 1/m², 0.2C: 0.21 wt.%C and $\rho = 2.5 \times 10^{15}$ 1/m² and 0.3C: 0.31 wt.%C and $\rho = 3.5 \times 10^{15}$ 1/m²). Figure 68 shows the results of segregation calculations as a function of the temperature.

The carbon concentration in the matrix increases with the temperature for the three steels as the trapping efficiency becomes lower, as mentioned above. Even if the dislocation density is higher when increasing the carbon content of the steel (which tends to decrease x_{dislo} and x_{matrix}), the carbon concentration in the matrix increases with the carbon content of the alloy at a given temperature. Hence, the effect of the nominal carbon content is higher than the pinning effect of the dislocation density

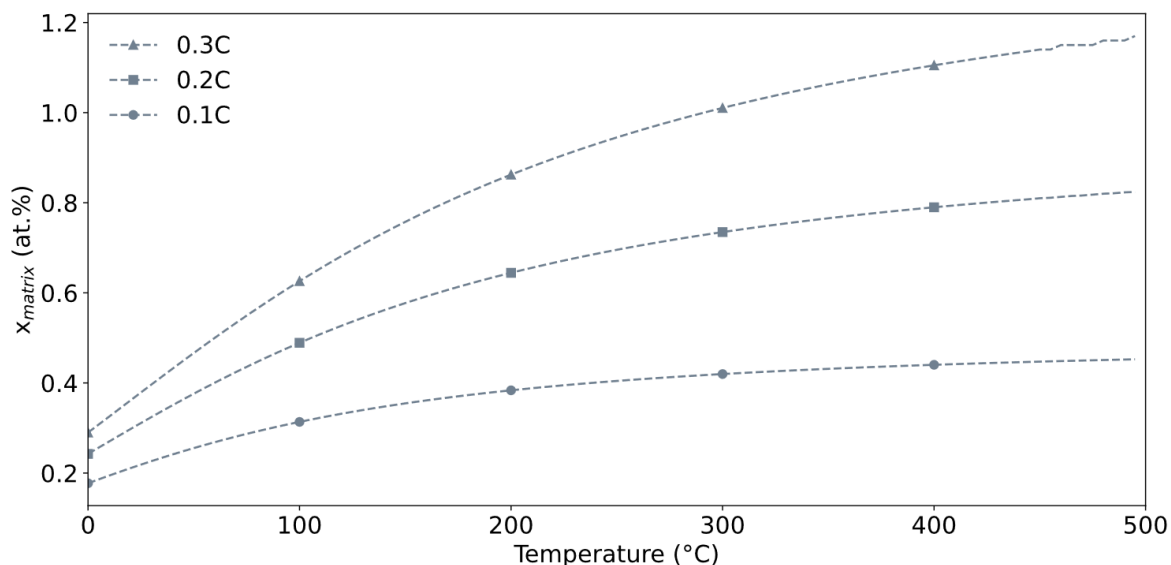


Figure 68: Equilibrium carbon concentration as function of the temperature for the three studied steels, by taking account of the steel carbon content and dislocation density.

III.3.A.2 Results of the segregation model

The segregation model is used here to study the segregation kinetics in the 0.2C steel, during either water quench (WQ) or gas quench (GQ), followed by aging for 2 months at room temperature (which were the conditions characterized by APT). The calculated concentration of carbon segregated are compared with the experimental ones in order to validate the model and its parameters. For the calculations, the dislocation densities measured by HEXRD are used: $2.0 \times 10^{15} \text{ 1/m}^2$ for GQ and $2.5 \times 10^{15} \text{ 1/m}^2$ for WQ.

The simulations results corresponding to both conditions are plotted in Figure 69. Figure 69.a shows the evolutions of temperature, Figure 69.b shows x_{dislo} and Figure 69.c x_{matrix} . The simulations encompass the cooling and the aging at room temperature (25 °C). Both simulations start at 350 °C, which corresponds to ca. first 20 wt.% of martensite formed upon cooling. Hence, the simulations focus on the segregation phenomena that will occur in this part of the martensitic microstructure.

For both cooling rates, a fast segregation of carbon to the dislocations is predicted, in less than 10^{-2} s after the start of the simulations. The concentrations x_{dislo} and x_{matrix} reach the values fixed by the temperature at the start of the simulation (350 °C) and by the respective dislocation densities. This fast segregation kinetics at the start of the simulations is due to the fast diffusion of carbon at high temperatures and to the high driving force coming from the small difference between x_{dislo} and x_{matrix} .

In the GQ condition, a second regime is visible with further segregation at a moderate rate (between 300 and 75 °C). In the WQ condition, this second regime is also detectable at low temperature but less obvious. In both cases, this second regime is due to the decrease of the temperature, which increases the efficiency of the dislocations as traps for carbon (as shown by McLean equation). At the end of the quench treatments, the carbon concentration in the dislocation atmospheres (x_{dislo}) in the GQ condition is 9.55 at.% while after the WQ condition it is 6.96 at.%. This result of the simulations confirms that the segregation of carbon is significant during auto-tempering, even in the case of the water-quenched martensite.

The cooling rate has also a significant influence on the degree of tempering after the quench and before the aging at 25 °C. These simulation results are in good agreement with the observations just after the quench reported in the literature. Carbon segregation into matrix defects or spinodal decomposition [165] and even the formation of transition carbides [231] (which requires more carbon diffusion) have indeed been reported. Badinier found a clear effect of the cooling rate on the carbon segregation (with a relatively homogenous carbon distribution in the water-quench sample as by [87]) but in a higher carbon steel, which has a lower M_s temperature [74].

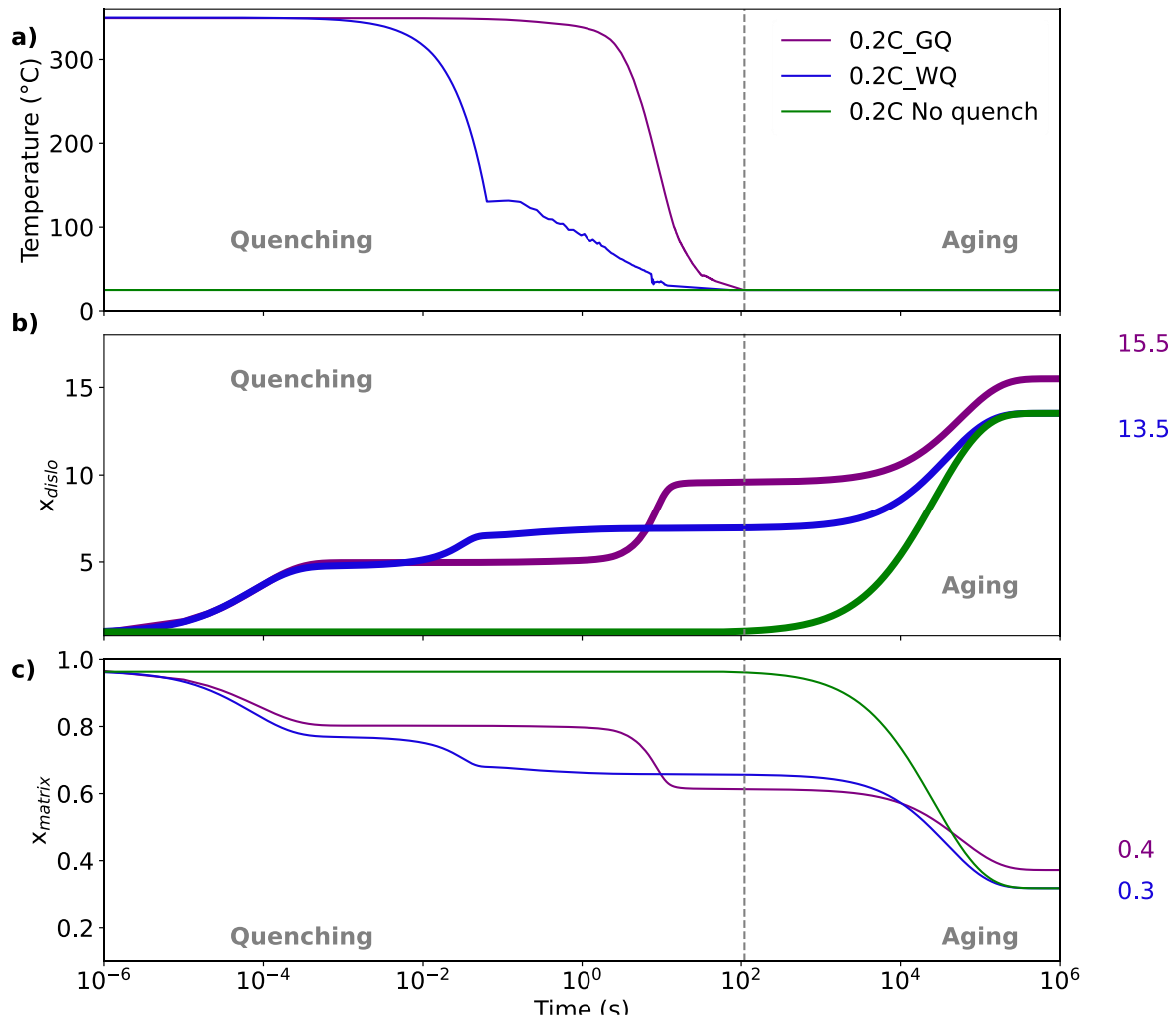


Figure 69: Evolution of the carbon concentration at the dislocations and in the matrix after quench by gas and in water and aged 2 months at room temperature. a) Temperature-time curves used for the simulations while b) presents the carbon concentration in the dislocations (x_{dislo}) and c) in the matrix (x_{matrix}).

The carbon segregation continues during the aging at room temperature but at a lower rate. After 2 months aging, x_{dislo} is equal to 15.5 at.% and 13.5 at.% in the GQ and WQ conditions respectively. The difference is due to the dislocation density. The comparison with the experimental results (7.6 and 8.4 at.% C concentration for the 0.2C_GQ and 0.2C_WQ respectively) and the literature values [41,151,213] shows that the model predicts an excess of segregation, although we used the lowest trapping energy reported in the review of [223], 0.41 eV. Let us mention that lower values (0.2-0.25 eV) of trapping energy were actually envisaged, e.g. in [232]. So one could consider to reduce the average value of ΔE in our simulations. In addition, in the present simulations, only the segregation into dislocation atmospheres was considered while segregation at planar defects such as lath boundaries could also be considered, as done by the simulation by Svoboda et al. [153].

The comparison of calculated x_{matrix} with 3DAPT measurements is more difficult, due to the lack of precision of these experiments regarding the matrix. The measured matrix carbon concentration in the 0.2C_GQ samples was measured equal to 1.1 at.% and in the 0.2C_WQ samples, it was equal to 0.3 at.%. This latter value is in good agreement with the simulation while the first one is too high (but it is even higher than the nominal composition of the steel).

To highlight the importance of segregation during cooling, the same simulation was done (with the dislocation density of WQ condition, $2.5 \times 10^{15} \text{ 1/m}^2$ and ΔE set to 0.1 eV), but considering only the aging for 2 months at 25 °C (green curves in Figure 69). One can see that several hours are necessary to reach the carbon concentrations which were obtained at the end of the cooling, when the cooling stage was accounted for. This simulation also shows that in usual experimental conditions (i.e. when one waits significant time between the quench and further experiments), the same degree of segregation will tend to be reached, whatever the quench method, provided that this time is longer than a few hours. All the simulations reach the same values of x_{dislo} and x_{matrix} , which correspond to the equilibrium at 25 °C, imposed by ΔE and the dislocation density.

III.3.B Precipitation model

The precipitation model used in the present study allows to predict the nucleation, growth and coarsening coupled kinetics of epsilon and cementite carbides by using a mean-field approach. It is based on previous versions developed at IJL [39,154]. Its main features are briefly recalled here, while the new developments done for this study will be presented in the next section. The nucleation kinetics is calculated with the classical nucleation theory. The growth and dissolution rates of the precipitates are limited by the diffusion of the carbon in the matrix. Coarsening is driven by the Gibbs Thomson effect. Both epsilon and cementite carbides are assumed to form without partition of the substitutional elements, due to the relatively low tempering temperature and short duration of the holding times. The absence of partition of substitutional elements for similar tempering treatments is well established in the literature (e.g. [191,192,215,233]). Other similar simulations work [234,235] also assumed that the carbides form under paraequilibrium conditions. The thermodynamic data necessary for the epsilon carbides are taken from [236]. These consist of a solubility limit as a function of temperature established in binary Fe-C system (but without accounting of the presence of other alloying elements).

As for the cementite, it is assumed to grow or to dissolve under paraequilibrium conditions at the interface cementite/ferrite. The thermodynamic data necessary for cementite (nucleation driving force, solubility limit) were calculated by using ThermoCalc software and the TCFE9 database.

The epsilon carbides are considered to nucleate homogeneously in the matrix [39,158,171] and as this type of carbide is coherent with the matrix, an elastic strain energy must be added to the nucleation barrier. The effect of the elastic strain energy on the thermodynamic equilibrium between the epsilon carbide and the matrix is also considered [237]. The epsilon/matrix interface energy influences the nucleation barrier. Due to the Gibbs-Thomson effect, it also changes the solubility limit, and thus the growth and dissolution rates.

The cementite is assumed to nucleate heterogeneously, on dislocations. As a consequence, the nucleation barrier is multiplied by a parameter (named ζ in the present work) lower than 1. The cementite/matrix interface energy affects the nucleation and the growth/dissolution like for the epsilon carbide. But, as the interface with the matrix is incoherent, there is no elastic strain energy.

Each precipitate is assumed to have a spherical shape. Its growth or dissolution is calculated with the steady-state Zener equation. The model calculates size distributions for the epsilon and the cementite carbides by using a Kampmann-Wagner scheme modified by Myhr and Grong [238,239]. The classes are discretized by size and the flux between each class is computed, following an Euler-like approach. This method allows to predict the precipitation sequence (epsilon followed by cementite) and also the successive stages of nucleation, growth and coarsening.

The model equations of latest model version are fully presented in [39]. The modifications introduced in the present study are detailed in the next section.

III.3.B.1 Precipitation model implementation

In the present study, several modifications were implemented in the previously introduced model. The first one is that the thermodynamic data related to cementite have been calculated using ThermoCalc and the TCFE9 database for the three studied alloys compositions. (The data related to the epsilon carbides still come from reference [236]).

The most significant modification is the introduction of the carbon segregation into dislocation atmospheres (with the model for carbon segregation previously presented). The importance of this modification is related to the low carbon content of the steels investigated in the present work (from 0.1 wt.%C to 0.3 wt.%C). As shown in a previous section, a significant proportion of the carbon segregates to dislocations and this hinders the formation of transition carbides. Conversely, in the previous versions of the model, the considered steels had a carbon content of 0.8 wt.% C [171] and 0.67 wt.% C [39]. Even if carbon segregation also occurs, the precipitation of transition carbides remains possible in those high-carbon steels.

The expected precipitation sequence considering the carbon segregation into dislocations is schematized in Figure 70. The initial state consists of ferrite and dislocations with homogeneous carbon concentration, both inside the matrix and near the defects. The next stage, corresponding to the zeroth stage of tempering, consists in the segregation of carbon from the matrix to the dislocations atmospheres. Next

stage consists in the epsilon carbides nucleation and growth inside the depleted matrix, if the carbon concentration remaining in the matrix after the segregation is high enough to promote the precipitation of epsilon carbides. Finally, the last stage consists in the nucleation, growth and coarsening of cementite. Any epsilon carbides previously formed before will dissolve concomitantly with the formation of cementite, by transfer of carbon from epsilon to cementite via the matrix. As mentioned, the cementite carbides nucleate heterogeneously on dislocations. The local higher carbon concentration due to the segregation is taken into account in the model, as will be elaborated below.

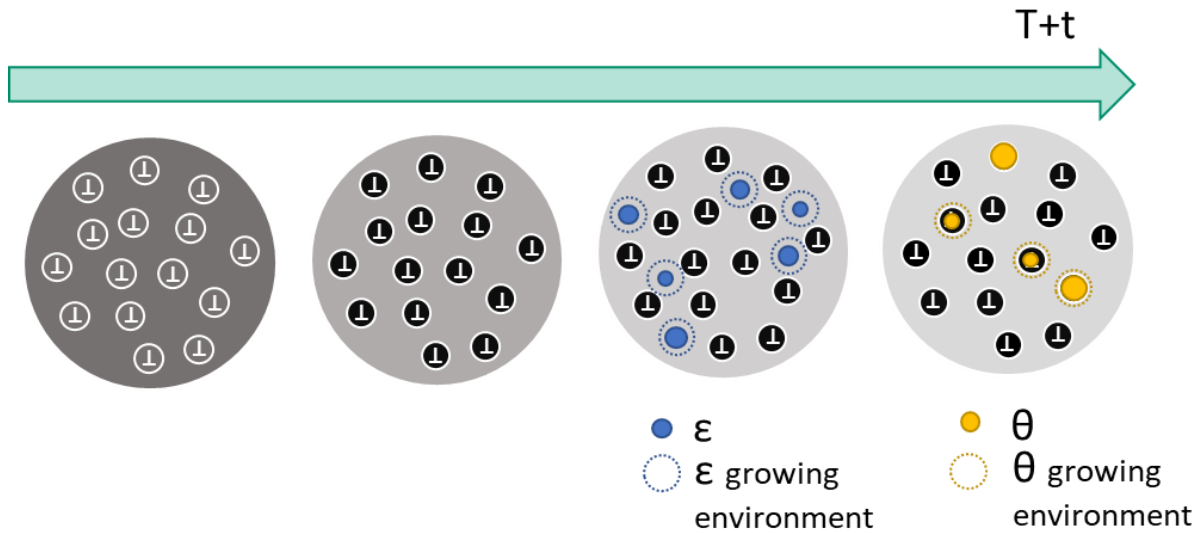


Figure 70: Schematic representation of the precipitation sequence. From left to right: initial state with homogenous supersaturation of carbon, carbon segregation from the matrix to the dislocation atmospheres, nucleation and growth of epsilon in the depleted matrix, and nucleation of cementite in the segregated dislocation atmospheres and its growth. The dashed lines represent the growth environment: the carbon depleted matrix for the epsilon carbides and the carbon-enriched atmospheres for the cementite carbides.

Hence, the main modification in the sequence consists in the addition of the segregation stage (zeroth stage). As a result, the matrix becomes heterogenous in carbon composition. The mass balance has to be modified in consequence, as well as the treatment of the carbide's nucleation and growth.

In the previous version of the model, in presence of epsilon and cementite carbides, the carbon balance was calculated as:

$$\bar{x}^C = f_\epsilon x_\epsilon^C + f_\theta x_\theta^C + (1 - (f_\epsilon + f_\theta)) x_{matrix}^C \quad \text{Equation 31}$$

where \bar{x}^C is the nominal carbon concentration (molar fraction) of the alloy (previously referred as \bar{x}), x_ϵ^C and x_θ^C are the carbon concentration in the epsilon and cementite carbides respectively, x_{matrix}^C is the carbon concentration in the matrix and f_ϵ and f_θ are the volume fraction of the epsilon and the cementite respectively. Molar volumes of all phases are assumed to be equal for the sake of simplicity

The latter carbon balance is modified when carbon segregation is taken into account. The new carbon balance is written as:

$$\bar{x}^C = f_{dislo}x_{dislo}^C + f_{\epsilon}x_{\epsilon}^C + f_{\theta}x_{\theta}^C + (1 - (f_{\epsilon} + f_{\theta} + f_{dislo}))x_{matrix}^C \quad \text{Equation 32}$$

with f_{dislo} calculated by Equation 26 and x_{dislo}^C by Equation 29.

Nucleation and growth of the epsilon carbides is treated like in [39,154]. The only difference is that the carbon concentration in the matrix now takes account of its depletion due to the segregation of the carbon into dislocation atmospheres. The nucleation driving force of epsilon is calculated by assuming that it takes place inside the matrix with concentration x_{matrix}^C . The growth/dissolution rate of epsilon carbides is calculated with the following equation, giving the velocity of the epsilon/ferrite interface:

$$v = \frac{D^C}{r_{\epsilon}} \frac{x_{matrix}^C - x_{\alpha/\epsilon}^C}{x_{\epsilon}^C - x_{\alpha/\epsilon}^C} \quad \text{Equation 33}$$

where D^C is the carbon diffusion coefficient in the matrix, r_{ϵ} is the radius of the spherical epsilon carbide, $x_{\alpha/\epsilon}^C$ is the carbon composition in the matrix at the interface, x_{ϵ}^C is the carbon concentration in the epsilon carbide (29.5 at.%). Note that the molar volumes of the matrix and the precipitates are again assumed to be the same. Otherwise, the latter equation should be modified as presented in [238].

This calculation of the growth/dissolution rate assumes that the epsilon carbides grow inside the matrix (as represented in Figure 70). This means there is no direct interaction between the epsilon carbides and the Cottrell atmospheres. However, the epsilon carbides will consume the carbon of the matrix upon growth, and this will make decrease the carbon concentration inside the Cottrell atmospheres, as seen in the part on the segregation model. Hence, the carbon concentrations in the matrix and in the Cottrell atmospheres will undergo complex coupled evolutions, as a consequence of the combined effects of segregation, and of epsilon or cementite growth/dissolution. This will be discussed when presenting the simulation results.

The nucleation and growth of cementite is treated differently. As the cementite carbides are assumed to nucleate on the dislocations, the higher local carbon concentration due to segregation has to be accounted for. This is done as follows to calculate the nucleation driving force for cementite. Assuming that there is no partition of substitutional elements in the cementite nucleus, the nucleation driving force per unit volume, ΔG_{θ} reads:

$$\Delta G_{\theta}(x_{dislo}, T) = \frac{G_{\theta}^{PE}(T) - (x_{\theta}^C \mu_{matrix}^C(x_{dislo}, T) + \sum^{i \in subs} x_{\theta}^i \mu_{matrix}^i(x_{dislo}, T))}{V_{\theta}} \quad \text{Equation 34}$$

where G_{θ}^{PE} is the molar Gibbs energy of the cementite having the same composition in substitutional elements as the matrix (nominal u-fractions of the steel), V_{θ} is the cementite molar volume and x_{θ}^i are the molar fractions in the cementite and μ_{matrix}^i the chemical potential in the matrix of element i .

The carbon segregation in the dislocation atmospheres will also affect the growth/dissolution rate of cementite. The cementite carbides will evolve in a matrix having a heterogenous concentration in carbon (higher near the dislocations, lower in the matrix). We introduce $x_{\text{non-prec}}^C$, the average carbon concentration inside the segregated carbon atmospheres and in the depleted matrix. It also corresponds to the carbon which is not inside epsilon or cementite carbides. For the sake of simplicity, one assumes that the growth rate of the carbides can be calculated by using this concentration. The velocity of the cementite/matrix interface is calculated as:

$$v = \frac{D^C x_{\text{non-prec}}^C - x_{\alpha/\theta}^C}{r_\theta x_\theta^C - x_{\alpha/\theta}^C} \quad \text{Equation 35}$$

where r_θ is the radius of the spherical cementite carbide, $x_{\alpha/\theta}^C$ is the carbon composition in the matrix at the interface, x_θ^C is the carbon concentration in the cementite (25 at.%).

$x_{\alpha/\theta}^C$ is tabulated as a function of temperature by using ThermoCalc and TCFE9 database, assuming the cementite grows/dissolves under paraequilibrium mode. The Gibbs-Thomson effect is also accounted for to modify $x_{\alpha/\theta}^C$ (c.f. [39]).

Besides the changes to the model related due to the segregation, another modification has been carried out, regarding the recovery of dislocations.

In a previous precipitation model version, a Friedel type recovery model was used [39]. In the present work, we use the recovery submodel and the parameters presented in the Chapter II. Let us mention that the most important phenomena involving dislocations are the segregation and the heterogenous nucleation of cementite. As will be seen, both phenomena occur at relatively low temperature, before the start of significant recovery of dislocations. Therefore, few interactions between recovery and segregation/precipitation were found, and this will not be discussed in this Chapter.

The model calculates precipitates sizes, from which volume fractions for each phase are calculated. Under the assumption of equal molar volumes, these volume fractions are assumed to be equal to the molar fractions, for simplicity. In some cases, these molar fraction will be converted to mass fractions for comparison with XRD results.

III.3.B.2 Model parameters

All the calculations were performed with the parameters presented in Table 12. The thermodynamic data are not detailed. The radius step (dr) corresponds to the discretization of the size distribution. The epsilon misfit (δ_ϵ) is the lattice mismatch between the epsilon carbide and the matrix (see [154]).

Some parameters are not known with precision: the interface energies of epsilon and cementite carbides, the misfit of the epsilon carbide (δ_ϵ) and the parameter ζ_θ which is used to calculate the heterogeneous nucleation energy barrier of cementite. The values selected for these parameters are in the range reported in literature. Although these parameters are adjusted, it will be seen that the model is able to simulate a large range of conditions (thermal treatment, steel composition and initial state...) without changing the

selected values. For the sake of brevity, the procedure to adjust these unknown parameters will not be presented here. Reference [171] presents such procedure in detail.

Table 12: Precipitation model parameters.

Parameter	Value
Time step (dt)	If T = 25 °C (aging), dt = 1 s
	If T > 25 °C, dt = 1 × 10 ⁻⁴ s
Radius step (dr)	0.5 × 10 ⁻⁹ m
Ferrite lattice parameter (a_α)	2.865 × 10 ⁻¹⁰ m
Ferrite molar volume (V_α)	7.09 × 10 ⁻⁶ m ³ /mol
Epsilon interface energy (γ_ϵ)	0.139 J/m ²
Epsilon misfit (δ_ϵ)	0.027
Epsilon molar volume (V_ϵ)	8.56 × 10 ⁻⁶ m ³ /mol
Cementite interface energy (γ_θ)	0.99 J/m ²
Cementite heterogenous nucleation (ζ_θ)	0.016
Cementite molar volume (V_θ)	7.83 × 10 ⁻⁶ m ³ /mol
Dislocation trapping energy (ΔE)	0.1 eV
C diffusion coefficient (D_α^C)	$D_0 = 3.95 \times 10^{-6}$ m ² /s and $Q_0 = 9.07 \times 10^4$ J/mol [TCFE9]
Fe bulk coefficient diffusion (D_α^{Fe})	$D_0 = 1.9 \times 10^{-4}$ m ² /s and $Q_0 = 2.39 \times 10^5$ J/mol [226]
Fe pipe coefficient diffusion (D_α^{Fe})	$D_0 = 3.0 \times 10^{-5}$ m ² /s and $Q_0 = 1.34 \times 10^5$ J/mol [147]
Young modulus (Y)	If steel is 0.1C, ct = 7.903
	If steel is 0.2C, ct = 7.842
	If steel is 0.3C, ct = 7.793
	$Y = ct \times \left(1 - 0.488 \times \left(\frac{T}{1043}\right)^2 + 0.1265 \times \left(\frac{T}{1043}\right)^3\right) \times 10^{10}$ Pa [148]
Poisson's ratio (ν)	0.3

The interface energy selected for the epsilon carbide in the range reported in the literature (from 0.06 to 0.394 J/m² [154,240]). The same misfit for the epsilon carbide (δ_ϵ) as in [171] has been considered. One should mention that this value is based on the assumption that the epsilon carbides nucleate inside

carbon-enriched regions of the matrix, resulting from spinodal decomposition process. Without this assumption, the misfit would be too large and the elastic strain energy of the epsilon would be higher than the driving force.

The selected cementite interface energy (0.99 J/m^3) is higher than the values usually reported in the literature in modeling works, ca. $0.7\text{-}0.74 \text{ J/m}^3$ [154,241], but it corresponds to the order of magnitude expected for an incoherent interface. Also, the cementite is assumed to nucleate inside carbon-rich Cottrell atmospheres in current version of the model which may affect the interface energy.

The Young modulus is calculated with the formula proposed by Ghosh & Olson [148] for the martensite in which the first parameter (denoted c_t in Table 12) varies with the chemical composition of the steel.

III.3.B.3 Precipitation model results

The results of the precipitation model as well as their comparison with the experimental ones are presented in the following. Firstly, the simulations of the tempering at $400 \text{ }^\circ\text{C}$ of the 0.2C steel (isothermal tempering preceded by heating the $10 \text{ }^\circ\text{C/s}$) will be presented. This example is chosen to show how the model “behaves ” and its potentialities. Secondly, the model is used to evaluate, in the same 0.2C steel, the impact of different parameters on the precipitation sequence. We will consider successively the influence of the tempering temperature, of the natural aging before tempering (which changes the initial amount of carbon segregated to dislocations), of the initial dislocation density, of more complex thermal path during heating (baths heat treatments, see Figure 7.b in the Chapter I). Finally, the results related to the other two steels (0.1C and 0.3C) will be introduced and the effect of the carbon content will be analyzed. As our study is focused on tempering, no results are shown here regarding auto-tempering (evolutions upon water quench or gas quench). However, the related simulations results are presented in Appendix B.

The precipitation model presented above has coupled a recovery model as previously mentioned. The evolutions of the dislocation density during tempering are not again presented in the following as those results have been previously presented in Chapter II.

III.3.B.3.a Detailed analysis of one simulation of tempering (0.2C, 400°C)

The tempering treatment considered in this section consists of a heating from room temperature at $10 \text{ }^\circ\text{C/s}$ up to $400 \text{ }^\circ\text{C}$ followed by 10 min of isothermal hold, applied to the 0.2C steel. The corresponding heat treatment is presented in the Chapter I, Figure 7.b with a previous 2 months aging at room temperature ($25 \text{ }^\circ\text{C}$) for the 0.2C steel. For the simulations, the initial dislocation density is set to $2.5 \times 10^{15} \text{ 1/m}^2$, on the basis of the measurements by HEXRD (in Chapter II).

During the experiments, this thermal treatment was preceded by austenitization, water quench and two months of aging at room temperature ($25 \text{ }^\circ\text{C}$). This led to the segregation of carbon at dislocations, as shown in Section III.2.A, but to the absence of any carbide precipitation. This initial state of carbon segregation has to be accounted for in the simulation by considering, before tempering treatment itself, the segregation kinetics upon cooling and aging at $25 \text{ }^\circ\text{C}$. The quenching was actually not considered in this prior simulation of segregation because, as shown in III.3.A Carbon segregation model (Figure 69)

simulating only the aging for 2 month at 25 °C allows the concentrations x_{matrix} and x_{dislo} to reach the “equilibrium” value at 25°C, the same values as if the cooling had been accounted for.

Figure 71 shows the simulation results (left column: heating; right column: isothermal hold at 400 °C). Second row shows the carbon concentrations, x_{matrix} and x_{dislo} . At the start of heating, the matrix is depleted and Cottrell atmospheres have formed, because of the aging at 25°C. The precipitation of the carbides will take place inside this matrix heterogenous in carbon, and this will make evolve the carbon concentrations x_{matrix} and x_{dislo} , as will be seen hereafter.

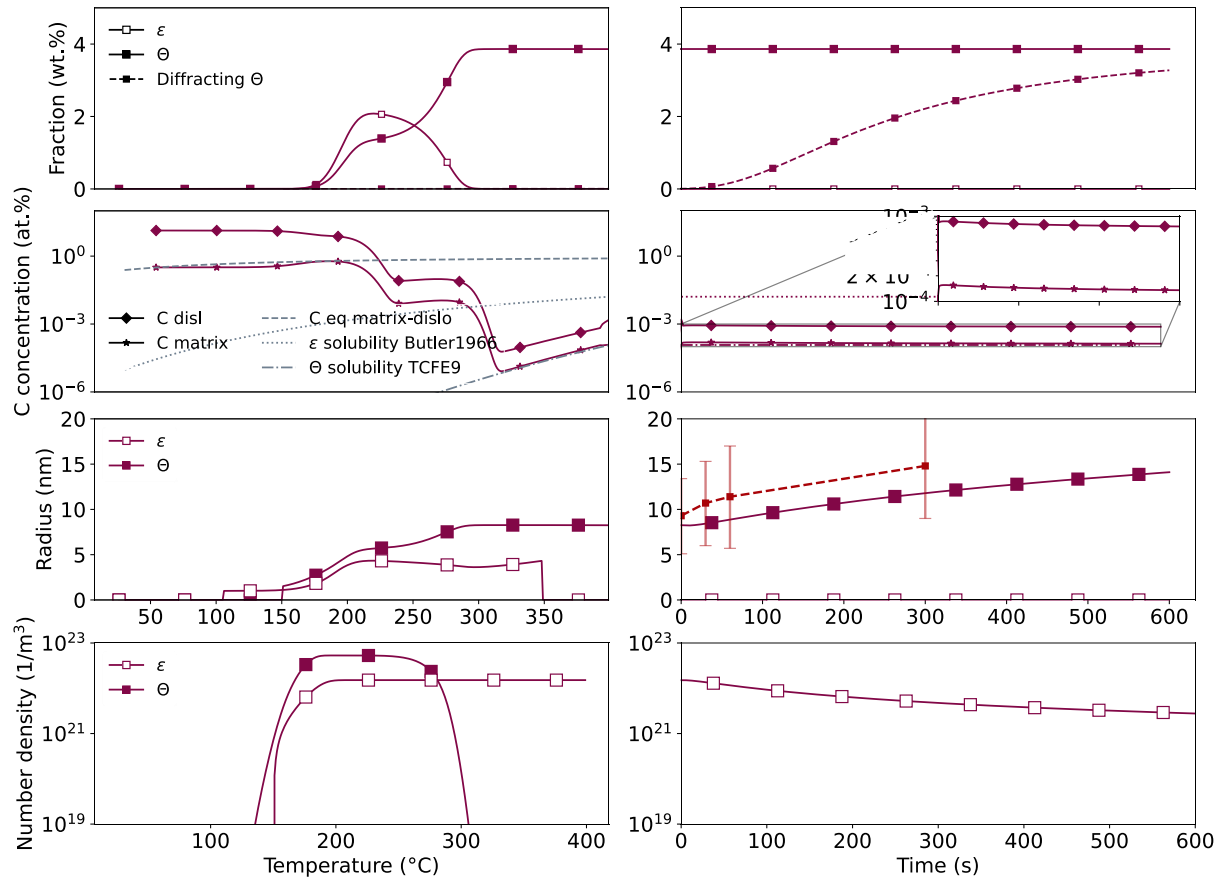


Figure 71: Simulation for tempering of 0.2C steel upon heating at 10 °C/s up to 400 °C (left, as function of temperature) followed by isothermal hold at 400 °C (right, as function of time). The evolutions of the carbides’ fractions are presented in the first line, while the carbon content evolution in the second line, the carbide radii in the third line and the number density in the last line. The concept of diffracting cementite will be clarified in the text (precipitate larger than 13 nm in the calculated distribution).

First row shows the fractions of epsilon and cementite carbides. The epsilon carbides start to form at ca. 140 °C and the cementite starts to precipitate at around 150 °C. The maximum epsilon fraction, 2.1 wt.% is reached at 205 °C. Then, the transition carbide fraction decreases as the cementite fraction increases, the latter reaching its maximum at ca. 300 °C. The formation of the cementite shows two stages. First one, up to ca. 225 °C is concomitant with the formation of epsilon. In this stage, the most part of the carbon in the matrix and at the dislocations is consumed by both carbides simultaneously (as shown by the decrease of x_{matrix} and x_{dislo}). The second stage of cementite formation corresponds to the dissolution of epsilon carbides. In this stage, the cementite takes the most part of its carbon from the dissolving

epsilon carbides. This is a slower process, but which accelerates with the increase of the temperature. Final fraction of cementite 3.75 wt.% is reached at ca. 300 °C.

Hence, the simulation predicts the concomitant precipitation of cementite and epsilon, which may be unexpected, because both carbides form sequentially in the usual reported sequence, according to both experiments [38,166,242] and simulations [39,154,171,209,243], especially those from previous versions of this model [39,154]. This comes from the fact that, unlike previous versions of this model, the precipitation of each carbide is assumed to occur in a different environment inside which carbon concentration is different (the carbon-depleted matrix for the transition carbides and the Cottrell atmospheres for the cementite). In current model's version, the cementite precipitates earlier than in the previous versions, because of the high carbon concentration inside the Cottrell atmospheres. Despite the concomitant start of the precipitation of epsilon and cementite, the epsilon carbides eventually dissolve to the benefit of the cementite. In that sense, the usual precipitation sequence is respected. The mechanism described by the model consists of a transfer in carbon from the epsilon to the cementite carbide through the matrix.

The precipitation sequence is also revealed by the evolutions of carbon concentration, presented in the second row of Figure 71. As mentioned above, the simulation starts with the carbon already segregated to the dislocation atmospheres, whereas the matrix is depleted, because of the aging at 25 °C. Figure 71 also shows the equilibrium value of the carbon concentration in the matrix (dashed line). It corresponds to the equilibrium which would be established between the matrix and the dislocation, if there were no carbides. It was calculated as presented in the part on the segregation model (Section III.3.A, Figure 68).

During heating up to ca. 150 °C, the carbon concentration in the matrix (x_{matrix}) becomes lower than the equilibrium value, which increases because the trapping of the carbon by the dislocations becomes less efficient. x_{matrix} then reaches again the equilibrium value, because of the faster diffusion of carbon. The precipitation of epsilon and cementite induces a decrease of the carbon content in the matrix and at the dislocations. The solubility limit of epsilon (from [236]) is not reached because of the Gibbs-Thomson effect and the coherency elastic strain energy. The end of the epsilon dissolution and the formation of cementite induces a new decrease of x_{matrix} , which approaches the solubility limit related to cementite, but with some difference because of the Gibbs-Thomson effect. During the holding section of the tempering, the only change in the carbon concentration curves is a small decrease of the carbon concentration in the matrix approaching the predicted solubility limit related to cementite, because the radius increases and the Gibbs-Thomson effects decreases.

The third row of the Figure 71 shows the evolution of the cementite and epsilon radius during the tempering heat treatment. Upon nucleation of epsilon starting above ca. 100 °C, the initial size is equal to 0.5 nm. This initial size is imposed by dr , the discretization step of the size distribution. The epsilon carbides grow up to ca. 210 °C to reach a size of 4.2 nm. The growth of epsilon carbides is concomitant with the increase of their fraction. Hence, it does not come only from the nucleation of new carbides. Then, the epsilon radius remains nearly constant up to 350 °C, due to combined growth and dissolution. The cementite growth presents two stages related to the evolution in two stages of the fraction of cementite mentioned above. After heating up to 400 °C, the final size of the cementite carbides is slightly larger than 8 nm. The cementite radius also increases during the holding due to coarsening.

The evolution of the number density of both carbides is presented in the last row of Figure 71. A fast increase of the epsilon number density occurs above 100 °C to reach a maximum of ca. 5.5×10^{22} 1/m³ while the maximum cementite number density is 1.3×10^{22} 1/m³. The difference is mainly due to the number density of nucleation sites (homogenous for epsilon, at dislocations for cementite). For both carbides, there is some overlap of nucleation and growth stages (as seen with previous figures, between ca. 175 °C and 200 °C). It shows that a large part of the increase of the fraction of the carbides comes from their growth, more than the nucleation, according to these simulations. At 220 °C the epsilon number density starts to decrease indicating its dissolution. During the isothermal holding at 400 °C the cementite number density decreases because of the coarsening phenomenon.

Few experimental results are available to assess the model predictions regarding the epsilon carbides.

The experimental study presented previously in this work (Section III.2.B) is not fully conclusive regarding whether or not the precipitation of epsilon actually occurred in the 0.2C steel. If it is present, it may have been detected during the heating, around 325 °C (Table 11). This is above the range of temperature predicted by the model. But in view of the lack of accurate measurements of transition carbides formation kinetics, it was chosen to not adapt the model parameters accordingly.

Regarding the cementite, the radius predicted is in good agreement with the values measured by TEM, upon the isothermal holding stage at 400 °C (Figure 71). However, the temperature range predicted for the cementite formation upon heating (start at 150 °C, maximum value reached at 275 °C) is clearly below the range established experimentally by HEXRD (starting at 330 °C). This discrepancy may be related to the lack of detection by HEXRD of the smallest carbides, as will be discussed below.

In addition to the evolutions of the mean radius, the precipitation model also predicts the size distribution of each carbide. Figure 72 presents the cementite experimental size distribution of the 0.2C_WQ steel tempered at 400 °C 300s, its log-normal modeled curve, along with the same distribution obtained from the simulation. Although experimental and modeled distributions show a close mean value, the width and the skewness are different. The experimental distribution is left-skewed (positive skewness) as previously reported in the literature [39,149,207], while the modeled one is narrower and slightly right-skewed (negative skewness) as predicted by the classical coarsening models from the LSW theory [244,245]. Some of the larger carbides measure might correspond to inter-lath cementite which may have another growing kinetics.

The size distribution is used to calculate the fraction of diffracting cementite. It corresponds to the cementite carbides having a radius higher than some preestablished critical value, 13.3 nm). In order to determine experimentally this critical size, an interrupted tempering treatment was performed by heating at 10°C/s up to 350°C, i.e. slightly above the temperature at which cementite was firstly detected by HEXRD in the 0.2C steel. The maximum size of the cementite measured by TEM at the end of this treatment was equal to 13 nm.

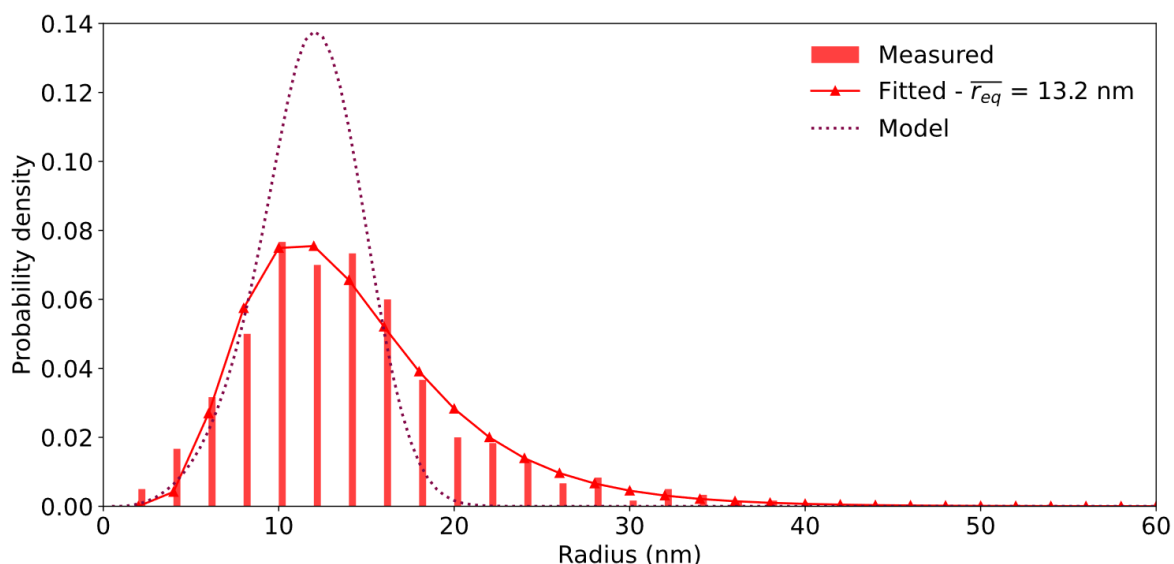


Figure 72: Experimentally determined distribution of the cementite equivalent radius at the 0.2C_WQ_400C300s condition as well as the radius distribution obtained from the precipitation model for the same condition.

The evolution of the cementite diffracting fraction is plotted in Figure 71 (dashed line). According to the simulation, the diffracting cementite would start to be observable only during the isothermal holding. At the end of the holding, 600s, the predicted diffracting cementite fraction remains lower than the total fraction. Hence, the simulation now predicts that the cementite will start to be detected by HEXRD significantly later than the actual observation. However, this attempt shows at least that the size of the carbides should be accounted for in the predictions.

III.3.B.3.b Influence of the tempering temperature

Simulations of tempering at 200, 300 and 400 °C are presented in Figure 73, still considering the 0.2C steel and a heating rate of 10 °C/s. Let us mention that to really investigate the influence of holding temperature, the heating stage should have been skipped, i.e. considering “instantaneous” heating, but such analysis was already done [39,171]. We focus here on simulations that can be compared with our experiments, and which will be used for the mechanical modeling presented in Chapter IV.

As the heating rate is the same for the three simulations during the heating section, one single curve is plotted for this stage.

In fact, for the tempering at 300 °C and 400 °C, most of the microstructural evolutions occur during the heating, according to the simulations, and these were already commented in last section. New outcome though is the fraction of diffracting cementite which is equal to zero upon isothermal hold at 200 °C and 300 °C. This is consistent again with the difficulty to detect these carbides by HEXRD during these treatments.

During the holding at 200 °C, the simulation predicts the dissolution of epsilon to benefit of the cementite, as seen from the evolutions of both carbides fractions and carbon concentrations x_{dislo} and x_{matrix} . The formation of cementite upon holding at 200 °C could not be confirmed from the experiment, even in the 0.3C steel which has more carbon. But this may be due to the too small size of the carbides. The epsilon carbides mean size remains nearly constant (like for the simulation at 400 °C, when the

epsilon carbides underwent simultaneously growth and dissolution). The cementite carbides sizes were measured upon isothermal hold at 300°C and 400°C, and the agreement with the simulation is satisfactory in terms of magnitude and influence of the temperature.

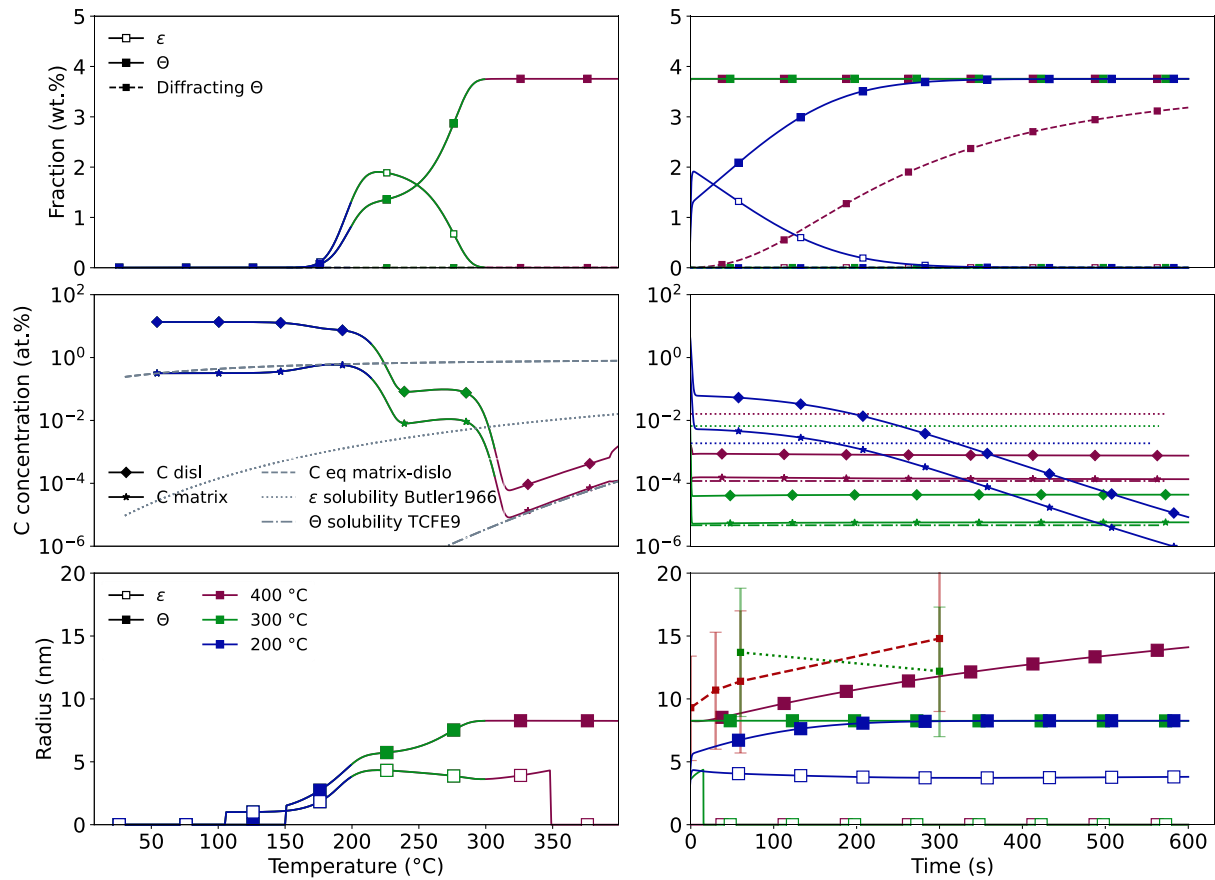


Figure 73: Simulation of precipitation kinetics for the 0.2C_WQ steel upon heating at 10 °C/s and isothermal hold at 200, 300 and 400 °C. The figure is composed as Figure 71.

III.3.B.3.c Influence of dislocation density

The dislocation density is an important microstructural input parameter for the model. The local carbon concentration in the dislocation atmospheres increases if the dislocation density is lower (Section III.3.A Carbon segregation model). The carbon concentration in the matrix decreases when the dislocation density is increased. The second effect of the dislocation density is to change the number density of cementite nucleation sites.

Previously in this work (in Chapter II), it has been shown experimentally that the dislocation density in the martensite is highly heterogenous with local values ranging, for 0.2C steel, between $7.5 \times 10^{14} \text{ 1/m}^2$ and $2.58 \times 10^{15} \text{ 1/m}^2$. During the cooling, the first formed and the last formed martensite have respectively the lowest and the highest dislocation density. In the following, we will consider the 10 first and the 10 last percent of martensite, by estimating the average dislocation density inside these respective fractions of the martensitic microstructure.

In the 0.2C alloy, the average dislocation density is $1.2 \times 10^{15} \text{ 1/m}^2$ in the first 10 wt.% formed martensite and $3.4 \times 10^{15} \text{ 1/m}^2$ in the last 10 wt.%. The results of the precipitation model using these two

values as input are presented in Figure 74. The results for low and high dislocation density are shown with thin lines/small symbols and thick lines/large symbols respectively.

The precipitation of epsilon is favored with the lower dislocation density: it starts at lower temperature and a higher fraction is reached (2.6 wt.% versus 1.2 wt.% for the high dislocation density). Conversely, for cementite, the precipitation is hindered when the dislocation density is decreased. It still occurs in two stages (as described in Section IV.3.B.2.a). The first stage is concomitant to the formation of epsilon. With the lower dislocation density, the fraction of cementite reached in this first stage is much lower. This is due to the lower carbon concentration segregated at dislocations and the lower density of available nucleation sites (the dislocations). The second stage, which is concomitant with the dissolution of epsilon, is shifted to higher temperatures. The dissolution of epsilon is achieved at ca. 280 °C with the higher dislocation density and at 300 °C with the lower dislocation density. The final fraction of cementite is the same for both simulations.

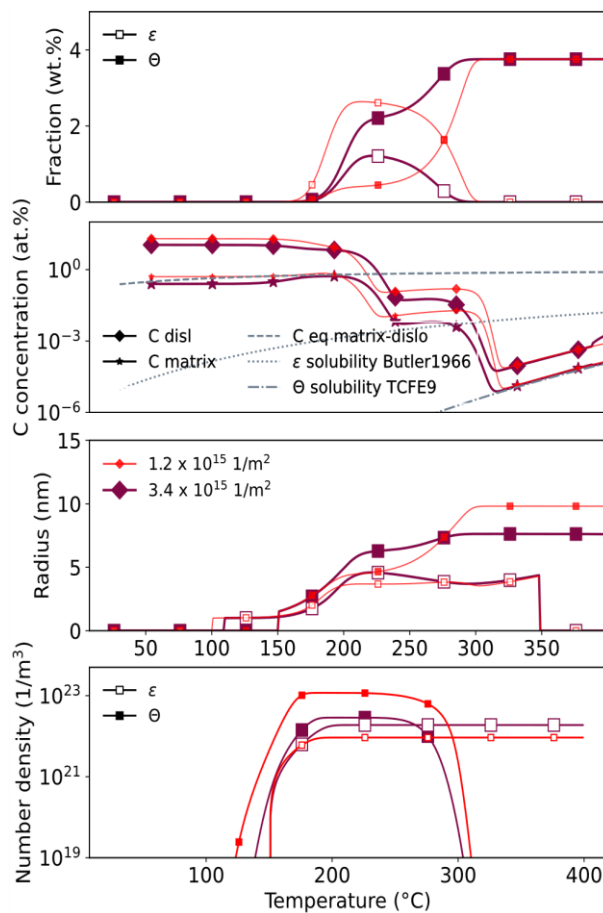


Figure 74: Effect of the dislocation density on the precipitation sequence according to the simulation in the 0.2C steel during heating at 10 °C/s up to 400 °C as holding temperature. Low and high dislocation density: thin and thick lines.

Regarding the effect of the dislocation density on the carbon concentrations during tempering, similar tendencies as established in previous Section III.3.A are observed.

The size reached by the epsilon is lower for the simulation with lower dislocation density (ca. 4 nm, when the fraction of epsilon is maximum) than the one with higher dislocation density (5 nm). This is

due to more intense nucleation of epsilon carbides, because of the higher carbon concentration in the matrix, which increased the nucleation driving force.

Regarding the cementite size, in the simulation with lower dislocation density the cementite carbides are smaller during the first stage and larger at the end of the second stage. In first stage, this is due to larger amount of carbon consumed by epsilon. In second stage, it is due to the lower density of cementite carbides, related to the lower dislocation density. Upon holding, the cementite carbide size related to both simulations will converge (results are not presented). This is the behavior expected upon coarsening.

These simulations show that the dislocation density has a significant impact on the sequence of precipitation, even when considering the range of dislocation density that can exist inside one single martensitic steel. Hence, one can expect that local precipitation state (size, fraction of carbides) and thus the local precipitation hardening (and carbon solution hardening) will differ between regions with lower and higher dislocation density. However, the most important differences between the high and the low dislocation density simulations were found during the heating, mostly upon epsilon carbides precipitation and dissolution. But once all the cementite is precipitated (end of heating, isothermal hold), the influence of the dislocation density becomes less important, and it eventually fully disappears. This results will serve to explain the observed mechanical trend in Chapter IV.

III.3.B.3.d Influence of the alloy carbon content

The effect of the alloy carbon content on the precipitation sequence was evaluated by performing simulations for the three studied steels, 0.1C, 0.2C and 0.3C, with the parameters detailed in Table 12. The dislocation density was changed for each alloy (0.1C: 1.5×10^{15} 1/m², 0.2C: 2.5×10^{15} 1/m² and 0.3C: 3.5×10^{15} 1/m²) in order to compare the simulations to the experiment. As explained in Section III.3.A, this changes the solubility limits related to segregation at dislocations (c.f. Figure 68). As the composition of each steel in substitutional elements is different (c.f. Chapter I, Table I), the solubility limit related to cementite in paraequilibrium with the ferrite was calculated for each steel. The solubility limits are plotted in Figure 75 as a function of temperature.

The simulations results are presented in Figure 75 for the three steels and considering a heating at 10 °C/s up to 400 °C. The evolutions of the epsilon carbide fraction show a clear effect of the carbon content. The maximum epsilon fraction are 0.13 %, 1.9 % and 4.2 % in the 0.1C, 0.2C and 0.3C steels respectively. It can be directly seen that this fraction is not simply proportional to the carbon content of the steel. Conversely, the maximum fraction of cementite is nearly proportional to the steel carbon content. Hence, in the 0.1C steel, the formation of epsilon carbides is hindered, compared to the cementite.

It is thought that the precipitation of epsilon carbides is hindered in the 0.1C steel because of the carbon segregation into the dislocations. The segregation phenomenon is illustrated by the evolutions of the carbon concentration in the matrix, which are plotted in Figure 75.

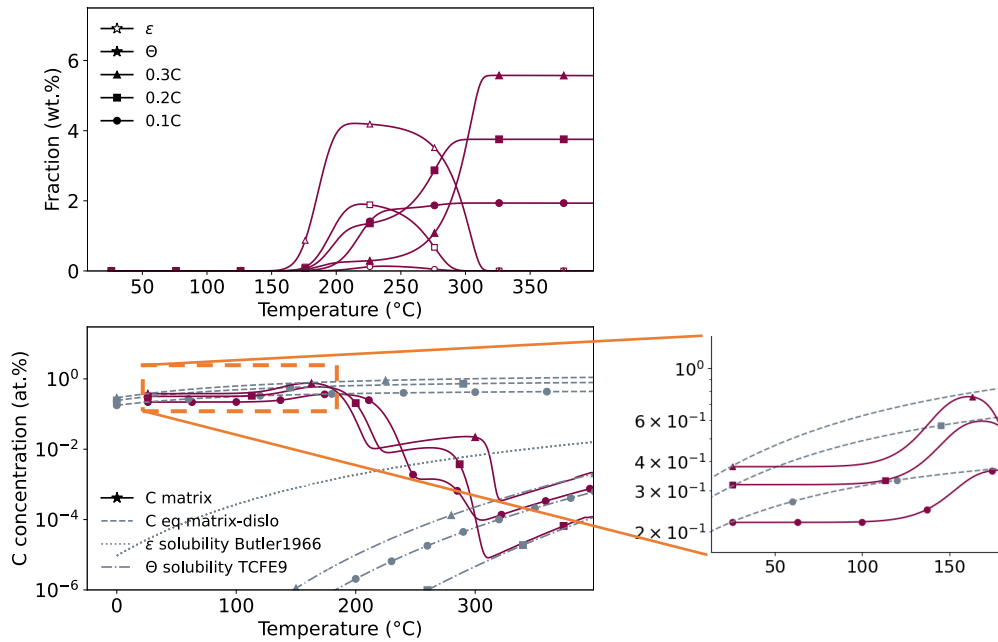


Figure 75: Evolutions of phase fraction as well as carbon concentration in the matrix for the three studied steels (0.1C, 0.2C and 0.3C) during a linear 10 °C/s heating up to 400 °C. A closeup of the carbon concentration in the matrix between room temperature and 175 °C is also presented.

For all the three steels, it remains constant up to 100-125 °C upon heating (with increasing concentration as carbon content of the steels is increased). Then, as diffusion is activated, it increases to reach the dislocation/matrix equilibrium value. The higher the carbon content of the steel, the higher equilibrium value. As a result, the nucleation driving force for epsilon nucleation is lower for the 0.1C steel than for the other two. It is too low for the 0.1C steel, and sufficiently large for the 0.2C and 0.3C steels. The situation is different regarding the cementite nucleation, because it occurs inside the Cottrell atmospheres located at the dislocations. The carbon concentration in the dislocation atmospheres also increases with the carbon content (9.7 at.%, 13.5 at.%, and 15.7 at.% for the 0.1C, 0.2C and 0.3C steel respectively). But even for the 0.1C steel, it is high enough to promote the precipitation of the cementite.

The nominal carbon content, the matrix carbon concentration as well as the concentration of the dislocation atmospheres at 150 °C (temperature at which epsilon carbide formation is observable in Figure 75) for the three studied steels are presented in Table 13.

Table 13: Nominal carbon content, the matrix carbon concentration as well as the concentration inside the dislocation atmospheres at 150 °C (temperature at which epsilon formation is observable in Figure 75) for the three studied steels.

Steel	Nominal carbon content (at.%)	Matrix carbon content (at.%)	Dislocation carbon content (at.%)
0.1C	0.5	0.28	7.43
0.2C	0.96	0.51	9.74
0.3C	1.4	0.71	11.17

The effect of the carbon concentration in the matrix and, therefore, of the segregation on the epsilon carbide nucleation rate is presented in Figure 76 (considering the temperature of 150 °C, about which nucleation of epsilon is predicted). The driving force (Figure 76.a) increases (in absolute value) with the carbon content as expected. The carbon content in the matrix after segregation, x_{matrix} , is represented in grey for the 0.1C, 0.2C and 0.3C steels. Even if the difference of driving force seems low between the three steels, it has a strong effect when the nucleation rate is calculated. The nucleation rates (accounting for the Gibbs-Thomson effect and the elastic strain effect) are presented in Figure 76.b. Their variation spans several orders of magnitude for the 0.1C, 0.2C and 0.3C steels. The nucleation rate of the 0.2C steel is ca. 60 times higher than the one of the 0.1C steel. This is why in the latter steel, the epsilon carbides have not enough time to form, before the cementite.

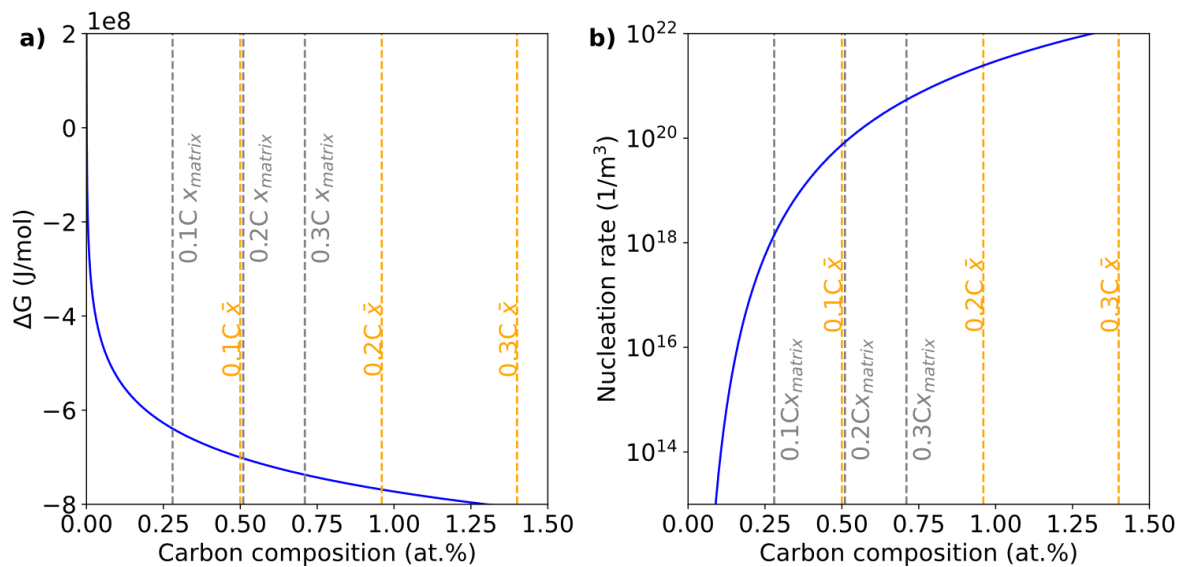


Figure 76: a) Driving force for the nucleation of epsilon as function of the carbon composition at 150 °C. b) Nucleation rate of the epsilon carbide as function of the carbon composition at 150 °C based on a) and accounting for the Gibbs-Thomson effect and the elastic strain.

Let us mention that in a previous version of the model without accounting the segregation of carbon into the dislocation atmospheres the mitigation of the epsilon carbide could not be found by the simulation, even for the 0.1C steel (whatever the model parameters). For all three steels, fast formation of epsilon carbides were predicted. This is probably due to the fact that in this previous version, the nominal carbon content of the steel was considered to calculate the nucleation rate of the epsilon carbides. The corresponding concentrations are represented (yellow dashed lines) in Figure 76.b. The concentration of all three steels is inside the composition range in which the nucleation rate is significant (above ca. 0.5 at.%). For example, nominal composition of the 0.1C steel is close to the matrix composition (x_{matrix} , grey dashed line) of the 0.2C steel after segregation.

The evolution of the carbides radii during the heating and holding at 400 °C are presented in Figure 77. Whatever the steel composition the epsilon carbide radius reaches a size around 5 nm. Conversely, the cementite radius at the end of the heating depends strongly on the carbon content. It increases for increasing carbon content as one may expect: about ca. 7 nm, 8 nm, and 15 nm for the 0.1C, 0.2C and 0.3C steel respectively. But this tendency changes during the holding at 400 °C. The cementite radius

of the 0.2C steel becomes the smallest one, while the one for the 0.1C steel is intermediate between the 0.2C and the 0.3C steels values. Hence, the size of the cementite carbides at the end of the holding is not simply correlated to the steel composition.

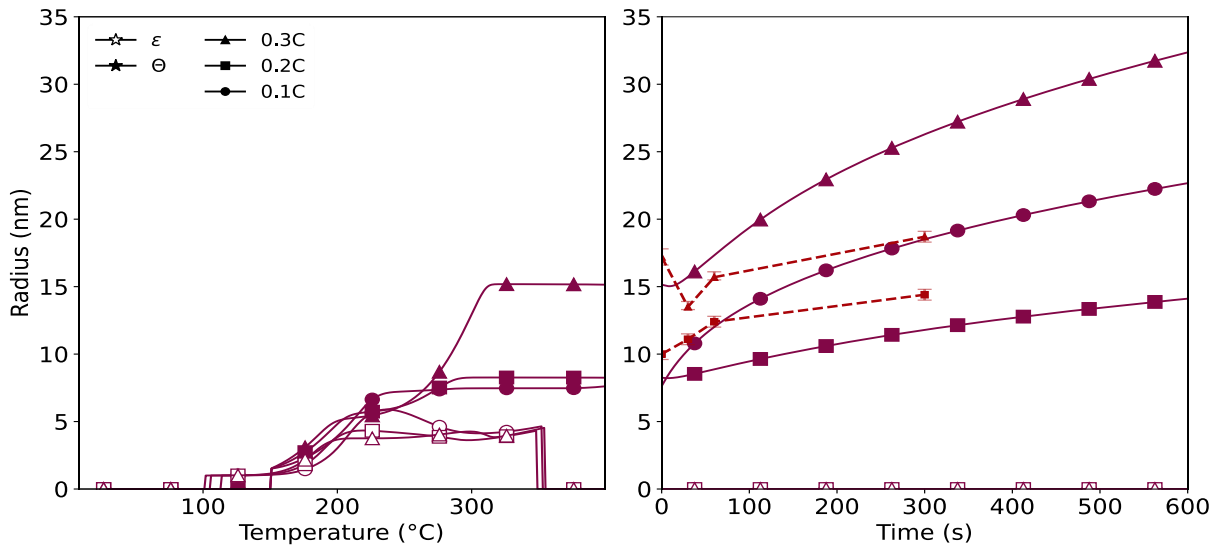


Figure 77: Evolution of the epsilon (empty symbols) and cementite (full symbols) radius during heating at 10 °C/s up to 400 °C followed by an isothermal holding for the three studied steels.

The unexpected evolutions of cementite carbides sizes as a function of the steel carbon content can be interpreted by considering the number density of the carbides, presented in Figure 78. The 0.2C steel has the highest number density of cementite during the heating and the isothermal holding, whereas one could expect the 0.3C steel to have the highest density. This is explained by the chronology of the precipitation sequence in 0.2C and 0.3C steels. In the latter steel, the epsilon carbides form earlier than the cementite nucleation. This makes decrease the carbon concentration (both in matrix and in segregated atmospheres). Conversely in 0.2C, the precipitation of epsilon occurs at the same time as the nucleation of cementite.

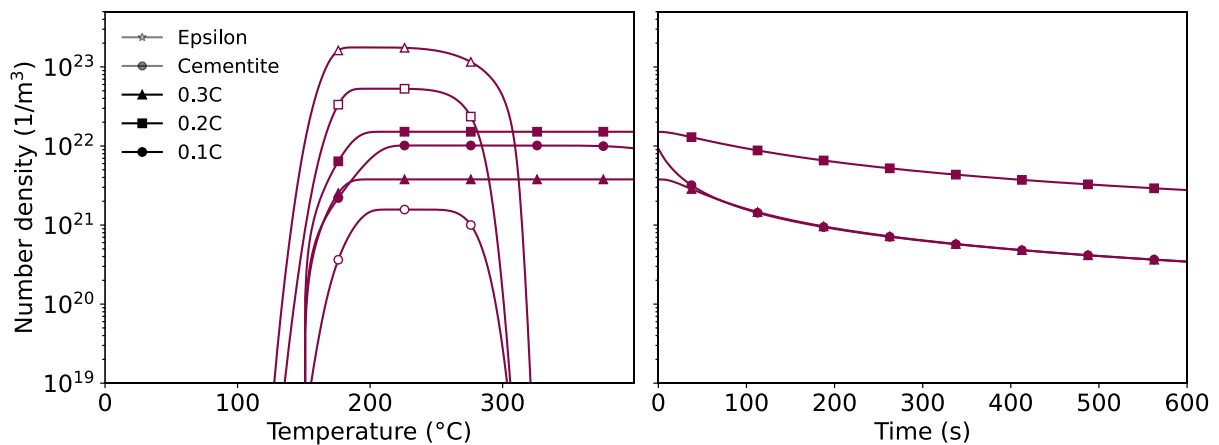


Figure 78: Evolution of the epsilon (empty markers) and cementite (full markers) number density during the linear tempering at 400 °C for the three studied steels (identified by the markers shape).

Hence, according to the simulations, the size and density of both carbides epsilon and cementite do not depend simply on the carbon content. It depends both on the accounting of the carbon segregation to dislocations and on the precise chronology of the precipitation sequence. The trends predicted by the simulation could only be partly assessed by experiments. As shown before, HEXRD only provide partial information on the precipitation kinetics. Besides, the cementite carbide sizes were measured by TEM in 0.2C and 0.3C steels (Section III.2.B.3). The comparison with the experiment is shown in Figure 77b. At the start of the holding, the size prediction is satisfactory, in terms of the radii predicted and effect of temperature. However, predicted coarsening rate seems too fast. Main adjustable parameter is the interface energy, which is not known with precision. The analysis of TEM micrographs may also be reconsidered, as the actual shape of the carbides is between the oblate and the prolate one. Indeed, if the equivalent radius of cementite carbides is calculated presupposing an oblate shape instead of a prolate shape, then the equivalent radius at 300s at 400 °C of the 0.3C steel is 32.5 nm which is closer to the model's prediction.

III.3.C Conclusions of the segregation and precipitation models

In this modeling study, the full sequence of tempering, from the segregation of carbon to the precipitation of transition and cementite carbides, has been simulated. To this aim, two models of the literature have been combined: the first one, introduced by Svoboda et al. [153], on the segregation and the second one on the precipitation of the carbides, which had been developed previously in this laboratory [39,154].

By using data from literature (carbon diffusion coefficient and trapping energy of carbon at dislocations), the simulations of segregation kinetics show that the segregation of carbon is already well advanced before the tempering treatment, at the end of the quench which follows austenitization, and whatever the considered cooling rate (gas quench, water quench). The segregation continues during aging at room temperature for two months. The concentrations predicted in the segregated carbon atmospheres are in good agreement with the experiment. The effect of different parameters has been examined: increasing the dislocation density, the temperature or decreasing the carbon content of the steel make decrease the amount of carbon segregated to the Cottrell atmospheres.

The previous precipitation model was modified to examine the consequences of the segregation on the precipitation sequence upon tempering. The segregation makes the matrix heterogeneous in carbon, with the enriched Cottrell atmospheres on the one hand and the depleted matrix on the other hand. In the new version of the model, this is accounted for by treating the nucleation and growth of the carbides as a function of their environment (poor or rich in carbon for epsilon and cementite respectively).

Original outcomes of this modeling study regard the accounting of the segregation to dislocations. First, increasing the dislocation density tends to retard the precipitation of epsilon and to decrease its fraction. This is due to the higher amount of carbon segregated, which reduces the carbon content of the matrix, and thus the nucleation driving force for epsilon. Similar conclusions were reached in [103,127]. The simulation also predicts a retardation of the epsilon nucleation when a pre-aging is applied before the tempering heat treatment, as the carbon concentration of the matrix becomes lower. As shown in Chapter II, the dislocation density is highly heterogeneous in martensitic microstructures, and this will have to be accounted for in the modeling of mechanical behavior, in Chapter IV.

One of the most important effects of the segregation captured by the precipitation model is that it hinders the formation of the transition carbides. The latter are almost fully suppressed in the lowest carbon steel (0.1C) and their maximum fraction is limited in the 0.2C steel. This has an impact on the formation of cementite which occurs afterwards, and this results in complex evolutions of its sizes and densities as a function of the steel carbon content. The quasi suppression of epsilon in 0.1C steel is not simply related to the selection of the model parameters (e.g. the interface energy of epsilon). If the segregation is not accounted for, fast formation of epsilon is predicted for 0.1C, 0.2C and 0.3C steels, whatever the model parameters selected in realistic range. This was the behavior shown in previous versions of the model [39,171], and in simulations not presented in this work.

Apart from these effects of the carbon segregation, the model predicts the usual sequence of epsilon carbides precipitation followed by their dissolution to the benefit of cementite. It also predicts the usual effects of heating rate and tempering temperature on precipitation kinetics and carbides sizes.

A study of the influence of the room temperature aging on the precipitation sequence is presented in Appendix C. In Appendix D, the effects of the heating rate are analyzed.

III.4 Conclusions of the chapter

The precipitation sequence in low-carbon low-alloyed martensitic steels was investigated with special focus on the carbon atoms migration from the supersaturated matrix to defects atmospheres, as well as its consequences on the precipitation of transition carbides and cementite which occur afterwards. Several experimental approaches (3DAPT, TEM, in situ HEXRD) were combined to overcome the difficulty to track the carbon distribution in the microstructure (segregation, carbides), which is related to the low carbon content of the investigated steels (0.1, 0.2, 0.3 wt.% C). However, a complete characterization of the segregation/precipitation sequence could not be established experimentally. This is why the simulation was essential to complete our analysis.

- 1) A specific study of the segregation was conducted, because of its expected impact on the precipitation sequence. Observations by 3DAPT of the segregation state were combined to simulations by using the model introduced by Svoboda et al. [153]. The segregation already starts during the quench and the aging at room temperature, which precede the tempering. This makes the matrix heterogeneous, with carbon-rich Cottrell atmospheres at dislocations and carbon - depleted matrix. This depletion of the matrix is increased when the dislocation density is increased.
- 2) The precipitation sequence was established by in situ HEXRD experiments combined to TEM observations. A previous model for precipitation was coupled to the model for segregation, whose impact on the precipitation sequence was evaluated. Main outcomes are:
 - a. To show that in the lowest-carbon steel (0.1C), the segregation almost fully inhibits the formation of transition carbides. It is mitigated in 0.2C steel, and there is limited impact in 0.3C steel.
 - b. The dislocation density has key role in the precipitation sequence: at high values, the transition carbides are at a disadvantage compared to cementite. This is because the transition carbides form in a matrix which is more depleted in carbon, whereas the cementite nucleates at the dislocations, which are always enriched in carbon, because of the Cottrell atmospheres.
 - c. The temperature ranges at which the carbides precipitate differ sometimes from usual observations. Upon heating at 10 °C/s, transition carbides have been observed up to 375 °C, whereas the simulation predicts that cementite can start to form at 150 °C, along with the transition carbides.

These results highlight the importance of the first stages of tempering on the overall precipitation sequence: the segregation of carbon to defects and the formation of transition carbides, especially in low-carbon steels. If the segregation seems well understood at the end of this work, further work is required regarding the transition carbides. The model developed here assumed some mechanisms and the simulation were conform to experimental trends. However, the mechanism of transition carbides formation still needs to be clarified, as our 3DAPT observations and the literature suggest the formation of carbon clusters as precursors. Also, other mechanisms can be actually envisaged to explain the inhibition of the transition carbides by the segregation as boundary segregation.

Chapter IV

Tensile behavior of as-quenched and tempered martensite

- IV.1 Focused state of the art - 132 -
 - IV.1.A Experimentally determined martensitic mechanical properties - 133 -
 - IV.1.B Models for martensite tensile behavior - 139 -
- IV.2 Results: tensile behavior of the studied steels - 145 -
 - IV.2.A Tensile curves of as-quenched state..... - 146 -
 - IV.2.B Effect of tempering on the tensile curves..... - 146 -
- IV.3 Tensile behavior model - 149 -
 - IV.3.A Microstructure YS distributions and internal stresses - 151 -
 - IV.3.B Calculation of the flow stress distributions..... - 160 -
 - IV.3.C Micromechanical model bases - 164 -
- IV.4 Results and discussion of tensile behavior model..... - 166 -
 - IV.4.A As-quenched martensite - 166 -
 - IV.4.B Tempered martensite..... - 171 -
 - IV.4.C Perspectives..... - 178 -
- IV.5 Conclusions of the chapter - 180 -

As previously stated, one objective of the present work was to understand and model the tensile behavior of martensitic steel on physical basis. To do so, the microstructure key features have been quantified and their strengthening phenomena now must be understood.

The present chapter aims at presenting our physical-based micromechanical model accounting for all previously described microstructural features, already disclosed in the previous chapters, and their respective hardening mechanism. The specificity of this model is to describe the behavior of martensite as an extended elastic-plastic transition, which require as an input the spatial distribution of the mechanisms and not only their mean contributions. The model will be compared to the experimental tensile behavior of the studied steels.

In the following, the model will be calibrated on the studied steels on the basis of four main contributions; the dislocation density, the segregation/precipitation state of carbon, the microstructure effective size and the internal stresses. At the as-quenched state, each of them presents a spatial distribution due to the sequential nature of the martensitic transformation. The carbon contribution may be considered constant if quench is fast enough. The combination of these contributions produces a combined distribution of flow stress governing the tensile behavior related to the martensitic microstructure.

The tempering heat treatments that may be applied to the as-quenched state have several effects on the microstructure. The dislocation density is reduced by the recovery phenomenon (presented in Chapter II). The carbon supersaturated matrix will decompose in carbides and in a matrix with a lower carbon content (presented in Chapter III). The internal stresses may relax and if the heat treatment is performed at high enough temperature changes in the microstructure sizes may occur. All these effects affect the distribution of local yield stresses and in turn the macroscopic tensile behavior.

The present chapter is thus divided in three sections:

- A focused state of the art recalling the fundamentals about the mechanical behavior of as quenched/tempered martensitic steels. It includes experimental results but also modeling strategies.
- The experimental tensile tests on the studied steels are presented and discussed at the light of the literature.
- The basis of the micromechanical model are presented. The model is then calibrated on the basis of our experimental findings and its performance is discussed in comparison with models from the literature.

IV.1 Focused state of the art

For many years the macroscopic martensitic tensile behavior has been described by the effects of the mean values of the microstructural features (size, dislocation density) as well as by the nominal carbon content of the steels. The evolution of the martensitic tensile behavior as a function of the tempering was also treated as function of the evolution of the mean values. Some of the important works presenting those results are the works of Krauss, Leslie, Thomas among others [98,99,155,246–249].

It's hard to be comprehensive on that and we hope the forgotten will forgive us. Excellent literature reviews have been also produced as [9] and the ICOMAT/ESOMAT lecture series show that the subject of the martensitic steels remains very topical.

More recently, the focus of the investigations has switched to a more local scale considering the heterogeneities of the microstructure, its internal stresses state and the local deformations. We will focus in particular on these issues.

The present state of the art is divided in two sub-sections, the first one is about the experimental findings about the link between the microstructure and mechanical properties of the martensitic steels and the second one focuses on the modelling approaches.

IV.1.A Experimentally determined martensitic mechanical properties

The behavior of martensitic steels has been the subject of numerous reviews of literature and synthesis, such of those [9,19,250]. So, there is no question of revisiting this subject in detail. It is well admitted that the mechanical properties of the as-quenched martensite are affected by different metallurgical features as the chemical composition (mainly the nominal carbon content of the steel) [246], by the PAGS [98,251], by the dislocation density [251]. The effect of the PAGS may be indirect and related to the hierarchical organization of the microstructures packets and blocks, whose size are known to scale with the PAGS [252]. The mechanical behavior of the as-quenched martensite can also be tailored by tempering treatment. The variations produced by this treatment are highly dependent of the temperature and holding time.

IV.1.A.1 Effects of the carbon content

One of the most determinant alloying elements in steels is carbon and its effects on the hardness and nanohardness of the martensitic steels has been reported by [169,253] among others. Figure 79 presents the evolution of the Vickers hardness with the carbon content with results obtained from the literature and from the herein studied steels. The relation between the hardness and the carbon content can be expressed as [254]:

$$H_V = -820 \times (wt. \%C)^2 + 1552 \times wt. \%C + 167 \quad \text{Equation 36}$$

The hardness of the three studied steels calculated with Equation 36 are 328 HV, 457 HV and 569 HV for the 0.1C, 0.2C and 0.3C steels respectively. The experimental values are higher than the calculated ones for the three studied compositions.

An early work of Muir [255] studies the carbon effects on the tensile behavior as well as a more recent one presented by Saeglitz and Krauss [246]. An increase of the yield strength with the carbon content is also observed.

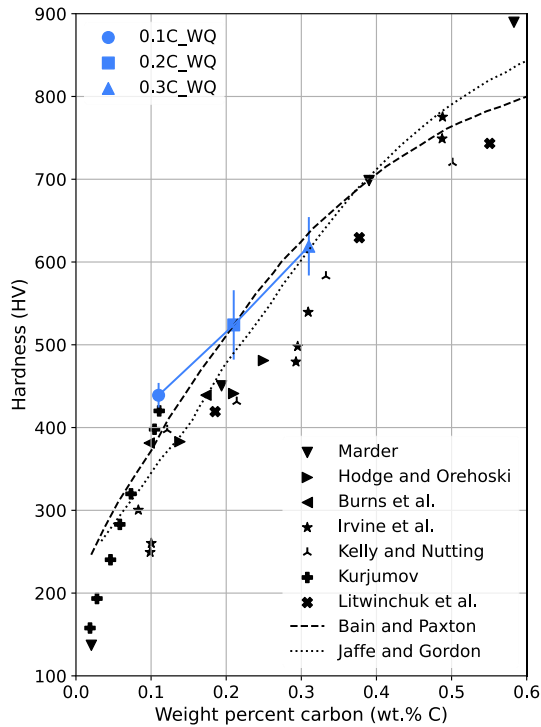


Figure 79: Vickers hardness as a function of the carbon content for the three alloys studied in the present work as well as values from the bibliography compiled by [9].

As reported by Krauss [9] from [99], the 0.2 % offset yield strength has a linear correlation with the square root of carbon content in as-quenched martensite as illustrated in Figure 80.a. At low carbon content a deviation of the linear correlation is observed due to the presence of polygonal ferrite in the microstructure as the hardenability becomes very low. The reason to this tendency is not totally clarified after [99].

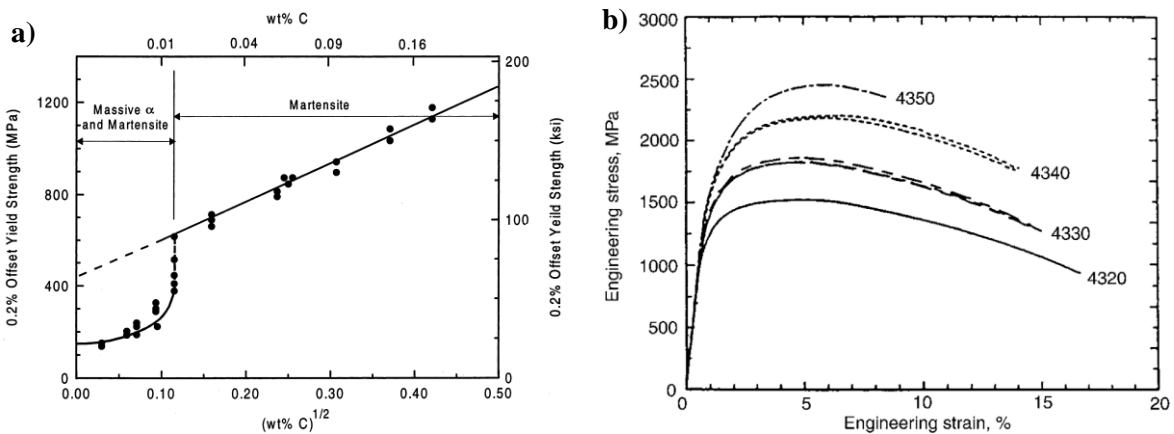


Figure 80: a) Yield strength (0.2 % offset) as function of the square root of the carbon content, from [9] based on [99]. b) Tensile curves of four tempered martensitic steels with different carbon contents (range 0.2 - 0.5 wt.%, ca. 2 wt.% Ni, ca. 2 wt.% Cr.), from [19].

For one side, the contribution due to solid solution in as-quenched martensite increase with the carbon content. However, as previously presented in Chapter II, the microstructure size decreases with the carbon content of the steel [92] as well as the dislocation density increases [27,92]. The evaluation of

the respective contributions of these hardening feature has not been discussed in detail in [99] and will be addressed in the present chapter. The real difficulty is that all the microstructural characteristics are in fact more or less linked in martensitic steels.

The carbon content has also an effect on the ultimate tensile strength (UTS) as can be observed in Figure 80.b. This trend was attributed to those of the yield strength evolution with the carbon content. This trend is not surprising as the hardness is known to be correlated to the ultimate tensile strength by the Tabor relationship ($UTS = 3 H_v$).

A possible interpretation of this sensibility of the YS is related to the strengthening by carbon in solid solution. It can be estimated by the Friedel's theory as [256]:

$$\sigma_c = \frac{C_T \mu}{30} \left(1 - \frac{T}{T_c}\right)^{3/2} \sqrt{X_c} \quad \text{Equation 37}$$

where C_T is the Taylor constant, T is the absolute temperature, T_c is the temperature at which the carbon solid solution strengthening is zero (estimated to 620 K) and X_c is the carbon atomic fraction. Krauss proposed also a square root law between the YS and the carbon content [9], but Winchell and Cohen a cube root [155]. So there is absolutely no consensus on the subject in the literature.

In the present work, if all the carbon atoms are in solid solution and contributing to the strengthening, carbon contribution to the YS is calculated as 208 MPa for the 0.1C steel [256]. In 0.3C steel the same contribution is 350 MPa [256]. Note that the observed relationship presented in Figure 80.a is linear. Therefore, other microstructural contributions also have to be considered. Although Rodriguez and Gutierrez proposed a linear equation between the carbon content and the strengthening [257], an overestimation of the carbon contribution is usually obtained by their relationship (758 MPa for the 0.3C steel).

As presented in Chapter II, the size of the microstructure domains (blocks or packets) is dependent on PAG size which is in particular related to the austenitization conditions among others (as carbide pinning). The increase of the hardness with the decrease of the PAGS has been reported by [258] while the linear effect of the block and packet sizes (related to the PAGS) on YS is reported by [86].

In Chapter II, the dependence of the dislocation density with the carbon content in low-carbon as-quenched martensite has been shown. In this case, a linear relationship was found. The strengthening due to dislocations predicted by the Taylor law presents a square root relationship with the dislocation density.

IV.1.A.2 Effect of the tempering treatments

The carbon in solid solution, the dislocation density and residual internal stresses would evolve during the tempering treatments. Hence, martensite behavior would evolve as a consequence.

The effects of the tempering heat treatments have been characterized by the evolution of the hardness by Speich and Leslie [169]. The authors showed a constant or increasing tendency up to 200 °C followed

by a decrease if the hardness at higher temperatures. A second increase may arise if the precipitation of secondary carbides occurs. A similar conclusion was found by Ohmura et al. [259] revealing the evolution of the microhardness and the nanohardness with the tempering. The decrease of the nanohardness with the tempering has been also reported by Tanaka et al. [260].

The evolution of the mechanical behavior including the tensile behavior due to tempering heat treatments has been studied for instance by Saeglitz and Krauss [246] and by Winchell and Cohen [155]. The latter focused on the effect of the carbon content as well as low tempering aging while the former focused on higher temperature tempering conditions. In their study, they show that the UTS decreases linearly with the Hollomon-Jaffe parameter² for three steels with different carbon contents as presented in Figure 81.a. In Figure 81.a, the linear correlations depend on the carbon content of the steels. A more complete analysis is presented for one of the 4340 alloys, with ca. 0.4 wt.% C, in Figure 81.b. The UTS of the steel decreases with the tempering temperature as previously observed while the yield strength presents an increase from the as-quenched state up to 150 °C, followed by a decreasing tendency.

In Figure 81.b, the difference between the UTS and the yield strength decreases with the temperature, which can be correlated with a decrease in the work hardening. The evolution of the tensile behavior of martensitic steels after different tempering conditions has been also studied more recently by Wang et al. [222]. In their steels, the yield strength decreases slowly up to 400 °C and then rapidly above. On the contrary, the decrease in their UTS is more regular versus the Hollomon-Jaffe parameter without any stages to put into evidence.

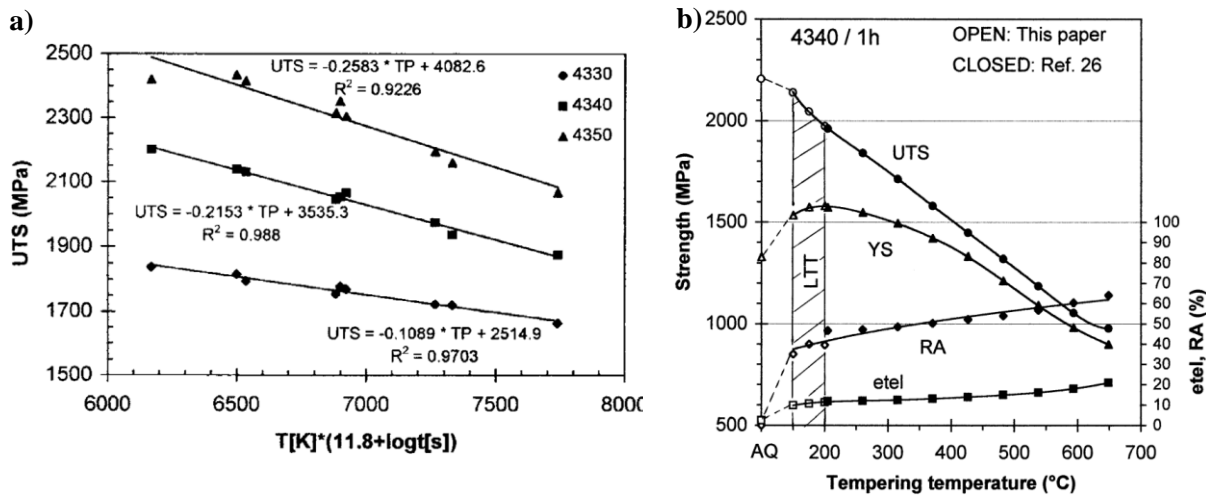


Figure 81: a) Evolution of the UTS with the Hollomon-Jaffe parameter for three steels with different carbon contents. b) Evolution of the UTS, YS, total elongation and area reduction of a 4340 steel tempered 1 hour at different temperatures, from [246].

In the same work the evolutions of the so-called microstrains related to the FWHM of diffracting peaks during tensile tests are presented, Figure 82. The authors observed that for non-tempered conditions and for tempered conditions (up to 300 °C) a decrease of the microstrain occurred during the tensile test.

² The Hollomon-Jaffe is an empirical parameter describing the severity of a heat treatment with a time/temperature couple. It serves to compare different tempering heat treatments with an implicit equivalence between the time and the temperature.

However, this tendency is not present for severely tempered conditions as 400, 500 and 600 °C. The first behavior is interpreted as a relaxation of internal stresses phenomenon while at higher tempering temperatures the distribution of local yield strengths and internal stresses effects are removed. At 500 and 600 °C, the microstrain increases with the deformation possibly due to a dislocation storage related mechanism. The evolution of the FWHM of diffracting peaks during the tensile test of the water-quenched state of the 0.2C steel is presented in Appendix E.

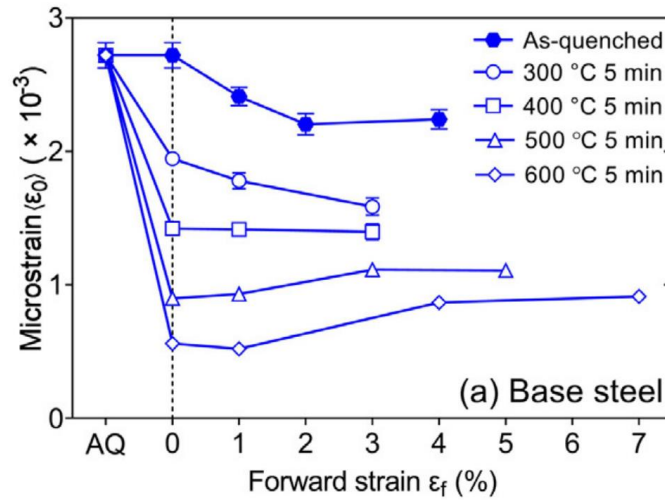


Figure 82: Evolution of the microstrain measured by X-Ray diffraction as a function of the macroscopic strain for an as-quenched condition and four tempered conditions for a 0.25 wt.% C, 2.4 wt.% Mn steel, from [222].

V.1.A.3 Local heterogeneities during mechanical testing

The lath martensitic microstructure presents a high complexity with several kinds of boundaries, different orientations of the sub-microstructure elements with different sizes, dislocation densities, tempering states and internal stresses. As a consequence, it is likely that all the sub-structure elements present different mechanical behaviors. In order to reveal these heterogeneities, local characterization technics must be employed.

In [45], nanohardness measurements were performed on a martensitic structure and correlated to the size of the studied domain and the proximity to the boundaries [45]. It appears, as expected, that the hardness in coarser sub-structures is lower than the one obtained in thinner ones.

Another largely used characterization technic is the digital image correlation (DIC). It allows to track the local strains at the scale of the microstructure during mechanical test.

In Morsdorf et al. [261], strain maps were obtained by DIC at different states of the tensile curve. The deformation response of martensite laths depends on three factors; the slip system orientation affecting the in-plane-slip, the interface orientation and the local characteristics of the microstructure (dislocation density, size and carbon distribution). Figure 83 presents a summary proposed by [261]. In the same work, it is also concluded that the nano-scale film austenite present before the deformation early transforms and, therefore, it might not contribute effectively to the overall plastic process. This last point as well as the high dislocation density presented in Chapter II challenge the theory proposed by Maresca

et al. [142,262]. Sugiyama et al. [263] also reported by DIC the strain heterogeneities in martensite at the microscale.

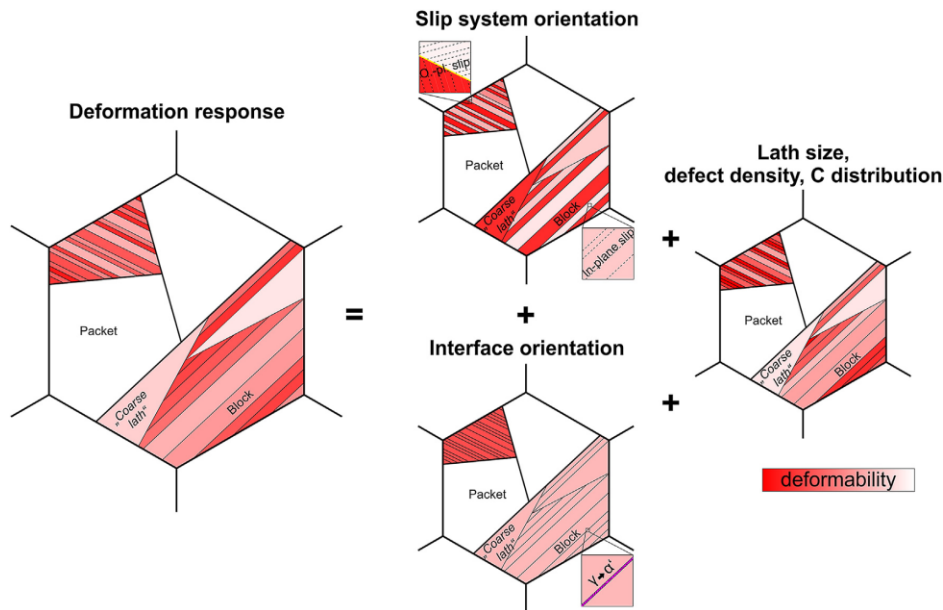


Figure 83: Schematic representation of the observed deformation response of the martensite at the microstructure scale (on the left) as a superposition of different deformation mechanisms depending on the slip system orientation, the interface orientation and the initial yield strength (function of microstructural features), from [261].

Tanaka et al. [260] combined DIC characterization with finite element modelling (FEM) and nanohardness measurements. The authors observed that with higher tempering temperatures the deformation of martensite becomes more homogenous and the distribution of nanohardness decreases, both indicators of a more uniform yield strength at the microstructure scale. The effects of tempering in the nanohardness are presented in Figure 84, showing a decrease of the mean values and of the dispersions with harder tempering conditions.

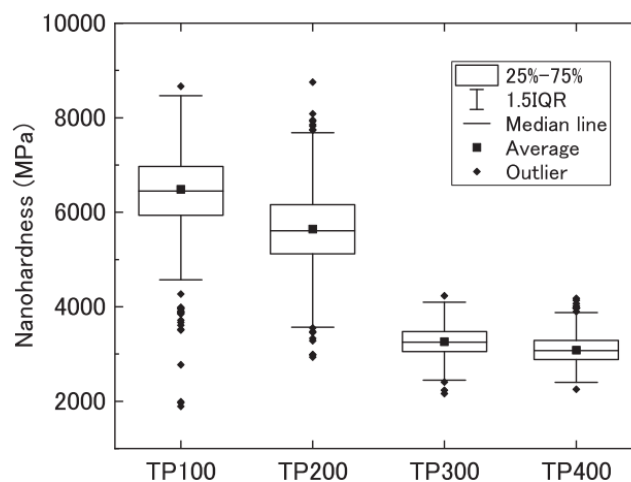


Figure 84: Nanohardness box plots at different tempering states (100, 200, 300 and 400 °C) of a 0.2C-2.0Mn steel, from [260]

Applying a different approach Harjo and Ungar et al. [42,115] observed the evolution of the diffracting peaks of martensite by neutron diffraction during a tensile test in order to deduce the evolution of the

dislocation density. The authors concluded that the observed behavior could be explained by considering the martensite as a bi-constituent aggregate. One constituent named as “soft-oriented” plasticizes before and its dislocation density decreases by in-plane-slip, while the other one named “hard-oriented” is not favored and its dislocation density increases during the tensile test.

The martensite present an interesting phenomenon when it is submitted to a tensile test, a narrowing of the diffraction peaks (observed in the AQ curve in Figure 82). This phenomenon has been reported in the literature by several authors [42,264–266], in relation also with Figure 82. Different interpretations have been proposed to explain the described behavior. While some authors proposed a fast mechanical recovery [42,264,265], others proposed instead a relaxation of internal stresses [266,267].

In conclusion, the link between microstructure and the mechanical properties of martensitic steels has been thoroughly studied in the last 50 years, highlighting the specific role played by the carbon content of the steel as well as the tempering conditions.

More recent studies have highlighted the short-coming of the previous works to describe the observed local behavior heterogeneities at the microstructure scale. This is the reason why new kinds of micromechanical frameworks have been designed to overcome such additional complexity.

IV.1.B Models for martensite tensile behavior

At least two different approaches are found in the literature regarding the modeling of the tensile behavior of martensite. The first one focuses on the prediction of the sole 0.2 % offset yield strength due to its importance for structural calculations (aircraft or automobile parts are supposed to work in the elastic regime). The aim of the second ones is to predict the work-hardening in the plastic regime and, thus, the whole tensile curve (up to necking at least). These latter are nevertheless less numerous. One of the underlying reasons is that the uniform elongation of martensitic steels is low. However, the study of the behavior of a material must not be limited to this range of uniform deformation because material continues to deform in the neckings. Thus, the prediction of true behavior beyond this uniform elongation is necessary, especially to understand the behavior until the rupture. Martensitic steels also show in that senses excellent fracture deformation, in particular tempered steels.

IV.1.B.1 Yield strength calculation

One of the most recurrent values extracted from a tensile curve is the 0.2 % offset yield strength (in the following usually referred as ‘YS’) as it is admitted to correspond to the beginning of the macroscopic plasticization of a material. The prediction of this important value from a technological point of view is a key subject.

In 1972, Malik and Lund proposed a simple equation to calculate the YS of a 0.4C tempered martensitic steel taking into account the precipitation and the dislocation density [268]. A more complex equation was proposed by Norström in 1976 [109] introducing additional size effects:

$$\sigma_{YS} = \sigma_0 + \sigma_i + k_y D^{-1/2} + k_s d^{-1/2} + k_{dislo} \mu b \rho^{1/2} + \frac{2\mu b}{L} \quad \text{Equation 38}$$

where σ_0 is the friction stress for pure iron (Peierls barrier), σ_i the strengthening of alloying elements in solid solution, D the grain size related to high-angle boundaries, d the grain size due to low-angle boundaries and k_y and k_s are coefficients. The last two terms refer to the dislocation strengthening (with k_{dislo} the dislocation-strengthening coefficient, μ the shear modulus, b the Burgers vector and ρ the dislocation density) and the last one to the precipitation strengthening (with L the mean distance between cementite particles). A similar equation is proposed by [269] for bainitic and martensitic structure with the exception that the size effect is not in a classical Hall-Petch formulation.

This formulation already made possible to integrate the contributions that we considered key in our work, modulo the effect of the internal stresses. Many formulations exist in the literature, and we have detailed this model as representative of the different works on YS prediction.

The Peierls stress is the minimum external stress required to overpass the lattice friction and drive a dislocation in a perfect and infinite crystal. There have been several estimations of this value reported in the literature for a BCC structure with values varying between 40 and 50 MPa at room temperature [270–273].

The substitutional solid solution strengthening depends on the concentration of the considered elements, their atomic size, the difference between their elastic modulus and the one of the iron and their electronic structure [171]. The total strengthening by alloying elements can be calculated as the linear sum of the contributions. The strengthening coefficients for the most common substitutional elements in a ferritic matrix are presented in Table 14.

Table 14: Effect of alloying elements on the YS for 1 wt.%, from [274].

	Mn	Si	Cr	Ni	Mo
σ_s	80	60	60	45	-

The strengthening by carbon in solid solution is much stronger due to the fact that it is an interstitial element in the iron matrix. It can be calculated by the Friedel's theory as presented in IV.1.A.1 Effects of the carbon content. In the mentioned model a homogenous distribution of carbon is considered. This last hypothesis is probably not totally true due to carbon segregation into defects (cf. Chapter III). Ansell proposed in his seminar work a model considering the carbon segregation produced in the austenite before the martensitic transformation [41]. The relationships proposed by [9,155] are not used in the present framework as they proposed a correlation between the carbon content and the YS and not the strengthening by solid solution.

The strengthening due to dislocations depends on the k_{dislo} constant which is the product of the constant of Taylor (C_T) and a geometrical parameter describing the dislocation interactions called α_{dislo} which usually varies between 0.25 and 0.45 at room temperature.

The size contribution can be considered using a Hall-Petch law as proposed by Norström [109] or as the inverse of the effective size as proposed by Bhadeshia and Young [269]. Zhu et al. [131] performed a study searching to determine the k_{size} constant on the bainite structures with a law as the one proposed by [269] and trying to define the structure size (as discussed in Chapter II).

The microstructure boundaries controlling in fact dislocation mobility and, thus, the plastic deformation of the lath martensitic structure does not reach consensus in the literature. The very local behavior of the lath structure has been studied by different authors combining micro-tensile test and crystal plasticity models. Although Kwak et al. [275] observed that the sub-block boundaries have not a significant effect on the yield strength, Du et al. [276] concluded that the sub-block boundaries are only slightly less effective than the block boundaries. On the contrary, Shamsujjoha [89] as well as HajyAkbari et al. [88] considered the block boundaries as the most effective and they applied a classical Hall-Petch equation to model the YS of their steel considering the block size. The Hall-Petch constant proposed by Shibata et al. for a block boundary and later used by HajyAkbari et al. was $210 \text{ MPa} \times \mu\text{m}^{1/2}$ which is higher than the value expected for a ferritic steel ($190 \text{ MPa} \times \mu\text{m}^{1/2}$) [277]. Recently, Kwak et al. determined that the k_{size} constant related to block boundaries is independent of the carbon content [278].

Regarding the precipitation strengthening encountered in tempered martensitic structures, different formulations are found depending on the considered precipitate/dislocation interactions (shearing or Orowan looping). In the previous mentioned work of Malik and Lund [268], the precipitation hardening is calculated as function of the mean planar spacing of carbide particles depending on the fraction and number of particles. Deschamps and Bréchet [279] calculated the precipitation strengthening for both mechanisms as well as Hirsch and Humphreys [280]. These contributions are both functions of the fraction and the size of the carbides. If the shearing mechanism is activated, the strengthening increases with the average particle radius. If looping is the activated mechanism the strengthening decreases with the average particle radius. The mechanism that is activated is the one that requires the lowest stress. Therefore, a critical radius permitting to minimize the hardening can be identified between both regimes.

The shearing possibility of transition carbides which are coherent with the matrix is an accepted fact but an open question remains regarding the shearing of the cementite. In a recent study [281], dislocations pile-up have been found at the cementite/ferrite interface proving their effectiveness to hinder obstacles for dislocation motion. Despite of being an incoherent precipitate, dislocations have been found inside some cementite carbide indicating that shearing mechanism is also possible.

If two kinds of carbides are present, i.e. transition carbides and cementite, it is also open to discussion whether the sum of both precipitation contribution should be linear or by a root sum of square laws. If both contributions are in a same order, meaning that dislocations encounter both carbides with a similar probability, the quadratic mean is preferable [282–284].

It is worth to mention that in the literature some non-linear sum of YS contributions are proposed as in the work of Galindo-Nava et al. [92]. In the mentioned work, the dislocation contribution as well as the size one are linearly sum. Then, a root sum of squares is performed with the precipitation hardening. A similar approach is used by HajyAkbari et al. [88] to determine indirectly the dislocation density based on the 0.2 % offset yield strength and the other microstructural strengthening mechanisms.

IV.1.B.2 Work-hardening models

The work-hardening curves of the martensite present key of characteristic features. First, the martensitic steels show a rather constant and relatively low microplasticity (around 400 MPa). The threshold of the microplasticity has been found independent of the carbon content [40]. Secondly, an initial high work-hardening rate was found for the martensitic steels [222], which increases with the nominal carbon

content [40], contrary to the conventional YS after 0.2% plastic strain which already depends on the work-hardening. The work-hardening curve present a soft decrease from the elastic regime (equal to the Young modulus) down to values close to 1×10^5 MPa at 4 % strain [222]. The higher work-hardening with the higher carbon content is sustained up to the end of the uniform elongation.

The work-hardening behavior of conventional steels is often interpreted as an isotropic hardening due to the increase in the SSD density. This is the reason why it could be modeled judiciously with a Mecking-Kocks-Estrin (MKE) approach. An example is the work of Bouaziz et al. observing the effect of size refinement in ferritic steels [81] or the one of Bonadé et al. [285,286] for tempered martensitic steels. These classes of model calculate a balance between defect creation and dynamic recovery. They could include strong interactions with grain boundaries with additional terms describing the SSDs but they are effective within the grain limit of few microns.

Two different model families have been developed in the literature to capture the as-quenched martensitic tensile behavior as well as the tempered one. In the first group the crystal plasticity method is based on MKE while in the second one the plastic behavior of martensite is interpreted as an extended elastic/plastic transition considering a polycrystalline aggregate.

The crystal plasticity models study the activity of the dislocations on each slip system, with its activation, possibility of change of slip system, formation and annihilation. A review of this method is presented by Roters and al. [287]. This method was applied to model lath martensite as by [275,288,289]. Sun et al. [289] showed that the width of the macroscopic slip band is related to the number of packets in the prior austenitic grain. Kwak et al. [275] showed that the effect of subblock boundaries is not very significant to increase the YS. The main disadvantages of this type of models are a higher computational cost as well as the need to a relatively high number of parameters to be calibrated. The results of this kind of model have to be revisited as Robertson showed that the plasticity mechanisms in lath ferrite (bainite/martensite) may differ from the conventional ones due to their size and orientation relationship [290]. It shall also be highlighted that the maximum strain hardening due to dislocation storage mechanism is about $Y/100$ (Y being the Young modulus) in BCC metals, according to [65]. As the measured strain hardening of the martensite upper-bounds this value, the strain hardening of martensite cannot be explained by a dislocation storage mechanism reasonably.

The second group of models are based on the distribution of internal stresses [266,267] and/or of distribution of local yield strength due to its sequential transformation [45]. The models based on the distribution of deviatoric internal stresses consider a distribution of the orientation of the internal stresses [266] or the magnitude of them [267]. One of the main achievements of this kind of models is the prediction of a decrease of the FWHM during the tensile test in accordance with the experimental results.

The model based on a volume distribution of local YS are based on the seminal work of Masing [46]. One of the first recent models using this approach is the continuum composite approach (CCA) proposed by Allain et al. [40]. The CCA model considers that the martensite is an heterogenous composite of phases with a distribution of local YS (called stress spectrum) as shown in Figure 85.a. It also supposes all the constituting phases of the composite are elastic-perfectly plastic. The distribution of YS is modeled empirically with an Avrami type distribution law, in which the width of the distribution increases with the carbon content. The localization conditions in is managed thanks to a single parameter law as:

$$\beta = - \frac{\Sigma - \sigma}{E - \varepsilon} \quad \text{Equation 39}$$

where Σ and E are the macroscopic stress and macroscopic strain respectively while σ and ε are local stress and strain respectively³. β is a fixed parameter adjusted to reproduce the strain heterogeneities observed in the literature (between different domains). It permits to tune the scale transition model between Voigt and Reuss bounds (iso-strain and iso-stress respectively). A previous version of the a model based on a YS distribution was postulated by Polak and Klesnil for the iso-strain condition [291].

The CCA model allows to predict with good accuracy different important characteristics of the martensite behavior, Figure 85.b. The first one is the low microplastic yield strength (around 400 MPa) which seems to be independent of the carbon content. The second one is the high work hardening which increases with the carbon content (consequence of the wider YS distribution). To explain such effect the width of the stress spectrum should also increase with the carbon content, revealing that the local stress/strain heterogeneities should also be more intense.

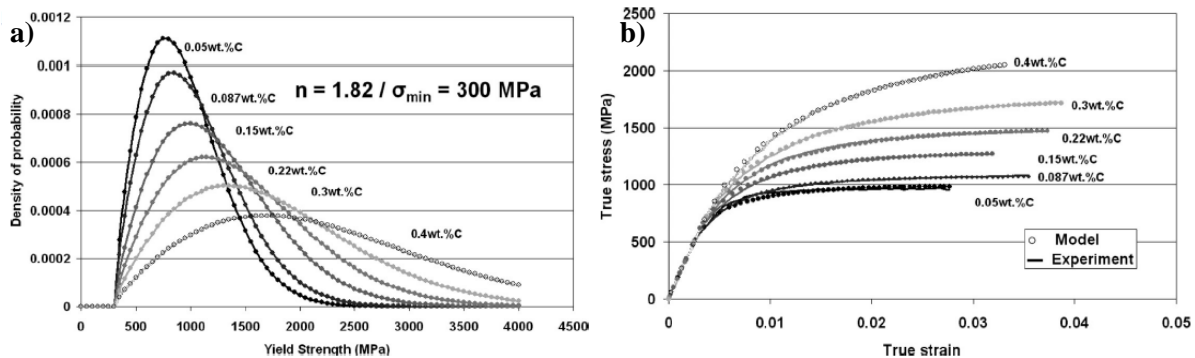


Figure 85: a) YS distribution as a function of the carbon content for different steels necessary to explain the work hardening of martensitic steels. b) The experimental tensile curves as well as the ones obtained with the distributions of YS shown in a) and the CCA model, from [40].

Third, the decrease in the strain hardening is due to the fact that as the macroscopic strain increases the plasticized fraction increases and as a consequence a higher fraction deforms plastically and a lower phase fraction (which remains elastic) continues to load.

The CCA model has been modified lately to consider not only the carbon content but also the manganese content in the YS distribution [292]. Another modification was lately incorporated by Cupertino et al. to modify the YS distribution as a function of tempering heat treatments [293]. Mathevon proposed in his thesis a modification to account for the tempering effects, introducing a parameter reproducing the narrowing of the YS distribution due to recovery and a precipitation hardening module [44]. Even if the CCA original model and its modifications allow to predict the tensile

³ In the present chapter the symbol ε will refer to the last definition, local strain, and the transition carbide epsilon will be referred as *eps*.

behavior of a wide range of martensitic microstructures, the presupposed YS distributions had no microstructural foundations.

A new model recently published by Wang et al. [43] takes into account a microstructural yield strength distribution, based on the CCA model, and an internal stress distribution, as assumed by Hutchinson et al. [266]. The so-called “integral composite model” (ICM) considers a YS distribution with a symmetrical gaussian shape as shown in Figure 86.a. This distribution presents a different shape compared to the original CCA model. ICM uses a uniform distribution regarding the deviatoric internal stresses presented in Figure 86.b. Although in this case no effective expansion of the yielding surface is produced, the starting stress of the element varies and thus the distance to the yielding surface changes, inset in Figure 86.b.

The apparent YS distribution is obtained by the combination of both distributions (microstructure and stresses). During the solicitation, the microstructure YS distribution, Figure 86.a, does not varies while a relaxation of the internal stresses occurs. The relaxation is calculated with a single parameter (in [43] called α_r). By considering the evolution of the apparent YS due to the variation of the deviatoric internal stresses distribution, this model is able to better capture the Bauschinger effect than the CCA model.

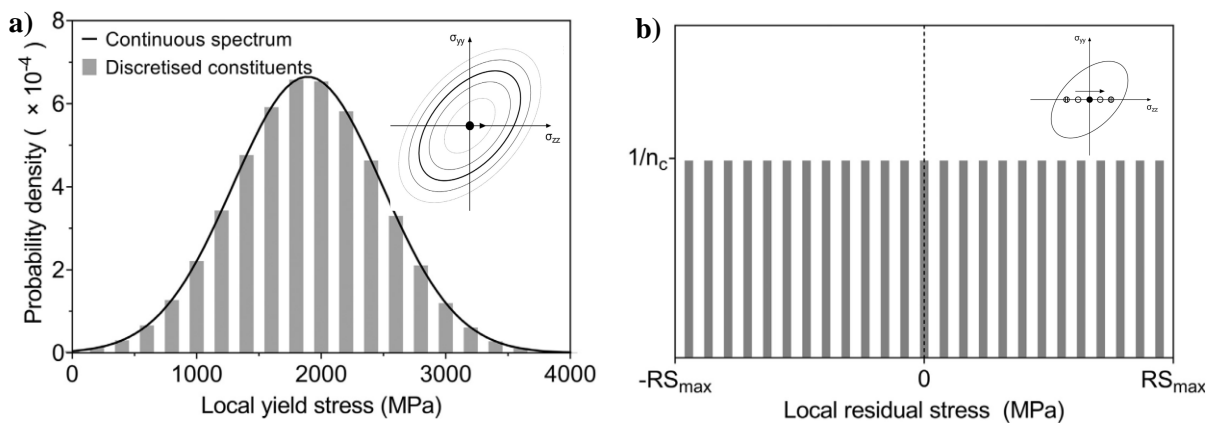


Figure 86: a) Local YS distribution with a gaussian type distribution, the different yielding surface in the insert. b) Uniform distribution of deviatoric internal stresses and its effect on the yielding. The presented figures are taken from [43].

One important drawback of the ICM is that as the probability distribution of the apparent YS varies, its integral does not remain constant and equal to one. This effect is clear in figures 8 and 9.a of [43]. The second one is that as well as in the original CCA model the YS distribution is presupposed and/or calibrated to obtain the experimental tensile curves.

The micromechanical model developed in this work will be based on the last introduced model taking into consideration both drawbacks. Special attention will be paid to the evolution of the probability densities during the simulations. The microstructural YS distribution will be based on measured microstructural features previously presented in this work.

In conclusion, martensitic steels have been known and used for millennia now, but the origins of their strength and work hardening have remained a source of controversy. Since few years, the understanding of their mechanical behavior is changing paradigm. Many researchers have put into evidence the interest

not to describe lath martensite as a homogeneous microstructure but more than as a multiphase aggregate, a composite. The multiphase aggregate is the result from the sequential nature of the phase transformations at low temperature. According to such new stochastic schemes, the martensite behavior is controlled by the microstructural heterogeneities, i.e. the spatial distribution of lath sizes, of dislocations, of carbon segregations and of the carbides and not only by their mean values. To these observable microstructural elements are added large distributions of hydrostatic and deviatoric internal stresses resulting from the transformation strains. This work contributes to this new movement by providing a quantitative description of these distributions in as-quenched and further tempered martensitic steels and their impact on their mechanical behaviors thanks to a complete micromechanical approach.

IV.2 Results: tensile behavior of the studied steels

In this section, we will present and discuss the results of the tensile tests on the studied steels in the as-quenched (water quenched) and tempered conditions.

Two tensile tests were performed for each studied condition considering the three studied alloys and the different tempering temperatures and holding times. The results were similar in both cases considering possible scattering due to the experimental configuration (excellent reproducibility of the experiments) as shown in Figure 87. In the following only one curve per condition will be shown as a consequence.

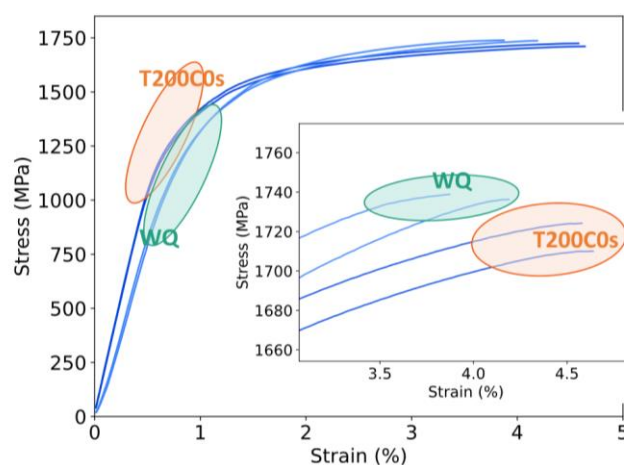


Figure 87: Duplets of true tensile curves at the water-quenched state and after heating upon 200 °C of the 0.2C steel.

In order to facilitate the present analysis as well the future comparison with model results, all the curves were normalized with an equal Young modulus set equal to 200 GPa. To do so, the apparent elastic behavior of each curve was determined between 200 and 500 MPa and, then, the elastic deformation was subtracted to all the tensile curves. Finally, an elastic contribution was reintroduced mathematically with the imposed Young modulus.

In the first following subsection the measured tensile curves are presented and compared pointing out the effect of carbon content, and the tempering effects. The evolution of the work hardening is also analyzed in the mentioned subsection.

IV.2.A Tensile curves of as-quenched state

The measured tensile curves of the as-quenched state of the three studied steels are shown Figure 88.a. Figure 88.b presents the work hardening rate for the three mentioned conditions. The tensile curves of the 0.1C and 0.3C steels present microplasticity in the range between 480 MPa and 550 MPa (more easily identified in Figure 88.b), which is in accordance with a low microplastic yield strength (around 400 MPa) almost independent of the carbon content, as reported in [40]. The 0.2C steels seems to presents microplasticity at higher stresses.

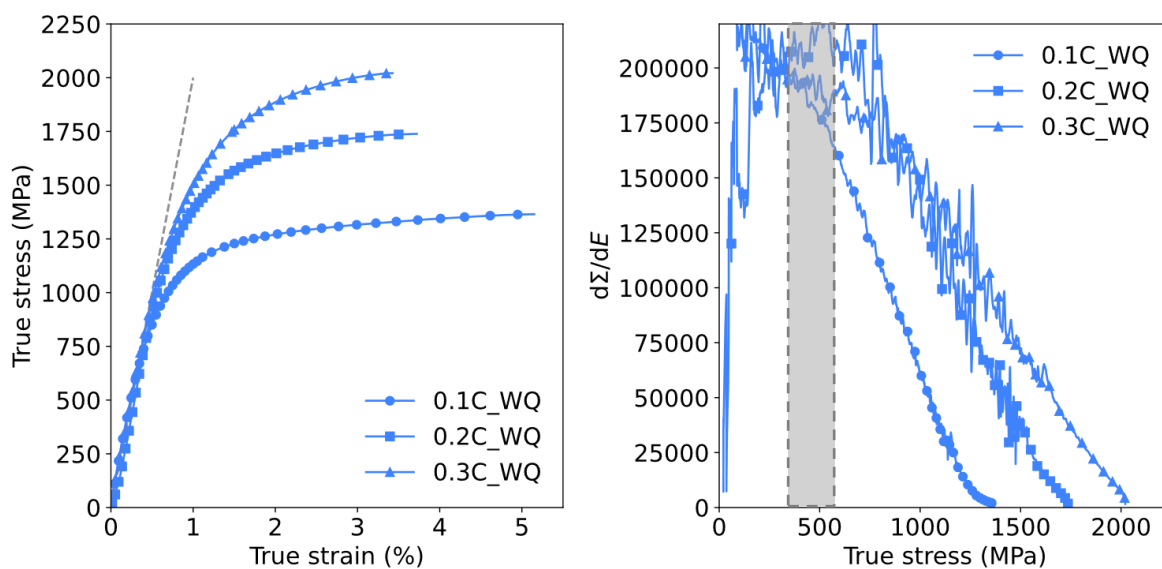


Figure 88: a) Tensile curves of the as-quenched state of the three as-quenched steels. The elastic behavior is represented by a dashed line b) Related work hardening curves. The grey region highlights the stress level corresponding to the start of their microplasticity ranges.

The work hardening rate of the three steels is high, higher than the maximal one due to dislocation storage mechanism [294] and it increases with the carbon content as described in [40].

IV.2.B Effect of tempering on the tensile curves

In Figure 89 the tensile curves of all the studied conditions are presented. In the first column the tensile curves are grouped by carbon content, 0.1C, 0.2C and 0.3C from top to bottom. In the second column the tensile curves are grouped by tempering temperature, 200, 300 and 400 °C from top to bottom. As previously, the 0.1C steel is marked with circles, the 0.2C with squares and the 0.3C with triangles. The 200 °C tempering heat treatments are represented in blue, the 300 °C ones in green and the 400 °C in red (the water quench samples in a light blue). The different time holdings are represented by different linstyles (WQ and 0s lines are solid lines, 30s are dashed, 60s are dash-point and 300s are dotted).

Firstly, the evolution of the YS is not strongly affected by the severity of the tempering. The evolution of the YS is more complex due to the presence of Lüders plateau at all the conditions treated at 400 °C and in the ones treated at 300 °C by 300s. The tensile curves of the tempering treatments at 300 °C for a shorter time do not present a discontinuous yielding but a shoulder

Secondly, for a given carbon content the work hardening rate and, thus, the maximal stress decrease with the severity of tempering. Higher maximum stresses in the tempered states are observed when increasing the carbon content. This last effect is an heritage of the as-quenched state.

Finally, a higher effect of the tempering is detected on work hardening rate and, thus, on the maximum stress when increasing the carbon content. The tensile curves of the 0.1C steels present low evolution of the maximum stress with the tempering (ca. 250 MPa) while the ones of the 0.3C steel present a variation of around 600 MPa.

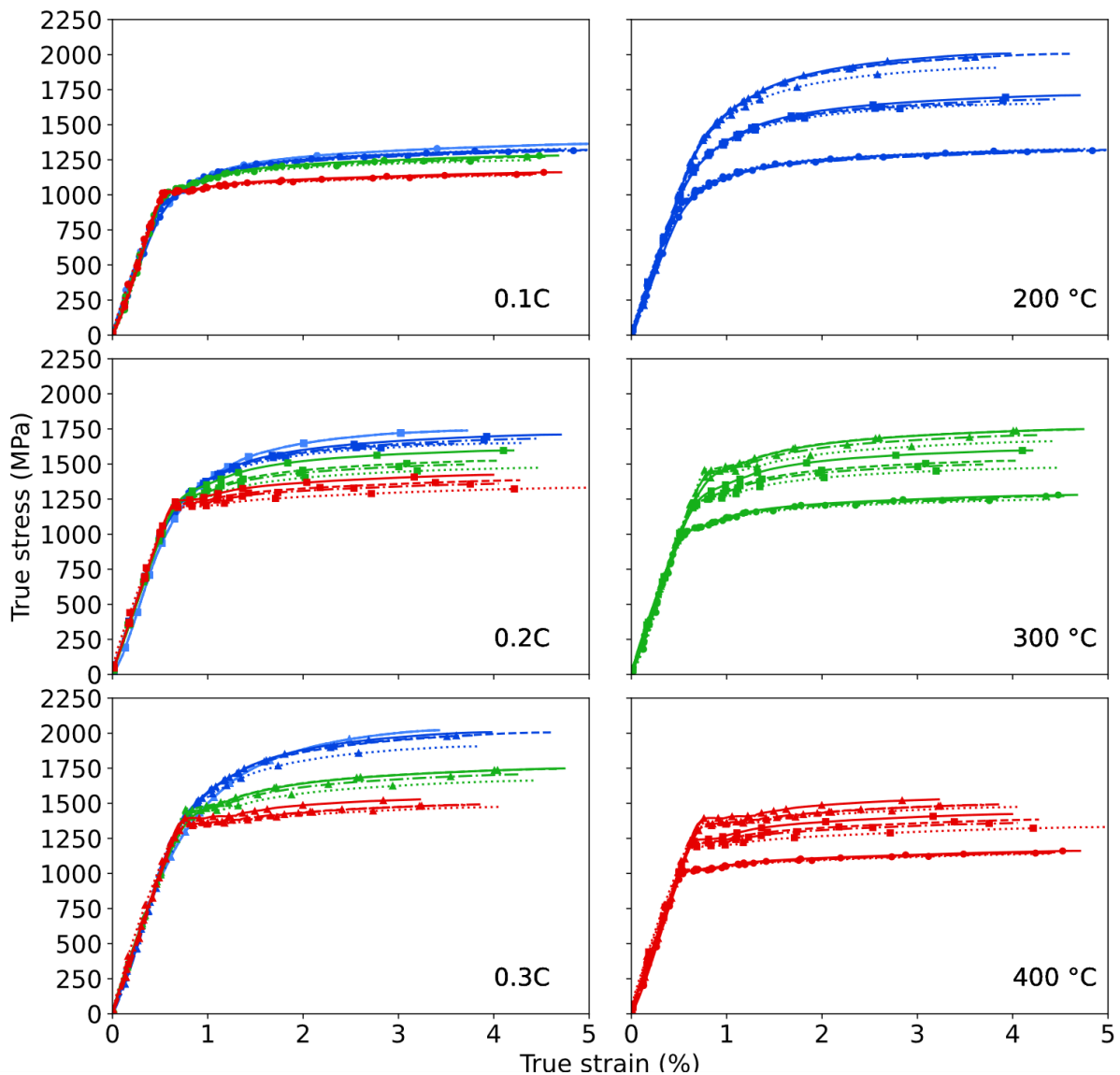


Figure 89: Tensile curves of all the tempering conditions plus the water quenched condition for the three studied steels in the first column. In the second column, same tensile curves at a given tempering temperature (200, 300 and 400 °C from top to bottom) for the different holding times for the three studied steels.

At the highest tempering temperatures the UTS decreases for all the carbon contents. However, the holding time does not present a clear effect in the 0.1C steel contrarily to the effect observed in the 0.2C and 0.3C steels in which longer holding times also induces a decrease in the UTS.

It is worth mentioning that in the tensile curves obtained after tempering at 400 °C, the elongation seems to decrease with the carbon content of the alloy and increase with the holding time.

The work hardening curves deduced from curves presented in Figure 89 have been calculated applying a moving average (a window of 20 points was selected) and represented in Figure 90. The structure of Figure 90 is the same of the one in Figure 89. The first column presents the results regrouped by steel while the second column is composed by three graphs regrouping the curves as function of the tempering temperature.

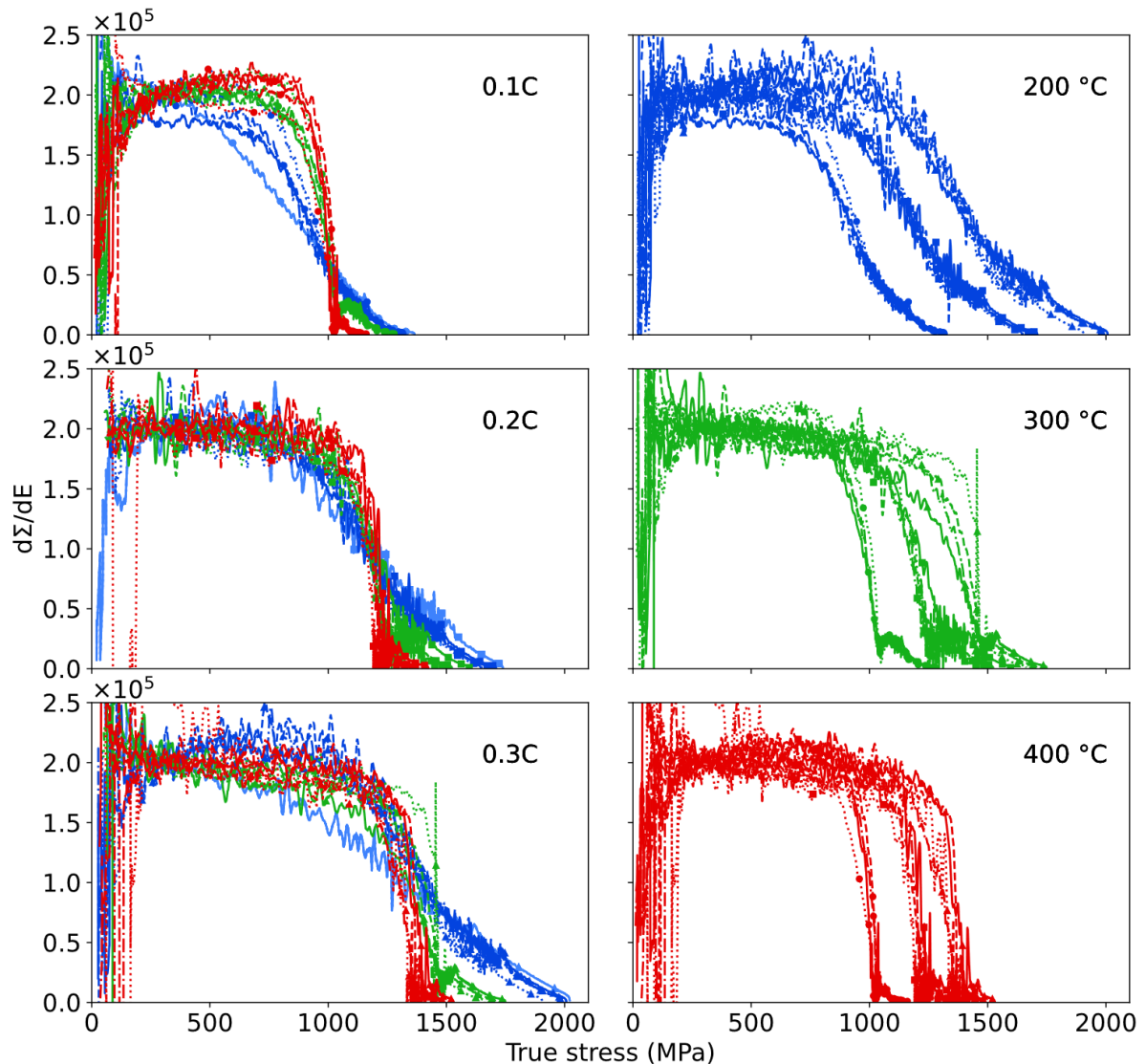


Figure 90: Work hardening rate as a function of the true stress, of each tensile curves presented in Figure 89. The same code applies.

All the curves regrouped by carbon content present a similar behavior for the three steels. The as-quenched condition (cf. Figure 88) presents an early yielding with a continuous decrease as the

macroscopic stress increases. As the temperature increases, the plasticity begins at higher stresses and the work hardening presents a faster decrease.

The main difference due to the carbon content is the start of the yielding. The slopes afterward depends only on the tempering but not on the steel.

In the work hardening curves obtained from the samples treated at 400 °C a fast decrease down to around zero is observed, corresponding to the Lüders plateau, followed by an increase and soft decrease up to the fracture. The work hardening curves from the samples treated at 300 °C also present a relatively fast decrease (slower than the ones presented at 400 °C) but then a second peak is observed, with a value around 2.5×10^4 .

The micromechanical model developed in the frame of the present work has as goal to predict the evolution of the tensile behavior of the different studied steels at the different tempering conditions. As a consequence, the evolution of the conventional YS and UTS as well as the work hardening could be calculated.

IV.3 Tensile behavior model

The micromechanical model developed in the present work seeks to understand and predict the tensile behavior of martensitic steels based on their main microstructural features, their distribution and the internal deviatoric stresses. Both contributions are essentially different as the first one expresses a distribution of local yield strengths at the microstructure scale (i.e. the threshold stress to trigger the plastic deformation) and the second one will be added locally to the applied stress state.

Making an analogy with the J2 theory, the first contribution would be more of an isotropic nature and the second one of a kinematical nature. The analogy ends there in that the CCA approach is based on the Masing's thesis as it considers that the material consists in different components with different elasticity limits (microstructural YS) and in mechanical interaction. The co-deformation of this multi-component material generates a macroscopic work hardening of kinematical nature based solely on the internal stresses between these components without any isotropic work-hardening at the component scale.

The proposed approach is in fact similar to the one developed by Wang et al. [43] (based on [40,266]) with two main additions:

- The distribution of the local Yield Strength related to the microstructure (later called microstructure YS distribution) will be predicted on the basis of the experimental observations presented in the previous chapters. The contributions of the dislocation densities, the microstructure sizes, the precipitates will be assessed separately and combined judiciously to describe the as-quenched and tempered states within a single framework. Contrary to Mathevon's approach, the evolution of these contributions with tempering will be described on a physical basis and not calibrated using JMAK functions.
- The model to predict relaxation of the internal stresses and, thus, the evolution of the related stress distributions have been reviewed to keep a more realistic sense of the density probability functions.

Like the models of Wang or Mathevon, the main interest of the approach is to propose a unified framework for treating both as-quenched and tempered steels, which makes it an extremely powerful prediction tool.

Our numerical simulation tool is a mean field multiphase aggregate approach considering numerous elements in interactions (typically more than 15000) with a simple localization law (same as [40]). These elements represent small volumes of our steel and have different individual mechanical behaviors. These behaviors are probabilistically dependent to the distributions of microstructural YS and internal stresses. The purpose of this section is to propose quantitative estimations of these distributions and to show how to combine the hardening contributions to predict the respective flow stresses of each constitutive element.

Figure 91 presents an schematic representation of the micromechanical model considering a microstructural Yield Strength distribution (left) and an internal stresses one (right). The microstructural Yield Strength of each element depends on the dislocation density (see color scale), the microstructural size (hatch spacing) and the precipitation state (dots). The internal stresses distribution is represented with a another color scale.

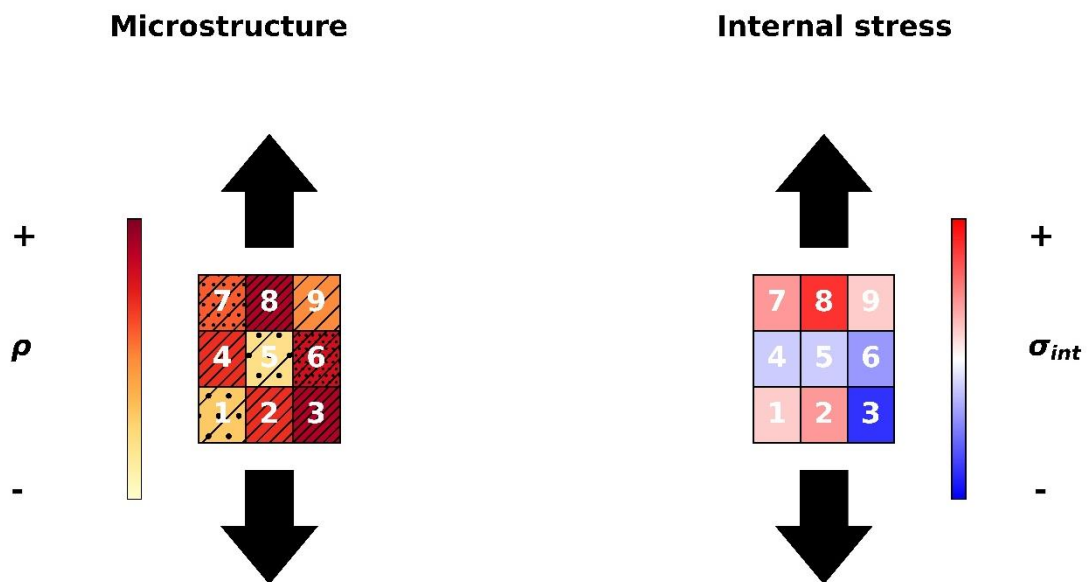


Figure 91: Schematic diagram of the micromechanical model considering a microstructure Yield Strength distribution (left) and an internal stresses distribution (right).

For instance, in the schematic diagram, elements 1 and 5 have a low dislocation density and larger microstructure (with precipitates) leading to a relatively low YS. However, the elements 3 and 8 have a high dislocation density and a finer microstructure and, therefore, a higher YS.

Even if the element 3 and 8 present a similar microstructural YS, they could present opposing internal stresses (left section of Figure 91). As a consequence, they will present different flow stresses.

IV.3.A Microstructure YS distributions and internal stresses

The microstructure YS is the local strength necessary to trigger plastic event in the microstructure, in an element of the aggregate. Or in other words, the stresses needed to make a dislocation move inside the martensite structure (lath, block, ...) taking into account all the microstructure obstacles hindering its movement.

This strength can be calculated as the sum of different contributions [109,269]; the Peierls barrier, the solid substitutional and interstitial solution strengthening, the size strengthening (related to the mean path of dislocations in between two “hard” boundaries), the dislocation density strengthening as well as the precipitation hardening, as discussed in the focus state of the art.

In the proposed model, these contributions for a given metallurgical state will be kept constant during the simulation of the tensile test. In fact the sole contribution which is expected to increase is the dislocation densities (at small plastic deformation). As discussed in [40] (CCA model), the initial dislocation densities in the martensite are so huge that a further increase during plastic deformation is unlikely. The possible increase is surely limited by dynamical recovery and the local work-hardening of a given element is also limited.

Note that as considered by [43], the presence of deviatoric internal stresses may affect the flow stress as a consequence they will be considered as a special contribution. The specificity of the internal stresses contribution comes from the fact that they evolve during the tensile test. As presented above, this kinematic contribution to the work-hardening will be considered.

IV.3.A.1 Lattice friction strength and solid solution strengthening

In the present work the Peierls barrier of the martensite is considered as a constant in each constitutive element and has been set equal to 50 MPa as in [92,272]. The substitutional solid solution strengthening (σ_{ss}) have been calculated for each steel as [274]:

$$\sigma_{ss} = 80 \times \text{wt. \% Mn} + 60 \times \text{wt. \% Si} + 60 \times \text{wt. \% Cr} \quad \text{Equation 40}$$

Substitutional solid solution strengthening has been calculated equal to 183 MPa, to 171.5 MPa, and to 107 MPa for 0.1C, 0.2C and 0.3C steel respectively. They are considered as constant. The main difference is due to the lower Mn content in the 0.3C steel. This second component of the microstructure YS is also supposed to be uniformly distributed (no Mn segregation between elements for instance).

IV.3.A.2 Size strengthening

The contribution to YS due to the mean free path of dislocations is calculated with the microstructure sizes determined in the Section II.2.B. As a reminder, the mentioned sizes have been determined by the line intercept method on SEM-EBSD micrographs. One has to keep in mind the importance of working with the spatial distribution and not with the occurrence distribution. The spatial distribution for the 0.1C, 0.2C and 0.3C steels with a misorientation angle threshold of 14° are presented in Figure 92.a.

The presented misorientation is higher than the misorientation expected between laths and sub-blocks, and would be related to the high angle boundaries (blocks, packets, PAGs) and, thus, to the more efficient boundaries in the microstructure to hinder dislocation motion and to provoke dislocations pile-ups (even if it is difficult to observe experimentally such mechanism), as discussed in the state of the art.

The strengthening induced by the size effect (σ_{size}) has been calculated with a Hall & Petch like model, even if the considered size are rather small:

$$\sigma_{size} = \frac{k_{size}(\text{misorientation angle})}{\sqrt{d}} \quad \text{Equation 41}$$

where d is the effective size and k_{size} is a constant depending on the considered misorientation angle. In the present study k_{size} has been set equal to $350 \text{ MPa} \times \mu\text{m}^{1/2}$ which is higher than the value reported by Shibata et al. for a block boundary ($210 \text{ MPa} \times \mu\text{m}^{1/2}$) [34] determined by microtesting and with a block size two times the one obtained in the present work.

As a consequence, the mean size hardening is 262 MPa for the 0.1C steel, 346 MPa for the 0.2C steel and 413 MPa for the 0.3C steel. With a higher carbon content a finer microstructure is obtained and, therefore, a higher size strengthening. This is the reason why it is often difficult to decorrelate the strengthening contributions in the martensitic steels.

Figure 92.b presents the calculated size strengthening distribution for each studied steels when applying the proceeding law to all the possible sizes found in the micrography. It can be observed that with a higher carbon content the mean value is not only higher but the distribution also widens. The minimal size strengthening in the 0.1C steel is 25 MPa meanwhile in the 0.3C it is 75 MPa. Only 2 vol.% of the 0.1C microstructure have a size strengthening higher than 700 MPa, while 3.6 vol.% of the 0.2C microstructure presents at least that hardening. In the case of the 0.3C steel the proportion is 7 vol.%.

These contributions will, then, serve to fix local properties of each constituting element of the aggregate using a stochastic approach.

In the present work, the size distribution is considered constant during the tempering because of the low temperature and the short holding times. Microstructure evolutions were reported by [100,101] but in the case of more severe tempering.

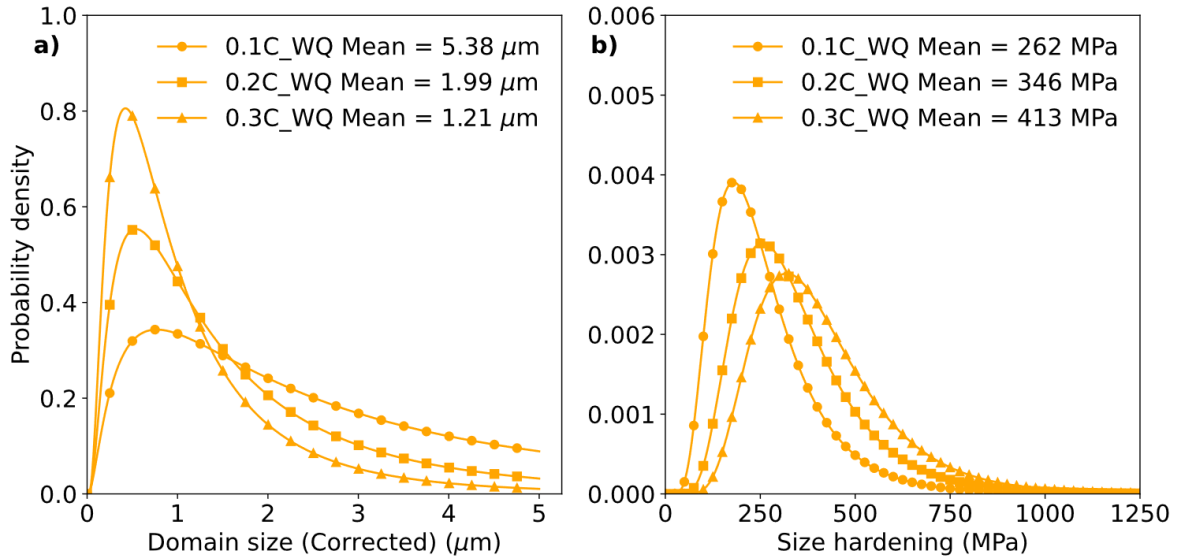


Figure 92: a) Size weighted distributions of domain size with critical misorientation set equal to 14° for the three studied steels. b) Distributions of size strengthening calculated from a) with Equation 41. The colors used in the present figure do not follow the chart presented in Section I.3.

IV.3.A.3 Dislocation density strengthening

In Chapter II it has been shown that the dislocation density is not homogeneously distributed in the microstructure. As a consequence, the dislocation strengthening of each element of our structure are potentially different.

The strengthening caused by the dislocation forest (σ_{dislo}) can be calculated by the Taylor law as:

$$\sigma_{dislo} = \alpha_{dislo} C_T \mu b \sqrt{\rho_{local}} \quad \text{Equation 42}$$

where α_{dislo} is a parameter related to the dislocation arrangement [83], C_T the Taylor constant, μ the shear modulus, b the Burgers vector and ρ_{local} the local dislocation density. In the present work α_{dislo} is set equal to 0.3, C_T equal to 3, b equal to 2.5×10^{-10} m and μ was calculated for each steel composition as by [148]. The α_{dislo} parameter for an as-quenched steel was reported to range between 0.17 and 0.3 with tensile strain, and between 0.33 and 0.44 for a 500 °C tempered condition by Dannoshita et al. [83]. Ungar et al reported 0.23-0.27 for cell-forming dislocation distribution and 0.45-0.47 for homogenous distributions [295]. The value herein utilized (0.3) is in the range of the reported values, and it is considered constant with the strain and for all tempering conditions.

IV.3.A.3.a As-quenched martensite

As for the size strengthening, the spatial distribution of dislocation strengthening is calculated from the spatial distribution function of the local densities (Figure 93.a). The results of this calculation are shown in continuous lines in Figure 93.b using a binning step of 25 MPa. The integral of the distribution is of course normalized as it corresponds to a density possibility function.

In order to smooth the experimental scattering and ease further calculations, the experimental distributions were modeled with reflected log-normal distributions functions, presented in Figure 93.b in dashed lines. The parameters of these empirical function have been calibrated with a least square method. The choice of this function will be justified later but its shape permit to describe well what happens during tempering.

The strengthening distributions of the 0.3C_WQ is better described than the one of the 0.1C_WQ steel. In this latter case, the fraction between 0 MPa and 550 MPa is overestimated while the one between 650 MPa and the maximum is slightly underestimated.

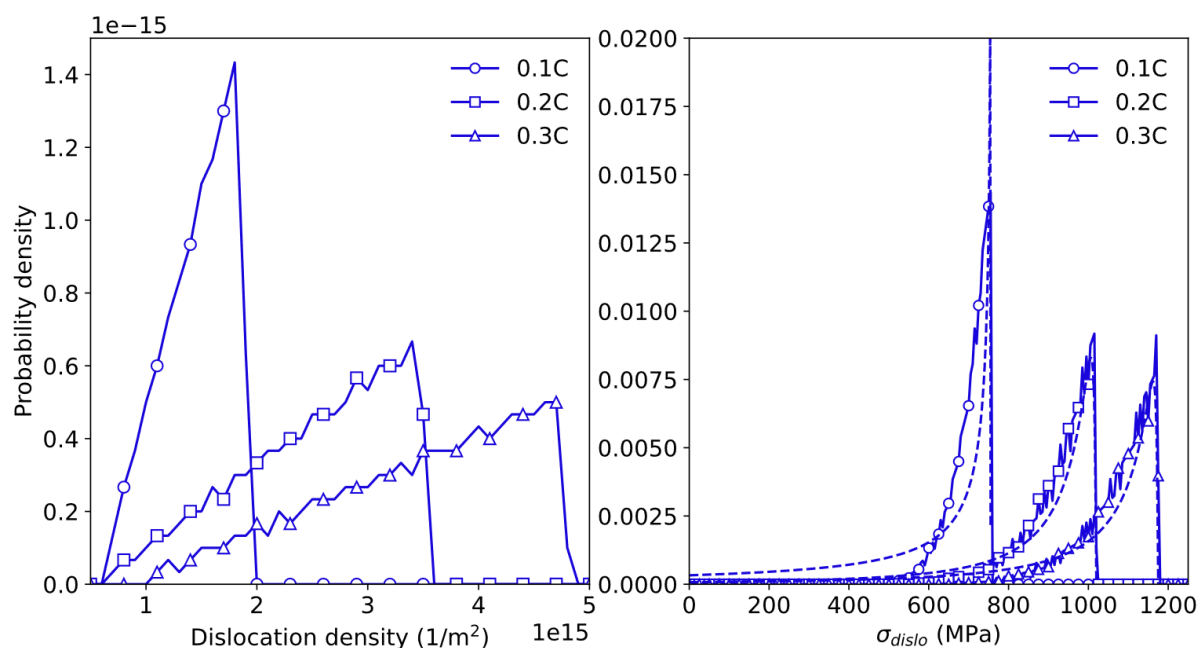


Figure 93: a) Distribution of local dislocation densities for the three studied steels. b) Distributions of dislocation strengthening calculated from the curves presented in a) (continuous curves) as well as the modeled reflected log-normal distributions (dashed curves).

Figure 93.b shows that the dislocation strengthening distributions are shifted to higher strength when the carbon content of the steel increases. The carbon content also leads to a widening of the distributions.

To exemplify, in the case of the 0.1C steel the proportion of martensite with a dislocation strengthening higher than 750 MPa is 10 % while in the case of the 0.2C it is 95 % and in the case of the 0.3C steel it is 99 %.

The dislocation strengthening of the softest and hardest possible elements are presented in Table 15 as well as the gap between both values.

The present calculations show that the dislocation strengthening is a significant contribution to the YS of as-quenched martensitic steels. If the mean value of the presented distributions are considered, then the dislocation density strengthening accounts for more than 0.7 times the conventional YS values (717 MPa over 1020 MPa for the 0.1C steel, 950 MPa over 1280 MPa for the 0.2C steel, and 1100 MPa over 1400 MPa for the 0.3C steel). HajyAkbariy et al. found for instance a contribution ratio ca. 0.5 [88], and Shamsujjoha close to 0.66 [89].

Table 15: Lowest and highest dislocation strengthening for the three studied steels as well as the difference between both values.

Steel	Lowest σ_{dislo} (MPa)	Highest σ_{dislo} (MPa)	$\Delta \sigma_{dislo}$ (MPa)
0.1C	460	760	300
0.2C	475	1045	570
0.3C	575	1180	610

The second important conclusion is the fact that a high dispersion of strengthening is obtained and, therefore, the dislocation strengthening is an important contribution of the microstructural YS distribution [40,43,44].

IV.3.A.3.b Tempered martensite

The distributions of local dislocation densities evolves with recovery during the tempering heat treatments, as previously presented in Figure 39 of Section II.3.B.2. Such mentioned distributions produce in turn a decrease in the dislocation strengthening. In Figure 94.a the distribution of the local dislocation densities of the 0.2C_WQ steel is presented as well as the ones obtained at different holding times at 300 °C. During the first 30 s the mean values decrease and the distributions narrow, then a slower evolution is observed with almost no change between 60 s and 300 s of holding.

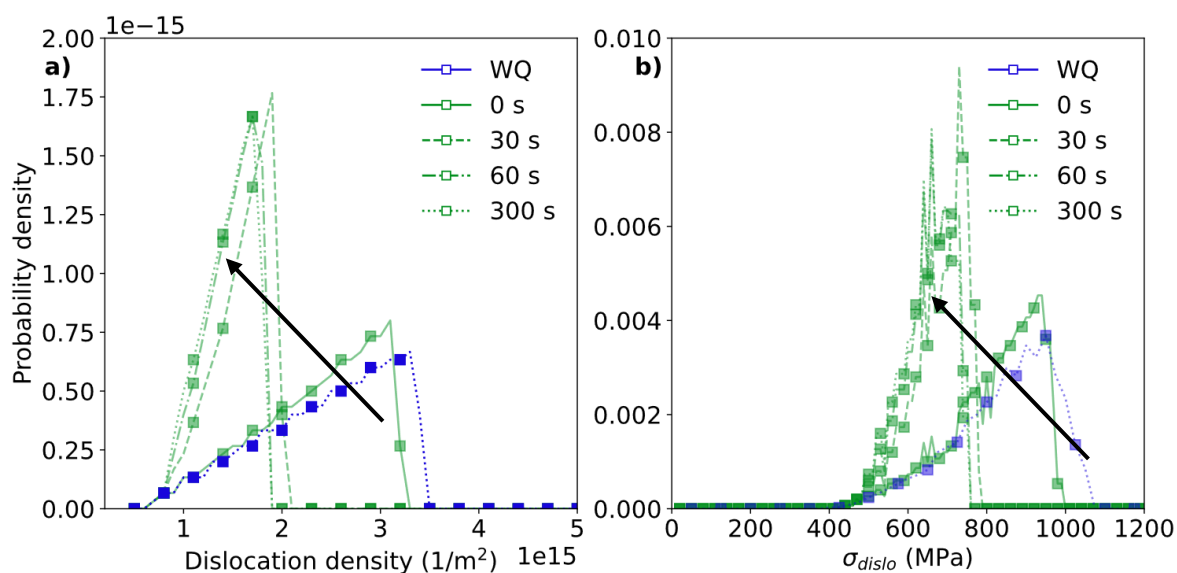


Figure 94: a) Distribution of local dislocation densities of the 0.2C_WQ steel tempered at 300 °C during different holding times (0, 30, 60 and 300 s) and in the as-quenched state. b) Dislocation strengthening for the distributions presented in a).

The corresponding evaluations of the strengthening distributions are shown in Figure 94.b. As expected, the statistical spread of the dislocation strengthening decreases with the holding time reaching a stagnant state after 60 s. The dispersion of the microstructural strengthening thus evolves with the tempering. In the case of the presented 300 °C tempering the largest spread is 530 MPa at 0s of holding, 320 MPa at

30s, 290 MPa at 60s and 280 MPa at 300s while in the initial water-quenched condition is was 570 MPa. In Figure 94 the calibrated log-normal functions are not presented for the sake of readability (the maximal reduced chi-square is 9×10^{-7}).

The same kinds of calculation have been carried on the three studied steels for all studied tempering conditions. The case shown here is just an example of the applied methodology.

IV.3.A.4 Strengthening due to carbon: interstitial solid solution strengthening and/or precipitation strengthening

Carbon atoms in solid solution occupy interstitial sites introducing lattice deformation which increases the strengthening of the material due to a higher resistance to the dislocation motion. Different mechanisms have been proposed to describe such interactions. As a consequence, the solid solution strengthening of carbon can be calculated by different equations found in the literature which presents different dependencies to the carbon concentration. In the present work, we propose to use also the Friedel's theory discussed in the state of the art (Equation 37).

The carbon atoms segregated on defects atmospheres could also induce a strengthening effect. The expected contribution should be similar to the strain ageing mechanism [296]. An extra stress is needed to unpin the mobile dislocations from their Cottrell's atmosphere. Nevertheless, when freed, the dislocations can move freely, the carbon in the former segregations only contributes to the solid solution (except that the carbon atoms are not strictly randomly spread). This is the reason why we will consider in the following that the calculated segregated carbon also contributes to the solid solution hardening, according to Equation 37. As a consequence, our modeling approach is not suitable so far to predict the possible Lüder's plateau that could appear in severe tempering conditions (cf. Figure 89) (300 °C and above).

Carbon can also form more stable precipitates during tempering. The precipitated carbides act as obstacles affecting the dislocation motion and two classical mechanisms are often involved to explain how the dislocations may overcome them; the shearing mechanism and the Orowan's looping. Depending on the local process, the precipitation strengthening can be calculated as:

Shearing:
$$\sigma_{shear-i} = K_{shear-i} \sqrt{f_i} \times r_i$$
 Equation 43 [279]

Bypassing:
$$\sigma_{bypass-i} = 0.4 K_{bypass-i} C_T \mu b \frac{\ln\left(\frac{2r_i}{b}\right)}{L\pi\sqrt{1-\nu}}$$
 Equation 44 [280]

with
$$L = r_i(\sqrt{\pi/f_i} - 2)$$

where $K_{shear-i}$ is a parameter related to the resistance of the precipitate to be sheared, r_i and f_i are the radius (nm) and fraction of the i precipitate, C_T is the Taylor factor (set equal to 3), μ the shear modulus (depending on the composition [148]) and ν the Poisson ratio. A parameter ($K_{bypass-i}$) has been introduced to take into consideration that not all the carbides are allocated in the matrix but a fraction of them is precipitated at boundaries with a different strengthening effect.

In the presence of both types of carbides (epsilon and cementite), the strengthening of each kind is calculated by Equation 43 and Equation 44 and then it has to be combined. If the dislocation obstacles are producing a relatively similar strengthening then a quadratic mean is used to calculate the combined precipitation strengthening (σ_{prec}) [282].

In the present model, the solid solution strengthening (including segregated carbon) and the precipitation strengthening are calculated during the tempering simulations for each element of the aggregate as both are affected by the density of dislocations. As a consequence, the strengthening contribution of carbon is not uniform at the microstructure scale and could depend on its state (solid solution, segregation, precipitates). However, in the as-quenched state, as the carbons atoms are either randomly distributed or segregated in the worst scenario, the contribution is thus considered as uniform (and calculated with Equation 37) before any tempering treatment.

The calculated strengthening by carbon in solid solution is 207, 288, and 351 MPa for the 0.1C, 0.2C and 0.3C steels respectively. The strengthening by precipitation would be calculated later as it is function of the carbide fractions and sizes.

IV.3.A.5 Deviatoric internal stresses

The specificity of the martensitic transformation is to be displacive and associated to a significant strain (shear and volume strain according to Bain theory). This characteristic explains that huge internal stresses (both hydrostatic and deviatoric) are built progressively at the microstructure scale between all the microstructure features. The presence of self-accommodating variants is not sufficient to relax the whole. As a consequence, different internal stresses are expected to be found in the elements of our micromechanical model, as sketched in Figure 91.

These internal stresses must be considered independently of the local microstructure YS which depends on the local microstructure size, carbon state, dislocation densities.

In fact, the yield strength of a material is usually calculated based on microstructural features as proposed by Norström et al. and Bhadeshia and Young [109,269]. However, if deviatoric internal stresses are present, then the material may be closer (or farther) of a flow surface as schematized in Figure 96. If the deviatoric stresses ($\sigma_{int, str}$) are aligned with the tensile direction (direction of the wide arrow), then they will be facilitate the yielding and a opposite effect occurs in the case of nonaligned stresses.

The main issue we have faced in this work is the description of this internal stress state. We have not been able to identify in the literature any sufficiently convincing experimental data or numerical simulation results to predict this state, except perhaps at the scale of a few blocks or PAGS [30,297,298].

The mean hydrostatic internal stress of the austenite can be obtained from the lattice parameter as in [138] with values up to 1 GPa in compression. From it, the mean hydrostatic stress of the martensite can be calculated (knowing the fractions and a neutral total stress state). However, no information about the deviatoric component of the stresses or their distribution can be obtained by this method.

As a consequence, as Wang et al., we have been obliged to presuppose a statistical and spatial distribution of these stresses. Although Wang et al. utilized a distribution of deviatoric internal stresses and the yield strength [43], the distribution of deviatoric internal stresses was considered as uniform. In

the present work a gaussian distribution will be considered as it seems more realistic. In fact it is unlikely that the same fractions of martensite are be summited to the maximum tensile/compression state and to with a neutral internal stresses state.

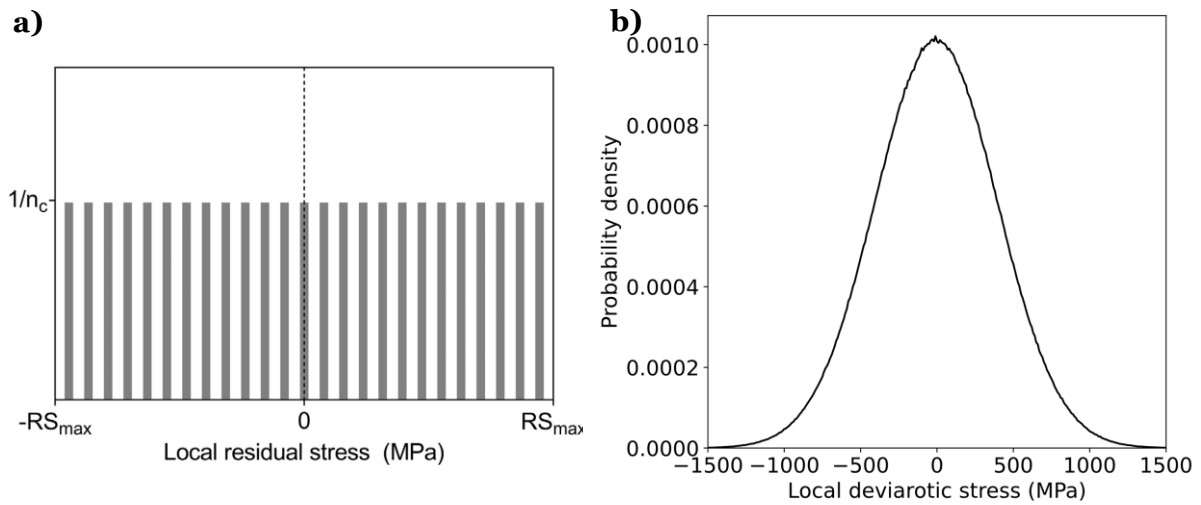


Figure 95: a) Uniform distribution of deviatoric internal stresses utilized by [43], from same work. b) Gaussian distribution proposed in the present work.

The deviatoric internal stresses produces a displacement of the stress state of the element, as represented in Figure 96. A positive deviatoric stress would reduce the gap to the flow surface while a negative one would increase it.

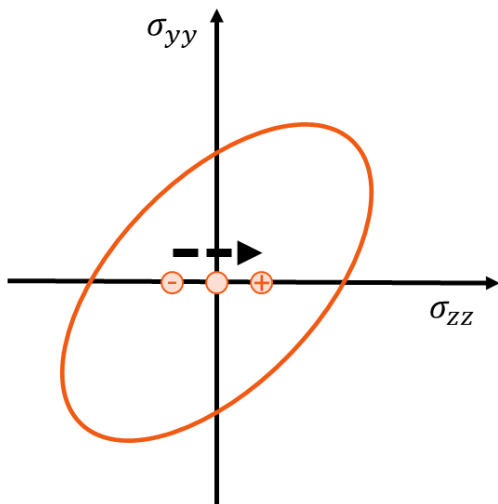


Figure 96: Effect of deviatoric internal stresses on a material, displacing the initial state with respect the yielding surface.

The local triggering of the plastic deformation is reached at the flow stress (σ_{flow}) which is calculated as the linear sum of the local microstructural YS (σ_{YS}) and the local deviatoric internal stresses ($\sigma_{int str}$) as:

$$\sigma_{flow} = \sigma_{YS} + \sigma_{int\ str}$$

Equation 45

IV.3.A.5.a As-quenched martensite

The distributions of the deviatoric internal stresses of the three steels at the as-quenched state were calculated with a gaussian probability distribution function. The standard deviation was set equal to 400 MPa for the three steels. The calculated distribution is presented in Figure 95.b. The analysis of the effect of the distribution of internal stress on the modeled tensile tests will be presented in Appendix F.

IV.3.A.5.b Tempered martensite

During tempering the internal stresses should relax progressively. This mechanism has been modeled using a Zener-Wert-Avrami function. The thermal residual stress relaxation can be calculated as [299]:

$$\sigma_{int\ str} = \sigma_{int\ str}^0 \exp(-(At)^m)$$

Equation 46

with

$$A = B \exp(-\Delta H/k_b T)$$

where $\sigma_{int\ str}^0$ is the initial deviatoric internal stresses, m is a constant which depends of the dominant relaxation mechanism, k_b the Boltzmann constant and B a material parameter. Different values are reported in [299] for the required constants; ΔH between 2.99 and 3.3 eV, m in the range 0.122 and 0.172, and B between 6.09×10^{17} 1/min and 1.22×10^{21} 1/min. In the present work as no possible calibration of the relaxation equation could be performed based on experimental results, the parameters were chosen in close relationship with the ones proposed by [299]. B was set equal to 1.22×10^{21} 1/min, m equal to 0.122 and ΔH equal to 3.1.

In Figure 97.a the evolution of the internal stresses with initial values of 200 MPa and 500 MPa during holdings at two temperatures (200 °C and 400 °C) are presented to illustrate the evolutions predicted by Equation 46. A fast relaxation occurs during the first seconds followed by a stagnation. The internal stress values at the stagnation depend on the initial value as well as on the holding temperature. At higher temperatures, a stronger relaxation phenomenon occurs as expected.

Figure 97.b presents the evolution of a gaussian distribution of internal stresses after 300s at 200 °C and 400 °C. The distribution before the holding is represented by a black line, while the one obtained after the relaxation is in blue and in red for the holdings at 200 °C and 400 °C. At 200 °C the effect of the relaxation is not significant while a clear effect is observed at 400 °C. Note that even if a clear shrink is produced by the holding at 400 °C, a spread remains.

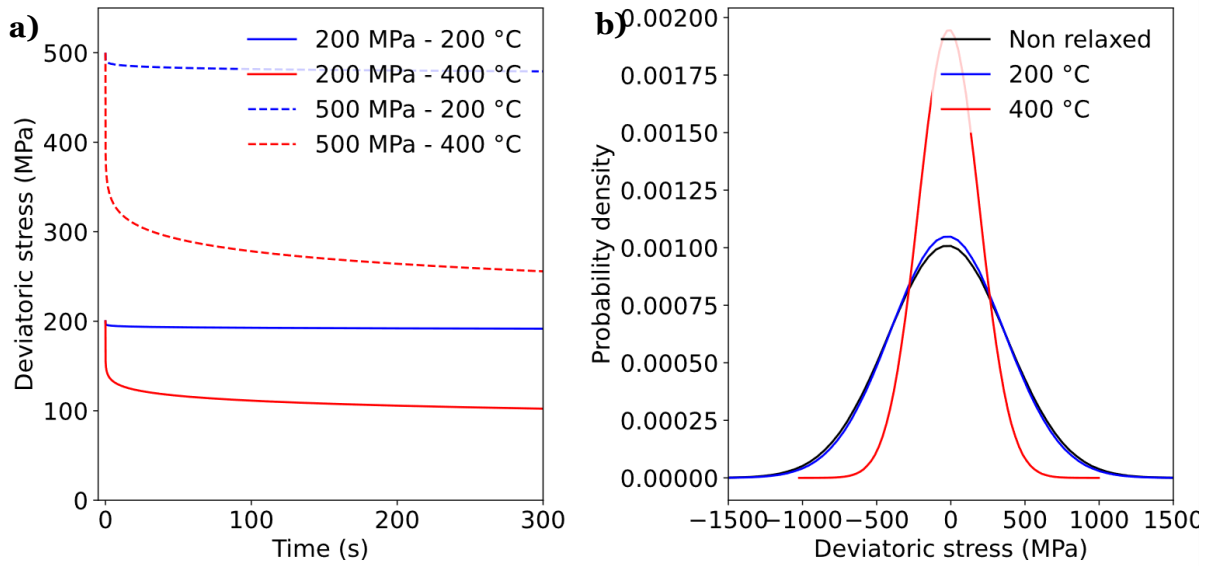


Figure 97: a) Relaxation of the internal stresses during a holding at 200 °C and 400 °C, with initial values of 200 MPa and 400 MPa. b) Evolution of a gaussian distribution of internal stresses (standard deviation set equal to 250 MPa) after 300 seconds at 200 °C and 400 °C.

IV.3.B Calculation of the flow stress distributions

IV.3.B.1 YS distributions

The yield strength involving different strengthening mechanisms can be calculated simple algebraic or quadratic mean according to the literature [92,109]. However, when taking into account the distributions two main issues must be considered; the addition rule and the stochastic approach to correlate the strengthening mechanisms.

It is not at all obvious that we can consider that the contributions to hardening are statistically uncorrelated, and meet randomly in the elements of our simulated aggregate. By analyzing the martensitic microstructure and the martensitic transformation sequence, Morsdorf et al. concluded that the first formed martensite presents the largest size with the lowest dislocation density while later formed martensite would present a smaller size and a higher dislocation density [45]. Thus, the first formed martensite would have low contributions from both mechanisms, while the later formed one would present high contributions from both mechanisms. As said above, the tempering mechanisms (segregation and precipitation) could also depend on the density of dislocations and are, thus, correlated.

The mentioned correlation between large sizes and low dislocation densities is the base from the here proposed “soft-soft correlation”. This correlation has been preferred to the random allocation of the properties based on the metallurgical observations described above.

When considering only the contributions of size and dislocation density, we can define the spatial density probabilities as:

$$F_{size}(\sigma_{size}) = \int_0^{\sigma_{size}} f_{size}(\sigma) d\sigma \quad \text{Equation 47}$$

$$F_{dislo}(\sigma_{dislo}) = \int_0^{\sigma_{dislo}} f_{dislo}(\sigma) d\sigma \quad \text{Equation 48}$$

Figure 98.a shows the cumulated functions ($F_{size}(\sigma_{size})$ and $F_{dislo}(\sigma_{dislo})$) while the probability density distributions ($f_{size}(\sigma_{size})$ and $f_{dislo}(\sigma_{dislo})$) are presented in Figure 98.b.

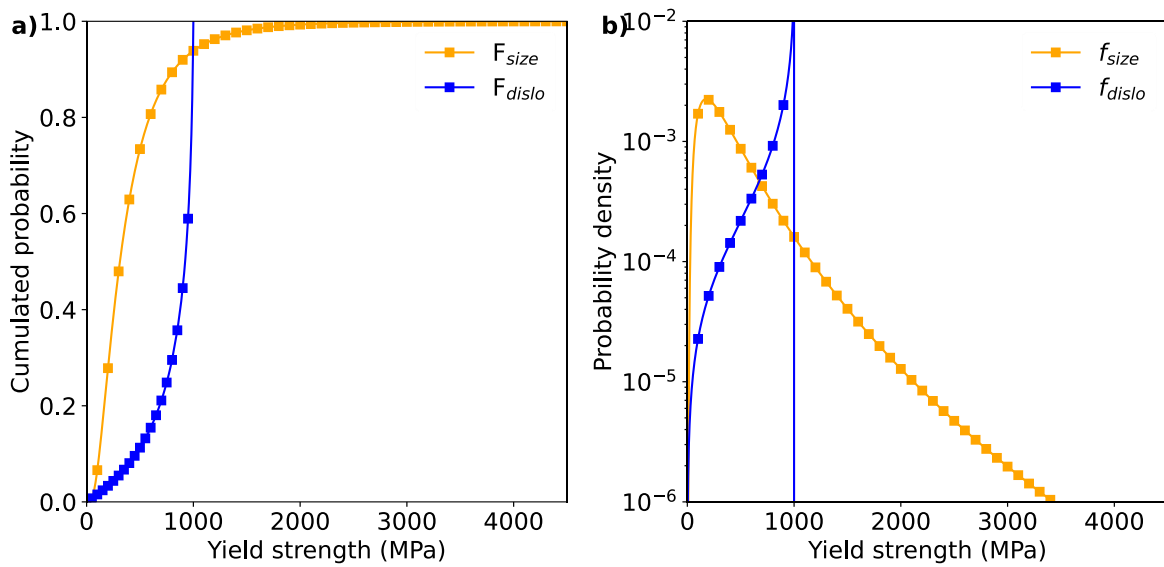


Figure 98: a) Cumulated distribution of the size hardening ($F_{size}(\sigma_{size})$) and dislocation hardening ($F_{dislo}(\sigma_{dislo})$). b) Corresponding probability density functions $f_{size}(\sigma_{size})$ and $f_{dislo}(\sigma_{dislo})$.

For a given fraction F of the microstructure the corresponding strength given by the dislocation hardening is σ_{dislo} and can be calculated as:

$$\sigma_{dislo} = F_{dislo}^{-1}(F) \quad \text{Equation 49}$$

and the corresponding strength given by the size hardening is σ_{size} :

$$\sigma_{size} = F_{size}^{-1}(F) \quad \text{Equation 50}$$

If a linear sum of the strengthening mechanisms is considered, the same fraction F is attended at:

$$F_{comb}(\sigma_{dislo} + \sigma_{size}) = F \quad \text{Equation 51}$$

The combined strengthening at the a fraction F is then defined as:

$$\sigma_{comb} = F_{dislo}^{-1}(F) + F_{size}^{-1}(F) \quad \text{Equation 52}$$

Finally, the following expression can be obtained:

$$F_{comb} \left(F_{dislo}^{-1}(F) + F_{size}^{-1}(F) \right) = F = \int_0^{\sigma_{comb}} f_{comb}(\sigma) d\sigma \quad \text{Equation 53}$$

This expression is difficult to exploit. Therefore, a numerical approach was developed to calculate this integral, step by step, starting from the weakest fractions. The correlations are expressed by the fact that the mechanical contributions of the two mechanisms (size and dislocation density) are sought for the same fraction, starting from the lowest strength for both contributions. The process is represented schematically in Figure 99.

Figure 100.a shows the previously presented cumulated probability F_{size} and F_{dislo} for the 0.2C_WQ steel. The calculated F_{comb} is presented in grey line. An additional curve is presented in which the constant contributions are added. It corresponds to a shift of F_{comb} to higher stress levels. It accounts for the substitutional solid solution strengthening as well as the carbon solid solutions strengthening (note that the chosen example is a water-quenched state).

From the calculated F_{comb} , the probability density of the combined distribution has been calculated and it is shown in Figure 100.b. In the same graph the respective probability density of the size and dislocation density strengthening are presented. The probability density of the combined distribution keeps a right skewness as the size strengthening distribution but is wider than the last one. The probability density of the combined effects plus the constants strengthening presents values non-zeros from 575 MPa up to 3700 MPa. The shape of the distribution (right skewness) and the range of the values shows remarkable similarity with the presupposed distribution of the work of Allain et al. [40], (cf. Figure 85).

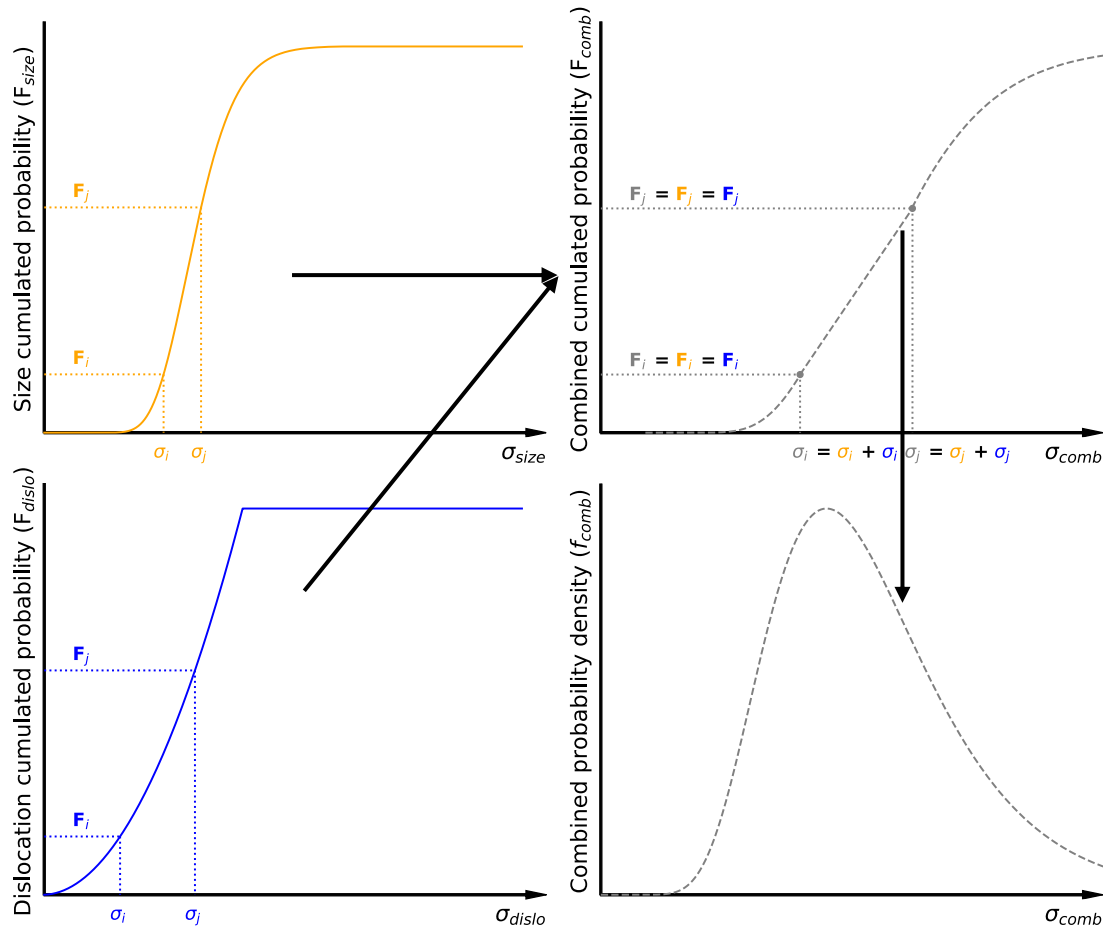


Figure 99: Schematic representation of the algorithm utilized to combine the strengthening mechanism and obtain the combined strength distribution of an as-quenched state.

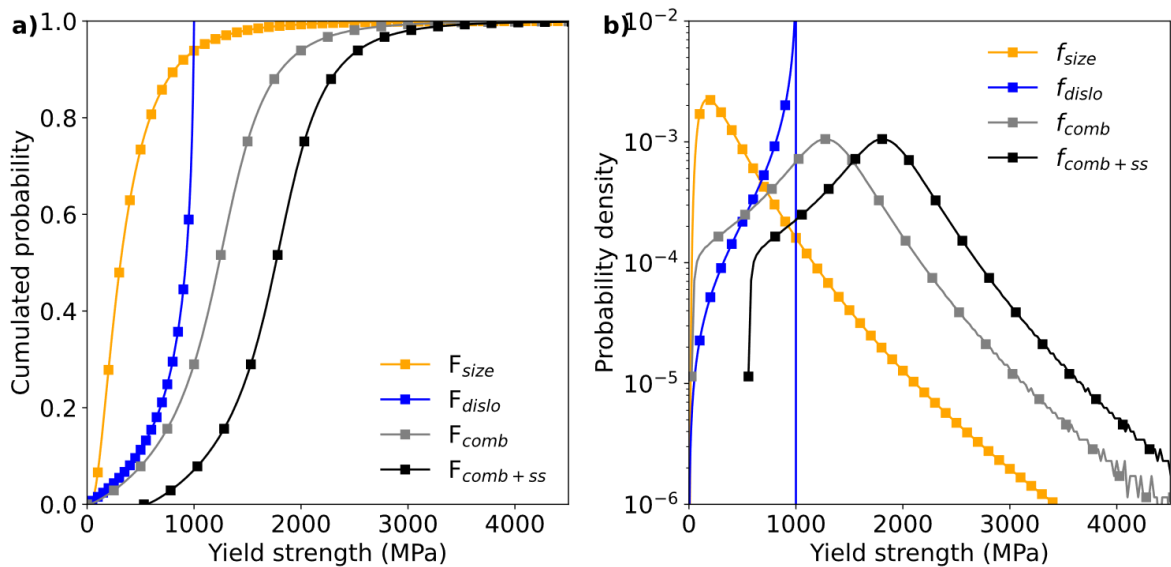


Figure 100: a) Cumulated distribution of the size (orange line) and dislocation density (blue line) strengthening as well as the calculated combined distribution (grey & black lines). The black line is shifted to higher strength to include solid solution strengthening b) Probability density associated to a) with same color code. The colors used in the present figure do not follow the chart presented in Section I.3.

IV.3.B.2 Application of internal stress distribution

Once the microstructure YS distribution has been calculated permitting to describe in a stochastic way the local properties of the elements, then the spreading of internal stresses is applied.

In practice, the microstructure YS dispersion is binned. For each bin, the probability can be calculated and the corresponding YS is known. Secondly, a gaussian distribution centered at zero and with a known standard deviation (here fixed to 400 MPa at the as-quenched states) is calculated which integral is equal to the probability of the bin. This second distribution can be binned as well to work in totally discrete way.

Hence, the probability to find an element with a certain YS and a given internal stress state can be calculated as the multiplication of both distributions, the one corresponding to the microstructure YS (and the one of the internal stress).

IV.3.C Micromechanical model bases

The micromechanical model developed in the present study is based on the previous works of Allain et al. [40] and Wang et al. [43], which are inspired by the seminal work of Masing [46] and the notion that martensite should be considered as a polycrystalline aggregate, i.e. composite (already proposed by Ansell in 1963 [41] for example).

The model aims at predicting the evolution of the macroscopic flow stress of a martensitic microstructure in quasi-static conditions along an uniaxial loading. As consequence, the results of the model can be directly compared to the experimental curves shown above and these experiments could serve in turn to calibrate the parameters of the model. Nevertheless, as in the CCA or in Wang's models it is adapted to the prediction of reverse loading (cf. V.4.B.4)

IV.3.C.1 Homogenization scheme

The model is based on the representation discussed in Figure 91. Perfect plastic behaviors are considered for each element and therefore the sequential yielding of elements of the microstructure would rule the macroscopic work hardening.

The macroscopic stress (Σ) and the macroscopic strain (E) are calculated as the weight average of the microscopic stresses (σ) and microscopic strains (ε) following the conventional scale transition of Hill as:

$$\Sigma = \sum_{i=0}^{i=n} f_i \times \sigma_i \quad \text{Equation 54}$$

$$E = \sum_{i=0}^{i=n} f_i \times \varepsilon_i \quad \text{Equation 55}$$

where f_i is the fraction of the i element, σ_i is the microscopic stress of the i element and ε_i the microscopic strain.

The local microscopic strain (ε_i) is the sum of the elastic and plastic deformation. The elastic deformation of the elements cannot be neglected as the model principle is to describe an elasto-plastic transition.

The interactions between the stress-strain states of the different elements and the macroscopic state are related by a single-parameter localization law defined as:

$$\beta = -\frac{\Sigma - \sigma_i}{E - \varepsilon_i} \quad \text{Equation 56}$$

where the β parameter is the same for all the elements and allows to manage different localization conditions ($\beta=0$ for iso-stress and $\beta=\infty$ for iso-strain) and, σ_i and ε_i are the local microscopic stress and strain states of element i . In the present work, the β parameter was set equal to a fraction of the Young modulus (Y) as previously done by [40,43,44] ($0.25 \times Y$). The internal stress of each element is recalculated during the modelled tensile test as the stress difference between the microscopic stress and the macroscopic one ($\Sigma - \sigma$).

The present model considers the flow stress (when plasticity starts) as the linear sum of the yield strength and the deviatoric internal stress:

$$\sigma_{flow} = \sigma_{Peierls} + \sigma_{ss} + \sigma_{size} + \sigma_{dislo} + \sigma_{prec} + \sigma_{int str} \quad \text{Equation 57}$$

being σ_i the local flow stress, i.e. the sum of the microstructure YS and the internal stresses.

A pedagogical example of the model behavior with a limited number of elements is presented in Appendix G. The effects of the distribution of yield strength and of the deviatoric internal stresses are evaluated.

IV.3.C.2 Micromechanical model parametrization and general managing

The whole set of water-quenched and tempering conditions for the three studied steels were modeled with the parameter list presented in Table 12. A binning step of 25 MPa was used and only the elements with a minimal fraction of 1×10^{-6} were considered. The elements with lower fraction do not affect significantly the results and impair the calculation time. Once the elements with a fraction lower than 1×10^{-6} are deleted, the fraction of the remaining elements is normalized to 1.

To illustrate the number of elements considered in the different simulation it can be mentioned that at the water-quenched state ca. 26000, ca. 37500 and ca. 43000 elements were utilized for the 0.1C, 0.2C and 0.3C simulations respectively.

Table 16: Micromechanical model parameters.

Parameter	Value
$k_{size}(14^\circ)$	$350 \text{ MPa} \times \mu\text{m}^{1/2}$
α_{dislo}	0.3
$K_{shear-eps}$	$950 \text{ MPa} \times \text{nm}^{-1/2}$
$K_{bypass-eps}$	1
$K_{shear-cem}$	$950 \text{ MPa} \times \text{nm}^{-1/2}$
$K_{bypass-cem}$	0.75
Standard deviation of $\sigma_{int str}$	400
Young modulus (Y)	200 GPa
β parameter	$-0.25 \times Y$

IV.4 Results and discussion of tensile behavior model

The present section will introduce firstly the microstructure YS distributions and modeled tensile behaviors of the as-quenched state of the three studied steels. The modeled tensile behaviors are compared with the experimental curves. Secondly, the effects of tempering are presented. Finally, some implications of the micromechanical model and some further developments are briefly discussed.

IV.4.A As-quenched martensite

A complete analysis of the simulation results of the 0.2C_WQ simulation will be firstly presented. Then, the effect of the carbon content will be discussed.

IV.4.A.1 Complete analysis of the 0.2C_WQ simulation

IV.4.A.1.a Tensile curve

The experimental tensile behavior of the 0.2C_WQ condition is presented in Figure 101.a as well as the one obtained by the micromechanical model. Both curves are almost juxtaposed up to 1600 MPa. Above, the modeled curve overpasses the experimental one. The difference between both curves at the end of the modeled one (stopped by the Considère criterion) is ca. 30 MPa which is lower than 2 % of the experimental UTS and is between the experimental incertitude obtained of the repeatability of the tensile tests.

In Figure 101.b the work-hardening rate as function of the macroscopic stress is shown. At stresses lower than 250 MPa it can be observed that the experimental values are lower than the normalized

Young modulus, some sliding might explain this artefact. Then, the experimental curve is higher than the modeled one reaching a similar behavior at 900 MPa. A new deviation is observed at stress levels higher than 1500 MPa which corresponds to the difference between the experimental and modeled tensile curves in Figure 101.a.

At the end of the simulation ($E=3.5\%$) the elements with the lowest yield strength presents the maximal microstrain, equal to 5.95 %, while the ones remaining elastic with initial tensile stress present the lower microstrain, equal to 0.355 %. 96 vol.% of the martensite has arrived to its flow stress and only 4 vol.% remains elastic.

Thus, the ratio between the most and the least deformed element is 16.8. Tanaka et al. [260] observed by Digital Image Correlation (DIC) regions with equivalent plastic strain up to 30 % (most of regions between 2.5 and 15 %) while others regions remains elastic (0 %). Morsdorf et al. presented the distribution of strains determined by DIC at different state of the tensile test [261]. When the average strain was equal to 3.7 %, some regions presented at local strain close to zero while others presented values up to 15 %.

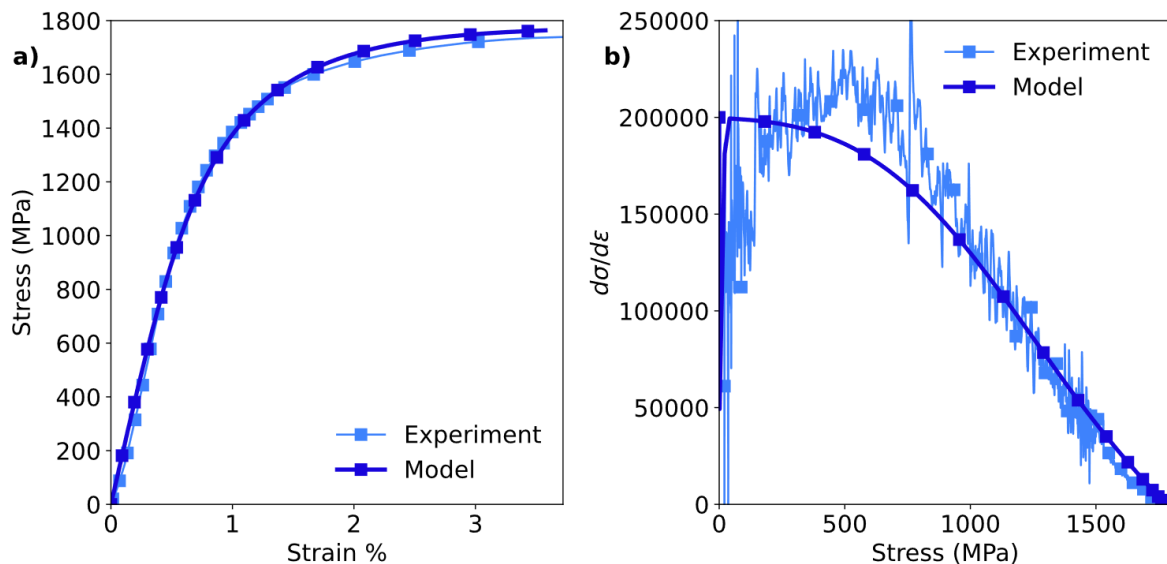


Figure 101: a) Experimental and modeled tensile behaviors of 0.2C_WQ steel. b) Work-hardening rate vs macroscopic true stress curves obtained from a).

The distribution of local strain obtained in the presented simulation is compared with the one reported by Morsdorf et al. at an average strain equal to 3.7 % in Figure 102. A similar shape and values are observed between both curves up to $E = 3\%$ (a slight decorrelation is observed). At higher deformations a higher difference is observed.

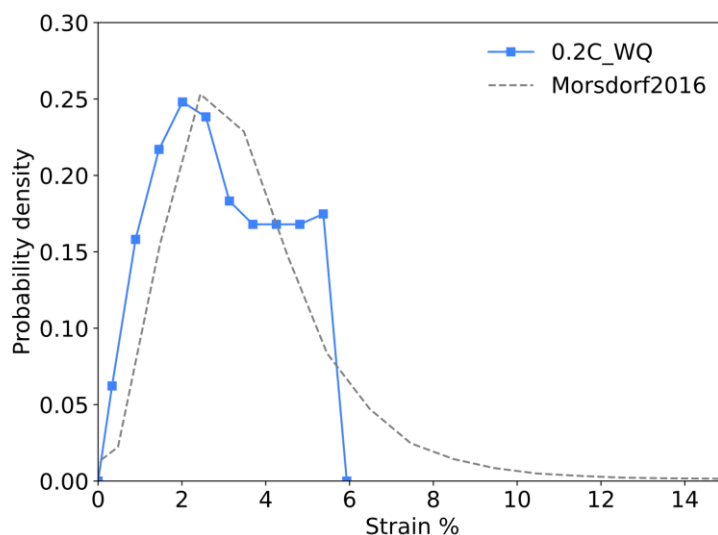


Figure 102: Distribution of local strain predicted by the herein presented model and the one reported in [261] at an average strain equal to 3.7 %

IV.4.A.1.b Internal stresses evolution

The deviatoric internal stress distribution of all elements is calculated at each simulation step and, therefore, the evolution of the internal stress distribution for all the elements at a given yield strength can be analyzed during the tensile test simulation. Figure 103 presents the evolution of the deviatoric internal stress state for elements with the same yield strength as a function of the macroscopic strain (in rows $YS = 900$ MPa, 2050 MPa and 3750 MPa respectively). In columns, four different macroscopic strains states are presented: the initial state, $E = 0.5$, 1.4 and 2.8 % respectively.

At the initial state ($E = 0$ %), all the elements present the imposed gaussian distribution of internal stress. Note that in the case of the higher microstructure YS , the phase fraction of elements with lower and higher values is below the threshold of 1×10^{-6} and, thus, the distribution is truncated. At a macroscopic strain equal to 0.5 % the elements with microstructure YS equal to 900 MPa are partially plasticized, only the elements with a negative internal stress contribution remains elastic. At the mentioned macrostrain $E = 0.5$ % all the elements with YS equal to 2050 MPa and 3750 MPa remain elastic.

At $E = 1.4$ % all the elements with YS equal to 900 MPa have plasticized and presents an internal stress state of -640 MPa. This state is explained by the fact that all the elements present a microscopic flow stress lower than the macroscopic one. This behavior was previously exemplified in the pedagogical example proposed in Appendix G (Figure 126.a by the green line (lowest YS)).

The elements with a YS equal to 2050 MPa are partially plasticized. A shift to higher deviatoric internal stresses is observed as the macroscopic stress curves deviates from the linear part of the tensile curve (Young modulus). Hence, the gap between the elastic elements and the macroscopic stress curve increases. The same shift is observed in all the elements with YS equal to 3750 MPa (third row) which remain elastic at $E = 1.4$ %.

Finally, at $E = 2.8$ % the stress state of the elements with YS equal to 900 MPa increases up to -840 MPa. Most of remaining elastic elements with YS equal to 2050 MPa are in a positive state while at the initial

state where in a negative state between -800 MPa and -500 MPa. The elements with YS equal to 3750 MPa remain elastic with an increased positive stress state.

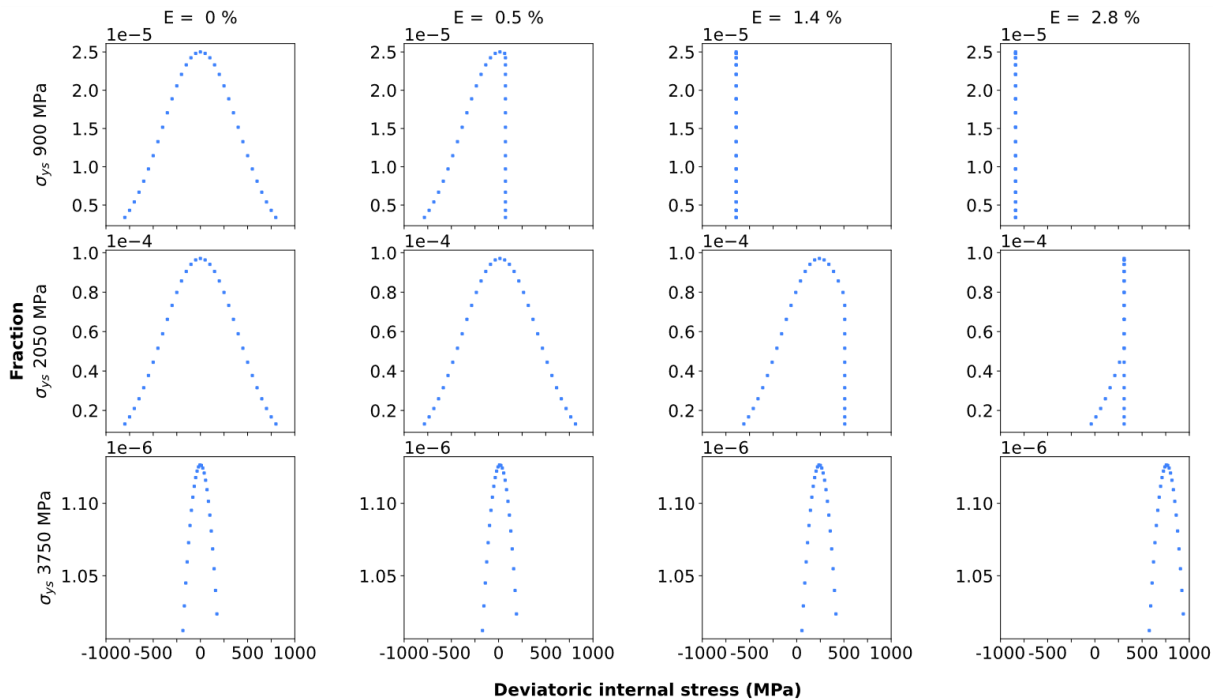


Figure 103: Evolution of the deviatoric internal stress distribution for the elements at three presenting different yield strengths (in rows) as function of the macroscopic strain (0, 0.5, 1.4 and 2.4 %, in columns) for the 0.2C_WQ condition.

IV.4.A.2 Effect of carbon on the microstructure YS distributions

The strengthening distributions due to the size and to the dislocation density for the three studied steels have been presented previously. In Figure 104.a the cumulated probability of the combined distributions plus the constant effects (solid solution) are presented for the 0.1C_WQ, 0.2C_WQ and 0.3_WQ steels while in Figure 104.b the deduced probability densities are shown for the same conditions. Although the minimal YS for each condition are in a narrow range (between 500 MPa and 575 MPa for the 0.1C_WQ and the 0.3C_WQ condition respectively), the maximal YS presents a clear separation (ca. 1500 MPa).

Allain et al. predicted an carbon-independent minimal YS (300 MPa) and a larger dispersion with the carbon content (in their study related to the parameter “ σ_0 ”) with maximal YS close to 4500 MPa for a 0.3 wt.% C steel [40]. The herein results present a good agreement with the mentioned study not only regarding the maximal YS obtained but also a similar minimal YS. As a consequence, the presupposed YS distributions by Allain et al. can be attributed to the size and dislocation density strengthening distributions as proven in the present study. Note that the effect of the deviatoric internal stresses affects also the flow stress distribution.

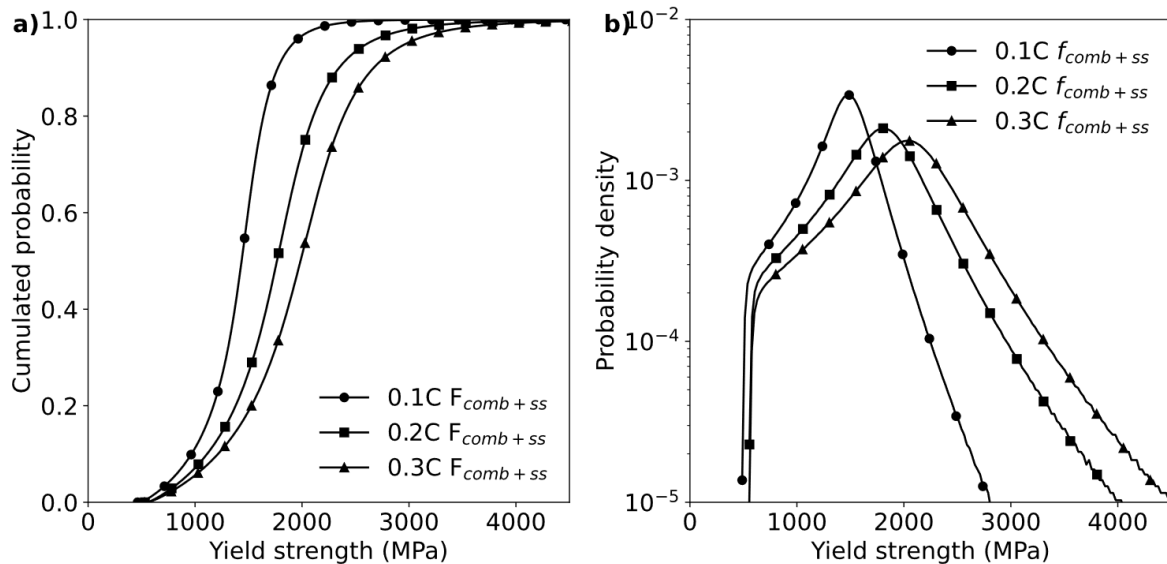


Figure 104: a) Cumulated distribution (size + dislocation density + constant strengthening mechanisms) for the 0.1C_WQ, 0.2_WQ and 0.3C_WQ steels. b) Probability density functions for the three same steels of a).

The calculated tensile behaviors of the 0.1C, 0.2C and 0.3C steels are presented in Figure 105.a. For the 0.3C_WQ steel a good agreement is again observed between the modeled curve and the the experimental one. At the UTS the difference between both curves is 40 MPa. The results of the 0.1C_WQ condition presents a higher gap (at the end of the simulation the difference is ca. 100 MPa). The higher difference can be observed as well in the work-hardening curves shown in Figure 105.b.

The good agreement shown by the 0.2C_WQ and 0.3C_WQ conditions prove that the martensitic tensile behavior is ruled by the distribution of the flow stress.

The higher difference between the modeled and the experimental results in the case of the 0.1C_WQ cannot be interpreted by any phenomenon of the authors knowledge, except by a higher self-tempering state (due to a higher Ms temperature). It has to be considered that the same parameters (detailed in Table 12) were utilized in all the simulations and, thus, better results could be obtained if the parameters were adjusted for each composition. The choice of the standard deviation of the internal stress distribution (400 MPa) plays an important role in the shape of the tensile behavior but not in the maximal stress (cf. Appendix F). Therefore, it cannot explain the difference of maximum stresses.

The remaining non-plasticized percentage in the 0.1C_WQ tensile behavior modelled is 3.25 vol.%, while the one of the 0.2C_WQ is 4 vol.% and the one of the 0.3C_WQ is 4.5 vol.%. In all three cases the remaining fraction is low and an increase is observed with the nominal carbon content and the wider distribution of yield strength.

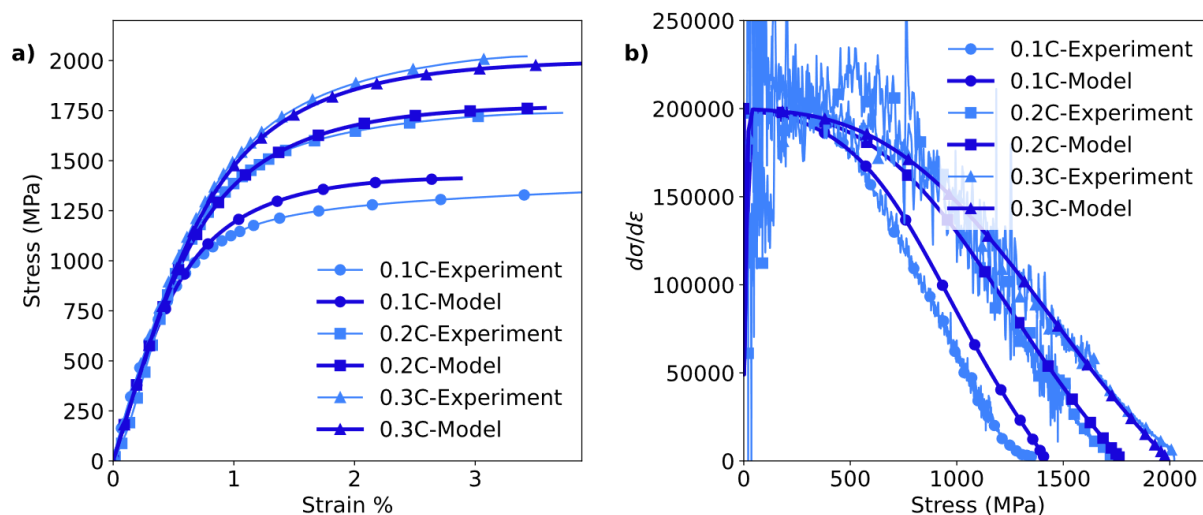


Figure 105: a) Experimental and modelled tensile curves of the three studied steels if the water-quenched state (0.1C_WQ, 0.2C_WQ and 0.3C_WQ). b) Work-hardening obtained from the tensile curves presented in a).

IV.4.B Tempered martensite

IV.4.B.1 Evolution of the microstructure YS distributions

During tempering, the size strengthening distribution was considered as fixed due to the low tempering temperature and short holding times [100,101]. However, recovery occurs during the tempering (especially between 300 °C and 400 °C) as presented in Section III.3.B. The evolution of the dislocation density produces a narrower distribution of strengthening as previously presented in Figure 94. It is then expected that the combined distribution considering the size and the dislocation density distributions will narrow with tempering.

For the water-quenched states three strengthening contributions were considered as constants; the Peierls barrier, the substitutional solid solution strengthening and the carbon solid solution strengthening. In the tempered state, the carbon contribution cannot be considered as constant anymore as the precipitation is affected by the dislocation density (as shown in Section III.3.B.3.c).

In order to take into account the spatial distribution of dislocations on the precipitation, the local dislocation density has been determined for each 10 wt.% of martensite. These local dislocation densities were used as an input for the precipitation model with the parameters presented in Table 5 in Section III.3.B.2.

10 precipitation simulations (one for each 10 % of martensite) were thus conducted for each tempering conditions (3 steels \times 3 holding temperatures) producing a set of 90 simulations. A finer binning would produce a less scattered distribution but at a high computational cost.

The results of these simulations are presented in Table 17 for the 0.2C steel at 200 °C, accounting for a natural aging of two months at room temperature. For each 10 wt.% of martensite the dislocation density is presented as well as the fractions and radii of epsilon and cementite carbides. The strengthening values calculated with Equation 43 and Equation 44 are shown as well as the estimated cumulated strengthening

(quadratic mean). The epsilon fraction decreases with the increase in the dislocation density. As a consequence, the cementite fraction increases. The radius of both precipitates increases with the dislocation density. Regarding the precipitation strengthening, the one related to epsilon carbides presents a decrease of 50 MPa for the range considered of increasing the dislocation densities in Table 17 while the cementite strengthening present an increase of over 200 MPa. By combining both contributions, the total precipitation strengthening has been calculated for each condition and a maximal variation of 80 MPa is found.

Table 17: Results of the precipitation simulations as a function of the initial dislocation density: radius and fraction of the epsilon and cementite carbides as well as their respective strengthening and the total precipitation strengthening for the 0.2C WQ T200C0s steel.

Fraction (wt.%)	ρ ($\times 10^{15}$ $1/m^2$)	Epsilon			Cementite			σ_{prec}
		Fraction (wt.%)	Radius (nm)	$\sigma_{prec(eps)}$ (MPa)	Fraction (wt.%)	Radius (nm)	$\sigma_{prec(cem)}$ (MPa)	
0.0-0.1	1.07	3.06	3.84	325	0.22	4.91	99	340
0.1-0.2	1.73	2.89	4.13	328	0.43	5.76	145	358
0.2-0.3	2.08	2.74	4.31	326	0.60	5.76	176	371
0.3-0.4	2.35	2.59	4.45	322	0.78	6.02	206	382
0.4-0.5	2.59	2.43	4.57	316	0.97	6.25	233	393
0.5-0.6	2.80	2.28	4.66	309	1.15	6.44	258	403
0.6-0.7	2.99	2.13	4.74	302	1.32	6.60	281	412
0.7-0.8	3.17	1.98	4.80	293	1.50	6.75	302	421
0.8-0.9	3.33	1.84	4.86	284	1.67	6.88	322	429
0.9-1.0	3.49	1.70	4.9	274	1.83	7.00	340	437

The distribution of precipitation strengthening has, therefore, a limited impact in the total distribution of yield strength. It is integrated as a third distribution when calculating the combined yield strength distribution with the methodology presented in Section IV.3.B.1.

The distributions of the different strengthening mechanisms as well as the combined ones are presented in Figure 106. The dispersion of the precipitation strengthening is much lower than the ones due to the size and dislocation density (ca. one order of magnitude). The slight instabilities observed in the probability density distributions are numerical artefacts due to our binning method. These instabilities do not affect the calculations so far.

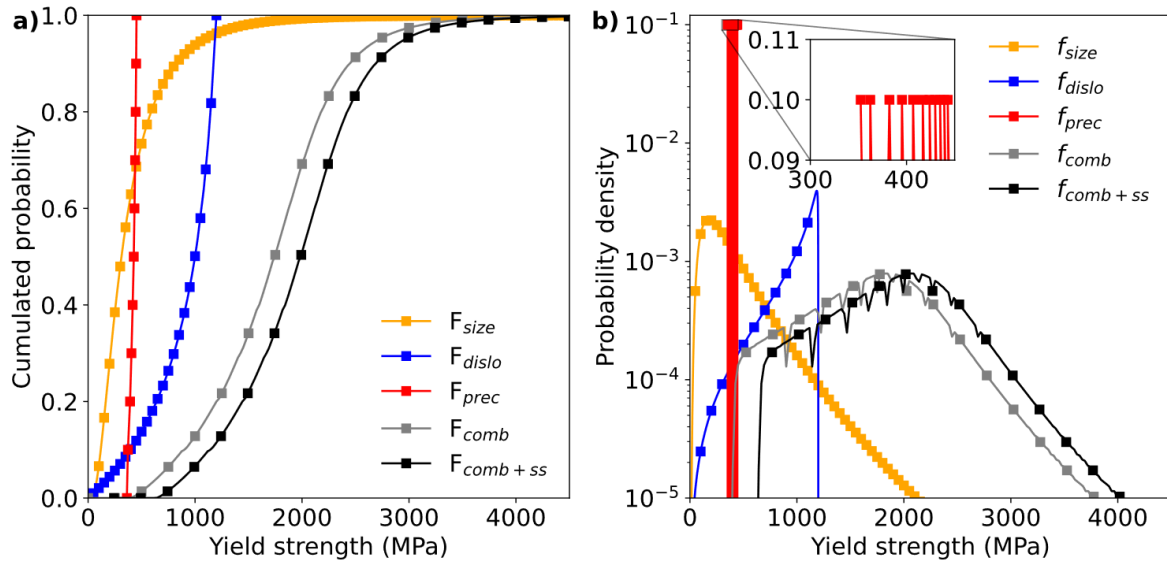


Figure 106: a) Cumulated distribution of the size (orange line), dislocation density (blue line) and precipitation (red line) strengthening as well as the calculated combined distribution (grey line & black line). b) Probability density functions associated to the curves shown in a). The colors used in the present figure do not follow the chart presented in Section I.3.

The evolutions with the tempering of the yield strength distributions combining all the considered distributions are presented in Figure 107. Figure 107.a shows the effect of the tempering temperature (200, 300 and 400 °C) just after heating (holding time = 0s) compared with the as-quenched distribution. The tempering at 200 °C produces mainly a shift of the distribution to higher yield strengths. The recovery is limited (with the modeled parameters presented in Chapter II) and the strengthening of the precipitates is higher than the effect of the carbon in solid solution. At 300 °C the distribution slightly narrows and shifts to lower yield strengths. A similar but more pronounced tendency is observed for the 400 °C tempering.

Figure 107.b presents the effect of the holding time during tempering at 300 °C of the 0.2C steel. Between the water-quenched condition and the holding 0s a clear change is observed with the decrease in the proportion of elements with a yield strength higher than 1750 MPa. The distribution presents a smaller variation between 0s and 30s of holding, and no observable changes are occur later.

The effect of tempering on the distribution of properties have been revealed by nanohardness experiences [260] (results not presented in the present manuscript).

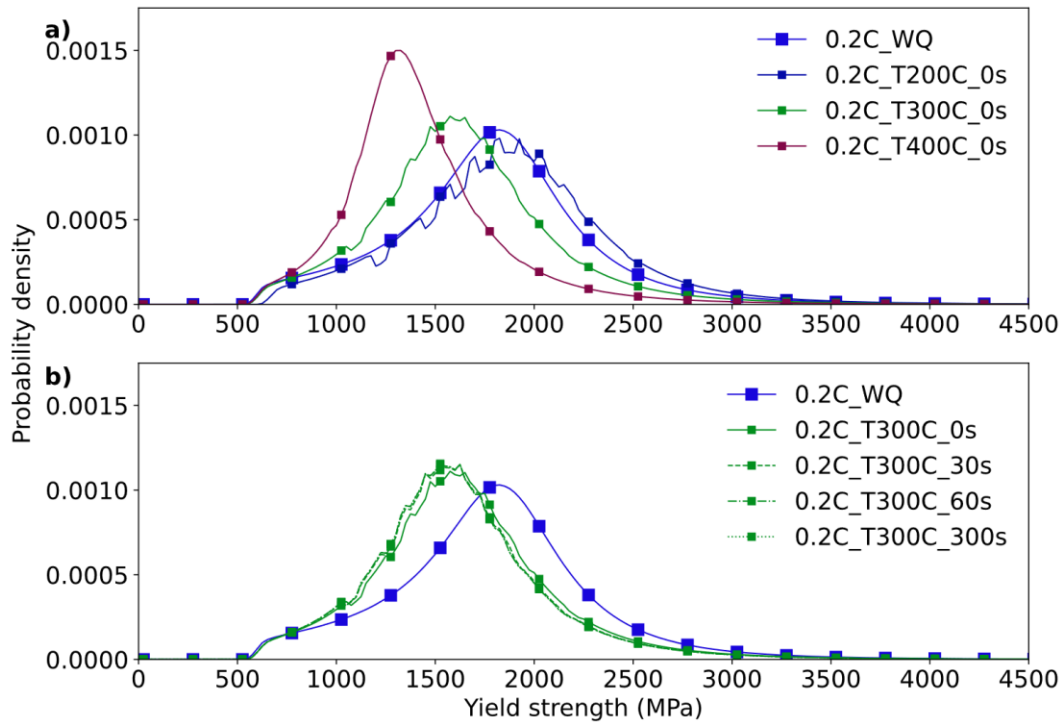


Figure 107: Evolution of the summed yield strength distribution as function of the tempering conditions for the 0.2C steel. a) Effect of tempering temperature. b) Effect of tempering time at 300°C.

IV.4.B.2 Tensile behavior results

The tensile behavior of the 3 studied martensitic steels after different tempering conditions were modeled. It corresponds to a set of 36 different conditions, combining three tempering temperatures (200, 300 and 400 °C) with four varying holding times (0, 30, 60 and 300s) for the three different nominal carbon contents.

Figure 108 presents a selected subset of experimental and predicted tensile curves for the 0.2C steel after different tempering conditions. In Figure 108.a the effect of the tempering temperature at constant holding time (0s) is presented. Figure 108.b shows the effect of the holding time for the tempering heat treatments at 300 °C.

The micromechanical model is able to capture the experimental decrease trend of the maximum stress with the increase of the tempering severity. The evolutions of the work-hardening are relatively well described (excepting the Lüder's plateau).

For the 200 °C-0s condition in Figure 108.a a gap of 200 MPa is observed at the end of the simulation. This difference between the experimental and modeled curves is related to the precipitation contribution and to the recovery phenomenon. The first one produces an increase of the yield strength between ca. 50 MPa and ca. 150 MPa higher than the one due to the carbon in solid solution. A slight recovery can be observed experimentally at 200 °C, which would counteract the precipitation strengthening. However, the herein recovery model predicts a lower recovery (c.f. Figure 38) and, therefore, the higher precipitation strengthening is not counteracted in the modeled tensile behavior.

At 300 °C the experimental curve presents a shoulder due to the incipient Lüders plateau. Excepting for the mentioned shoulder a better agreement is obtained between the experimental and the modeled curves than in the 200 °C case. At 400 °C the Lüders plateau is clearly visible up to 0.8 % strain. At the end of it a good agreement between the experimental and modeled curves is found.

When analyzing the effect of the holding time on the experimental tensile behaviors (Figure 108.b), a longer holding time produces a decrease of the UTS with an incipient shoulder at lower stresses. The modeled curves are able to reproduce the decrease of the UTS with the holding time but in a lower variation than the experimental ones.

The potential explanations of the decrease of the UTS with the holding time can be a higher recovery state and a decrease of the precipitation strengthening. The evolutions of the experimentally determined and modeled dislocation densities during the holding at 300 °C have been presented in Chapter II Figure 38. The modeled dislocation densities show a faster recovery than the experimental ones reaching a same saturation dislocation density at the end of the holding. Therefore, a faster but similar total variation of the UTS should be expected between the experimental and modeled curves.

The uncertainty of precipitation strengthening can be evaluated by comparing the precipitation model results with the experimental results. In Chapter III Figure 73 the modeled cementite radius is smaller than the experimental determined ones at 60s and 300s of holding. If higher precipitate radii are considered, a lower strengthening is expected by the bypassing mechanism. Thus, the difference between the experimental tensile behavior and the modelled one in the 300 °C tempering of the 0.2C steel can be related to some uncertainty of the precipitation model.

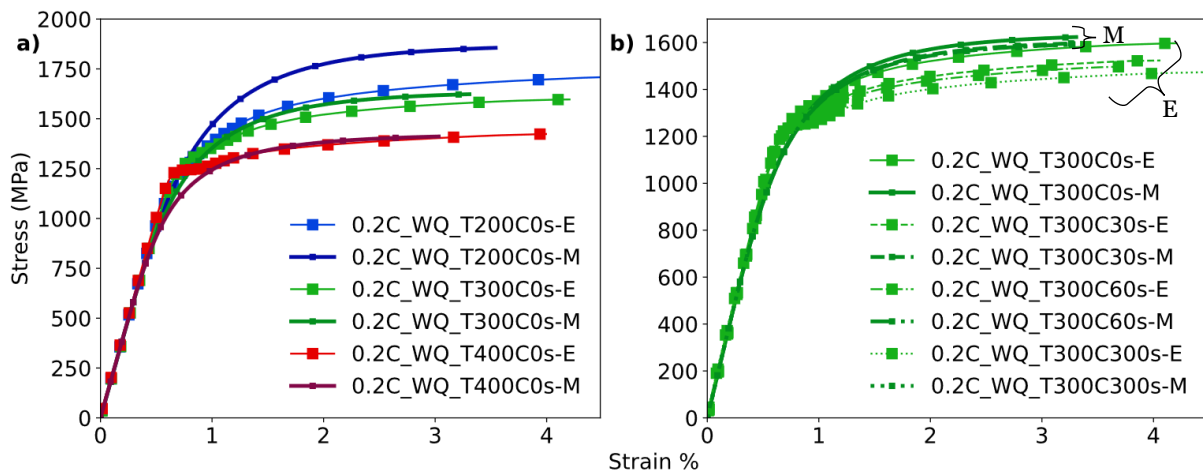


Figure 108: Evolution of the experimental (denoted by the suffix E) and modelled (denoted by the suffix M) tensile behaviors at different tempering conditions for the 0.2C steel. a) The tempering temperature effect is presented with constant holding time (0s). b) The effect of the holding time is presented for the 300 °C tempering.

As previously stated, the tensile behavior of 36 different tempering conditions were characterized and modeled. A simplifying method was applied in order to facilitate the comparison between the experimental and modelled results and the different tempering states. The macroscopic stresses of the experimental and modeled behaviors at a certain macroscopic strains (0.5, 1, 2 and 3 %) were determined and reported in Figure 109 for all the 36 conditions.

Regarding the 0.5 % strain values that the good agreement observed in the as-quenched and 200 °C tempered conditions deteriorates when tempering is applied at 300 °C and 400 °C due to the previously shown “shoulder” and the Lüders plateau. The 1 % and 2 % strain experimental values present the same tendencies as the 3 % strain ones with almost no variation at the 200 °C tempering (small decrease for the 0.1C and 0.2C steels, small increase for the 0.5 % strain in the 0.3C steel) and a decrease for higher tempering temperatures. The 0.1C steel presents variation of the experimental stress values with the temperature with no clear effect of the holding time which in some measure differs of the 0.2C steel tempered at 300 °C and 400 °C.

Despite an overestimation of strengthening at 200 °C for the 0.1C and 0.2C steels, the modeled values (connected by dashed lines) are able to predict the softening observed with the temperature at 300 °C and 400 °C. The over strengthening is probably due to a low accounting of the recovery softening. A remarkable good prediction of the 0.3C steel is accounted (neglecting the Lüders plateau). The better agreement at higher carbon content may be related to the more reliable experimental data and, thus, the better calibration of the models (especially related to the carbide size and dislocation density).

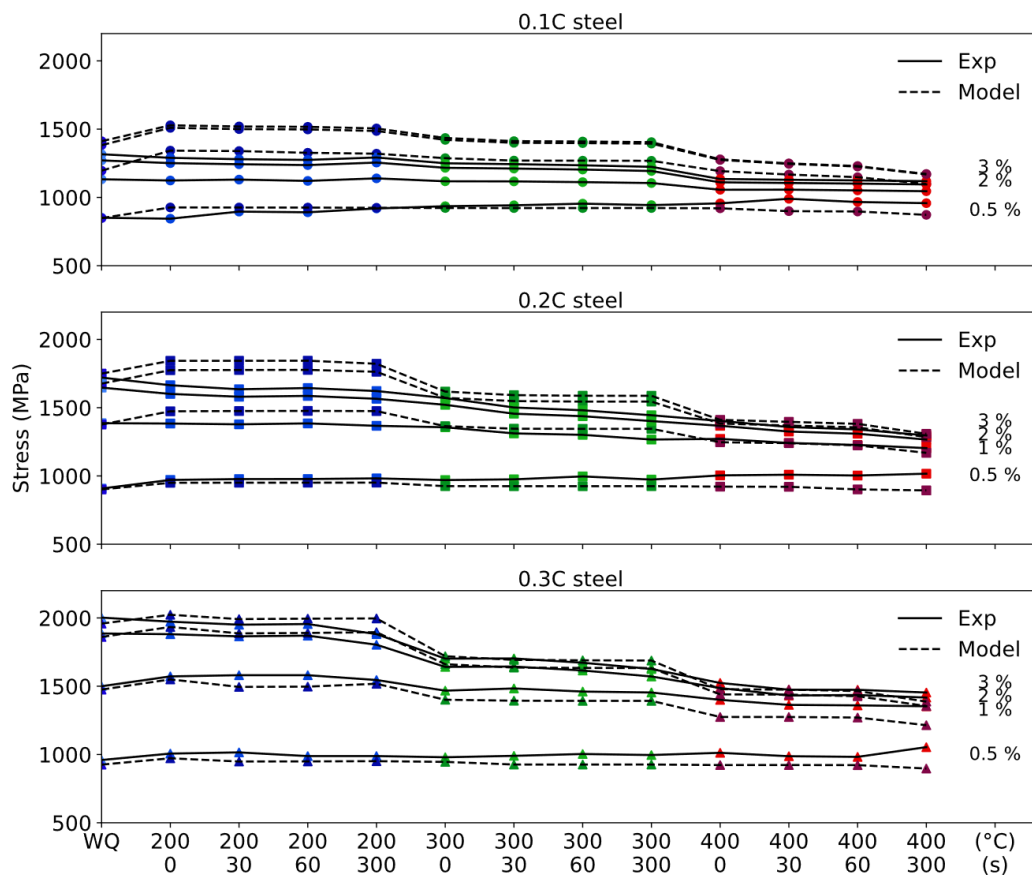


Figure 109: Evolution of the stress at 0.5, 1, 2 and 3 strain (%) for the three studied steels for all studied the tempering conditions studied (0, 30, 60 and 300s for holdings at 200, 300 and 400 °C).

IV.4.B.3 Discussion

The results of the model developed in the present work are compared to the ones obtained with the model for martensite proposed by Mathevon in Figure 110. Only the conditions as-quenched of the 0.3C steel, tempered at 300 °C for 300s (0.3C_WQ_T300C300s) and the one tempered at 400 °C for 300s (0.3C_WQ_T400C300s) are considered in the present comparison.

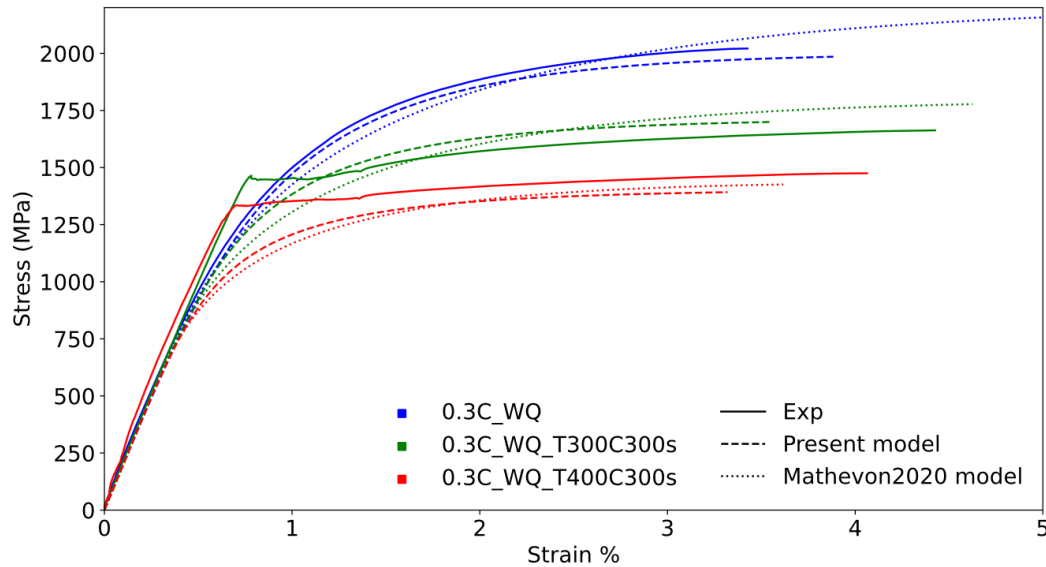


Figure 110: Comparison of the herein developed model, the model developed by Mathevon [44] and the experimental results for a selection of conditions.

The model developed in the present study has a better prediction of the as-quenched condition than the one of Mathevon, especially regarding the shape of the curve. For the tempered conditions, the difference between the experimental and simulated curves are similar. A slightly better description of the 0.3C_WQ_T300C300s is obtained with the herein developed model.

The microstructure YS distributions utilized for the preceding simulations are presented in Figure 111. The softest elements present similar values for both models. The physically-determined distributions used in the present study are narrower than the one considered in Mathevon's model. Note that in the present study an additional distribution is latter applied (the deviatoric internal stresses) spreading the flow stress distribution.

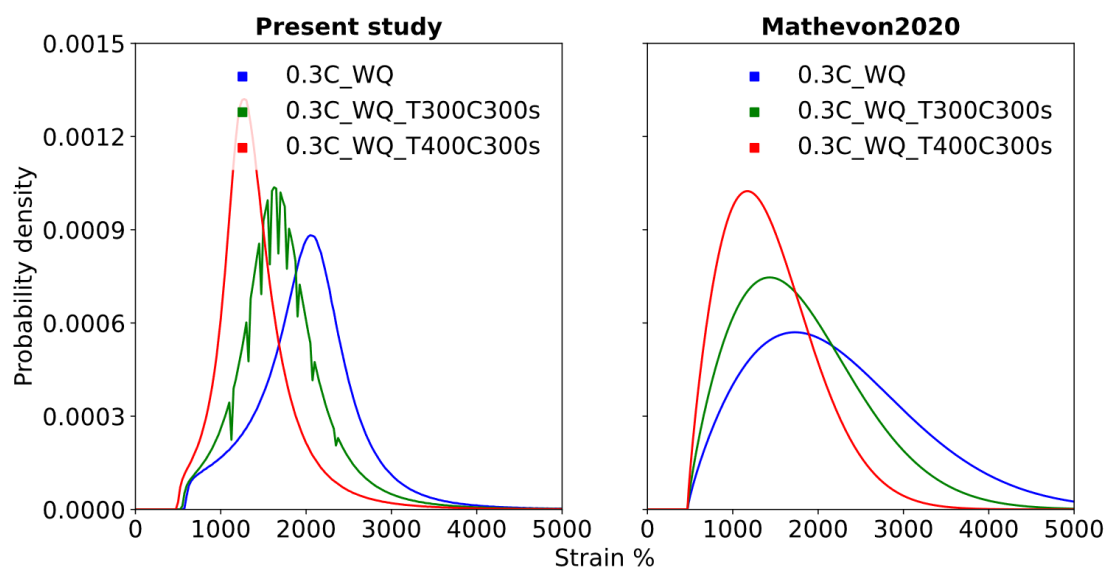


Figure 111: Distributions of microstructure YS used in the prediction of the tensile behavior of the as-quenched and tempered conditions in the present study (left) and Mathevon's model [44] (right).

Mathevon's model is more efficient from the calculation time point of view compared with the herein developed model with a time of simulation under the second vs some minutes. However, from a metallurgical point of view the model developed in the frame of the present study is richer as the evolution of the flow stress is calculated based on the physical description of the different phenomena and not by a set of Johnson-Mehl-Avrami-Kolmogorov (JMAK) phenomenological equations.

It can be concluded that the herein developed micromechanical model, based on the changing paradigm distribution of yield strength and deviatoric internal stresses, is able to predict not only the as-quenched martensite tensile behavior but also the tensile behavior of the tempered martensite. The mentioned distributions are based on the spatial size and dislocation density distributions on the as-quenched states. When considering tempering the dislocation density recovery as well as the relaxation of the deviatoric internal stresses must be taken into account. The precipitation strengthening from both possible carbides, which are calculated thanks to an associated precipitation model, are considered in the tempered states with the precaution of noting that a distribution of precipitation states are present in the martensite due to the spatial distribution of the dislocation density.

IV.4.C Perspectives

The micromechanical model developed in the present study considers a distribution of microstructure YS as well as a distribution of deviatoric internal stresses. The interaction between the elements is ruled by a single-parameter localization law. A following development of the model might be to consider more local interaction between the elements and their neighborhood. A second suggestion is to take into account the microstructure orientation distribution. The importance of the last one has been highlighted by [42,261].

The combination of a distribution of the yield strength and of deviatoric internal stress utilized in the present study has the potential to predict the Bauschinger effect (lower compressive yield strength in

compression after a tensile test) which is due to the evolution of internal stress during the tensile section of the test. This kind of combined approach has been applied to predict the Bauschinger effect by Wang et al. [43] considering a different shape of internal stress distribution and a presupposed distribution of yield strength. In a following work, it could be envisaged to perform Bauschinger tests for the sake of comparison.

An interesting phenomenon that has been observed when deforming martensite in tension is the narrowing of the diffracting peaks [42,264–266]. Our own experiments have confirmed this results. Different interpretations have been proposed to the mentioned phenomenon while some authors proposed a fast mechanical recovery [42,264,265] others proposed a relaxation of internal stresses [266,267]. Even if the present model considers deviatoric internal stresses and not hydrostatic ones (which affect the directly the lattice parameter and, thus, the diffracting position) the micromechanical model could be used to clarify the mentioned diffracting peak narrowing. A first attempt is presented in Appendix E.

IV.5 Conclusions of the chapter

This chapter finally proposes a synthesis of the results of the other chapters, results considered as inputs to the micromechanical approach.

- 1) The tensile behavior of the studied steels after quenching and tempering has been characterized. The observed evolutions of their mechanical properties as a function of the carbon and the tempering severity are in accordance with the literature. As rule of the thumb, the UTS increases with carbon content while both conventional YS and UTS decrease with tempering.
- 2) The strengthening distributions caused by the microstructural distributions previously presented (size and dislocation density) were evaluated, giving a spread over more than 1000 MPa. The strengthening distributions are broader with increasing the nominal carbon content of the steel and narrows with tempering.
- 3) The combined distribution of yield strength based on the different strengthening distributions was calculated thanks to a reasonable metallurgical hypothesis, called “soft-soft” correlation. For as-quenched martensite, the combined yield strength distributions are right-skewed, with lowest yield strengths around 500 MPa. The highest yield strengths of the distributions increase with the carbon content with values higher than 4000 MPa. The mentioned results are a strong microstructural justification of the presupposed yield strength distribution proposed in CCA type approaches [40,43,44,293].
- 4) The full probabilistic micromechanical model integrate the microstructure yield strength distribution and a distribution of internal deviatoric stresses as inputs. The model allows to predict the microscopic yield strength of the steels as well as its work-hardening. The evolution of the distribution of internal stresses can be followed all along the deformation process.
- 5) To the author’s knowledge the tensile behavior of different martensitic steels can be successfully related to experimentally determined microstructural based distributions for the first time. The approach used makes it possible to treat as-quenched and tempered martensite in the same frame. For tempering, additional mechanisms have been accounted for, namely the recovery of dislocation structure, the relaxation of internal stresses, the segregation/precipitation of carbon and their possible interactions.
- 6) The proposed micromechanical model has the potential to predict the Bauschinger effect of the studied steels as the one presented by Wang et al. [43]. It could also permit to explain the decrease of the Full Width at Half Maximum of the martensitic diffraction peaks during in situ tensile test, observed in the present study and in the literature [267]. The observed phenomenon is related to the evolution of the internal stresses distribution.

Chapter V

Conclusions and outlooks

"The greatest challenges humans face throw-out their lives are two:

1- the challenge of where to start

2- the challenge of when to stop."

-Sameh Elsayed

"Everything has to come to an end, sometime."

-L. Frank Baum, The Marvelous Land of Oz

V.1 Summary and key results

This work is an additional step towards a better understanding of low-carbon martensitic steels, with a special emphasis put on the role and importance of the microstructure heterogeneities and of internal stresses to explain their micromechanical behavior. To do so, an original model describing martensitic steels as polycrystalline aggregate and its behavior as an extended plastic-transition have been developed and calibrated on experimental basis.

The spatial heterogeneities of martensitic microstructure result from the sequential nature of the transformation and concern the microtexture components and their respective sizes (lath/block/packet organization of the variants), the density of dislocations and the carbon segregation/precipitation state. The experimental results presented in the present work are based on the systematic analysis of the set of three alloys with different carbon content from 0.1 to 0.3 wt.% C, in the as-quenched or quenched and tempered state, at different scales (schematically presented in Figure 112).

The as-quenched microstructures were first investigated by EBSD. The obtained maps revealed the known hierarchical and multiscale organization of the variant structure. The sizes of the different components have been measured on the basis of a misorientation criterion and the spatial size distribution of blocks were extracted from a non-trivial stereological analysis. As expected, the microstructure becomes finer with the increase in the carbon content but the size distribution narrows.

The mean dislocation density in the as-quenched martensitic steels has been then investigated by HEXRD / TEM /EBSD at room temperature and compared with a database obtained from a bibliographic study. A new method was developed to estimate the spatial distribution of local dislocation densities in the microstructure thanks to in situ HEXRD experiments during the transformation itself, i.e. during quenching. It has shown in particular that the higher carbon content, the larger is the spread of the distribution.

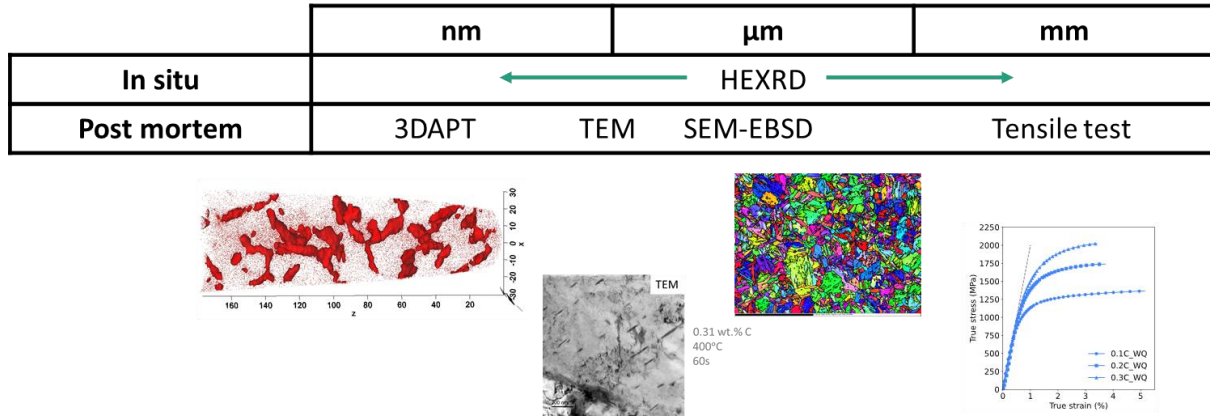


Figure 112: Multiscale characterization techniques utilized in the present study to characterized the quenched and tempered martensite.

The sequential nature of the martensitic transformation leads us to adopt a statistical correlation between both previously discussed microstructure spatial distributions. The resulting distribution of local yield strengths at the microstructure scale is the main input of the stochastically-physically based micromechanical model developed in the present work. To finish this summary about as-quenched martensite, a distribution of internal stresses was also considered in the micromechanical model, internal stresses that are gradually relaxed thanks to the load transfer as proposed by Wang et al. [43]. Our only disappointment is that we could not propose for this distribution either experimental data or modelling results to calibrate this parameters independently of our tensile results.

The mechanical behavior of the martensite is known to evolve when applying a tempering treatment due to different thermally activated phenomena. A multiscale study of the tempering (combining 3DAPT / TEM / in situ HEXRD techniques) has been carried out to determine the carbon segregation and precipitation. The segregation and precipitation of carbides were also modeled by a modified in-house mean-field thermo-kinetic model. The latter was able to predict the suppression of transition carbides at low carbon contents as a consequence of the carbon segregation to Cottrell atmospheres at dislocations as well as the key effect of the dislocation density on the precipitation.

The phenomenon known as recovery occurred during tempering and was also investigated by in situ HEXRD experiments and modeled. It was found that not only the average dislocation density decreases with the severity of the tempering but also their distributions narrows. During tempering, internal stresses also relax. Again, the evolution of their distribution have been modeled but without any experimental data to sustain our predictions.

The precipitation hardening (depending on the local dislocation density), the dislocation recovery and the internal stresses relaxation were integrated in the micromechanical model to describe tempering, in addition to the already discussed inputs. Therefore, we are able to understand and predict, within a single framework, the main characteristics of the mechanical behavior of tempered martensitic steels, in particular their lower strength and work hardening compared to as-quenched microstructures.

V.2 Future work

The present study introduced some important notions for the understanding of the low-carbon martensitic behavior. However, some topics require further investigations and development. Some of those are:

- 1) The carbon segregation at the as-quenched state would require further characterization, special at no-aged state in order to clearly evaluate the effect of carbon segregation during quench and during aging. A more detailed characterization of the transition carbides might be proposed, especially with the goal of determine the nucleation mechanism, homogenous or on previously formed clusters.
- 2) Three major improvements have been suggested for the precipitation model: It could be interesting first to model separately intra-lath and inter-lath cementite as both populations has different surface energies and undergo different diffusion rates. Secondly, in the actual version of the model, the major hypothesis is that all carbides are spherical. Therefore, considering a closer shape (as ellipsoidal prolate) should produce more realistic results. This results would be easier to compare with size distributions determined by TEM. Finally, an intermediate state between the segregation and carbide precipitation may be introduced by considering the formation of clusters who can act as nucleation sites for transition carbides.
- 3) The tempering conditions evaluated in the present work are in the low-temperature range. As a consequence, no evolution of the microstructure size was expected. In a future work, evaluating the evolution of the microstructure size produced by tempering at higher temperature might be studied. This new evolution could be, thus, incorporated in the micromechanical model for the cases of tempered martensite.
- 4) The micromechanical model has been validated by the prediction and comparison of the tensile behavior of different states of martensitic steels. However, an even more challenging goal could be to predict the Bauschinger effect and compare those results with experimentally obtained ones. The highlighting importance of this kind of mechanical testing is that the internal stresses play a major role. At the same time the distribution of internal stresses is the only one in this work that has not been experimentally determined.
- 5) The herein proposed micromechanical model does not account for the local interactions between laths/blocks/packets, for the crystalline orientation of the microstructure and the specific plasticity mechanisms encountered in lath structure. These three points may be the focus of further developments specially if a local field implementation (size-sensitive crystal plasticity framework) is envisaged with more proper localization schemes.
- 6) The micromechanical model developed in the present work is focused on the martensitic structure. However, an expansion to other lath microstructures, as bainite, might be envisaged. Also, micromechanical model could be incorporated to predict more complex microstructures as the one presented in Dual-Phase steels or Complex-Phase steels. The application to Press-Hardened Steels can be directly envisaged.

Appendix A

Asymmetry

The diffraction spectrum of a tetragonal cell ($a=b$, $a \neq c$ lattice parameters) has additional peaks when compared to that of a cubic cell. Indeed, some planes such as 200 and 002 are no longer equivalent and have different inter-lattice distances. Thus, we observe a phenomenon that can be described as a degeneration outbreak or a loss of the multiplicity of certain families of peaks.

In the general case, the different peaks can be indexed independently. However, if the degree of tetragonality is low, it is possible that the peaks resulting from this loss of multiplicity remain very close and are almost indissociable from the equivalent peaks in cubic symmetry. As a consequence, it is difficult to prove that the lattice is tetragonal or not. The presence of a possible tetragonality must in fact be sought in a possible asymmetry of the cubic lattice peaks.

An asymmetry parameter (Ψ) is defined by the following equation:

$$\Psi = \frac{FWHM_{Right} - FWHM_{Left}}{0.5 FWHM_{Right} + 0.5 FWHM_{Left}} \quad \text{Equation 58}$$

The position of the maximal intensity is measured. Then, the diffracting peak is modeled with one Pearson VII function for the right side obtaining $FWHM_{right}$ and another Pearson VII function is used for the left side obtaining $FWHM_{left}$, shearing the same position. As can be deduced from Equation 58, if low tetragonality is present negative values are expected for the {200} diffraction peak as the reticular distance for (002) will be higher than the distances corresponding to (200) and (020) planes respectively. In the case of the {220} diffraction peak, the asymmetry parameter (Ψ) will be positive for slightly tetragonal peaks.

This result should also be compared with the “global” c/a ratio provided by the Rietveld refinement procedure.

A.1 Quenching

The asymmetry parameters of the martensite {200} and {220} diffraction peaks were calculated during the cooling at -10 °C/s for the 0.3C steel (0.3C_GQ_10Cs) as function of the transformed martensite fraction and are presented in Figure 113.

The {200} asymmetry parameter is constantly positive but close to zero during the whole transformation (some scattering is found at the beginning when the peak is poorly defined), meaning that no tetragonality effect is observable in this peak. However, the {220} asymmetry

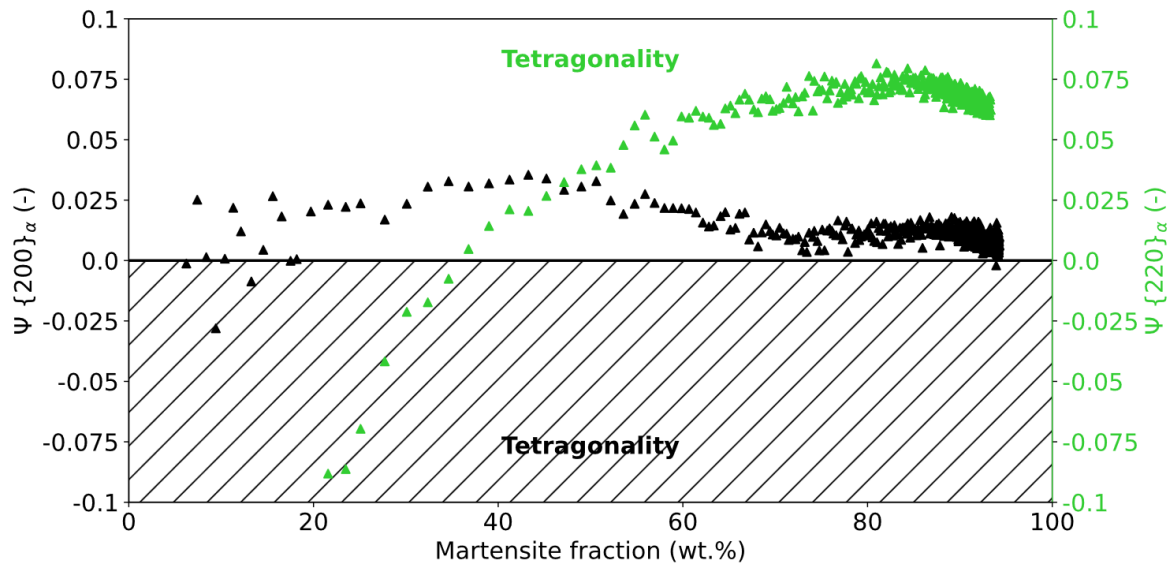


Figure 113: Evolution of the $\{200\}_\alpha$ (in black) and $\{220\}_\alpha$ (in green) asymmetry parameter with the martensite fraction. Colors used in the present graph do not follow the chart presented in Section I.3.

parameter evolution is different. For less than 40 wt.% of formed martensite the parameter is negative (the opposite of the effect produced by tetragonality), then it becomes positive reaching a maximum value of 0.075 and at the end of the transformation its value is 0.06. The tetragonality ratio determined by Rietveld refinement at room temperature is 1.0077 which corresponds to a 0.17 wt.% [22] or to a 0.25 wt.% [143] carbon content of the matrix, 55 and 81 % of the nominal carbon composition respectively.

Table 18 presents the $\{200\}_\alpha$ and $\{220\}_\alpha$ asymmetry parameters and tetragonality ratios obtained for the three studied steels at room temperature after being quenched at the four cooling rates considered in this work (-10, -50, -100 °C/s and water quenched). The $\{200\}_\alpha$ asymmetry parameter is in all the cases closer to zero than the $\{220\}_\alpha$, and in most of the studied conditions it is positive (no tetragonality) while $\{220\}_\alpha$ remains in the tetragonality region (positive value). The only three conditions in which $\Psi\{200\}_\alpha$ is negative are 0.1C_GQ_100Cs, 0.2C_WQ and 0.3C_WQ. The last one being in the same magnitude than most of the $\Psi\{220\}_\alpha$ values.

The tetragonality of martensite due to Zener's order [300] is a subject of debate in the literature [18,301,302] for low carbon steels. For a carbon content of 0.3 wt.% (as the 0.3C steel) tetragonality is expected at room temperature [303], which is detected by the Rietveld refinement. However, the observation of opposite asymmetry for all the gas quenched conditions in some of the diffracting peak is, to the authors knowledge, a new outcome. To the authors knowledge there is no evidence nor explanation in the literature of the presence of tetragonality on the reflection of a family of planes, $\{220\}_\alpha$, and not in another family of planes, $\{200\}_\alpha$. This point remains an open question.

The only cases in which the asymmetry analysis of the individual peaks prove undoubtedly the tetragonal nature of the lattice correspond to the 0.1C steel quenched at -100 °C/s, and the 0.2C and 0.3C steels water-quenched. The tetragonality is favored by the fast cooling, limiting the auto-tempering, and high carbon content, higher expected tetragonality and limiting the auto-tempering by lower Ms.

Appendix A Asymmetry

Table 18: Asymmetry parameter of the {200} and {220} of the martensite and the tetragonality ratio at room temperature for the three steel studied at the for cooling rate used during the quenching.

Steel	Cooling rate	$\Psi\{200\}_a$	$\Psi\{220\}_a$	c/a ratio	C in matrix [22] - [143]
0.1C	-10 °C/s	0.007	0.057	1.0051	0.11-0.16
	-50 °C/s	0.020	0.067	1.0052	0.12-0.17
	-100 °C/s	-0.008	0.068	1.0051	0.11-0.16
	WQ	0.025	0.100	1.0058	0.13-0.16
0.2C	-10 °C/s	0.008	0.072	1.0066	0.15-0.21
	-50 °C/s	0.006	0.063	1.0068	0.15-0.22
	-100 °C/s	0.024	0.097	1.0069	0.15-0.22
	WQ	-0.010	0.076	1.0071	0.16-0.23
0.3C	-10 °C/s	0.022	0.066	1.0076	0.17-0.23
	-50 °C/s	0.005	0.079	1.0082	0.18-0.26
	-100 °C/s	0.001	0.077	1.0082	0.18-0.26
	WQ	-0.054	0.066	1.0089	0.20-0.29

A.2 Tempering

The c/a ratio determined by the Rietveld refinement decreases during the tempering of water-quenched samples as shown in Figure 37 in Section II.3.B.1. Therefore, a decrease of the asymmetry parameters is also expected.

Figure 114 presents the evolution of the asymmetry parameter of the {200} peak, in black, and of the {220} peak during the tempering at 400 °C of the 0.3C steel. A first segment with no variation is observed in the left part of the graph corresponding to the room temperature holding before the heat treatment. In this segment both peaks presents an asymmetry which indicate a possible tetragonality of the lattice. During the second segment (during the heating), two behaviors are observed. In the first one, an increase of the parameters occurs, the asymmetry parameter of the {220} peak seems to indicate a higher tetragonality while the one of the {200} peak is inverted. Then, both parameters decreases. In the last section (during the holding), a continuous decrease in the parameters is observed up to 150 s follow by an stagnation. The asymmetry of the {220} peak may refer to low tetragonality while the one of the {200} peak prove the contrary.

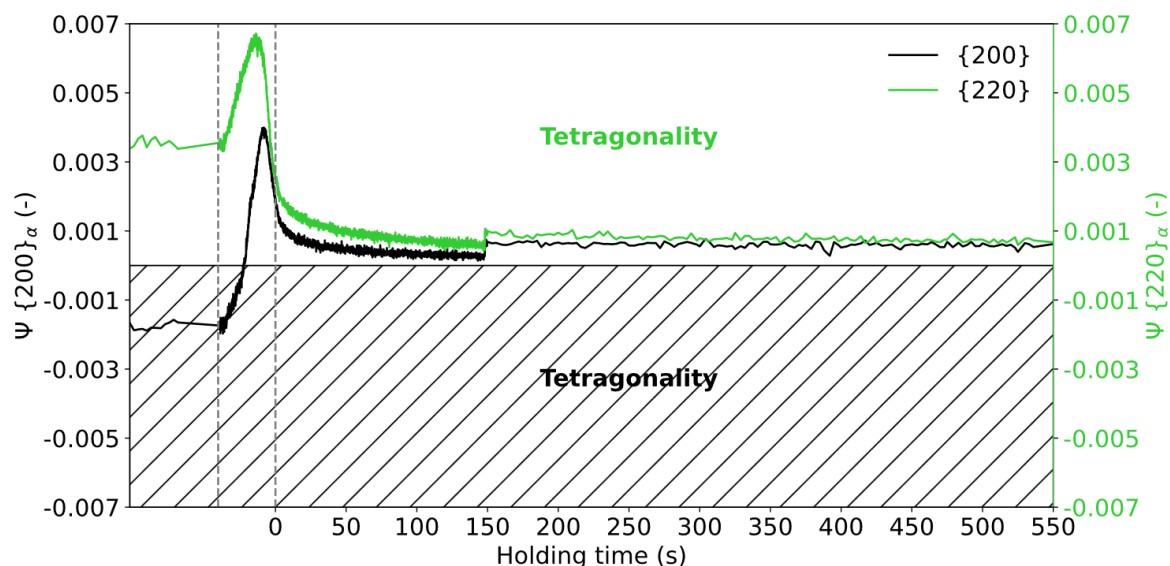


Figure 114: Evolution of the asymmetry parameter of peaks {200} (in black) and {220} (in light green) during the tempering at 400 °C of the 0.3C steel.

From the evolution of the asymmetry parameters, it can be concluded that at room temperature the c/a ratio may reflect actual tetragonality of the lattice while during the tempering the confidence of the c/a ratio obtained by the Rietveld analysis is lower. The {200} asymmetry parameter has in fact the opposite sign of the one expected in the case of tetragonality. At the end of the tempering, the tetragonality values reported by the Rietveld refinement are thus mostly related to a technical adjustment of the FWHM of the diffracting peaks and not to the asymmetry and, therefore, to a true tetragonality.

Appendix B

Comparison between gas-quenched and water-quenched 0.2C martensite

In the present work the as-quenched state of the 0.2C steel has been characterized in detail after being quenched by non-controlled gas and by water. Some of the results have been previously presented in Chapter III.

The cooling path of both quenching conditions are presented in Figure 115. Between 350 °C and 150 °C, the gas quench presented an average cooling rate equal to -20 °C/s while the water quench between -1000 °C/s and -5000 °C/s . In this last case different configurations were studied in order to analyze if the size of the sample (between tensile test and dilatometric size) or the presence of bubbles may affect the cooling rate. At lower temperatures, gas and water quench decrease their rate but the water quench reach much faster the room temperature than the gas quench.

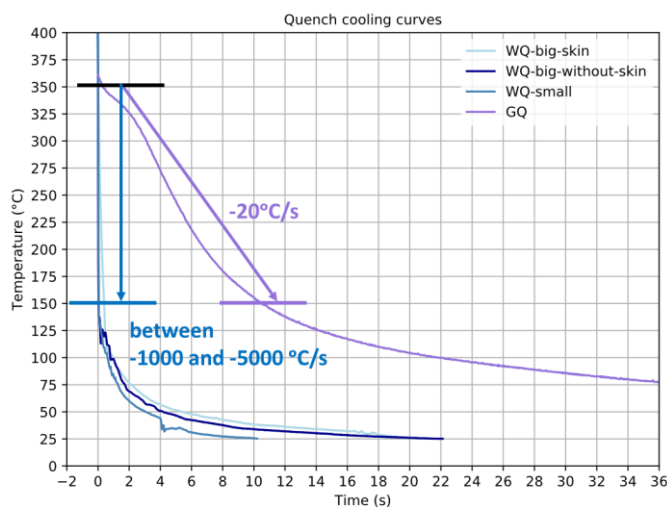


Figure 115: Cooling path of the non-controlled gas quench as well as different configurations of the water quench.

Firstly the microhardness (0.1 kg) of both microstructures has been characterized, obtaining 450 Vickers for the 0.2C_GQ and 525 Vickers for the 0.2C_WQ. The nanohardness were then measured for both conditions producing ca. 700 indentations for each condition. The obtained nanohardness ⁴distributions are shown in Figure 116. The 0.2C_GQ presents a lower mean value than the one of 0.2C_WQ but a higher dispersion. The increase of the dispersion may be due to the presence of indentations on austenite which transformed in ultra-fresh martensite or by the presence of carbides.

⁴ Nanohardness measurements were performed by Alejandro Pachon and his team at ArcelorMittal Research SA.

The presence of nanosized carbides in the 0.2C_GQ condition was revealed by TEM characterization, Figure 48.a. The same technique did not put in evidence any carbide for the 0.2C_WQ samples, Figure 48.b. In both conditions the presence of nanotwin was observed.

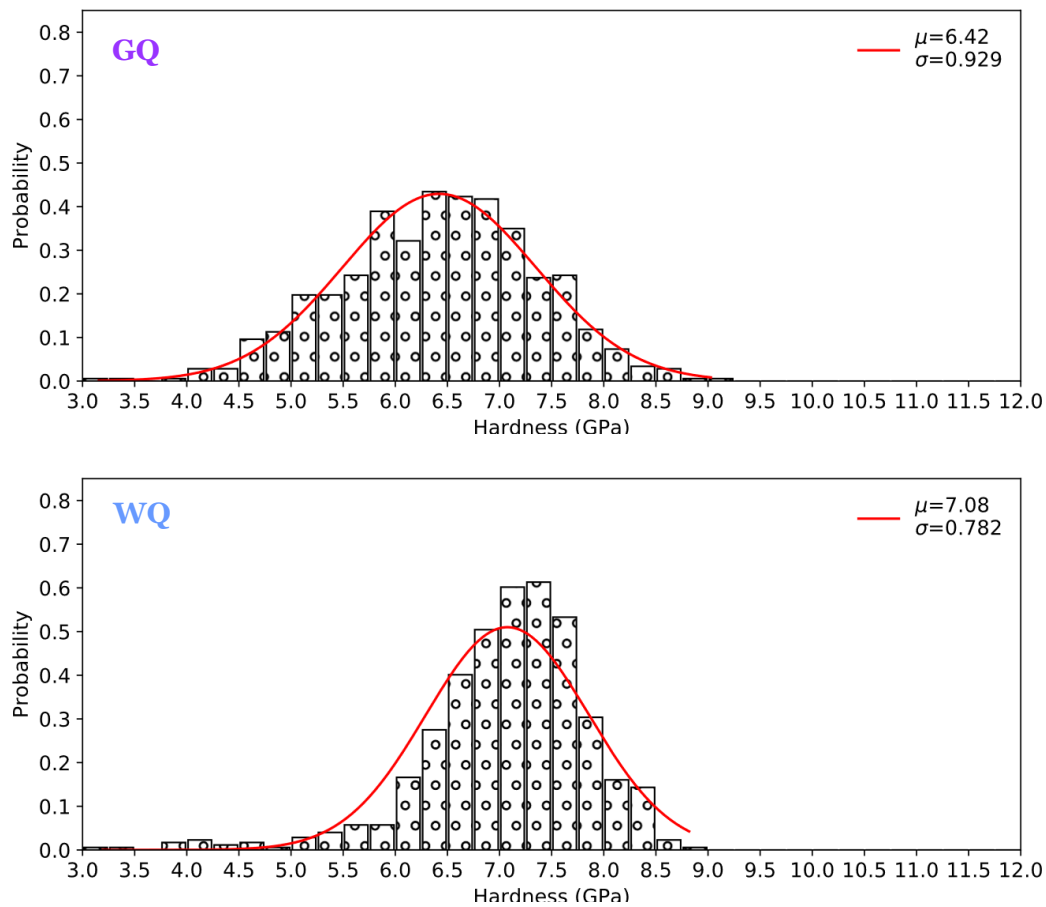


Figure 116: Distribution of nanohardness of the 0.2C_GQ and 0.2C_WQ condition.

Atom Probe Tomography analysis was performed in both quenched conditions in order to determine the state of the carbon segregation into dislocations and, therefore, to calibrate a segregation model. The results, presented in Chapter III in more detail, shown that in both cases similar segregation level were reached when characterized two months after the quench. The equivalent carbon concentration around dislocations was 7.6 at.% in the 0.2C_GQ condition and 8.4 at.% in the 0.2C_WQ one. Both values can be considered as similar between the expected incertitude and are in good accordance with the Cottrell atmospheres reported in the literature [41,151,213], between 7 and 10 at.%.

In the 3DAPT results of the 0.2C_GQ a film of carbon-enriched austenite is observed (Chapter III Figure 43.a). The carbon concentration in the mentioned austenite film varied between 6 and 8 at.% (1.25-1.5 wt.%). Therefore, a chemical stabilization of the austenite is expected. No substitutional partial profiles were observed, due to the much lower diffusivity of those elements. No austenite was found in any of the 5 tips of the 0.2C_WQ condition characterized by APT.

The high stability of the austenite in the gas-quenched conditions is confirmed by Rietveld refinement of HEXRD measurements at room temperature in which the fraction of austenite after the gas quench was equal to 4 wt.% and after water quench 1.8 wt.%. Note that by the Koistinen-Marburger equation

with an equal M_s temperature a same residual austenite fraction is expected. The effect of the cooling rate on the stability of the austenite have been addressed by Godin et al. [186] and Sherman et al. [185].

The Rietveld refinement results also allows to determine the c and a parameters of the martensite and, thus, the c/a ratio. The same is equal to 1.0055 in the 0.2C_GQ condition and equal to 1.0073 in the 0.2C_WQ condition. The presented tetragonality ratios are related to a carbon in solid solution equal to 0.12-0.18 wt.% for the 0.2C_GQ condition and equal to 0.16-0.24 wt.% for the 0.2C_WQ condition [22,143]. The lower carbon content in the gas-quenched condition may be partially due to the previously presented precipitation as well as to the carbon partitioning into the residual austenite.

From the HEXRD results the dislocation density was determined for both conditions, obtaining 2×10^{15} $1/m^2$ in the 0.2C_GQ sample and 2.5×10^{15} $1/m^2$ in the 0.2C_WQ sample. The higher dislocation density with the higher cooling rate have been discussed in Section II.3.A.1 of the present study.

The precipitation model developed in Chapter III was utilized to predict the precipitation during the two quenching conditions. The selected parameters are set equal to the values reported in Table 12. The simulations were started at 340 °C, temperature at which 50 wt.% of martensite have been already transformed (by HEXRD results) and the dislocation density was set equal to 2.4×10^{15} $1/m^2$ for the 0.2C_GQ condition and to 2.7×10^{15} $1/m^2$ for the 0.2C_WQ one. Both dislocation densities are the ones calculated with parameters A_{dislo} and B_{dislo} and the Equation 20 of Chapter II.

Figure 117 presents the result of the precipitation simulations. The 0.2C_GQ condition produces a fraction of epsilon carbides of 2 % concomitant with cementite precipitates. Then the epsilon carbides dissolves and the cementite fraction increases up to ca. 4 %. The 0.2C_WQ condition presents a small precipitation of epsilon and a negligible fraction of cementite in the same temperature range (330 °C - 200 °C) with maximum fractions of 0.4 % and 0.11 % respectively. Then no further evolutions are visible. The final predicted sizes of the cementite are 10.5 nm and 3.5 nm for the GQ and WQ conditions while the ones of the epsilon are 4.2 nm and 3 nm.

The precipitated state of the gas-quenched sample is consistent with the TEM observations, relatively high fraction and visible precipitates. A good accordance is also present between the TEM results and the ones of the simulations for the WQ condition.

A summary of the comparison between both cooling rates is presented in Table 19.

Appendix B Comparison between gas-quenched and water-quenched 0.2C martensite

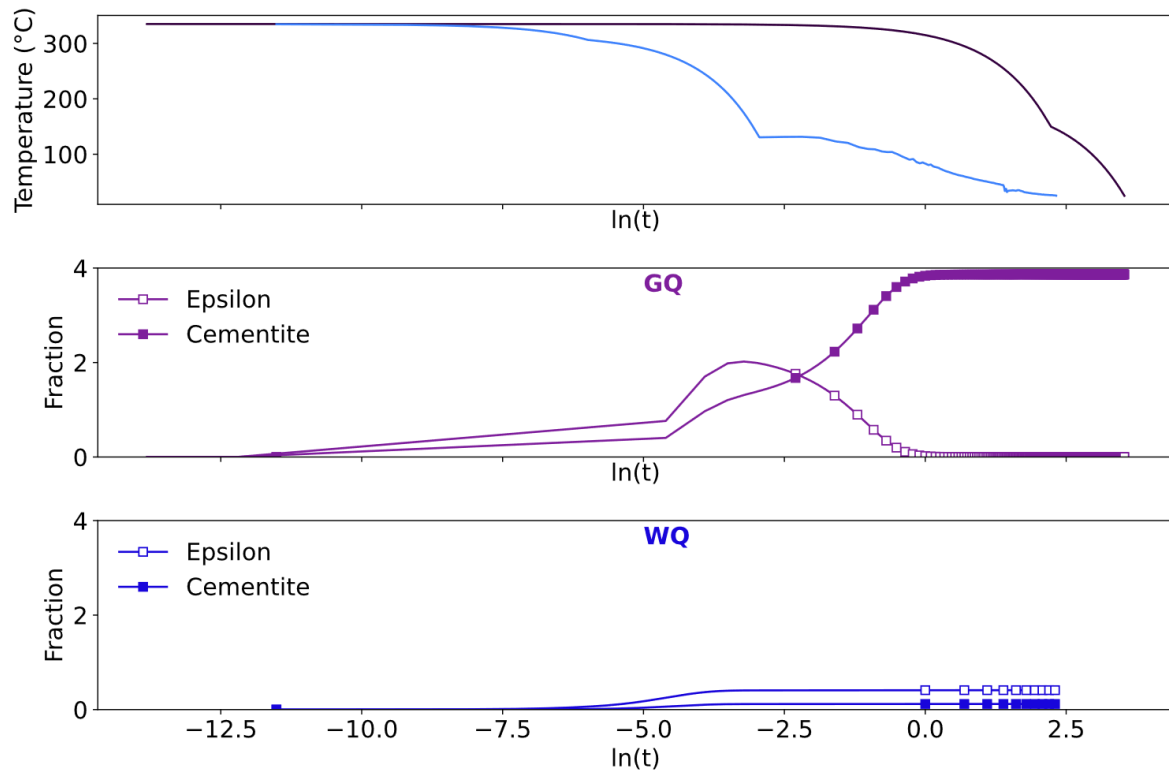


Figure 117: Precipitation model results for both simulated cooling path. Top figure: cooling paths. Center figure: Carbides fraction for the 0.2C_GQ condition. Bottom figure: Carbides fraction for the 0.2C_WQ condition.

Table 19: Summary of the comparison between the gas-quench and que water-quench conditions.

0.2C	GQ	WQ
Cooling rate	-20 °C/s	between -1000 and -5000 °C/s
TEM	Carbides	No carbides
APT	Dislocation segregation & enriched austenite	Dislocation segregation
Microhardness	450 Vickers 0.1kg	525 Vickers 0.1kg
Nanohardness	6.42 GPa, sigma 0.93	7.08 GPa, sigma 0.782
HEXRD austenitic fraction	4 wt.%	1.8 wt.%
Dislocation density	2.00E+15	2.50E+15
c/a	1.0055	1.0073
C in mart (1+0.045x%C)	0.12	0.16
C in mart (1+0.030x%C)	0.18	0.24

Appendix C

Influence of aging before tempering on precipitation

The simulations shown in previous sections took into account the aging for 2 months at room temperature before the tempering, in order to reproduce the experimental conditions. In order to determine the effect of the aging, simulations are performed here by considering again the heating at 10 °C/s up to 400 °C, but to a martensite inside which no carbon segregation would have occurred. This means that there is an equal carbon concentration in the dislocation atmospheres and in the matrix before the start of the heating, the one of the 0.2C steel.

The main differences with the previous simulation regarding the evolutions of carbon concentration occur below 200 °C, as shown in Figure 118 (dashed orange rectangle). In the new simulation, the carbon takes significant time to segregate to the dislocations upon heating, and this process can be considered to be completed at ca. 150 °C when x_{matrix} reaches the equilibrium value. Hence, compared to previous simulations, the matrix keeps a higher concentration for a longer time.

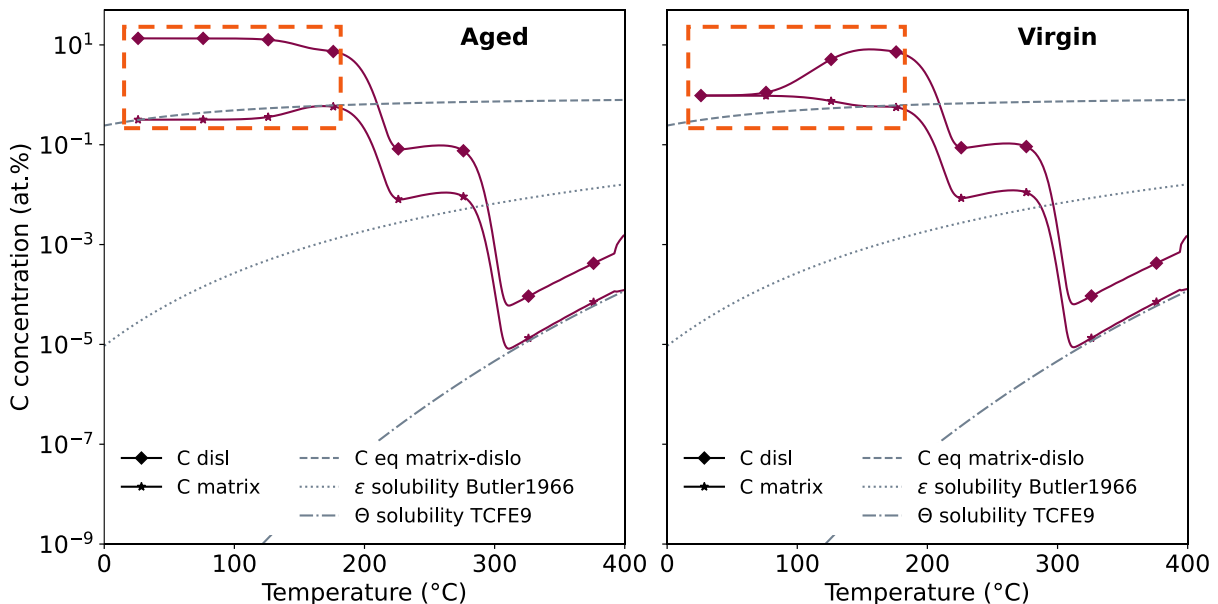


Figure 118: Effect of aging previously to tempering on the carbon concentration curves from the 0.2C steel heated up to 400 °C.

The consequence on the formation of carbides is shown in Figure 119, in which the evolutions of the number densities of epsilon and cementite carbides are plotted. The nucleation of epsilon is retarded by ca. 25 °C if the prior aging is accounted for. Conversely, the cementite precipitation occurs slightly earlier (less than 5 °C) than for the virgin martensite. Both trends come from the fact that in the aged

Appendix C Influence of aging before tempering on precipitation

martensite, the carbon concentration is lower in the matrix and higher in the dislocation atmospheres at temperatures below 200 °C.

No clear effects of the aging on the carbide fractions kinetics are observed, and these are not plotted. With the exception of a reduction of 0.2 wt.% on the epsilon fraction when aging is accounted for. This is because of the faster formation of the cementite.

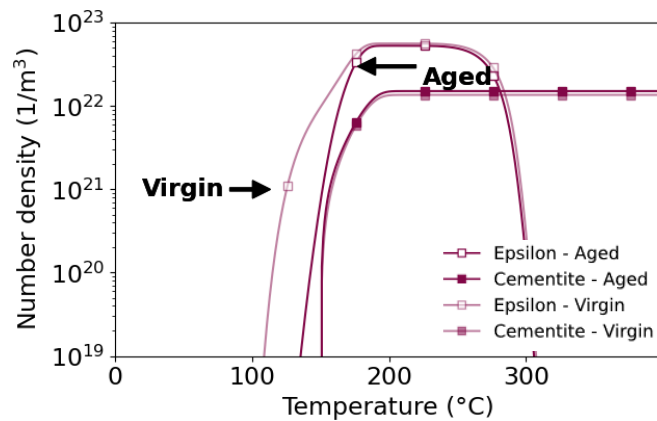


Figure 119: Evolution of the number density of epsilon and cementite according to the simulation with and without prior aging, for the 0.2C steel and upon heating at 10 °C/s up to 400 °C.

Hence, the effects of prior aging predicted by the simulation do not seem significant. But the difference between the virgin and the aged martensite would increase if a higher heating rate was applied, or if a higher trapping energy was considered (which would lead to lower carbon concentration in the matrix and higher concentration in the dislocation atmospheres).

Appendix D

Influence of heating rate on the precipitation

In the present study no systematic study of the effect of the linear heating rate was performed. Such study has already been done in previous versions of the precipitation model in [39,171]. We will focus on a more practical point, the actual heat treatments applied to the tensile samples.

In the preceding, the precipitation model has been evaluated and calibrated with linear heat treatments, for which constant heating rate at 10 °C/s up to the different holding temperatures were considered. However, more complex temperature evolutions are applied during heating, particularly when preparing the tensile test samples considered in Chapter IV. The tensile test samples were heat treated in baths (oil bath at 200 °C, salt bath at 300 °C and 400 °C). The corresponding temperature-time curves were measured with thermocouples for the three holding temperatures and are plotted in (Chapter I, Figure 7). They show a fast heating at the start of the treatment followed by a slower heating as the sample temperature is gets closer to the temperature of the oil/salt bath.

The precipitation model is applied here, still using the parameters presented in Table 12, in order to simulate the heat treatments in salt bath and with heating up to 400 °C. The simulations are compared to those presented in Section III.3.B.2.e with the linear heating rate (10 °C/s) and for the 0.2C steel. As shown in Figure 120, the main difference between both heat treatments regards the evolution of the carbide fractions, whereas the effect on the sizes are less important. The formation of the epsilon carbides starts at lower temperature than for the linear heat treatment. This is due to the lower heating rate up to 350 °C for the linear heat treatment. Consequently, the related evolutions of the carbon concentrations are shifted by about 50 °C higher for the treatment in salt bath. As for the cementite, its formation is also shifted to higher temperature. During the first stage of cementite formation, the gap between both simulations is about 50 °C but during the second stage, it is lower than 20 °C. Hence, the “slower” formation of epsilon was not to the benefit of the cementite (as it was the case, for example, when studying the effect of the dislocation density). Both carbides showed slower nucleation and growth due to the faster heating. The kinetics effects may be less important for the cementite because it forms at higher temperature, when the heating rate for the treatment in salt bath is slower. The high carbon concentration in the Cottrell atmospheres may also let the cementite carbide formation less sensitive to the heating rate. It can be also postulated that the heating rate effects are more important in the phenomena occurring at lower temperature, when the diffusion is slower.

The epsilon carbides present similar radius in both simulations (related to the similar number density of carbides) while at the end of the heating the cementite formed by the salt bath tempering is ca. 5 nm

Appendix D Influence of heating rate on the precipitation

bigger than the one formed in the linear heat treatment. The difference in the final size of the cementite carbides is due to a higher number density for the linear heating.

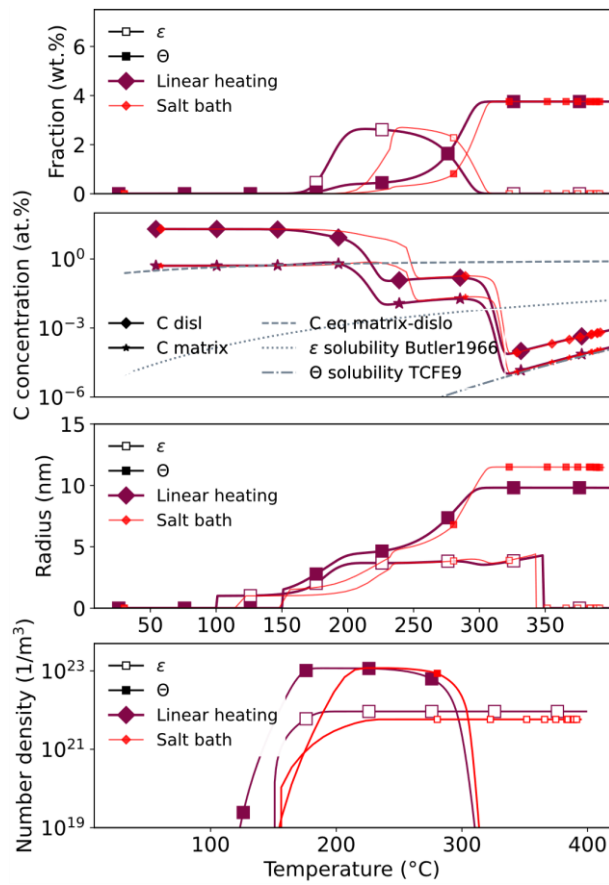


Figure 120: Effect of the heating rate on the precipitation sequence in the 0.2C steel heating up to 400 °C, at a constant rate 10 °C/s (thick lines) or with treatment in salt bath (thin lines).

The shift to higher temperatures of the precipitation of epsilon and cementite is in agreement with experimental and simulation works of the literature (with prior version of this model [39,171] and also [190,304]). A small increase of carbides number is also reported in the literature. However, in the present case it was observed for the epsilon and not for the cementite.

Appendix E

In situ tensile test

Martensite presents an interesting phenomenon when submitted to a tensile test. The width of its diffraction peaks narrows at least up to the uniform elongation. This phenomenon has been reported in the literature by several authors [42,264–266].

An in situ tensile test followed by HEXRD was performed also in this study on 0.2C_WQ steel. The obtained 2D diffractograms were integrated only in the range $\pm 4^\circ$ from the vertical axis, considering the planes which are perpendicular to the tensile direction. The measured FWHM of the corresponding {220} peak are presented in Figure 121.

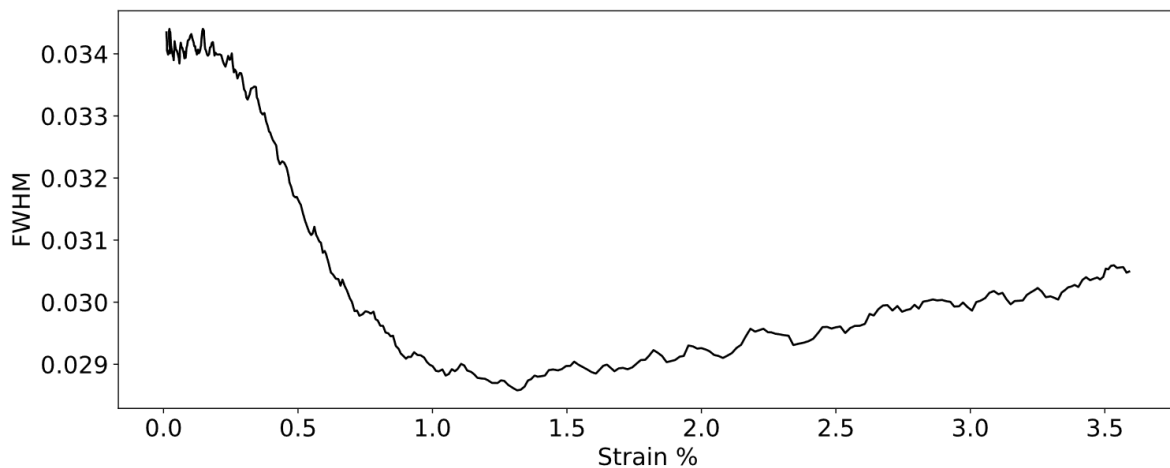


Figure 121: Evolution of the FWHM of the {220} peak during an in situ HEXRD tensile test of the 0.2C_WQ condition.

At the beginning of the curve, the curve is almost constant in the elastic stage of the tensile test. The FWHM then decreases suddenly during the first percent of plastic deformation as expected from the literature. Above that value, an incipient increase is observed.

Different interpretations have been proposed to explain the described behavior. While some authors proposed a fast mechanical recovery [42,264,265] associated to a decrease in the mean dislocation density, others proposed a relaxation of internal stresses [266,267] (sharpened distribution of hydrostatic internal stresses).

Our work sustains mainly the second hypothesis. We consider in fact that the first decrease is due to a narrowing of the distribution of internal stresses. The stagnation value may be related to the minimal FWHM related to the density of defects in the microstructure. Finally, the incipient increase can be interpreted as an increase of the dislocation density during the tensile test or due to a reverse spreading of the distribution of internal stresses due to different plasticization of the phase constituents. Our

micromechanical model is able to capture this latter evolution during the tensile simulation. As a consequence, its effect on the diffraction peak can also be estimated.

To do so, a strong hypothesis must be made which consist in assuming that the hydrostatic internal stresses evolve proportionally to the deviatoric internal stresses.

$$\sigma_{hydro} = K_{prop} \times \sigma_{int} \quad \text{Equation 59}$$

where σ_{int} is the deviatoric internal stress, σ_{hydro} is the hydrostatic internal stress and K_{prop} is a proportionality constant. K_{prop} has been arbitrarily set to 1.

The lattice parameter under stress (a_{stress}) can be calculated as [138]:

$$a_{stress} = a_{free} \times \left(1 + \frac{\sigma_{hydro}}{3K}\right) \quad \text{Equation 60}$$

with
$$K = \frac{2\mu(1+\nu)}{3(1-2\nu)}$$

where μ is the shear modulus and ν the Poisson ratio.

With the lattice parameter, the position of the peak can be calculated with the Bragg law. The intensity of the peak is proportional to the fraction of the constituent, a fixed FWHM is set for all the constituents of the aggregate. Therefore, a Pearson VII function can be modeled for each constituent and the sum of all gives the macroscopic martensitic peak. The martensitic peak is then analyzed to determine a macroscopic FWHM ($FWHM_{macro}$), which can be compared to the experimental data.

The evolution of global FWHM of the {220} is presented in Figure 122 (considering a proportionality constant equal to 1).

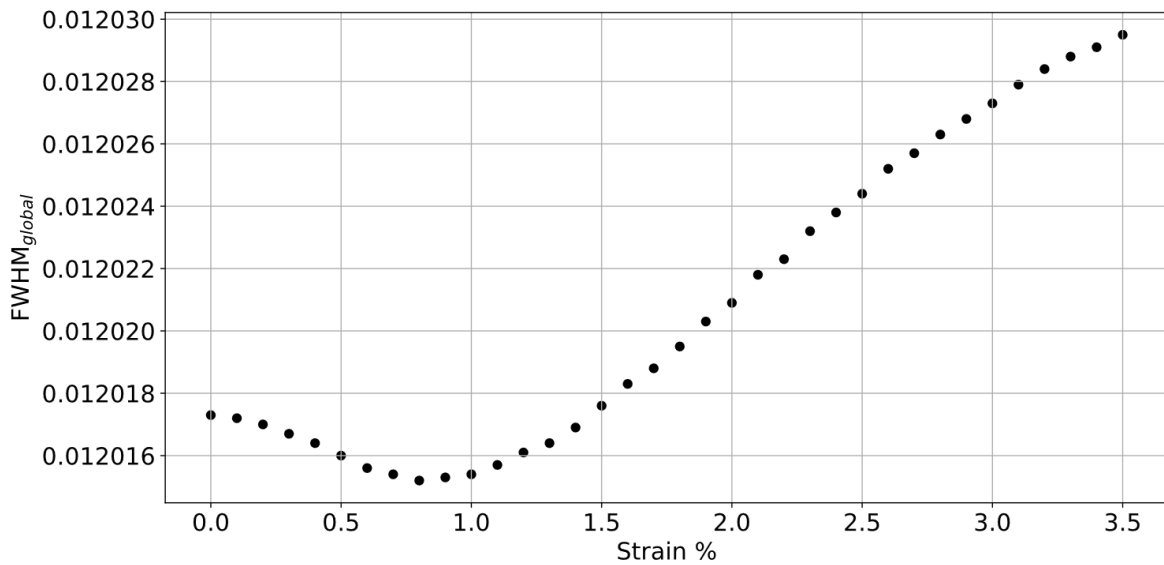


Figure 122: FWHM evolution of the modeled diffracting peak during the tensile test simulation.

Appendix E In situ tensile test

A constant stage is observed in which most of the phases remains elastic. Then, global FWHM presents a small decrease which is followed by a strong increase. This simulation result explain quite well the experimental observation and sustain our hypothesis even if the change of values are lower than the ones observed experimentally.

The decrease in the internal stress distribution of the softer phases is responsible for the initial decrease of the FWHM. The increase observed after 1% is on the contrary related to genesis of new internal stresses during the macroscopic loading due to the difference of behavior between the components. Even if a model describing hydrostatic stresses should be desirable, the present model presents the basis for a better understanding of the evolution of FWHM during the tensile test of martensitic steels

Appendix F

Effect of the distribution of deviatoric internal stresses

The micromechanical model developed in this thesis considers as an input the distribution of microstructure YS and the distribution of deviatoric internal stresses. The first distribution is estimated thanks to experimental observations. The distribution of deviatoric internal stresses is not sustained by any experimental determinations gathered in the frame of the present study. In the literature, very few data are available except maybe some local values presented by analyzing the deformation due to relaxation of FIB-milled micro-pillars [30].

As the deviatoric internal stresses distribution could not be obtained experimentally, a gaussian kind distribution was presupposed. The distribution must be centered and globally symmetric to maintain the macroscopic equilibrium. The second parameter is the standard deviation (ζ). Figure 123 presents a set of three distributions of deviatoric internal stresses varying the standard deviation, including $\zeta=200$ MPa, $\zeta=400$ MPa and $\zeta=600$ MPa.

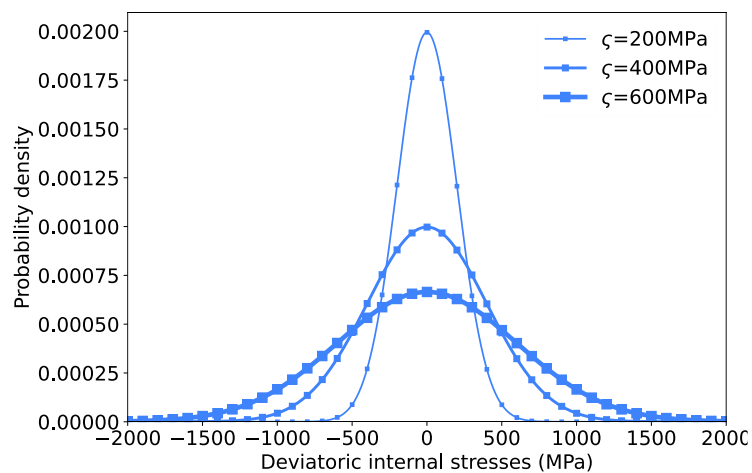


Figure 123: Gaussian distribution of deviatoric internal stresses with the standard deviation varying from 200 to 600 MPa.

These distributions were used to describe the behavior of the water-quenched 0.2C condition (0.2C_WQ). The used microstructure YS distribution is presented in Figure 100 in chapter IV. The modeled tensile curves are presented in Figure 124 as well as the experimental one.

Appendix F Effect of the distribution of deviatoric internal stresses

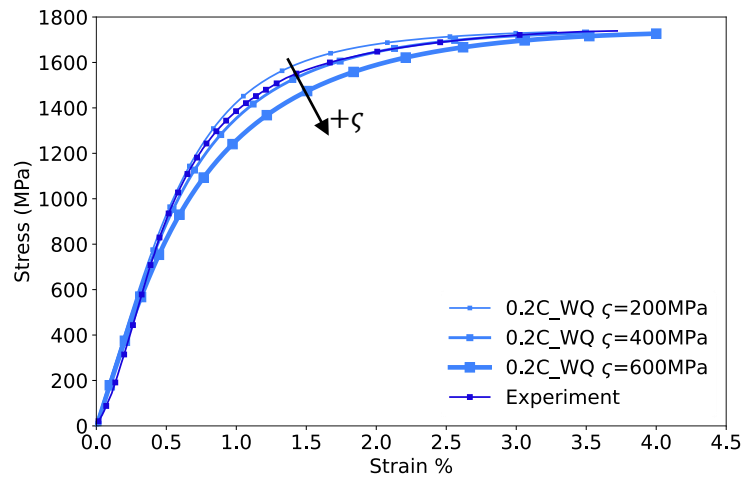


Figure 124: Modelized tensile behavior of the 0.2C_WQ condition varying the distribution of deviatoric internal stresses. The experimental curve is presented for comparison.

According to Figure 124, the spread of the distribution of internal stresses plays a minor role on the obtained maximal stress (the difference is lower than 10 MPa) but affect the work-hardening rate. A higher spread produced a lower work-hardening at low strains. However, this tendency is inverted at strains higher than 1 % as observed more clearly in Figure 125.

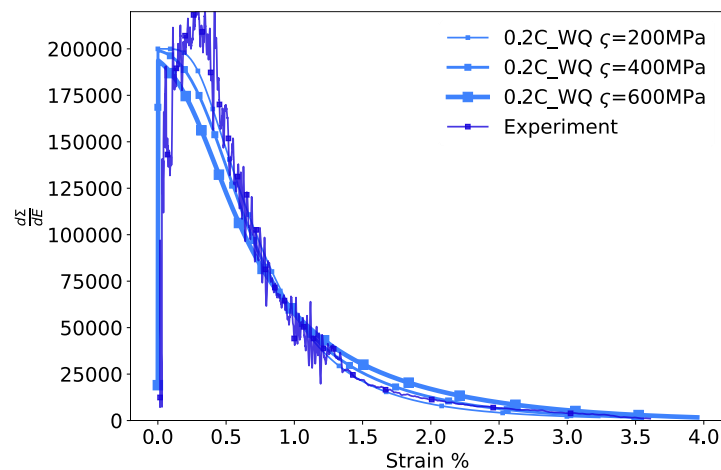


Figure 125: Work-hardening of the curves presented in Figure 124 as function of the strain.

It can be concluded that the major effect of the deviatoric internal stresses distribution is on the work-hardening and not in the maximal stress of the modelized tensile curves. A standard deviation of 400 MPa seems a good first approximation for the following calculations.

Appendix G

Pedagogical example of the micromechanical model

In the following, a simplified example is proposed to elucidate the model behavior. A total set of nine elements is proposed and presented in Table 20. Elements with three different yield strengths are proposed as well as three internal stress states per each yield strength. The Young modulus is set equal to 200 GPa and the β parameter to 50 GPa. For all the present simulations the elements are considered to have all the same fraction.

Table 20: Set of the nine elements presenting different yield strengths and deviatoric internal stresses utilized to exemplify the micromechanical model

N°	Yield strength (MPa)	Deviatoric internal stress (MPa)
1	300	20
2	300	0
3	300	-20
4	400	20
5	400	0
6	400	-20
7	500	20
8	500	0
9	500	-20

To study the effect of the yield strength a subset presenting the same internal stress state but different YS is proposed with the elements 2, 5 and 8. The results of this first simulation with the mentioned elements is presented in Figure 126.a. On the left the microscopic tensile behavior of the three considered elements as well as the calculated macroscopic stress are shown. On the right the evolution of the internal stresses on each element is shown. The macroscopic stress follows the microscopic stresses during the elastic stage, then the element with lower YS plasticizes changing its slope and,

Appendix G Influence of heating rate on the precipitation

therefore, the one of the macroscopic curve. As linearity is followed the internal stresses are constants for each element but when plasticization arrives different changes are observed. The softer element goes into compression as its microscopic stress is lower than the macroscopic and the two others elements are in traction (as in the Masing model). When plasticization of the second element arrives, a second change in the macroscopic work hardening is observed as well as in the internal stresses evolution. At all strains, the sum of internal stresses is zero. The simulation stops once the last elements plasticizes and, thus, the work hardening becomes zero, this occurs at 0.46 % strain.

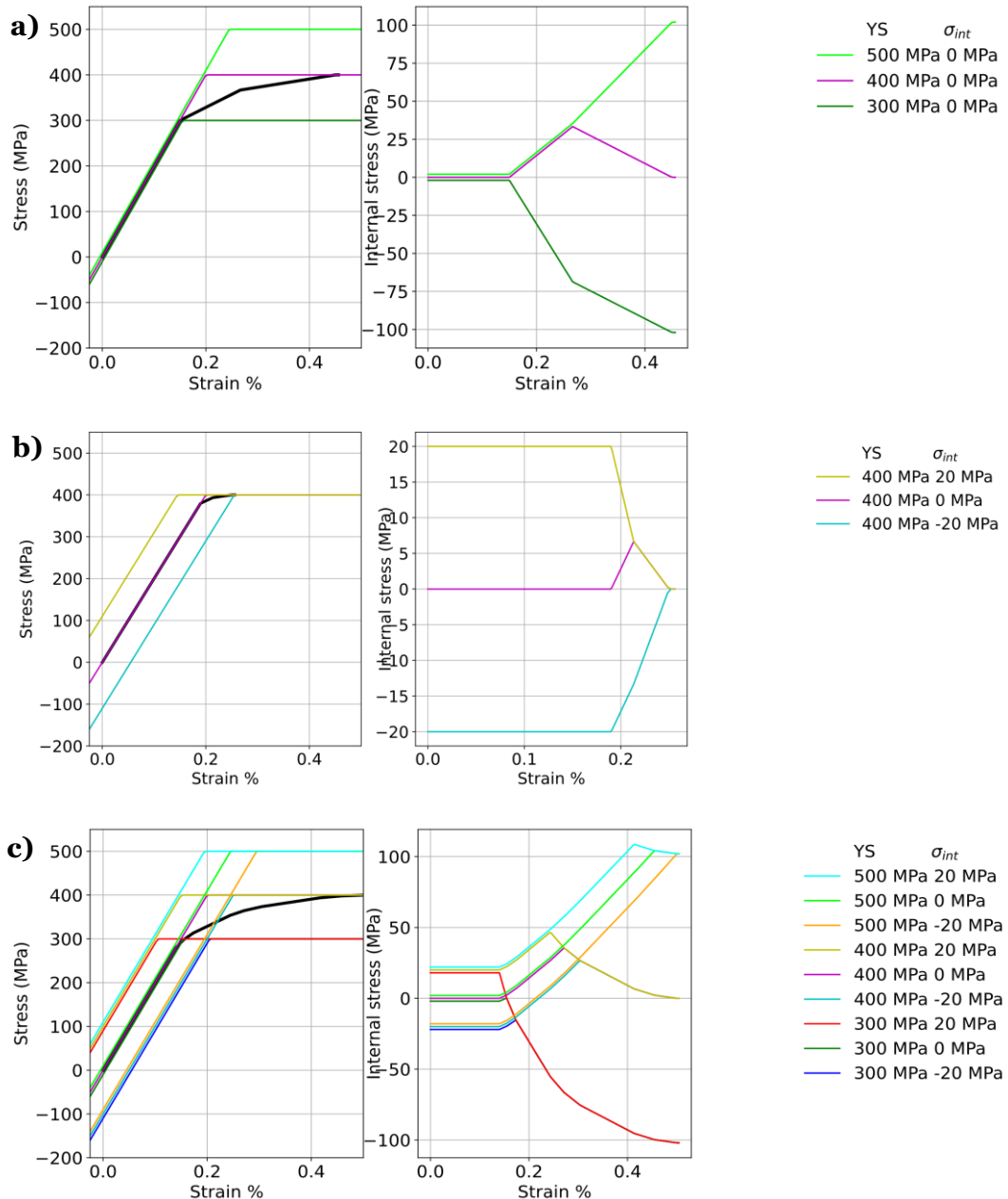


Figure 126: Micromechanical model results of the simplified dataset analyzing the effect of different yield strength in a), of different internal stresses in b) and combining both effects in c). The colors used in the present figure do not follow the chart presented in Section I.3.

The effect of the deviatoric internal stresses is analyzed in a second simulation and presented in Figure 126.b. In this case the elements selected were 4, 5 and 6 with microstructure YS equal to 400 MPa and

Appendix G Influence of heating rate on the precipitation

-20, 0 and 20 MPa as initial deviatoric internal stress states. Note that the values of the internal stresses are obtained in the equilibrium state (all the elements on the β line passing by zero). A similar behavior as the previously described one is observed with first plasticization of the element with positive internal stress and final plasticization of the one in compression. The last element plasticization and end of the simulation occurred at 0.26 % strain. If the same tensile curves were considered under an isostrain hypothesis, the same results of Figure 126.a would have been found.

Finally, the third simulation considering all nine elements is shown in Figure 126.c (the curves have been slightly shift to avoid juxtaposition). The change of the slope of macroscopic curve are softer than in both previously presented cases due to the combination of nine successive break points. The first element to plasticize is the one with the lowest yield strength and positive internal stresses (red curve) while the last one is the one with highest yield strength and negative internal stresses (orange curve). The last plasticization occurred 0.5 % strain, which is higher than both previous ultimate elongations. At the end of the simulation (with all the elements plasticized) the internal stress state of each element is only ruled by its yield strength and not by the initial internal stress.

Bibliography

- [1] WorldSteel Association, 2018. (n.d.). <https://www.worldsteel.org/>.
- [2] R.H. Smith, R. Maddin, J.D. Muhly, T. Stech, Bronze Age Steel From Pella, Jordan, *Curr. Antropol.* 25 (1984) 234–236. <https://doi.org/10.1086/203118>.
- [3] R. Schwab, Evidence for carburized steel and quench-hardening in the ‘Celtic’ oppidum of Manching, *Hist. Metall.* 36 (2002) 6–16. <https://hmsjournal.org/index.php/home/article/view/270> (accessed October 3, 2022).
- [4] C. Mori, G. Ghiara, P. De Montis, P. Piccardo, G.D. Gatta, S.P. Trasatti, Archaeometallurgical Analyses on Two Renaissance Swords from the “Luigi Marzoli” Museum in Brescia: Manufacturing and Provenance, *Heritage.* 4 (2021) 1269–1283. <https://doi.org/10.3390/HERITAGE4030069>.
- [5] K. Chantziara, F. Javadzadeh Kalahroudi, J. Bergström, M. Grehk, P. Ulfberg, A case study of mechanical and thermal fatigue of press hardening dies, *IOP Conf. Ser. Mater. Sci. Eng.* 1238 (2022) 012025. <https://doi.org/10.1088/1757-899X/1238/1/012025>.
- [6] K.F. Best, High Strength Materials for Aircraft Landing Gear, *Aircr. Eng. Aerosp. Technol.* 58 (1986) 14–24. <https://doi.org/10.1108/EB036313/FULL/XML>.
- [7] Ams_tomtaylor, Still going strong, *Automotivemanufacturingsolutions.* (n.d.). <https://www.automotivemanufacturingsolutions.com/joining/still-going-strong/36141.article> (accessed September 16, 2022).
- [8] M. Tisza, I. Czinege, Comparative study of the application of steels and aluminium in lightweight production of automotive parts, *Int. J. Light. Mater. Manuf.* 1 (2018) 229–238. <https://doi.org/10.1016/J.IJLMM.2018.09.001>.
- [9] G. Krauss, Martensite in steel: strength and structure, *Mater. Sci. Eng. A.* 273–275 (1999) 40–57. [https://doi.org/10.1016/S0921-5093\(99\)00288-9](https://doi.org/10.1016/S0921-5093(99)00288-9).
- [10] C. Zhang, Q. Wang, J. Ren, R. Li, M. Wang, F. Zhang, K. Sun, Effect of martensitic morphology on mechanical properties of an as-quenched and tempered 25CrMo48V steel, *Mater. Sci. Eng. A.* 534 (2012) 339–346. <https://doi.org/10.1016/j.msea.2011.11.078>.
- [11] Hot Stamped B-pillar solution, (n.d.). <https://antb.co.in/hot-stamped-b-pillar-solution/> (accessed September 11, 2022).
- [12] E. Pereloma, D. V. Edmonds, eds., *Phase transformations in steels Volume 2*, Woodhead Publishing Limited, 2012.
- [13] H.S. Yang, H.K.D.H. Bhadeshia, Uncertainties in dilatometric determination of martensite start temperature, *Mater. Sci. Technol.* 23 (2007) 556–560. <https://doi.org/10.1179/174328407X176857>.
- [14] J. Macchi, S. Gaudez, G. Geandier, J. Teixeira, S. Denis, F. Bonnet, S.Y.P. Allain, Dislocation densities in a low-carbon steel during martensite transformation determined by in situ high energy X-Ray diffraction, *Mater. Sci. Eng. A.* 800 (2021) 140249. <https://doi.org/10.1016/j.msea.2020.140249>.
- [15] J. Wang, P.J. Van Der Wolk, S. Van Der Zwaag, Determination of martensite start temperature in engineering steels. Part I. Empirical relations describing the effect of steel chemistry, *Mater. Trans. JIM.* 41 (2000) 761–768. <https://doi.org/10.2320/matertrans1989.41.761>.
- [16] S.M.C. van Bohemen, L. Morsdorf, Predicting the Ms temperature of steels with a thermodynamic based model including the effect of the prior austenite grain size, *Acta Mater.* 125 (2017) 401–415. <https://doi.org/10.1016/j.actamat.2016.12.029>.
- [17] J.L. Collet, M. Caruso, G. Lannoo, S. Cobo, S.M.C. van Bohemen, D. Ponge, C. Tasan, L. Morsdorf, L. Bracke, L. Moli Sanchez, *New Metallurgical Tools for optimum design of modern Ultra High Strength Low Carbon Martensitic Steels*, 2019. <https://doi.org/10.2777/674520>.
- [18] H.K.D.H. Bhadeshia, Carbon in cubic and tetragonal ferrite, *Philos. Mag.* 93 (2013) 3714–3725.

Bibliography

- <https://doi.org/10.1080/14786435.2013.775518>.
- [19] G. Krauss, Tempering of Lath Martensite in Low and Medium Carbon Steels: Assessment and Challenges, *Steel Res. Int.* 88 (2017) 1–18. <https://doi.org/10.1002/srin.201700038>.
- [20] G. Badinier, C.W. Sinclair, S. Allain, F. Danoix, M. Gouné, The Mechanisms of Transformation and Mechanical Behavior of Ferrous Martensite, *Ref. Modul. Mater. Sci. Mater. Eng.* (2017) 1–34. <https://doi.org/10.1016/b978-0-12-803581-8.02518-2>.
- [21] N. Fonstein, *Advanced High Strength Sheet Steels: Physical Metallurgy*, SPRINGER, 2015.
- [22] H.K.D.H. Bhadeshia, R. Honeycombe, *Steels: Microstructure and Properties*, 2006. <https://doi.org/10.1016/B978-0-7506-8084-4.X5000-6>.
- [23] Bain E.C., The nature of martensite, *AIME*. 70 (1924) 25–47.
- [24] G. Kurdjumov, G. Sachs, Über den Mechanismus der Stahlhärtung, *Zeitschrift Für Phys.* 64 (1930) 325–343. <https://doi.org/10.1007/BF01397346>.
- [25] Z. Nishiyama, X-ray investigation of the mechanism of the transformation from face centered cubic lattice to body centered cubic, *Sci. Rep. Tohoku Univ.* 23 (1934) 637-. <https://cir.nii.ac.jp/crid/1570854175128630400> (accessed October 3, 2022).
- [26] A.B. Greninger, A.R. Troiano, The mechanism of Martensite formation, *JOM*. 1 (1949) 590–598. <https://doi.org/10.1007/BF03398900>.
- [27] S. Morito, J. Nishikawa, T. Maki, Dislocation Density within Lath Martensite in Fe–C and Fe–Ni Alloys, *ISIJ Int.* 43 (2003) 1475–1477. <https://doi.org/10.2355/isijinternational.43.1475>.
- [28] S. Morito, Y. Edamatsu, K. Ichinotani, T. Ohba, T. Hayashi, Y. Adachi, T. Furuhashi, G. Miyamoto, N. Takayama, Quantitative analysis of three-dimensional morphology of martensite packets and blocks in iron-carbon-manganese steels, *J. Alloys Compd.* 577 (2013) S587–S592. <https://doi.org/10.1016/j.jallcom.2012.02.004>.
- [29] E. Gautier, J.S. Zhang, X.M. Zhang, Martensitic Transformation under Stress in Ferrous Alloys. Mechanical Behaviour and Resulting Morphologies, “*Le J. Phys. IV.*” 05 (1995) C8-41-C8-50. <https://doi.org/10.1051/jp4:1995805>.
- [30] D. Fukui, N. Nakada, S. Onaka, Internal residual stress originated from Bain strain and its effect on hardness in Fe–Ni martensite, *Acta Mater.* 196 (2020) 660–668. <https://doi.org/10.1016/j.actamat.2020.07.013>.
- [31] S. Denis, S. Sjöström, A. Simon, Coupled temperature, stress, phase transformation calculation; model numerical illustration of the internal stresses evolution during cooling of a eutectoid carbon steel cylinder., *Metall. Trans. A*. 18 A (1987) 1203–1212. <https://doi.org/10.1007/BF02647190>.
- [32] A. V. Idesman, V.I. Levitas, D.L. Preston, J.Y. Cho, Finite element simulations of martensitic phase transitions and microstructures based on a strain softening model, *J. Mech. Phys. Solids*. 53 (2005) 495–523. <https://doi.org/10.1016/j.jmps.2004.10.001>.
- [33] T. Waterschoot, A.K. De, S. Vandeputte, B.C. de Cooman, Static strain aging phenomena in cold-rolled dual-phase steels, *Metall. Mater. Trans. A Phys. Metall. Mater. Sci.* 34 (2003) 781–791. <https://doi.org/10.1007/s11661-003-1006-z>.
- [34] A. Shibata, T. Nagoshi, M. Sone, S. Morito, Y. Higo, Evaluation of the block boundary and sub-block boundary strengths of ferrous lath martensite using a micro-bending test, *Mater. Sci. Eng. A*. 527 (2010) 7538–7544. <https://doi.org/10.1016/j.msea.2010.08.026>.
- [35] S.R. Babu, T. Nyyssönen, M. Jaskari, A. Järvenpää, T.P. Davis, S. Pallaspuuro, J. Kömi, D. Porter, Observations on the relationship between crystal orientation and the level of auto-tempering in an as-quenched martensitic steel, *Metals (Basel)*. 9 (2019) 1255. <https://doi.org/10.3390/MET9121255>.
- [36] D.P. Koistinen, R.E. Marburger, A general equation prescribing the extent of the austenite-martensite transformation in pure iron-carbon alloys and plain carbon steels, *Acta Metall.* 7 (1959) 59–60. [https://doi.org/10.1016/0001-6160\(59\)90170-1](https://doi.org/10.1016/0001-6160(59)90170-1).
- [37] S.M.C. Van Bohemen, Bainite and martensite start temperature calculated with exponential carbon dependence, *Mater. Sci. Technol.* 28 (2012) 487–495. <https://doi.org/10.1179/1743284711Y.0000000097>.
- [38] G.R. Speich, Tempering of Low-Carbon Martensite, *Trans. AIME*. 245 (1969) 2553–2564.

Bibliography

- [39] S. Gaudez, Kinetics and microstructural evolutions during the tempering of martensitic and nano-bainitic low alloyed steel: in situ experimental study and modelling, PhD thesis, Université de Lorraine, 2021. <http://www.theses.fr/2021LORR0016> (accessed February 17, 2022).
- [40] S. Allain, O. Bouaziz, M. Takahashi, Toward a New Interpretation of the Mechanical Behaviour of As-quenched Low Alloyed Martensitic Steels, *ISIJ Int.* 52 (2012) 717–722. <https://doi.org/10.2355/isijinternational.52.717>.
- [41] G.S. Ansell, A. Arrot, The strengthening mechanism of ferrous martensite, *NASA Interdiscip. Mater. Res. Lab.* (1963).
- [42] T. Ungár, S. Harjo, T. Kawasaki, Y. Tomota, G. Ribárik, Z. Shi, Composite Behavior of Lath Martensite Steels Induced by Plastic Strain, a New Paradigm for the Elastic-Plastic Response of Martensitic Steels, *Metall. Mater. Trans. A.* 48 (2017) 159–167. <https://doi.org/10.1007/s11661-016-3845-4>.
- [43] L.Y. Wang, Y.X. Wu, W.W. Sun, Y. Bréchet, L. Brassart, A. Arlazarov, C.R. Hutchinson, Strain hardening behaviour of as-quenched and tempered martensite, *Acta Mater.* (2020). <https://doi.org/10.1016/j.actamat.2020.08.067>.
- [44] A. Mathevon, Characterization and modelling of microstructural evolutions and mechanical properties during the thermal treatments of Dual-Phase steels, PhD thesis, Université de Lyon, 2020. <http://www.theses.fr/2020LYSEI120> (accessed September 14, 2022).
- [45] L. Morsdorf, C.C. Tasan, D. Ponge, D. Raabe, 3D structural and atomic-scale analysis of lath martensite: Effect of the transformation sequence, *Acta Mater.* 95 (2015) 366–377. <https://doi.org/10.1016/j.actamat.2015.05.023>.
- [46] G. Masing, Zur Heyn'schen Theorie der Verfestigung der Metalle durch verborgen elastische Spannungen, *Wissenschaftliche Veröffentlichungen Aus Dem Siemens-Konzern.* (1923) 231–239. https://doi.org/10.1007/978-3-642-99663-4_17.
- [47] How does a synchrotron radiation source work?, (n.d.). https://photon-science.desy.de/research/students__teaching/primers/synchrotron_radiation/index_eng.html (accessed May 6, 2022).
- [48] PerkinElmer, 16-inch Digital X-ray Detectors - XRD 1621 N ES Series, (n.d.). www.optoelectronics.perkinelmer.com (accessed May 6, 2022).
- [49] G. Ashiotis, A. Deschildre, Z. Nawaz, J.P. Wright, D. Karkoulis, F.E. Picca, J. Kieffer, The fast azimuthal integration Python library: pyFAI, 48 (2015) 510–519. <https://doi.org/10.1107/S1600576715004306>.
- [50] R. Rementeria, J.A. Jimenez, S.Y.P. Allain, G. Geandier, J.D. Poplawsky, W. Guo, E. Urones-Garrote, C. Garcia-Mateo, F.G. Caballero, Quantitative assessment of carbon allocation anomalies in low temperature bainite, *Acta Mater.* 133 (2017) 333–345. <https://doi.org/10.1016/j.actamat.2017.05.048>.
- [51] S. Allain, S. Aoued, A. Quintin-Poulon, M. Gouné, F. Danoix, J.-C. Hell, M. Bouzat, M. Soler, G. Geandier, In Situ Investigation of the Iron Carbide Precipitation Process in a Fe-C-Mn-Si Q&P Steel, *Materials (Basel)*. 11 (2018) 1087. <https://doi.org/10.3390/ma11071087>.
- [52] S.D. Catteau, H.P. Van Landeghem, J. Teixeira, J. Dulcy, M. Dehmas, S. Denis, A. Redjaïmia, M. Courteaux, Carbon and nitrogen effects on microstructure and kinetics associated with bainitic transformation in a low-alloyed steel, (2015). <https://doi.org/10.1016/j.jallcom.2015.11.007>.
- [53] J. Rodríguez-Carvajal, Recent advances in magnetic structure determination by neutron powder diffraction, *Phys. B Condens. Matter.* 192 (1993) 55–69. [https://doi.org/10.1016/0921-4526\(93\)90108-I](https://doi.org/10.1016/0921-4526(93)90108-I).
- [54] G. K. Williamson, W. H. Hall, X-ray line broadening from filed aluminium and wolfram, *Acta Metall.* 1 (1953) 22–31. [https://doi.org/10.1016/0001-6160\(53\)90006-6](https://doi.org/10.1016/0001-6160(53)90006-6).
- [55] T. Ungár, A. Borbély, The effect of dislocation contrast on x-ray line broadening: A new approach to line profile analysis, *Appl. Phys. Lett.* 69 (1996) 3173–3175. <https://doi.org/10.1063/1.117951>.
- [56] T. Ungár, G. Tichy, The effect of dislocation contrast on X-ray line profiles in untextured polycrystals, *Phys. Status Solidi Appl. Res.* 171 (1999) 425–434. [https://doi.org/10.1002/\(SICI\)1521-396X\(199902\)171:2<425::AID-PSSA425>3.0.CO;2-W](https://doi.org/10.1002/(SICI)1521-396X(199902)171:2<425::AID-PSSA425>3.0.CO;2-W).
- [57] T. Ungár, Dislocation model of strain anisotropy, *Powder Diffr.* 23 (2008) 125–132. <https://doi.org/10.1154/1.2918549>.

Bibliography

- [58] S. Takaki, T. Masumura, T. Tsuchiyama, Proposal of simplified modified Williamson-Hall equation, *ISIJ Int.* 58 (2018) 2354–2356. <https://doi.org/10.2355/isijinternational.ISIJINT-2018-517>.
- [59] A. Borbély, The modified Williamson-Hall plot and dislocation density evaluation from diffraction peaks, *Scr. Mater.* 217 (2022) 114768. <https://doi.org/10.1016/j.scriptamat.2022.114768>.
- [60] B.E. Warren, B.L. Averbach, The effect of cold-work distortion on x-ray patterns, *J. Appl. Phys.* 21 (1950) 595–599. <https://doi.org/10.1063/1.1699713>.
- [61] Z.M. Shi, W. Gong, Y. Tomota, S. Harjo, J. Li, B. Chi, J. Pu, Study of tempering behavior of lath martensite using in situ neutron diffraction, *Mater. Charact.* 107 (2015) 29–32. <https://doi.org/10.1016/j.matchar.2015.06.040>.
- [62] N. Sallez, X. Boulnat, A. Borbély, J.L. Béchade, D. Fabrègue, M. Perez, Y. De Carlan, L. Hennet, C. Mocuta, D. Thiaudière, Y. Bréchet, In situ characterization of microstructural instabilities: Recovery, recrystallization and abnormal growth in nanoreinforced steel powder, *Acta Mater.* 87 (2015) 377–389. <https://doi.org/10.1016/j.actamat.2014.11.051>.
- [63] J. Leese, A.E. Lord, Elastic stiffness coefficients of single-crystal iron from room temperature to 500°C, *J. Appl. Phys.* 39 (1968) 3986–3988. <https://doi.org/10.1063/1.1656884>.
- [64] D.J. Dever, Temperature dependence of the elastic constants in α -iron single crystals: Relationship to spin order and diffusion anomalies, *J. Appl. Phys.* 43 (1972) 3293–3301. <https://doi.org/10.1063/1.1661710>.
- [65] D.G. Isaak, K. Masuda, Elastic and viscoelastic properties of α iron at high temperatures, *J. Geophys. Res.* 100 (1995). <https://doi.org/10.1029/95jb01235>.
- [66] Y. Zhao, L. Le Joncour, A. Baczmanski, E. Gadalińska, S. Wroński, B. Panicaud, M. François, C. Braham, T. Buslaps, Stress distribution correlated with damage in duplex stainless steel studied by synchrotron diffraction during plastic necking, *Mater. Des.* 113 (2016) 157–168. <https://doi.org/10.1016/j.matdes.2016.10.014i>.
- [67] A. Borbély, J. Dragomir-Cernatescu, G. Ribárik, T. Ungár, Computer program ANIZC for the calculation of diffraction contrast factors of dislocations in elastically anisotropic cubic, hexagonal and trigonal crystals, *J. Appl. Crystallogr.* 36 (2003) 160–162. <https://doi.org/10.1107/S0021889802021581>.
- [68] J. Macchi, G. Geandier, J. Teixeira, S. Denis, F. Bonnet, S.Y.P. Allain, Time-resolved in-situ dislocation density evolution during martensitic transformation by high-energy-XRD experiments: A study of C content and cooling rate effects, *Materialia.* 26 (2022) 101577. <https://doi.org/10.1016/J.MTLA.2022.101577>.
- [69] D. Viladot, M. Véron, M. Gemmi, F. Peiró, J. Portillo, S. Estradé, J. Mendoza, N. Llorca-Isern, S. Nicolopoulos, Orientation and phase mapping in the transmission electron microscope using precession-assisted diffraction spot recognition: State-of-the-art results, *J. Microsc.* 252 (2013) 23–34. <https://doi.org/10.1111/jmi.12065>.
- [70] I. Ghamarian, Application of ASTAR/precession electron diffraction technique to quantitatively study defects in nanocrystalline metallic materials, Iowa State University, Digital Repository, 2017. <https://doi.org/10.31274/ETD-180810-5139>.
- [71] M.K. Miller, P.A. Beaven, G.D.W. Smith, Study of the Early Stages of Tempering of Iron-Carbon Martensites By Atom Probe Field Ion Microscopy., *Metall. Trans. A.* 12 A (1981) 1197–1204. <https://doi.org/10.1007/BF02642333>.
- [72] C. Zhu, A. Cerezo, G.D.W. Smith, Carbide characterization in low-temperature tempered steels, *Ultramicroscopy.* 109 (2009) 545–552. <https://doi.org/10.1016/j.ultramic.2008.12.007>.
- [73] D. Blavette, A. Bostel, J.M. Sarrau, B. Deconihout, A. Menand, An atom probe for three-dimensional tomography, *Nature.* 363 (1993) 432–435. <https://doi.org/10.1038/363432a0>.
- [74] G. Badinier, Effect of Carbon Segregation and Carbide Precipitation on the Mechanical Response of Martensite, PhD thesis, University of British Columbia, 2013. <https://doi.org/10.14288/1.0073612>.
- [75] W. Sha, L. Chang, G.D.W. Smith, L. Cheng, E.J. Mittemeijer, Some aspects of atom-probe analysis of FeC and FeN systems, *Surf. Sci.* 266 (1992) 416–423. [https://doi.org/10.1016/0039-6028\(92\)91055-G](https://doi.org/10.1016/0039-6028(92)91055-G).
- [76] F. Danoix, D. Julien, X. Sauvage, J. Copreaux, Direct evidence of cementite dissolution in drawn pearlitic steels observed by tomographic atom probe, *Mater. Sci. Eng. A.* 250 (1998) 8–13. [https://doi.org/10.1016/S0921-5093\(98\)00529-2](https://doi.org/10.1016/S0921-5093(98)00529-2).

Bibliography

- [77] G. Da Rosa, P. Maugis, J. Drillet, V. Hebert, K. Hoummada, Co-segregation of boron and carbon atoms at dislocations in steel, *J. Alloys Compd.* 724 (2017) 1143–1148. <https://doi.org/10.1016/j.jallcom.2017.07.096>.
- [78] L. Germain, Apports des reconstructions des microtextures parentes dans l'étude des aciers et des alliages de titane, HDR, Université de Lorraine, 2014.
- [79] C. García de Andrés, F.G. Caballero, C. Capdevila, D. San Martín, Revealing austenite grain boundaries by thermal etching: advantages and disadvantages, *Mater. Charact.* 49 (2002) 121–127. [https://doi.org/10.1016/S1044-5803\(03\)00002-0](https://doi.org/10.1016/S1044-5803(03)00002-0).
- [80] Q. Liu, D. Juul Jensen, N. Hansen, Effect of grain orientation on deformation structure in cold-rolled polycrystalline aluminium, *Acta Mater.* 46 (1998) 5819–5838. [https://doi.org/10.1016/S1359-6454\(98\)00229-8](https://doi.org/10.1016/S1359-6454(98)00229-8).
- [81] O. Bouaziz, A. Aouafi, S. Allain, Effect of Grain Refinement on the Mechanical Behaviour of Ferritic Steels: Evolution of Isotropic Hardening and Kinematic Hardening, *Mater. Sci. Forum.* 584–586 (2008) 605–609. <https://doi.org/10.4028/www.scientific.net/MSF.584-586.605>.
- [82] S. Takaki, K. Kawasaki, Y. Kimura, Mechanical properties of ultra fine grained steels, *J. Mater. Process. Technol.* 117 (2001) 359–363. [https://doi.org/10.1016/S0924-0136\(01\)00797-X](https://doi.org/10.1016/S0924-0136(01)00797-X).
- [83] H. Dannoshita, H. Hasegawa, S. Higuchi, H. Matsuda, W. Gong, T. Kawasaki, S. Harjo, O. Umezawa, Evolution of dislocation structure determined by neutron diffraction line profile analysis during tensile deformation in quenched and tempered martensitic steels, *Mater. Sci. Eng. A.* 854 (2022) 143795. <https://doi.org/10.1016/J.MSEA.2022.143795>.
- [84] K. Koumatos, A. Muehleemann, A theoretical investigation of orientation relationships and transformation strains in steels, *Acta Crystallogr. Sect. A Found. Adv.* 73 (2017) 115–123. <https://doi.org/10.1107/S2053273316020350/AE5027SUP1.PDF>.
- [85] C. Cayron, One-step theory of fcc-bcc martensitic transformation, *Acta Crystallogr. Sect. A Found. Crystallogr.* 69 (2012) 498–509. <https://doi.org/10.1107/S0108767313019016>.
- [86] S. Morito, H. Yoshida, T. Maki, X. Huang, Effect of block size on the strength of lath martensite in low carbon steels, *Mater. Sci. Eng. A.* 438–440 (2006) 237–240. <https://doi.org/10.1016/j.msea.2005.12.048>.
- [87] B. Hutchinson, J. Hagström, O. Karlsson, D. Lindell, M. Tornberg, F. Lindberg, M. Thuvander, Microstructures and hardness of as-quenched martensites (0.1-0.5% C), *Acta Mater.* 59 (2011) 5845–5858. <https://doi.org/10.1016/j.actamat.2011.05.061>.
- [88] F. HajyAkbari, J. Sietsma, A.J. Böttger, M.J. Santofimia, An improved X-ray diffraction analysis method to characterize dislocation density in lath martensitic structures, *Mater. Sci. Eng. A.* 639 (2015) 208–218. <https://doi.org/10.1016/j.msea.2015.05.003>.
- [89] M. Shamsujjoha, Evolution of microstructures, dislocation density and arrangement during deformation of low carbon lath martensitic steels, *Mater. Sci. Eng. A.* 776 (2020) 139039. <https://doi.org/10.1016/j.msea.2020.139039>.
- [90] A. Chakraborty, R.F. Webster, S. Primig, Lath martensite substructure evolution in low-carbon microalloyed steels, *J. Mater. Sci.* 57 (2022) 10359–10378. <https://doi.org/10.1007/s10853-022-07275-9>.
- [91] T. Maki, K. Tsuzaki, I. Tamura, The Morphology of Microstructure Composed of Lath Martensites in Steels, *Trans. ISIJ.* 20 (1980) 207–214.
- [92] E.I. Galindo-Nava, P.E.J. Rivera-Díaz-Del-Castillo, A model for the microstructure behaviour and strength evolution in lath martensite, *Acta Mater.* 98 (2015) 81–93. <https://doi.org/10.1016/j.actamat.2015.07.018>.
- [93] H. Hoseiny, F.G. Caballero, D.S. Martin, C. Capdevilla, The influence of austenitization temperature on the mechanical properties of a prehardened mould steel, *Mater. Sci. Forum.* 706–709 (2012) 2140–2145. <https://doi.org/10.4028/WWW.SCIENTIFIC.NET/MSF.706-709.2140>.
- [94] C.A. Apple, R.N. Caron, G. Krauss, Packet microstructure in Fe-0.2 pct C martensite, *Metall. Trans.* 5 (1974) 593–599. <https://doi.org/10.1007/BF02644654>.
- [95] B. Kim, E. Boucard, T. Sourmail, D. San Martín, N. Gey, P.E.J. Rivera-Díaz-Del-Castillo, The influence of silicon in tempered martensite: Understanding the microstructure-properties relationship in 0.5-0.6 wt.% C steels, *Acta Mater.* 68 (2014) 169–178. <https://doi.org/10.1016/j.actamat.2014.01.039>.

Bibliography

- [96] H. Ghassemi-Armaki, R.P. Chen, K. Maruyama, M. Yoshizawa, M. Igarashi, Static recovery of tempered lath martensite microstructures during long-term aging in 9-12% Cr heat resistant steels, *Mater. Lett.* 63 (2009) 2423–2425. <https://doi.org/10.1016/j.matlet.2009.08.024>.
- [97] G. Krauss, A.R. Marder, The morphology of martensite in iron alloys, *Metall. Trans.* 2 (1971) 2343–2357. <https://doi.org/10.1007/BF02814873>.
- [98] T. Swarr, G.G. Krauss, The effect of structure on the deformation of as-quenched and tempered martensite in an Fe-0.2 pct C alloy, *Metall. Trans. A.* 7 (1976) 41–48. <https://doi.org/10.1007/BF02644037>.
- [99] G.R. Speich, H. Warlimont, Yield Strength and transformation substructure of low-carbon martensite, *Iron Steel Inst.* 206 (1968) 385–392. <https://doi.org/10.1017/CBO9781107415324.004>.
- [100] F. Abe, H. Araki, T. Noda, The Effect of Tungsten on Dislocation Recovery and Precipitation Behavior of Low-Activation Martensitic 9Cr Steels, *Metall. Trans.* 22 (1991) 2225–2235.
- [101] C. Garcia-Mateo, M. Peet, F.G.G. Caballero, H.K.D.H. Bhadeshia, Tempering of hard mixture of bainitic ferrite and austenite, *Mater. Sci. Technol.* 20 (2004) 814–818. <https://doi.org/10.1179/026708304225017355>.
- [102] G.I. Taylor, Plastic Strain in Metals, *J. Inst. Met.* 62 (1938) 307–324.
- [103] D. Kalish, E.M. Roberts, On the distribution of carbon in martensite, *Metall. Trans.* 2 (1971) 2783–2790. <https://doi.org/10.1007/BF02813252>.
- [104] S. Harper, Precipitation of carbon and nitrogen in cold-worked alpha-iron, *Phys. Rev.* 83 (1951) 709–712. <https://doi.org/10.1103/PhysRev.83.709>.
- [105] D. V. Wilson, Effects of plastic deformation on carbide precipitation in steel, *Acta Metall.* 5 (1957) 293–302. [https://doi.org/10.1016/0001-6160\(57\)90041-X](https://doi.org/10.1016/0001-6160(57)90041-X).
- [106] I. Gutierrez-Urrutia, D. Raabe, Dislocation density measurement by electron channeling contrast imaging in a scanning electron microscope, *Scr. Mater.* 66 (2012) 343–346. <https://doi.org/10.1016/j.scriptamat.2011.11.027>.
- [107] C. Garcia-Mateo, F.G. Caballero, C. Capdevila, C.G. de Andres, Estimation of dislocation density in bainitic microstructures using high-resolution dilatometry, *Scr. Mater.* 61 (2009) 855–858. <https://doi.org/10.1016/j.scriptamat.2009.07.013>.
- [108] M. Kehoe, P.M. Kelly, The role of carbon in the strength of ferrous martensite, *Scr. Metall.* 4 (1970) 473–476. [https://doi.org/10.1016/0036-9748\(70\)90088-8](https://doi.org/10.1016/0036-9748(70)90088-8).
- [109] L. Norström, The relation between microstructure and yield strength in tempered low-carbon lath martensite with 5% nickel, *Met. Sci.* 10 (1976) 429–436. <https://doi.org/10.1179/030634576790431868>.
- [110] T. Berecz, P. Jenei, A. Csóré, J. Lábár, J. Gubicza, P.J. Szabó, Determination of dislocation density by electron backscatter diffraction and X-ray line profile analysis in ferrous lath martensite, *Mater. Charact.* 113 (2016) 117–124. <https://doi.org/10.1016/j.matchar.2015.11.014>.
- [111] G. Kapoor, T. Kvackaj, A. Heczal, J. Bidulská, R. Kociško, Z. Fogarassy, D. Simcak, J. Gubicza, The Influence of Severe Plastic Deformation and Subsequent Annealing on the Microstructure and Hardness of a Cu–Cr–Zr Alloy, *Mater.* 2020, Vol. 13, Page 2241. 13 (2020) 2241. <https://doi.org/10.3390/MA13102241>.
- [112] M.J. Starink, Dislocation versus grain boundary strengthening in SPD processed metals: Non-causal relation between grain size and strength of deformed polycrystals, *Mater. Sci. Eng. A.* 705 (2017) 42–45. <https://doi.org/10.1016/J.MSEA.2017.08.069>.
- [113] F. Christien, M.T.F. Telling, K.S. Knight, Neutron diffraction in situ monitoring of the dislocation density during martensitic transformation in a stainless steel, *Scr. Mater.* 68 (2013) 506–509. <https://doi.org/10.1016/j.scriptamat.2012.11.031>.
- [114] M. Yonemura, H. Nishibata, R. Fujimura, N. Ooura, K. Hata, K. Fujiwara, K. Kawano, I. Yamaguchi, T. Terai, Y. Inubushi, I. Inoue, T. Yabuuchi, K. Tono, M. Yabashi, Fine microstructure formation in steel under ultrafast heating and cooling, *Sci. Rep.* 12 (2022) 2237. <https://doi.org/10.1038/s41598-022-06280-x>.
- [115] S. Harjo, T. Kawasaki, Y. Tomota, W. Gong, K. Aizawa, G. Tichy, Z. Shi, T. Ungár, Work Hardening, Dislocation Structure, and Load Partitioning in Lath Martensite Determined by In Situ Neutron Diffraction

Bibliography

- Line Profile Analysis, *Metall. Mater. Trans. A.* 48 (2017) 4080–4092. <https://doi.org/10.1007/s11661-017-4172-0>.
- [116] A. Rollett, G.S. Rohrer, J. Humphreys, *Recrystallization and Related Annealing Phenomena*, Pergamon, 2017. <https://doi.org/10.1016/j.matchar.2020.110382>.
- [117] H. Ghassemi-Armaki, R. Chen, K. Maruyama, M. Igarashi, Premature creep failure in strength enhanced high Cr ferritic steels caused by static recovery of tempered martensite lath structures, *Mater. Sci. Eng. A.* 527 (2010) 6581–6588. <https://doi.org/10.1016/j.msea.2010.07.037>.
- [118] H.L. Andrade, M.G. Akben, J.J. Jonas, Effect of molybdenum, niobium, and vanadium on static recovery and recrystallization and on solute strengthening in microalloyed steels, *Metall. Trans. A.* 14 (1983) 1967–1977. <https://doi.org/10.1007/BF02662364>.
- [119] J. Pešička, A. Dronhofer, G. Eggeler, Free dislocations and boundary dislocations in tempered martensite ferritic steels, *Mater. Sci. Eng. A.* 387–389 (2004) 176–180. <https://doi.org/10.1016/J.MSEA.2004.03.080>.
- [120] M. Moreno, J. Teixeira, G. Geandier, J.C. Hell, F. Bonnet, M. Salib, S.Y.P. Allain, Real-time investigation of recovery, recrystallization and austenite transformation during annealing of a cold-rolled steel using high energy X-ray diffraction (HEXRD), *Metals (Basel)*. 9 (2019) 1–8. <https://doi.org/10.3390/met9010008>.
- [121] J. Friedel, *Dislocations*, Pergamon, 1964.
- [122] F.J. Humphreys, A unified theory of recovery, recrystallization and grain growth, based on the stability and growth of cellular microstructures—I. The basic model, *Acta Mater.* 45 (1997) 4231–4240. [https://doi.org/10.1016/S1359-6454\(97\)00070-0](https://doi.org/10.1016/S1359-6454(97)00070-0).
- [123] E. Nes, Recovery revisited, *Acta Metall. Mater.* 43 (1995) 2189–2207. [https://doi.org/10.1016/0956-7151\(94\)00409-9](https://doi.org/10.1016/0956-7151(94)00409-9).
- [124] G. Stechauner, E. Kozeschnik, Self-diffusion in grain boundaries and dislocation pipes in Al, Fe, and Ni and application to AlN precipitation in steel, in: *J. Mater. Eng. Perform.*, 2014: pp. 1576–1579. <https://doi.org/10.1007/s11665-014-0921-z>.
- [125] K. Mukunthan, E.B. Hawbolt, Modeling recovery and recrystallization kinetics in cold-rolled Ti-Nb stabilized interstitial-free steel, *Metall. Mater. Trans. A.* 27 (1996) 3410–3423. <https://doi.org/10.1007/BF02595434>.
- [126] M. Oyarzábal, A. Martínez-De-Guerenu, I. Gutiérrez, Effect of stored energy and recovery on the overall recrystallization kinetics of a cold rolled low carbon steel, *Mater. Sci. Eng. A.* 485 (2008) 200–209. <https://doi.org/10.1016/j.msea.2007.07.077>.
- [127] Y. V. Shan, M. Soliman, H. Palkowski, E. Kozeschnik, Modeling of Bake Hardening Kinetics and Carbon Redistribution in Dual-Phase Steels, 92 (2021) 2000307. <https://doi.org/10.1002/SRIN.202000307>.
- [128] D. Wedberg, Dislocation Density Based Material Model Applied in FE-simulation of Metal Cutting, Luleå, 2010. <https://www.diva-portal.org/smash/get/diva2:999440/FULLTEXT01.pdf> (accessed August 17, 2022).
- [129] C. Couchet, S.Y.P. Allain, G. Geandier, J. Teixeira, S. Gaudez, J. Macchi, M. Lamari, F. Bonnet, Recovery of severely deformed ferrite studied by in situ high energy X-ray diffraction, *Mater. Charact.* 179 (2021) 111378. <https://doi.org/10.1016/j.matchar.2021.111378>.
- [130] F. Riedlsperger, B. Gsellmann, E. Povoden-Karadeniz, O. Tassa, S. Matera, M. Dománková, F. Kauffmann, E. Kozeschnik, B. Sonderegger, Thermodynamic Modelling and Microstructural Study of Z-Phase Formation in a Ta-Alloyed Martensitic Steel, *Materials (Basel)*. 14 (2021) 1332. <https://doi.org/10.3390/MA14061332>.
- [131] K. Zhu, O. Bouaziz, C. Oberbillig, M. Huang, An approach to define the effective lath size controlling yield strength of bainite, *Mater. Sci. Eng. A.* 527 (2010) 6614–6619. <https://doi.org/10.1016/j.msea.2010.06.061>.
- [132] J.C. Hell, *Aciers bainitiques sans carbure : Caractérisations microstructurales multi-échelles et in situ de la transformation austénite-bainite et relations entre microstructure et comportement mécanique*, PhD thesis, Université Paul Verlaine - Metz, 2011. http://docnum.univ-lorraine.fr/public/UPV-M/Theses/2011/Hell.Jean_Christophe.SMZ1131.pdf (accessed May 20, 2022).
- [133] S. Morito, A.H. Pham, T. Hayashi, T. Ohba, Block Boundary Analyses to Identify Martensite and Bainite,

Bibliography

- Mater. Today Proc. 2 (2015) S913–S916. <https://doi.org/10.1016/J.MATPR.2015.07.430>.
- [134] E.E. Underwood, Particle-size Distribution, in: R.T. DeHoff, F.N. Rhines (Eds.), *Quant. Microsc.*, McGraw-Hill, New York, 1968: pp. 149–199.
- [135] H.K.D.H. Bhadeshia, Thermodynamic extrapolation and martensite-start temperature of substitutionally alloyed steels, *Met. Sci.* 15 (1981) 178–180. <https://doi.org/10.1179/030634581790426697>.
- [136] S.M.C. van Bohemen, J. Sietsma, The kinetics of bainite and martensite formation in steels during cooling, *Mater. Sci. Eng. A.* 527 (2010) 6672–6676. <https://doi.org/10.1016/j.msea.2010.06.091>.
- [137] Y. Wang, Y. Tomota, T. Ohmura, S. Morooka, W. Gong, S. Harjo, Real time observation of martensite transformation for a 0.4C low alloyed steel by neutron diffraction, *Acta Mater.* 184 (2020) 30–40. <https://doi.org/10.1016/j.actamat.2019.11.051>.
- [138] S.Y.P. Allain, S. Gaudez, G. Geandier, J.C. Hell, M. Gouné, F. Danoix, M. Soler, S. Aoued, A. Poulon-Quintin, Internal stresses and carbon enrichment in austenite of Quenching and Partitioning steels from high energy X-ray diffraction experiments, *Mater. Sci. Eng. A.* 710 (2018) 245–250. <https://doi.org/10.1016/j.msea.2017.10.105>.
- [139] M. Dehmas, F. Bruneseaux, G. Geandier, E. Gautier, B. Appolaire, S. Denis, B. Denand, A. Settefrati, A. Mauro, M. Peel, G. Gonzales Aviles, T. Buslaps, Apport de la diffraction synchrotron à l'étude de la transformation martensitique dans les aciers, *Matériaux Tech.* 97 (2009) 61–69. <https://doi.org/10.1051/mattech/2010012>.
- [140] F. Archie, M.Z. Mughal, M. Sebastiani, E. Bemporad, S. Zaeferrer, Anisotropic distribution of the micro residual stresses in lath martensite revealed by FIB ring-core milling technique, *Acta Mater.* 150 (2018) 327–338. <https://doi.org/10.1016/j.actamat.2018.03.030>.
- [141] G. Miyamoto, A. Shibata, T. Maki, T. Furuhashi, Precise measurement of strain accommodation in austenite matrix surrounding martensite in ferrous alloys by electron backscatter diffraction analysis, *Acta Mater.* 57 (2009) 1120–1131. <https://doi.org/10.1016/j.actamat.2008.10.050>.
- [142] F. Maresca, V.G. Kouznetsova, M.G.D. Geers, On the role of interlath retained austenite in the deformation of lath martensite, *Model. Simul. Mater. Sci. Eng.* 22 (2014). <https://doi.org/10.1088/0965-0393/22/4/045011>.
- [143] Y. Lu, H. Yu, R.D. Sisson, The effect of carbon content on the c/a ratio of as-quenched martensite in Fe-C alloys, *Mater. Sci. Eng. A.* 700 (2017) 592–597. <https://doi.org/10.1016/j.msea.2017.05.094>.
- [144] W.T. Read, *Dislocations in Crystals*, McGraw-Hill, New York, 1953.
- [145] S. Nambu, N. Shibata, M. Ojima, J. Inoue, T. Koseki, H.K.D.H. Bhadeshia, In situ observations and crystallographic analysis of martensitic transformation in steel, *Acta Mater.* 61 (2013) 4831–4839. <https://doi.org/10.1016/j.actamat.2013.04.065>.
- [146] S.Y.P. Allain, G. Geandier, J.C. Hell, M. Soler, F. Danoix, M. Gouné, In-situ investigation of quenching and partitioning by High Energy X-Ray Diffraction experiments, *Scr. Mater.* 131 (2017) 15–18. <https://doi.org/10.1016/j.scriptamat.2016.12.026>.
- [147] G.B. Olson, M. Cohen, Early Stages of Aging and Tempering of Ferrous Martensites, *Metall. Trans. A.* 14 (1983) 1057–1065. <https://doi.org/10.1007/BF02659854>.
- [148] G. Ghosh, G.B. Olson, The isotropic shear modulus of multicomponent Fe-base solid solutions, *Acta Mater.* 50 (2002) 2655–2675. [https://doi.org/10.1016/S1359-6454\(02\)00096-4](https://doi.org/10.1016/S1359-6454(02)00096-4).
- [149] S. Zamberger, L. Whitmore, S. Krisam, T. Wojcik, E. Kozeschnik, Experimental and computational study of cementite precipitation in tempered martensite, *Model. Simul. Mater. Sci. Eng.* 23 (2015) 055012. <https://doi.org/10.1088/0965-0393/23/5/055012>.
- [150] D. Ning, C.R. Dai, J.L. Wu, Y.D. Wang, Y.Q. Wang, Y. Jing, J. Sun, Carbide precipitation and coarsening kinetics in low carbon and low alloy steel during quenching and subsequently tempering, *Mater. Charact.* 176 (2021). <https://doi.org/10.1016/j.matchar.2021.111111>.
- [151] J. Wilde, A. Cerezo, G.D.W. Smith, Three-dimensional atomic-scale mapping of a Cottrell atmosphere around a dislocation in iron, *Scr. Mater.* 43 (2000) 39–48. [https://doi.org/10.1016/S1359-6462\(00\)00361-4](https://doi.org/10.1016/S1359-6462(00)00361-4).
- [152] Y.X. Wu, W.W. Sun, M.J. Styles, A. Arlazarov, C.R. Hutchinson, Cementite coarsening during the

Bibliography

- tempering of Fe-C-Mn martensite, *Acta Mater.* 159 (2018) 209–224. <https://doi.org/10.1016/j.actamat.2018.08.023>.
- [153] J. Svoboda, G.A. Zickler, E. Kozeschnik, F.D. Fischer, Kinetics of interstitial segregation in Cottrell atmospheres and grain boundaries, *Philos. Mag. Lett.* 95 (2015) 458–465. <https://doi.org/10.1080/09500839.2015.1087652>.
- [154] Y. Wang, S. Denis, B. Appolaire, P. Archambault, Modelling of precipitation of carbides during tempering of martensite, *J. Phys. IV.* 120 (2004) 103–110. <https://doi.org/10.1051/jp4:2004120011>.
- [155] P.G. Winchell, M. Cohen, The Strength of Martensite, *Trans. ASM.* 33 (1962) 347–361.
- [156] K.A. Taylor, L. Chang, G.B. Olson, G.D.W. Smith, M. Cohen, J.B.V. Sande, Spinodal decomposition during aging of Fe-Ni-C martensites, *Metall. Trans. A.* 20 (1989) 2717–2737. <https://doi.org/10.1007/BF02670166>.
- [157] M. Kusunoki, S. Nagakura, Modulated structure of iron-carbon martensite studied by electron microscopy and diffraction, *J. Appl. Crystallogr.* 14 (1981) 329–336. <https://doi.org/10.1107/S0021889881009485>.
- [158] K.A. Taylor, G.B. Olson, M. Cohen, J.B. Vander Sande, Carbide precipitation during stage I tempering of Fe-Ni-C martensites, *Metall. Trans. A.* 20 (1989) 2749–2765. <https://doi.org/http://dx.doi.org/10.1053/j.sart.2010.06.010>.
- [159] M.J. Van Genderen, A. Böttger, R.J. Cernik, E.J. Mittemeijer, Early stages of decomposition in iron-carbon and iron-nitrogen martensites: Diffraction analysis using synchrotron radiation, *Metall. Trans. A.* 24 (1993) 1965–1973. <https://doi.org/10.1007/BF02666331>.
- [160] N. DeCristofaro, R. Kaplow, W.S. Owen, The kinetics of carbon clustering in martensite, *Metall. Trans. A.* 9 (1978) 821–825. <https://doi.org/10.1007/BF02649791>.
- [161] L. Cheng, C.M. Brakman, B.M. Korevaar, E.J. Mittemeijer, The tempering of iron-carbon martensite; dilatometric and calorimetric analysis, *Metall. Trans. A.* 19 (1988) 2415–2426. <https://doi.org/10.1007/BF02645469>.
- [162] L. Morsdorf, E. Emelina, B. Gault, M. Herbig, C.C. Tasan, Carbon redistribution in quenched and tempered lath martensite, *Acta Mater.* 205 (2021) 116521. <https://doi.org/10.1016/J.ACTAMAT.2020.116521>.
- [163] M.J. Van Genderen, M. Isac, A. Böttger, E.J. Mittemeijer, Aging and tempering behavior of iron-nickel-carbon and iron-carbon martensite, *Metall. Mater. Trans. A* 1997 283. 28 (1997) 545–561. <https://doi.org/10.1007/S11661-997-0042-5>.
- [164] O.N.C. Uwakweh, J.P. Bauer, J.M.R. Génin, Mössbauer study of the distribution of carbon interstitials in iron alloys and the isochronal kinetics of the aging of martensite: The clustering-ordering synergy, *Metall. Trans. A.* 21 (1990) 589–602. <https://doi.org/10.1007/BF02671931>.
- [165] S. Allain, F. Danoix, M. Goune, K. Houmada, D. Mangelinck, Static and dynamical ageing processes at room temperature in a Fe₂₅Ni_{0.4}C virgin martensite: Effect of C redistribution at the nanoscale, *Philos. Mag. Lett.* 93 (2013) 68–76. <https://doi.org/10.1080/09500839.2012.742590>.
- [166] A. Vieweg, E. Povoden-Karadeniz, G. Ressel, P. Prevedel, T. Wojcik, F. Mendez-Martin, A. Stark, J. Keckes, E. Kozeschnik, Phase evolution and carbon redistribution during continuous tempering of martensite studied with high resolution techniques, *Mater. Des.* 136 (2017) 214–222. <https://doi.org/10.1016/j.matdes.2017.09.065>.
- [167] A.H. Cottrell, B.A. Bilby, Dislocation theory of yielding and strain ageing of iron, *Proc. Phys. Soc. Sect. A.* 62 (1949) 49–62. <https://doi.org/10.1088/0370-1298/62/1/308>.
- [168] J.Z. Zhao, A.K. De, B.C. De Cooman, Kinetics of Cottrell atmosphere formation during strain aging of ultra-low carbon steels, *Mater. Lett.* 44 (2000) 374–378. [https://doi.org/10.1016/S0167-577X\(00\)00062-8](https://doi.org/10.1016/S0167-577X(00)00062-8).
- [169] G.R. Speich, W.C. Leslie, TEMPERING OF STEEL., *Met. Trans.* 3 (1972) 1043–1054. <https://doi.org/10.1007/BF02642436>.
- [170] K.H. Jack, Structural Transformations in the Tempering of High-Carbon Martensitic Steels, *J. Iron Steel Inst.* 169 (1951) 26–36.
- [171] Y. Wang, Etude et modélisation de l'effet du revenu sur les évolutions des microstructures, du

Bibliography

- comportement thermomécanique et des contraintes résiduelles de trempe, PhD thesis, Vandoeuvre-les-Nancy, INPL, 2006. <http://www.theses.fr/2006INPL047N> (accessed October 9, 2022).
- [172] S. Murphy, A. Whiteman, The precipitation of epsilon-carbide in twinned martensite, *Metall. Trans.* 1 (1970) 843–848. <https://doi.org/10.1007/BF02811763>.
- [173] Y. Hirotsu, S. Nagakura, Crystal structure and morphology of the carbide precipitated from martensitic high carbon steel during the first stage of tempering, *Acta Metall.* 20 (1972) 645–655. [https://doi.org/10.1016/0001-6160\(72\)90020-X](https://doi.org/10.1016/0001-6160(72)90020-X).
- [174] G. Baozhu, G. Krauss, The effect of low-temperature isothermal heat treatments on the fracture of 4340 steel, *J. Heat Treat.* 4 (1986) 365–372. <https://doi.org/10.1007/BF02833092>.
- [175] H.C. Lee, G. Krauss, Intralath carbide transitions in martensitic medium-carbon steels tempered between 200 and 300°C, in: G. R (Ed.), *Speich Symp. Proc. Fundam. Aging Tempering Bainitic Martensitic Steel Prod.*, Iron and Steel Society, Warrandale, 1992: pp. 39–43.
- [176] Y. Imai, Phases in Quenched and Tempered Steels., *Trans Jpn Inst Met.* 16 (1975) 721–734. <https://doi.org/10.2320/matertrans1960.16.721>.
- [177] T. Waterschoot, K. Verbeken, B.C. De Cooman, Tempering kinetics of the martensitic phase in DP steel, *ISIJ Int.* 46 (2006) 138–146. <https://doi.org/10.2355/isijinternational.46.138>.
- [178] S. Aoued, F. Danoix, S.Y.P. Allain, S. Gaudez, G. Geandier, J.C. Hell, M. Soler, M. Gouné, Microstructure evolution and competitive reactions during quenching and partitioning of a model Fe–C–Mn–Si alloy, *Metals (Basel)*. 10 (2020) 137. <https://doi.org/10.3390/met10010137>.
- [179] S.W. Thompson, Structural characteristics of transition-iron-carbide precipitates formed during the first stage of tempering in 4340 steel, *Mater. Charact.* 106 (2015) 452–462. <https://doi.org/10.1016/j.matchar.2015.05.030>.
- [180] A.S. Nishikawa, G. Miyamoto, T. Furuhashi, A.P. Tschiptschin, H. Goldenstein, Phase transformation mechanisms during Quenching and Partitioning of a ductile cast iron, *Acta Mater.* 179 (2019) 1–16. <https://doi.org/10.1016/j.actamat.2019.08.001>.
- [181] Y. Hirotsu, S. Nagakura, Electron Microscopy and Diffraction Study of the Carbide Precipitated At the First Stage of Tempering of Martensitic Medium Carbon Steel., *Trans Jap Inst Met.* 15 (1974) 129–134. <https://doi.org/10.2320/matertrans1960.15.129>.
- [182] A. Bénétteau, E. Aeby-Gautier, G. Geandier, P. Weisbecker, A. Redjaïmia, B. Appolaire, Tempering of a martensitic stainless steel: Investigation by in situ synchrotron X-ray diffraction, *Acta Mater.* 81 (2014) 30–40. <https://doi.org/10.1016/j.actamat.2014.07.050>.
- [183] C. Aubry, Modélisation et étude expérimentale des cinétiques de revenu/autorevenu d’aciers trempés : prévision des contraintes résiduelles de trempe dans un acier cémenté en incluant l’autorevenu., PhD thesis, Université de Lorraine, 1998. <https://www.theses.fr/en/1998INPL030N> (accessed March 5, 2019).
- [184] K.W. Andrews, Heat Treatment for Improvement in Low Temperature Mechanical Properties of 0.40 pct C-Cr Steels., *J. Iron Steel Inst.* 203 (1965) 721.
- [185] D.H. Sherman, S.M. Cross, S. Kim, F. Grandjean, G.J. Long, M.K. Miller, Characterization of the carbon and retained austenite distributions in martensitic medium carbon, high silicon steel, *Metall. Mater. Trans. A.* 38 (2007) 1698–1711. <https://doi.org/10.1007/s11661-007-9160-3>.
- [186] H. Godin, J.-D. Mithieux, C. Parrens, G. Badinier, M. Sennour, A.-F. Gourgues-Lorenzon, Effects of cooling path and resulting microstructure on the impact toughness of a hot stamping martensitic stainless steel, *Mater. Sci. Eng. A.* 742 (2019) 597–607. <https://doi.org/10.1016/j.msea.2018.11.036>.
- [187] Y. Ohmori, S. Sugisawa, Precipitation of carbides during tempering of high carbon martensite, *Trans Jap Inst Met.* 12 (1971) 170–178. <https://doi.org/10.2320/matertrans1960.12.170>.
- [188] D.L. Williamson, R.G. Schupmann, J.P. Materkowski, G. Krauss, Determination of small amounts of austenite and carbide in hardened medium carbon steels by Mössbauer spectroscopy, *Metall. Trans. A.* 10 (1979) 379–382. <https://doi.org/10.1007/BF02658350>.
- [189] S. Primig, H. Leitner, Separation of overlapping retained austenite decomposition and cementite precipitation reactions during tempering of martensitic steel by means of thermal analysis, *Thermochim. Acta.* 526 (2011) 111–117. <https://doi.org/10.1016/j.tca.2011.09.001>.

Bibliography

- [190] T. Furuhashi, K. Kobayashi, T. Maki, Control of cementite precipitation in lath martensite by rapid heating and tempering, *ISIJ Int.* 44 (2004) 1937–1944. <https://doi.org/10.2355/isijinternational.44.1937>.
- [191] Y.X. Wu, W.W. Sun, X. Gao, M.J. Styles, A. Arlazarov, C.R. Hutchinson, The effect of alloying elements on cementite coarsening during martensite tempering, *Acta Mater.* 183 (2020) 418–437. <https://doi.org/10.1016/j.actamat.2019.11.040>.
- [192] G. Ghosh, G.B. Olson, Precipitation of paraequilibrium cementite: Experiments, and thermodynamic and kinetic modeling, *Acta Mater.* 50 (2002) 2099–2119. www.actamat-journals.com (accessed March 5, 2019).
- [193] J. Janovec, A. Výrostková, A. Holý, Effect of tempering on development of carbide particles in 2.7Cr-0.6Mo-0.3V steel, *J. Mater. Sci.* 27 (1992) 6564–6572. <https://doi.org/10.1007/BF01165937>.
- [194] A. Deschamps, C.R. Hutchinson, Precipitation kinetics in metallic alloys: Experiments and modeling, *Acta Mater.* 220 (2021) 117338. <https://doi.org/10.1016/j.actamat.2021.117338>.
- [195] J. Lépinoux, C. Sigli, Multiscale modelling of precipitation in concentrated alloys: from atomistic Monte Carlo simulations to cluster dynamics I thermodynamics, *Philos. Mag.* 98 (2018) 1–19. <https://doi.org/10.1080/14786435.2017.1390620>.
- [196] B. Lüthi, F. Berthier, L. Ventelon, B. Legrand, D. Rodney, F. Willaime, Ab initio thermodynamics of carbon segregation on dislocation cores in bcc iron, *Model. Simul. Mater. Sci. Eng.* 27 (2019) 074002. <https://doi.org/10.1088/1361-651X/AB28D4>.
- [197] R. Kubo, The fluctuation-dissipation theorem, *Reports Prog. Phys.* 29 (1966) 255. <https://doi.org/10.1088/0034-4885/29/1/306>.
- [198] T.W. Heo, L.-Q. Chen, Phase-Field Modeling of Nucleation in Solid-State Phase Transformations, *JOM.* 66 (2014) 1520–1528. <https://doi.org/10.1007/s11837-014-1033-9>.
- [199] L.Q. Chen, Phase-field models for microstructure evolution, *Annu. Rev. Mater. Sci.* 32 (2002) 113–140. <https://doi.org/10.1146/annurev.matsci.32.112001.132041>.
- [200] N. Moelans, B. Blanpain, P. Wollants, An introduction to phase-field modeling of microstructure evolution, *Calphad.* 32 (2008) 268–294. <https://doi.org/10.1016/J.CALPHAD.2007.11.003>.
- [201] J. Svoboda, Y. V. Shan, G.A. Zickler, E. Kozeschnik, F.D. Fischer, Local approach for coarsening of precipitates, *Scr. Mater.* 178 (2020) 232–235. <https://doi.org/10.1016/j.scriptamat.2019.11.029>.
- [202] E. Povoden-Karadeniz, E. Kozeschnik, Simulation of Precipitation Kinetics and Precipitation Strengthening of B2-precipitates in Martensitic PH 13–8 Mo Steel, *ISIJ Int.* 52 (2012) 610–615. <https://doi.org/10.2355/ISIJINTERNATIONAL.52.610>.
- [203] S. Denis, P. Archambault, C. Aubry, A. Mey, J.C. Louin, A. Simon, Modelling of phase transformation kinetics in steels and coupling with heat treatment residual stress predictions, *J. Phys. IV.* 9 (1999). <https://doi.org/10.1051/jp4:1999933>.
- [204] and S.B. Andersson J.O., Helander T., Höglund L., Shi P.F., Thermo-Calc and DICTRA, Computational tools for materials science, *Calphad.* 26 (2002) 273–312.
- [205] O. Prat, J. García, D. Rojas, J.P. Sanhueza, C. Camurri, Study of nucleation, growth and coarsening of precipitates in a novel 9%Cr heat resistant steel: Experimental and modeling, *Mater. Chem. Phys.* 2 (2014) 754–764. <https://doi.org/10.1016/J.MATCHEMPHYS.2013.10.010>.
- [206] J.P. Sanhueza, D. Rojas, O. Prat, J. Garcia, R. Espinoza, C. Montalba, M.F. Melendrez, Precipitation kinetics in a 10.5%Cr heat resistant steel: Experimental results and simulation by TC-PRISMA/DICTRA, *Mater. Chem. Phys.* 200 (2017) 342–353. <https://doi.org/10.1016/J.MATCHEMPHYS.2017.07.083>.
- [207] Z. Hou, R.P. Babu, P. Hedström, J. Odqvist, Early stages of cementite precipitation during tempering of 1C–1Cr martensitic steel, *J. Mater. Sci.* 54 (2019) 9222–9234. <https://doi.org/10.1007/S10853-019-03530-8/FIGURES/8>.
- [208] MatCalc 6: The Materials Calculator, (n.d.). <https://www.matcalc.at/>.
- [209] M. Perez, A. Deschamps, Microscopic modelling of simultaneous two-phase precipitation: Application to carbide precipitation in low-carbon steels, *Mater. Sci. Eng. A.* 360 (2003) 214–219. [https://doi.org/10.1016/S0921-5093\(03\)00431-3](https://doi.org/10.1016/S0921-5093(03)00431-3).
- [210] A.J. Clarke, J.G. Speer, M.K. Miller, R.E. Hackenberg, D. V Edmonds, D.K. Matlock, F.C. Rizzo, K.D.

Bibliography

- Clarke, E. De Moor, Carbon partitioning to austenite from martensite or bainite during the quench and partition (Q&P) process: A critical assessment, *Acta Mater.* 56 (2008) 16–22. <https://doi.org/10.1016/j.actamat.2007.08.051>.
- [211] Z.J. Xie, C.J. Shang, S. V Subramanian, X.P. Ma, R.D.K. Misra, Atom probe tomography and numerical study of austenite stabilization in a low carbon low alloy steel processed by two-step intercritical heat treatment, *Scr. Mater.* 137 (2017) 36–40. <https://doi.org/10.1016/j.scriptamat.2017.05.002>.
- [212] S.Y.P. Allain, S. Gaudez, G. Geandier, F. Danoix, M. Soler, M. Goune, Carbon heterogeneities in austenite during Quenching & Partitioning (Q&P) process revealed by in situ High Energy X-Ray Diffraction (HEXRD) experiments, *Scr. Mater.* 181 (2020) 108–114. <https://doi.org/10.1016/j.scriptamat.2020.02.022>.
- [213] O. Waseda, R.G. Veiga, J. Morthomas, P. Chantrenne, C.S. Becquart, F. Ribeiro, A. Jelea, H. Goldenstein, M. Perez, Formation of carbon Cottrell atmospheres and their effect on the stress field around an edge dislocation, *Scr. Mater.* 129 (2017) 16–19. <https://doi.org/10.1016/j.scriptamat.2016.09.032>.
- [214] C.G. Gianopoulos, Z. Chua, V. V. Zhurov, A. Alan Pinkerton, $\lambda/2$ contamination in X-ray diffraction data—the impact of heavy atoms, *J. Appl. Crystallogr.* 50 (2017) 643–646. <https://doi.org/10.1107/S160057671700317X>.
- [215] A.J. Clarke, M.K. Miller, R.D. Field, D.R. Coughlin, P.J. Gibbs, K.D. Clarke, D.J. Alexander, K.A. Powers, P.A. Papin, G. Krauss, Atomic and nanoscale chemical and structural changes in quenched and tempered 4340 steel, *Acta Mater.* 77 (2014) 17–27. <https://doi.org/10.1016/j.actamat.2014.05.032>.
- [216] G. Ghosh, A first-principles study of cementite (Fe₃C) and its alloyed counterparts: Elastic constants, elastic anisotropies, and isotropic elastic moduli, *AIP Adv.* 5 (2015) 087102. <https://doi.org/10.1063/1.4928208>.
- [217] Y.L. Tian, R.W. Kraft, Mechanisms of Pearlite Spheroidization, *Metall. Trans. A* 1987 188. 18 (1987) 1403–1414. <https://doi.org/10.1007/BF02646654>.
- [218] D.N. LEE, H.N. HAN, Orientation Relationships between Precipitates and Their Parent Phases in Steels at Low Transformation Temperatures, *J. Solid Mech. Mater. Eng.* 6 (2012) 323–338. <https://doi.org/10.1299/JMMP.6.323>.
- [219] I. Pushkareva, J. Macchi, F. Shalchi-Amirkhiz, Babak Fazeli, G. Geandier, F. Danoix, J. Da Costa Teixeira, S.Y.P. Allain, C. Scott, A study of the carbon distribution in bainitic ferrite, *Scr. Mater.* 224 (2023) 115140. <https://doi.org/https://doi.org/10.1016/j.scriptamat.2022.115140>.
- [220] S. Gaudez, J. Teixeira, S. Denis, G. Geandier, S.Y.P. Allain, Martensite and nanobainite transformations in a low alloyed steel studied by in situ high energy synchrotron diffraction, *Mater. Charact.* 185 (2022). <https://doi.org/10.1016/j.matchar.2022.111740>.
- [221] F.C. An, J.J. Wang, S.X. Zhao, C.M. Liu, Tailoring cementite precipitation and mechanical properties of quenched and tempered steel by nickel partitioning between cementite and ferrite, *Mater. Sci. Eng. A.* 802 (2021) 140686. <https://doi.org/10.1016/J.MSEA.2020.140686>.
- [222] L.Y. Wang, Y.X. Wu, W.W. Sun, Y. Bréchet, L. Brassart, A. Arlazarov, C.R. Hutchinson, Transitions in the strain hardening behaviour of tempered martensite, *Acta Mater.* 221 (2021) 117397. <https://doi.org/10.1016/J.ACTAMAT.2021.117397>.
- [223] E. Clouet, S. Garruchet, H. Nguyen, M. Perez, C.S. Becquart, Dislocation interaction with C in α -Fe: A comparison between atomic simulations and elasticity theory, *Acta Mater.* 56 (2008) 3450–3460. <https://doi.org/10.1016/j.actamat.2008.03.024>.
- [224] F.D. Fischer, J. Svoboda, H. Petryk, Thermodynamic extremal principles for irreversible processes in materials science, *Acta Mater.* 67 (2014) 1–20. <https://doi.org/10.1016/j.actamat.2013.11.050>.
- [225] K. Tapasa, Y.N. Osetsky, D.J. Bacon, Computer simulation of interaction of an edge dislocation with a carbon interstitial in α -iron and effects on glide, *Acta Mater.* 55 (2007) 93–104. <https://doi.org/10.1016/j.actamat.2006.08.015>.
- [226] M. Hillert, The kinetics of the first stage of tempering, *Acta Metall.* 7 (1959) 653–658. [https://doi.org/10.1016/0001-6160\(59\)90141-5](https://doi.org/10.1016/0001-6160(59)90141-5).
- [227] B.S. Lement, M. Cohen, A dislocation-attraction model for the first stage of tempering, *Acta Metall.* 4 (1956) 469–476. [https://doi.org/10.1016/0001-6160\(56\)90043-8](https://doi.org/10.1016/0001-6160(56)90043-8).
- [228] D. Kalish, M. Cohen, Structural changes and strengthening in the strain tempering of martensite, *Mater.*

Bibliography

- Sci. Eng. 6 (1970) 156–166. [https://doi.org/10.1016/0025-5416\(70\)90045-5](https://doi.org/10.1016/0025-5416(70)90045-5).
- [229] R.G.A. Veiga, M. Perez, C.S. Becquart, C. Domain, Atomistic modeling of carbon Cottrell atmospheres in bcc iron, *J. Phys. Condens. Matter.* 25 (2013) 25401–25408. <https://doi.org/10.1088/0953-8984/25/2/025401>.
- [230] D. McLean, *Grain Boundaries in Metals*, Oxford University Press, London, 1957.
- [231] W. Lu, M. Herbig, C.H. Liebscher, L. Morsdorf, R.K.W. Marceau, G. Dehm, D. Raabe, Formation of eta carbide in ferrous martensite by room temperature aging, *Acta Mater.* 158 (2018) 297–312. <https://doi.org/10.1016/j.actamat.2018.07.071>.
- [232] K. Kamber, D. Keefer, C. Wert, Interactions of interstitials with dislocations in iron, *Acta Metall.* 9 (1961) 403–414. [https://doi.org/https://doi.org/10.1016/0001-6160\(61\)90134-1](https://doi.org/https://doi.org/10.1016/0001-6160(61)90134-1).
- [233] E. Kozeschnik, H.K.D.H. Bhadeshia, Influence of silicon on cementite precipitation in steels, *Mater. Sci. Technol.* 24 (2008) 343–347. <https://doi.org/10.1179/174328408X275973>.
- [234] Z. Hou, P. Hedström, Y. Xu, W. Di, J. Odqvist, Microstructure of Martensite in Fe-C-Cr and its Implications for Modelling of Carbide Precipitation during Tempering, *ISIJ Int.* 54 (2014) 2649–2656. <https://doi.org/10.2355/isijinternational.54.2649>.
- [235] S. Yamasaki, *Modelling Precipitation of Carbides in Martensitic Steels*, Dr. Diss. Univ. Cambridge. (2004) 207.
- [236] P.A. Beaven, E.P. Butler, Precipitate nucleation on dislocations in Fe-N, *Acta Metall.* 28 (1980) 1349–1359. [https://doi.org/10.1016/0001-6160\(80\)90004-8](https://doi.org/10.1016/0001-6160(80)90004-8).
- [237] J.W. Cahn, F. Larché, A simple model for coherent equilibrium, *Acta Metall.* 32 (1984) 1915–1923. [https://doi.org/10.1016/0001-6160\(84\)90173-1](https://doi.org/10.1016/0001-6160(84)90173-1).
- [238] M. Perez, M. Dumont, D. Acevedo-Reyes, Implementation of classical nucleation and growth theories for precipitation, *Acta Mater.* 56 (2008) 2119–2132. <https://doi.org/10.1016/j.actamat.2007.12.050>.
- [239] O.R. Myhr, O. Grong, Modelling of non-isothermal transformations in alloys containing a particle distribution, *Acta Mater.* 48 (2000) 1605–1615. [https://doi.org/10.1016/S1359-6454\(99\)00435-8](https://doi.org/10.1016/S1359-6454(99)00435-8).
- [240] B. Sonderegger, E. Kozeschnik, H. Leitner, H. Clemens, J. Svoboda, F.D. Fischer, P. Staron, Kinetics of Precipitation in a Complex Hot-work Tool Steel, *Steel Res. Int.* 81 (2010) 64–73. <https://doi.org/10.1002/SRIN.200900069>.
- [241] Y. Yang, B. Wang, Z.D. Wang, Y.M. Li, G.D. Wang, R.D.K.K. Misra, Modeling the Precipitation Kinetics of Cementite in Bainite in 0.17% Carbon Steel, *Mater. Sci. Forum.* 898 (2017) 832–839. <https://doi.org/10.4028/WWW.SCIENTIFIC.NET/MSF.898.832>.
- [242] P. Bała, J. Krawczyk, A. Hanc, P. Baa La, A. Hanc, The Mossbauer spectroscopy studies of epsilon to cementite carbides transformation during isothermal heating from as-quenched state of high carbon tool steel, *Acta Phys. Pol. A.* 114 (2008). <https://rebus.us.edu.pl/handle/20.500.12128/8285>.
- [243] D. Ju, X. Deng, Modeling and Simulation of Iron-Carbon Phase Transformation During Tempering of Steel, *Rare Met. Mater. Eng.* 41 (2012) 6–12.
- [244] C. Wagner, Theorie der Alterung von Niederschlägen durch Umlösen (Ostwald-Reifung), *Zeitschrift Für Elektrochemie, Berichte Der Bunsengesellschaft Für Phys. Chemie.* 65 (1961) 581–591. <https://doi.org/10.1002/BBPC.19610650704>.
- [245] I.M. Lifshitz, V. V. Slyozov, The kinetics of precipitation from supersaturated solid solutions, *J. Phys. Chem. Solids.* 19 (1961) 35–50. [https://doi.org/10.1016/0022-3697\(61\)90054-3](https://doi.org/10.1016/0022-3697(61)90054-3).
- [246] M. Saeglitz, G. Krauss, Deformation, fracture, and mechanical properties of low-temperature-tempered martensite in SAE 43xx steels, *Metall. Mater. Trans. A.* 28 (1997) 377–387. <https://doi.org/10.1007/s11661-997-0139-x>.
- [247] G.C. Rauch, W.C. Leslie, The extent and nature of the strength-differential effect in steels, *Metall. Trans.* 3 (1972) 377–389. <https://doi.org/10.1007/BF02642041>.
- [248] D. Huang, G. Thomas, Structure and Mechanical Properties of Tempered Martensite and Lower Bainite in Fe-Ni-Mn-C Steels, *Metall. Trans.* 2 (1971) 1587–1598.
- [249] J.P. Hirth, M. Cohen, On the strength-differential phenomenon in hardened steel, *Metall. Trans.* 1 (1970)

Bibliography

- 3–8. <https://doi.org/10.1007/BF02819235>.
- [250] R.L. Klueh, Reduced-activation bainitic and martensitic steels for nuclear fusion applications, *Curr. Opin. Solid State Mater. Sci.* 8 (2004) 239–250. <https://doi.org/10.1016/J.COSSMS.2004.09.004>.
- [251] S.C. Kennett, G. Krauss, K.O. Findley, Strengthening mechanisms in low carbon lath martensite as influenced by austenite conditioning, *Mater. Sci. Forum.* 941 (2018) 574–582. <https://doi.org/10.4028/www.scientific.net/MSF.941.574>.
- [252] E.I. Galindo Nava, P.E.J. Rivera Díaz del Castillo, E.I. Galindo-Nava, P.E.J. Rivera-Díaz-Del-Castillo, Understanding the factors controlling the hardness in martensitic steels, *Scr. Mater.* 110 (2016) 96–100. <https://doi.org/10.1016/j.scriptamat.2015.08.010>.
- [253] T. Ohmura, K. Tsuzaki, S. Matsuoka, Nanohardness measurement of high-purity Fe-C martensite, *Scr. Mater.* 45 (2001) 889–894. [https://doi.org/10.1016/S1359-6462\(01\)01121-6](https://doi.org/10.1016/S1359-6462(01)01121-6).
- [254] L. Toth, The possibilities of the retained austenite reduction on tool steels, *Eur. J. Mater. Sci. Eng.* 6 (2021) 99–105. <https://doi.org/10.36868/EJMSE.2021.06.02.099>.
- [255] H. Muir, B. Averbach, M. Cohen, The elastic limit and yield behavior of hardened steels., *Trans. ASM.* 47 (1955) 380–407.
- [256] M. Roberts, W. Owen, Solid solution hardening by carbon and nitrogen in ferrous martensites, *Phys. Prop. Martensite Bainite.* (1965) 171–178.
- [257] R. Rodriguez, I. Gutierrez, Unified Formulation to Predict the Tensile Curves of Steels with Different Microstructures, *Mater. Sci. Forum.* 426–432 (2003) 4525–4530. <https://doi.org/10.4028/WWW.SCIENTIFIC.NET/MSF.426-432.4525>.
- [258] J. Hidalgo, M.J. Santofimia, Effect of Prior Austenite Grain Size Refinement by Thermal Cycling on the Microstructural Features of As-Quenched Lath Martensite, *Metall. Mater. Trans. A.* 47 (2016) 5288–5301. <https://doi.org/10.1007/s11661-016-3525-4>.
- [259] T. Ohmura, T. Hara, K. Tsuzaki, Evaluation of temper softening behavior of Fe-C binary martensitic steels by nanoindentation, *Scr. Mater.* 49 (2003) 1157–1162. <https://doi.org/10.1016/j.scriptamat.2003.08.025>.
- [260] M. Tanaka, T. Morikawa, S. Yoshioka, K. Takashima, S. Kaneko, Inhomogeneity of Plastic Deformation after Yielding in Low-carbon Martensitic Steels, *ISIJ Int.* 62 (2022) 353–360. <https://doi.org/10.2355/ISIJINTERNATIONAL.ISIJINT-2021-287>.
- [261] L. Morsdorf, O. Jeannin, D. Barbier, M. Mitsuhara, D. Raabe, C.C. Tasan, Multiple mechanisms of lath martensite plasticity, *Acta Mater.* 121 (2016) 202–214. <https://doi.org/10.1016/j.actamat.2016.09.006>.
- [262] F. Maresca, V.G. Kouznetsova, M.G.D.D. Geers, Deformation behaviour of lath martensite in multi-phase steels, *Scr. Mater.* 110 (2016) 74–77. <https://doi.org/10.1016/j.scriptamat.2015.08.004>.
- [263] M. Sugiyama, G. Sawa, K. Hata, N. Maruyama, Heterogeneous microstructure of low-carbon lath martensite with continuous yielding behavior in Fe-C-Mn alloys, *IOP Conf. Ser. Mater. Sci. Eng.* 580 (2019). <https://doi.org/10.1088/1757-899X/580/1/012045>.
- [264] S. Morooka, Y. Tomota, T. Kamiyama, Heterogeneous Deformation Behavior Studied by in Situ Neutron Diffraction during Tensile Deformation for Ferrite, Martensite and Pearlite Steels, *ISIJ Int.* 48 (2008) 525–530. <https://doi.org/10.2355/ISIJINTERNATIONAL.48.525>.
- [265] S. Takaki, K.-L.L. Ngo-Huynh, N. Nakada, T. Tsuchiyama, Strengthening Mechanism in Ultra Low Carbon Martensitic Steel, *ISIJ Int.* 52 (2012) 710–716. <https://doi.org/10.2355/isijinternational.52.710>.
- [266] B. Hutchinson, D. Lindell, M. Barnett, Yielding Behaviour of Martensite in Steel, *ISIJ Int.* 55 (2015) 1114–1122. <https://doi.org/10.2355/isijinternational.55.1114>.
- [267] B. Hutchinson, P. Bate, D. Lindell, A. Malik, M. Barnett, P. Lynch, Plastic yielding in lath martensites – An alternative viewpoint, *Acta Mater.* 152 (2018) 239–247. <https://doi.org/10.1016/j.actamat.2018.04.039>.
- [268] L. Malik, J.A.A. Lund, A study of strengthening mechanisms in tempered martensite from a medium carbon steel, *Metall. Trans.* 3 (1972) 1403–1406. <https://doi.org/10.1007/BF02643024>.
- [269] H.K.D.H. Bhadeshia, C.H. Young, Strength of mixtures of bainite and martensite, *Mater. Sci. Technol.* 10 (1994) 209–214. <http://www.maneyonline.com/doi/abs/10.1179/mst.1994.10.3.209>.
- [270] J.P. Naylor, The influence of the lath morphology on the yield stress and transition temperature of

Bibliography

- martensitic- bainitic steels, *Metall. Trans. A.* 10 (1979) 861–873. <https://doi.org/10.1007/BF02658305>.
- [271] S. Maropoulos, J.D.H. Paul, N. Ridley, Microstructure–property relationships in tempered low alloy Cr–Mo–3.5Ni–V steel, *Mater. Sci. Technol.* 9 (1993) 1014–1020. <https://doi.org/10.1179/mst.1993.9.11.1014>.
- [272] P.E.J. Rivera Díaz del Castillo, K. Hayashi, E.I. Galindo-Nava, Computational design of nanostructured steels employing irreversible thermodynamics, *Mater. Sci. Technol.* 29 (2013) 1206–1211. <https://doi.org/10.1179/1743284712y.0000000179>.
- [273] V.A. Lubarda, X. Markenscoff, Configurational force on a lattice dislocation and the Peierls stress, *Arch. Appl. Mech.* 77 (2007) 147–154. <https://doi.org/10.1007/s00419-006-0068-y>.
- [274] G. Beranger, G. Henry, G. Sanz, *Le livre de l'acier*, Technique & Documentation Lavoisier, 1999.
- [275] K. Kwak, T. Mayama, Y. Mine, K. Takashima, Anisotropy of strength and plasticity in lath martensite steel, *Mater. Sci. Eng. A.* 674 (2016) 104–116. <https://doi.org/10.1016/j.msea.2016.07.047>.
- [276] C. Du, J.P.M. Hoefnagels, R. Vaes, M.G.D. Geers, Block and sub-block boundary strengthening in lath martensite, *Scr. Mater.* 116 (2016) 117–121. <https://doi.org/10.1016/j.scriptamat.2016.01.043>.
- [277] K. Takeda, N. Nakada, T. Tsuchiyama, S. Takaki, Effect of Interstitial Elements on Hall–Petch Coefficient of Ferritic Iron, *ISIJ Int.* 48 (2008) 1122–1125. <https://doi.org/10.2355/ISIJINTERNATIONAL.48.1122>.
- [278] K. Kwak, Y. Mine, S. Morito, T. Ohmura, K. Takashima, Correlation between strength and hardness for substructures of lath martensite in low- and medium-carbon steels, *Mater. Sci. Eng. A.* 856 (2022) 144007. <https://doi.org/10.1016/J.MSEA.2022.144007>.
- [279] A. Deschamps, Y. Brechet, Influence of predeformation and ageing of an Al–Zn–Mg Alloy-II. Modeling of precipitation kinetics and yield stress, *Acta Mater.* 47 (1998) 293–305. [https://doi.org/10.1016/S1359-6454\(98\)00296-1](https://doi.org/10.1016/S1359-6454(98)00296-1).
- [280] P.B. Hirsch, F.J. Humphreys, *Physics of strength and plasticity*, MIT Press, Cambridge, 1969.
- [281] N. Jia, Y.F. Shen, J.W. Liang, X.W. Feng, H.B. Wang, R.D.K. Misra, Nanoscale spheroidized cementite induced ultrahigh strength-ductility combination in innovatively processed ultrafine-grained low alloy medium-carbon steel, *Sci. Reports* 2017 71. 7 (2017) 1–9. <https://doi.org/10.1038/s41598-017-02920-9>.
- [282] J. Klemm-Toole, J. Benz, S.W. Thompson, K.O. Findley, A quantitative evaluation of microalloy precipitation strengthening in martensite and bainite, *Mater. Sci. Eng. A.* 763 (2019) 138145. <https://doi.org/10.1016/j.msea.2019.138145>.
- [283] A.J.E. Foreman, M.J. Makin, Dislocation movement through random arrays of obstacles, *Can. J. Phys.* 45 (1967) 511–517. <https://doi.org/10.1139/P67-044>.
- [284] T.J. Koppelaar, D. Kuhlmann-Wilsdorf, THE EFFECT OF PRESTRESSING ON THE STRENGTH OF NEUTRON-IRRADIATED COPPER SINGLE CRYSTALS, *Appl. Phys. Lett.* 4 (2004) 59. <https://doi.org/10.1063/1.1753962>.
- [285] R. Bonadé, P. Spätig, M. Victoria, T. Yamamoto, G.R. Odette, Tensile properties of a tempered martensitic iron-chromium-carbon model alloy, *J. Nucl. Mater.* 329–333 (2004) 278–282. <https://doi.org/10.1016/j.jnucmat.2004.04.054>.
- [286] R. Bonadé, P. Spätig, R. Schäublin, M. Victoria, Plastic flow of martensitic model alloys, *Mater. Sci. Eng. A.* 387–389 (2004) 16–21. <https://doi.org/10.1016/j.msea.2004.02.074>.
- [287] F. Roters, P. Eisenlohr, L. Hantcherli, D.D. Tjahjanto, T.R. Bieler, D. Raabe, Overview of constitutive laws, kinematics, homogenization and multiscale methods in crystal plasticity finite-element modeling: Theory, experiments, applications, *Acta Mater.* 58 (2010) 1152–1211. <https://doi.org/10.1016/j.actamat.2009.10.058>.
- [288] T.M. Hatem, M.A. Zikry, Dislocation density crystalline plasticity modeling of lath martensitic microstructures in steel alloys, *Philos. Mag.* 89 (2009) 3087–3109. <https://doi.org/10.1080/14786430903185999>.
- [289] F. Sun, E.D. Meade, N.P. O'Dowd, Microscale modelling of the deformation of a martensitic steel using the Voronoi tessellation method, *J. Mech. Phys. Solids.* 113 (2018) 35–55. <https://doi.org/10.1016/j.jmps.2018.01.009>.
- [290] C. Robertson, *Endommagement des alliages métalliques et plasticité cristalline*, HDR, Institut national Polytechnique de Grenoble, 2008.

Bibliography

- [291] J. Polak, M. Klesnil, The hysteresis loop 1. A statistical theory, *Fatigue Fract. Eng. Mater. Struct.* 5 (1982) 19–32. <https://doi.org/10.1111/J.1460-2695.1982.TB01221.X>.
- [292] A. Arlazarov, O. Bouaziz, A. Hazotte, M. Gouné, S. Allain, Characterization and Modeling of Manganese Effect on Strength and Strain Hardening of Martensitic Carbon Steels, *ISIJ Int.* 53 (2013) 1076–1080. <https://doi.org/10.2355/isijinternational.53.1076>.
- [293] L.R.C. Cupertino Malheiros, E.A.P. Rodriguez, A. Arlazarov, Mechanical behavior of tempered martensite: Characterization and modeling, *Mater. Sci. Eng. A.* 706 (2017) 38–47. <https://doi.org/10.1016/j.msea.2017.08.089>.
- [294] A.S. Keh, S. Weissmann, Deformation Substructure in bcc Metals, in: *Electron Microsc. Strength Cryst.*, 1963: pp. 231–300.
- [295] T. Ungár, A.D. Stoica, G. Tichy, X.L. Wang, Orientation-dependent evolution of the dislocation density in grain populations with different crystallographic orientations relative to the tensile axis in a polycrystalline aggregate of stainless steel, *Acta Mater.* 66 (2014) 251–261. <https://doi.org/10.1016/J.ACTAMAT.2013.11.012>.
- [296] L.P. Kubin, Y. Estrin, Evolution of dislocation densities and the critical conditions for the Portevin-Le Châtelier effect, *Acta Metall. Mater.* 38 (1990) 697–708. [https://doi.org/10.1016/0956-7151\(90\)90021-8](https://doi.org/10.1016/0956-7151(90)90021-8).
- [297] A. Lambert-Perlade, Rupture par clivage de microstructures d'aciers bainitiques obtenues en conditions de soudage, PhD thesis, École Nationale Supérieure des Mines de Paris, 2004. <https://pastel.archives-ouvertes.fr/tel-00005749> (accessed October 14, 2022).
- [298] A. Malik, G. Amberg, A. Borgenstam, J. Ågren, Effect of external loading on the martensitic transformation – A phase field study, *Acta Mater.* 61 (2013) 7868–7880. <https://doi.org/10.1016/J.ACTAMAT.2013.09.025>.
- [299] D. Löhe, O. Vöhringer, Stability of residual stresses, in: *Handb. Residual Stress Deform. Steel*, ASM International, 2002: pp. 54–69.
- [300] C. Zener, Theory of strain interaction of solute atoms, *Phys. Rev.* 74 (1948) 639–647. <https://doi.org/10.1103/PhysRev.74.639>.
- [301] P. Maugis, D. Connétable, P. Eyméoud, Stability of Zener order in martensite: an atomistic evidence, *Scr. Mater.* 194 (2021). <https://doi.org/10.1016/j.scriptamat.2020.113632>.
- [302] P. Maugis, A Temperature–Stress Phase Diagram of Carbon-Supersaturated bcc-Iron, Exhibiting “Beyond-Zener” Ordering, *J. Phase Equilibria Diffus.* 41 (2020) 269–275. <https://doi.org/10.1007/s11669-020-00816-2>.
- [303] N. Maruyama, S. Tabata, H. Kawata, Excess Solute Carbon and Tetragonality in As-Quenched Fe-1Mn-C (C:0.07 to 0.8 Mass Pct) Martensite, *Metall. Mater. Trans. A.* 51 (2020) 1085–1097. <https://doi.org/10.1007/s11661-019-05617-y>.
- [304] J. Hoyos, A. Ghilarducci, H. Salva, J. Vélez, Evolution of Martensitic Microstructure of Carbon Steel Tempered at Low Temperatures, *Procedia Mater. Sci.* 1 (2012) 185–190. <https://doi.org/10.1016/j.mspro.2012.06.025>.

Resume en anglais

Martensitic steels have been known and used for millennia now, but the origins of their strength and work hardening have remained a source of controversy. Since few years, the understanding of their mechanical behavior is changing paradigm. Many researchers have put into evidence the interest not to describe lath martensite as an homogeneous microstructure but more as a multiphase aggregate, a composite, resulting from the sequential nature of the phase transformation at low temperature. According to such new schemes, the martensite behavior is controlled by the microstructural heterogeneities, ie. the spatial distribution of lath sizes, of dislocations, of carbon segregations and of carbides and not only by their mean values. To these microstructural elements are added large distributions of hydrostatic and deviatoric internal stresses resulting from the displacive phase transformation process. This work contributes to this new movement by providing a quantitative description of these distributions in as-quenched and further tempered martensitic steels and their impact on their mechanical behaviors thanks to a integrated physical-based micromechanical approach, including probabilistic aspects.

We have first developed a methodology to determine the dislocation densities in martensite and in austenite along the transformation by in situ HEXRD experiments. Based on a metallurgical reasoning, the spatial dislocation density distribution as well as its associated hardening were estimated for the first time. In situ HEXRD tempering experiments were also performed to characterize the recovery from the as-quenched state. An original modeling approach accounting for the spatial distribution of dislocations was set up to predict their density decrease during a heat treatment.

In the same way, the microtextures of the studied microstructures were investigated by SEM-EBSD in order to assess the size distribution of the different features of martensite, as laths, blocks, packets and prior austenite grains. A statistical approach combining this latter contribution to the hardening with the one associated with dislocations explains successfully the observed distribution of the local yield strength in the as-quenched microstructures.

In situ HEXRD tempering experiments and additional APT and TEM observations were used to characterize also the respective precipitation state of transition carbides and cementite as well as the carbon segregations along heat treatments. All this experimental work has served to develop and calibrate a phase transformation model to calculate carbon segregation on dislocations, transition carbides and cementite precipitation states. Such model was for instance able to predict the suppression of transition carbide precipitation in very low carbon steels. The investigation of tempering is necessary to understand the strengthening due the sole carbon in martensite.

Finally, our original micromechanical model describing the martensite behavior as an extended elastic/plastic transition accounts for the previous combined hardening due to size effects and dislocations, the distribution of internal stresses due to the transformation and the tempering state (relaxation, recovery, segregation and precipitation state). The model successfully explains the strength and work-hardening of the studied steels (as quenched and tempered) in a unified framework.

Résumé en français

Les aciers martensitiques sont connus et utilisés depuis des millénaires, mais l'origine de leur résistance et de leur écrouissage reste une source de controverse. Depuis quelques années, la compréhension de leur comportement mécanique est en train de changer de paradigme. De nombreux chercheurs ont mis en évidence l'intérêt de ne pas décrire la martensite en lattes comme une microstructure homogène mais plutôt comme un agrégat multiphasé, un composite, résultant de la nature séquentielle de la transformation de phase à basse température. Selon ces nouveaux schémas, le comportement de la martensite est contrôlé par les hétérogénéités microstructurales, c'est-à-dire la distribution spatiale des tailles des lattes, des dislocations, des ségrégations de carbone et des carbures, et pas seulement par leurs valeurs moyennes. A ces éléments microstructuraux s'ajoutent la distribution de contraintes internes hydrostatiques et déviatoriques résultant du processus de transformation de phase displacive. Ce travail contribue à cette nouvelle tendance en fournissant une description quantitative de ces distributions dans les aciers martensitiques trempés et revenus et leur impact sur leurs comportements mécaniques grâce à une approche micromécanique complète à base physique, incluant les aspects probabilistiques.

Nous avons d'abord développé une méthodologie pour déterminer les densités de dislocation dans la martensite et dans l'austénite le long de la transformation par des expériences in situ de DRXHE. Sur la base d'un raisonnement métallurgique, la distribution spatiale de la densité de dislocation ainsi que le durcissement associé ont été estimés pour la première fois. Des expériences de revenu en DRXHE in situ ont également été réalisées pour caractériser la restauration de l'état trempé. Une approche originale de modélisation tenant compte de la distribution spatiale des dislocations a été mise en place pour prédire la diminution de leur densité lors d'un traitement thermique.

De même, les microtextures des microstructures étudiées ont été étudiées par MEB-EBSD afin d'évaluer la distribution en taille des différentes caractéristiques de la martensite, comme les lattes, les blocs, les paquets et les anciens grains d'austénite. Une approche statistique combinant cette dernière contribution au durcissement avec celle associée aux dislocations explique avec succès la distribution observée de la limite d'élasticité locale dans les aciers trempés.

Des expériences de revenu DRXHE in situ et des observations complémentaires APT et MET ont été utilisées pour caractériser également l'état de précipitation des carbures de transition et de la cémentite ainsi que les ségrégations de carbone au cours des traitements thermiques. Ce travail expérimental a servi à développer et calibrer un modèle de transformation de phase pour calculer la ségrégation du carbone sur les dislocations, les carbures de transition et les états de précipitation de la cémentite. Ce modèle a par exemple permis de prédire la suppression de la précipitation des carbures de transition dans les aciers à très faible teneur en carbone. L'étude du revenu est nécessaire pour comprendre la contribution dû au seul carbone au durcissement et à la plasticité de la martensite.

Enfin, notre modèle micromécanique original décrivant le comportement de la martensite comme une transition élastique/plastique étendue tient compte du durcissement combiné précédent dû aux effets de taille et aux dislocations, de la distribution des contraintes internes dues à la transformation et de l'état de revenu (relaxation, restauration, ségrégation et état de précipitation). Le modèle explique avec succès la résistance et l'écrouissage des aciers étudiés (trempés ou trempés/revenus), dans un cadre unifié.